Liquid crystals and novel gain materials for thin-film photonic devices

Simon Wood

Balliol College

A thesis submitted for the degree of

Doctor of Philosophy in Engineering Science

Abstract

Liquid crystals and novel gain materials for thin-film photonic devices

Submitted for the degree of *Doctor of Philosophy*

Simon Wood, Balliol College, Trinity Term 2016

This thesis describes work to create a variety of thin-film photonic devices based upon liquid crystalline materials. Firstly, a variety of liquid crystal phases are polymer-templated by combining a liquid crystalline material with photo-polymerisable reactive mesogens. Upon photo-curing, a polymer scaffold, which is a template of the original phase, is formed with liquid crystal molecules in interstitial sites. This liquid crystal is removed to yield a polymer scaffold which can be used to template the original phase. Here, polymer-templating is used to template the smectic A liquid crystal alignment onto nematic liquid crystals for the first time; this results in materials with improved contrast ratios and faster response times than conventional nematic devices. Next, a study is performed to compare the electro-optic properties of polymer-templated and polymer-stabilised chiral nematic liquid crystals. The enhanced tuning range of polymer-templated liquid crystals is applied to create a polymer-templated liquid crystal laser and to electrically tune its emission wavelength. Subsequently, thin-film elastomeric liquid crystal lasers are created. The lasing wavelength of these films can be reversibly and selectively tuned without hysteresis by subjecting them to a mechanical stress. Finally, work is performed to study the potential of inorganic materials for use in liquid crystal lasers. Transition metal clustomesogens (liquid crystalline materials that contain highly emissive molybdenum clusters) and inorganic-organic perovskites are considered here. The dispersal and emissive properties of clustomesogens in liquid crystals are studied, and they are used to create circularly polarised light sources with a polarisation that can be controlled using electric fields. Layered structures of inorganic-organic perovskite and liquid crystal are created; these exhibit enhanced amplified spontaneous emission. Then, perovskites are used as the gain materials in distributed feedback lasers for the first time. These lasers may be wavelength-tuned by varying the grating spacing of the structure.

Abbreviation list

AFM – **A**tomic **F**orce **M**icroscopy

ASE – **A**mplified **S**pontaneous **E**mission

ALD – **A**tomic **L**ayer **D**eposition

CM – **C**lustomesogen

DFB – **D**istributed **F**eed**b**ack

LC – **L**iquid **C**rystal

PL – **P**hoto**l**uminescence

PLQE – **P**hoto**l**uminescence **Q**uantum **E**fficiency

SEM – **S**canning **E**lectron **M**icroscopy

SmA – **Sm**ectic **A**

Acknowledgements

Thanks to my supervisor, Prof Steve Morris – who has always gone above and beyond – for example reading and carefully editing anything I've sent him – whether it's a paper draft or a CV, and for involving me in a variety of collaborations and introducing me to many academics. Academically, he has provided a great deal of support – encouraging independence and allowing me the freedom to explore my own projects, while providing assistance and advice for improving ideas or taking them forwards.

Also, thanks to Prof Steve Elston for his help with experiments and his constant new ideas for novel or improved experiments as well as his deep expertise in the field – something which has greatly helped me to elucidate the theory of my experiments.

Dr Julian Fells provided a great deal of experimental help thanks to his expertise with electrical systems and MATLAB; this was invaluable in the final months of my DPhil. His constant professionalism and perspectives on situations were greatly helpful. It was nice to have someone else in the office to make the last 6 months of my DPhil less isolated, and Julian was the perfect person to fill that role – providing useful advice, pastoral support, and an ear for my rants. Thanks.

Thanks also to Grahame Faulkner, for providing logistical support and for always knowing the right person to speak to in in order to solve a problem – or where to look to find a vital piece of equipment.

Dr Flynn Castles provided me with guidance on polymer-templating liquid crystals, as well as regularly providing useful advice and good ideas to further my research.

The clustomesogen materials used in Chapter 6 were provided by researchers from the University of Rennes 1. I would like to thank Dr Yann Molard for his support in supplying the materials and advice for their use, and Dr Marianne Prévôt for helping set up the collaboration and providing advice on using the materials. Thanks to Prof Sai Ghosh and her team at the University of California, Merced, for performing photoluminescence-mapping experiments on the clustomesogens.

Many of the experiments performed in Chapter 7 on inorganic-organic perovskites were performed in collaboration with the Physics department at the University of Oxford. I would like to thank Prof Henry Snaith and Dr Moritz Riede for their advice, help and for providing me with access to their experimental resources and materials. I would particularly like to thank Dr Sam Stranks and Dr Michael Saliba for their assistance in the lab, enthusiasm and professionalism. Additionally, thanks to Prof Albert Schenning, Hitesh Khandelwhal and their lab at the University of Eindhoven for providing the liquid crystal reflectors integral to the work.

I would like to thank EPSRC for funding my DPhil. Furthermore, I would like to thank the IET, the British Liquid Crystal Society and Balliol College for providing me with funding to travel to attend conferences.

List of publications, patents, presentations and prizes

Publications

1) S. D. Stranks, **S. M. Wood**, K. Wojciechowski, F. Deschler, M. Saliba, H. Khandelwal, J. B. Patel, S. Elston, L. M. Herz, M. B. Johnston, A. P. H. J. Schenning, M. G. Debije, M. Riede, S. M. Morris, and H. J. Snaith, "Enhanced Amplified Spontaneous Emission in Perovskites using a Flexible Cholesteric Liquid Crystal Reflector.," *Nano Lett.*, **15**, 4293, May 2015.
2) **S. M. Wood,** M. Prévôt, M. Amela-Cortes, S. Cordier, S. J. Elston, Y. Molard, and S. M. Morris, "Polarized Phosphorescence of Isotropic and Metal-Based Clustomesogens Dispersed into Chiral Nematic Liquid Crystalline Films," *Adv. Opt. Mater.*, **3**, 1368, Jul. 2015.
3) M. Saliba, **S. M. Wood**, J. B. Patel, P. K. Nayak, J. Huang, J. A. Alexander-Webber, B. Wenger, S. D. Stranks, M. T. Hörantner, J. T.-W. Wang, R. J. Nicholas, L. M. Herz, M. B. Johnston, S. M. Morris, H. J. Snaith, and M. K. Riede, "Structured Organic-Inorganic Perovskite toward a Distributed Feedback Laser.," *Adv. Mater.*, **28**, 923, Dec. 2015.
4) **S. M. Wood,** F. Castles, S. Elston, and S. M. Morris, "Wavelength tuneable laser emission from stretchable chiral nematic liquid crystal gels via in-situ photopolymerization," *RSC Adv.*, **6**, 31919, Mar. 2016.
5) **S. M. Wood**, S. J. Elston and S. M. Morris, "Wavelength-tuneable laser emission from a dye-doped achiral nematic liquid crystal dispersed into a chiral polymer scaffold", *Mol. Cryst*, **632,** 89, 2016
6) **S. M. Wood**, J. A. J. Fells, S. J. Elston, S. M. Morris, "Wavelength tuning of the photonic band gap of an achiral nematic liquid crystal filled into a chiral polymer scaffold", *Macromolecules*, **29**, 8643, 2016
7) **S. M. Wood**, J. A. J. Fells, S. J. Elston, S. M. Morris "The electro-optic characteristics of an achiral nematic liquid crystal in a polymer template of the smectic A liquid crystal phase." Being prepared for submission to Advanced Materials.

Patent applications

Distributed Feedback Perovskite Laser

Presentations

British Liquid Crystal Society Conference 2014 – oral

International Liquid Crystal Society Conference 2014 – poster

European Material Research Symposium 2015 – poster

European Conference on Liquid Crystals 2015 – oral

British Liquid Crystal Society Workshop on Emerging Liquid Crystal Technologies 2016 – poster

Prizes

IET scholarship (£500) 2014

Oxford Photonics Society Best Poster Prize 2015 and 2016 (£375)

British Liquid Crystal Society Scholarship 2014 and 2015 (£250)

Balliol College 750 prize for the Sciences (£250)

MPLS three-minute thesis competition – Winner

Contents

Chapter 1 – Introduction

In this Thesis, I describe work to create a variety of thin-film photonic devices, mostly based upon liquid crystal (LC) materials. This Chapter serves as an introduction to the Thesis and provides an overview of the work described in the subsequent Chapters.

Chapter 2 details the background information pertinent to this work. This includes an introduction to LCs, the corresponding mesophases (particularly the nematic, chiral nematic and smectic A phases used in this work), their physical and optical properties and an explanation of how the different phases may be identified using optical polarising microscopy. Next, I introduce lasers and the basic principle of their operation. This is followed by an introduction to LC lasers specifically, including their potential modes of operation, their key characteristics and the materials that they are made from. Subsequently in Chapter 2, I will describe the core experimental techniques that are used throughout my work – particularly focussing on: making LC mixtures, filling them into cells and photo-curing them. I then detail the techniques used to characterise the devices and materials used here – techniques such as optical polarising microscopy, transmission spectroscopy and optical pumping experiments.

Chapters 3 and 4 detail work to polymer-template various LC phases. Polymer-templating of LCs is a recent innovation that involves mixing LCs with a reactive mesogen – a material that is itself a LC and that will photo-polymerise when exposed to UV radiation. When these reactive mesogen-containing materials are photo-cured, a polymer network is created that has been imprinted with the structure of the host LC. The LC itself may then be washed out to leave a polymer scaffold. This polymer scaffold may be refilled (for example with an achiral nematic LC); this results in it regaining the photonic structure of the original phase – a photonic band-gap in the case of a chiral nematic LC, for example.

Chapter 3 describes my work to use this polymer-templating technique on smectic A materials in order to imprint the alignment of the smectic A phase onto a nematic LC; this results in devices with improved electro-optic properties compared to a conventional nematic device. I describe how to make these devices and to characterise them. Particularly, I study their transmission-voltage curves, their response times and their contrast ratios and compare these properties to those of conventional nematics. The templated smectic A LCs show an improvement in the contrast ratio of ~12x, and a faster response time of ~6x.

The improved electro-optical properties in polymer-templated smectic A LCs led me to consider applying the polymer-templating technique to the chiral nematic LC phase and studying the effect of the templating procedure on the chiral nematic electro-optic properties. The chiral nematic phase is particularly interesting because it possesses a 1D photonic band-gap (reflection band) for visible light, which has resulted in a variety of applications for the phase (such as lasers and mirrors). To this end, in Chapter 4 I describe work to study the electro-optic properties of polymer-templated chiral nematic LCs and to compare them to those of conventional polymer-stabilised LCs. I have found that when an electric field is applied to the polymer-templated samples, there is an initial blue-shift of the long-wavelength edge of the band-gap that occurs on a relatively rapid timescale (τ ~1 ms) followed by a considerably slower blue-shift (τ ~6.5 s) of the entire band-gap. This is different behaviour to that seen in a conventional polymer-stabilised chiral nematic LC where a relatively fast blue-shift of only the long-wavelength band-edge is observed. I compare the wavelength tuning characteristics for the two different types of sample and find that for the templated sample the tuning range of the long wavelength band-edge is 2.5 times greater than that observed for the polymer-stabilised chiral nematic LC. I seek to provide a possible explanation for the two tuning mechanisms that are observed.

Subsequently, since chiral nematic LCs form the basis of many LC lasers, I continue Chapter 4 with a description of my work to apply these improved electro-optical properties to laser devices. I do this by refilling the polymer scaffold with a dye-doped achiral nematic. This resulted in the creation of the first polymer-templated chiral nematic LC laser. I compare this polymer-templated LC laser to a more conventional polymer-stabilised LC laser. As would be expected from the results for templated chiral nematics, I see a greater wavelength-tuning range in the case of the polymer-templated lasers (by a factor of 2.5 times). There was also an improvement in the device morphology – because in templated devices, the dye is added after photo-curing the dye does not interference with the curing process. Thus, polymer-templating offers a route towards widely wavelength-tuneable LC lasers, as well as providing additional utility by adding the dye after photo-curing has been performed.

In addition to applying electric-fields, a variety of other methods have been used to wavelength-tune LC lasers. In Chapter 5, I present work to create lasers that may be mechanically tuned by stretching them. I have created polymer-stabilised lasers that contain a sufficiently high reactive mesogen concentration that a free-standing,

elastomeric laser gel may be created after the photopolymerisation procedure. When these thin film lasers are stretched in a direction perpendicular to the LC helix axis, the film thins, the LC pitch decreases and so the chiral nematic photonic band gap blue-shifts. This is particularly exciting because the wavelength tuning is repeatable, reversible and does not exhibit hysteresis. This means that the laser gels are promising candidates for applications such as strain sensors and actuators. The technique I present here – where a combination of reactive and non-reactive LC material is used – is a much simpler manufacturing technique than those used previously to create LC elastomer lasers. Additionally, the technique yields improved photonic structures because in our technique I can use conventional glass cells coated with alignment layers to achieve a good alignment before photo-curing; this is not possible using other techniques in which the alignment is achieved using more complex means (such as anisotropic deswelling using a solvent).

I begin Chapter 5 with an outline of the procedure for fabricating the stretchable gels. This is followed by a study of the mechanical properties (particularly the mechanochromic range and sensitivity) of different elastomeric gels created using different reactive mesogen concentrations. From this, I determined an optimum reactive mesogen concentration and subsequently I describe work to dope the gels with a fluorescent dye and optically pump them. The films lase and the laser wavelength can be continuously tuned (by ~45 nm) by mechanically extending the films along a direction perpendicular to the helicoidal axis of the chiral nematic LC. This tuning of the wavelength is found to be reversible and does not exhibit any measurable hysteresis, thereby allowing repeatable selection of a desired laser wavelength by controlling the film elongation. Because the technique is so versatile, it is possible to photo-polymerise different areas of the thin-films at different temperatures to pattern the gels in such a way that different regions of the gel emit at different laser wavelengths.

While Chapters 4 and 5 describe methods for wavelength-tuning a LC laser, such lasers currently have a major disadvantage – they use fluorescent dyes as their gain materials. Fluorescent dyes are easily photo-bleached under continuous-wave illumination. This means that they can only be operated in a pulsed mode at low repetition rates, and this limits their utility. Thus, in Chapters 6 and 7 I explore novel gain materials that may be compatible with liquid crystalline materials. The most promising candidates to replace dyes are inorganic materials, however inorganic materials are not typically compatible with organic solvents (such as LCs) making device fabrication difficult (particularly in

contrast to a conventional LC laser where the fluorescent dye may simply be thermally dispersed into the LC).

In Chapter 6, I detail work to investigate transition metal clustomesogens (CMs) as potential gain media for LC lasers. The CMs used in this work are octahedral clusters of molybdenum with long organic ligands – thus, they are both emissive (from the metal cluster) and liquid crystalline (due to the long organic ligands). These CMs are not susceptible to photo-bleaching, have high quantum yields and good photo-stabilities. Furthermore, they are found to exhibit nematic LC phases and are also easily dispersed into a variety of other LC phases. This circumvents the usual incompatibility of inorganic and organic species with each other and so makes them ideal candidates for alternative gain media. The CMs used here were synthesised and supplied by our collaborators led by Dr Y. Molard from the University of Rennes 1.

Chapter 6 begins with a description of work to disperse such clusters into a nematic LC and to investigate the effect on their emissive properties. An optimum concentration of CM in LC is determined and the photoluminescence properties of the mixtures are probed in detail, including using photoluminescence-mapping (in collaboration with the University of California, Merced). Subsequently, the CMs are dispersed into chiral nematic LCs. However, the CM devices do not exhibit lasing in the same manner as the fluorescent dyes used in conventional devices; this could be because CMs are phosphorescent materials (unlike the fluorescent dyes). Nevertheless, it was possible to control the CM emission using the photonic band-gap of a chiral nematic LC and this led to the creation of devices in which the degree of circular polarisation of the emitted light could be controlled. Furthermore, by applying an ac electric field to influence the chiral nematic photonic band-gap, the circular polarisation of the light source could be switched off.

Chapter 7 details work on another potential gain material for lasers – specifically inorganic-organic perovskites. These are materials with the perovskite structure and the composition $CH_3NH_3PbX_3$, where X is a halogen (chlorine, bromine, iodine). They have recently received a lot of attention from the photovoltaic community due to their high photo-conversion efficiencies. However, such materials also have huge potential for use as emissive devices and are of particular interest for use in lasing applications because they are not susceptible to photo-bleaching, may be solution processed, have high efficiencies, high quantum yields and can exhibit photoluminescence at different

wavelengths (from 390 to 790 nm) depending on their composition. Also, as semiconductors, they offer potential for being electrically pumped. Thus, perovskite materials offer an exciting route towards solution-processed, electrically pumped, widely wavelength-tuneable continuous-wave lasers. I have performed work on these materials in collaboration with the team of Prof H. Snaith (University of Oxford), who has pioneered the development of these perovskite materials, Dr Moritz Riede (University of Oxford) and the team of Prof A. Schenning (University of Eindhoven) who has developed chiral nematic LC reflector materials for this work.

Because perovskites (like most inorganics) cannot simply be dispersed into LCs, Chapter 7 describes work to explore layered structures of perovskite and LC. Firstly, the perovskite was sandwiched between a chiral nematic LC reflector and a gold layer. When pumped, this device exhibited amplified spontaneous emission, a precursor to lasing. To improve this, the device was optimised with a higher-reflectivity LC reflector which further lowered the amplified spontaneous emission threshold and had the additional functionality of being flexible. Work was then performed to create a device that utilised a perovskite layer sandwiched between two LC reflectors with the aim of attaining further improvements towards creating a lasing device, and realising the potential of an all solution-processable device.

In order to utilise the desirable emission properties of the perovskites, I also worked to use it as the gain material in a laser without any LC element. To this end, I created a single-mode, wavelength-tuneable distributed feedback laser by patterning perovskite materials with a grating pattern. These lasers showed tuneable lasing that could be controlled by varying the grating spacing.

The Thesis will conclude with a description of potential future work to take the projects described in this thesis further.

Chapter 2 – Background information

In this Chapter, I will provide the background information pertinent to the work presented in this Thesis. To this end, I will introduce the topic of liquid crystals (LCs) and describe the LC phases used in the work presented here – particularly the nematic, chiral nematic and smectic A LC phases. This will include a description of the key features of the phases as well as methods for identifying them. Next, I will introduce lasers. This will incorporate both an introduction to lasers generally and to LC lasers specifically. I will consider the different modes of operation of LC lasers, the LC and gain materials used in such devices and I will describe the key LC laser characteristics. Finally, I will discuss the core experimental techniques that underpin the work described herein. These techniques include: making LC mixtures and devices, and methods for photo-polymerising reactive mesogen-containing LC mixtures. Core characterisation techniques – such as optical polarising microscopy and transmission spectroscopy – will be described, as well as methods for optically pumping devices.

2.1 – Liquid crystals

A LC is matter in a state with properties intermediate between those of a conventional liquid and a solid crystal – it is a mesophase [1]. In this Thesis, thermotropic LCs are used – LCs in which the order of the components of the system (and hence the mesophase exhibited) is changed by varying the temperature. At high temperatures (70-120°C in the case of the materials used here), such LCs exist in the isotropic phase (the properties of the phase are the same whatever direction they are viewed from) and as they are cooled various ordered states occur – such as the blue phase, smectic phases and the nematic phase (exactly which phases occur and the temperature at which they occur will depend upon the material composition). These LC phases may have positional order (the LC directors are arranged in an ordered lattice) and/or orientational order (the LC directors are roughly pointing in the same direction) [2].

LC molecules are usually organic molecules. The shape of these molecules can be broadly subdivided into ‘calamitic’ (rod-like) and ‘discotic’ (disk-like) depending on their molecular structure [3]. Discotic LCs have a disk-like rigid core and usually form columnar phases. However, for the work in this thesis calamitic LCs are used. Fig 1a shows an example calamitic LC – the molecule 5-cyanobiphenyl (5CB). Calamitic LCs usually have a rigid polarisable core (the cyanobiphenyl group in 5CB) and a flexible aliphatic tail. The polarised cores result in alignment and crystalline properties, while the flexible tail lowers the order and allows flow. Calamitic LCs can for the most part

be approximated as rods as shown in Fig 1b; this simplification will be used for the remainder of this introduction.

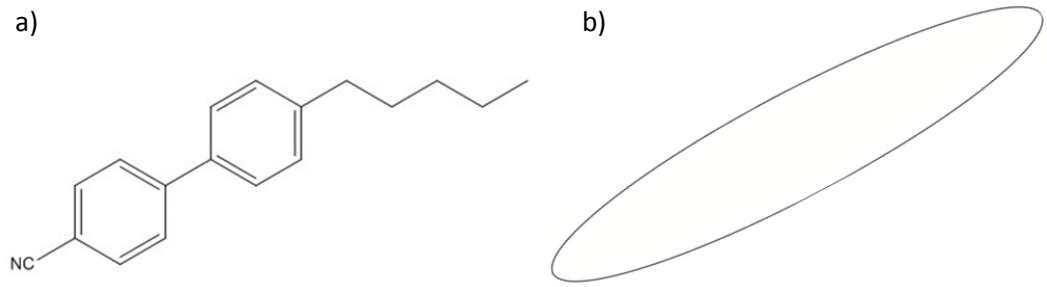

Figure 1 – The structure of a calamitic liquid crystal: a) Molecular structure of an example liquid crystal, 5-cyanobiphenyl; b) Simplified illustration of the 'rod-like' shape of a calamitic liquid crystal.

LC materials may exhibit a variety of phases. In the work described in this Thesis, the nematic, chiral nematic (also called cholesteric) and smectic A LC phases are considered.

2.2 – Nematic liquid crystals

The nematic phase is the least ordered LC phase. There is only long-range orientational order – the long axes of the molecules roughly point in the same direction, that of the director, $\hat{\mathbf{n}}$ [4] – as illustrated in Fig 2. $\hat{\mathbf{n}}$ is a directionless unit vector representing the direction of preferred orientation of molecules in the vicinity of any point. There is no positional order in a nematic LC – there is no long-range correlation between the centres of the molecules. The macroscopic optical axis is in the same direction as $\hat{\mathbf{n}}$. Because nematic LCs are not polar, $\hat{\mathbf{n}}$ and $-\hat{\mathbf{n}}$ are fully equivalent.

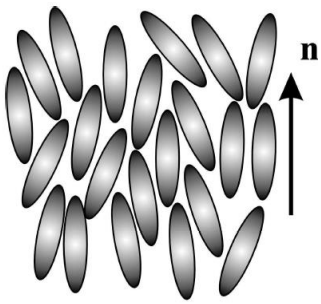

Figure 2 – An illustration of the nematic phase – all of the molecules point in roughly the same direction, that of the director, n̂.

2.2.1 – The order parameter of a nematic liquid crystal

The order in a LC system is measured using the order parameter. This describes the long-range orientational order from a microscopic perspective. It is defined as: $S = < {}^{1}/_{2(3\cos\theta - 1)} >$ where θ is the angle that the long axis of the molecule makes with the local director [5]. This is derived from the second Legendre polynomial. An

order parameter of 1 corresponds to perfect parallel alignment, while an order parameter of 0 corresponds to random orientation of the director (i.e. the isotropic phase). The order parameter is highly temperature dependent.

2.2.2 – Optical indicatrix

A nematic LC is uniaxial and has three independent refractive indices. The indicatrix is prolate shaped and the three principle refractive indices are n_x, n_y, and n_z. The equation that defines the ellipsoid can be written as:

$$\frac{x^2}{n_x^2} + \frac{y^2}{n_y^2} + \frac{z^2}{n_z^2} = 1, \tag{2.1}$$

where the direction along the z-axis is the optic axis [6]. For a uniaxial material (like a nematic LC), two of the three refractive indices are identical ($n_x = n_y$) These represent the ordinary refractive index, n_o. n_z represents the extraordinary refractive index n_e. For a uniformly aligned nematic liquid crystal the z-axis and the director axis are collinear thus the extraordinary and ordinary refractive indices become $n_e = n_{//}$ and $n_x = n_o = n_\perp$. The birefringence is then given by $\Delta n = n_{//} - n_\perp$.

2.2.3 – Dielectric properties of liquid crystals

For a nematic liquid crystal the electric permittivity is characterised by two principal components, $\varepsilon_{//}$ and $\varepsilon_\perp$ – the relative dielectric permittivities parallel and perpendicular to the director. These arise from the induced electronic polarisation and the orientational polarisation of the molecules. The induced electronic polarisation is caused by a relative displacement of the electronic and atomic densities. The orientational polarisation arises from the tendency of the permanent dipole moment to align in an electric field. The field induced polarisability depends upon the linkages in the molecule and its aromaticity. The orientational polarisation on the other hand depends upon the absolute values of the permanent dipole moments and the angles that they make with respect to the director. The dielectric anisotropy, $\Delta\varepsilon = \varepsilon_{//} - \varepsilon_\perp$, is used to characterise nematic LCs – if it is positive, then under the influence of an applied electric field the LC director will orient with the long axis in the direction of the applied field. For negative dielectric anisotropy materials, the director will orient perpendicular to the direction of the applied field.

2.2.4 – Identifying the nematic liquid phase

Nematic LCs can be identified by their optical textures when viewed on an optical polarising microscope. The texture seen will depend on how the LC is aligned [7]. Alignment is usually achieved by filling the mixtures between glass substrates that have

been treated in such a way as to encourage a particular alignment; the details of how to achieve this will be described in more detail in Section 2.6.

The texture seen when viewed on a bright-field optical polarising microscope will depend upon the transmission of light through the nematic LC. The transmission through a nematic is given by Equation 2.2, derived by considering the nematic as a uniaxial birefringent slab between crossed polarisers.

$$T = \sin^2(2\varphi)\sin^2\left(\frac{2\pi d\Delta n}{\lambda}\right), \tag{2.2}$$

where φ is the angle of the optical axis relative to the polariser axes, d is the thickness of the device, Δn is the birefringence of the LC and λ is the wavelength of incident light [8].

In a homeotropic alignment, the LC director is perpendicular to the glass substrates; thus, no birefringence is seen, only the ordinary refractive index.

In a planar-aligned LC, the LC director is aligned parallel to the substrates. The texture seen will depend whether the director is heterogenously or homogenously aligned (whether the nematic directors point in different directions or all in the same direction).

In the case of a heterogeneous planar orientation of a nematic, the director $\hat{\mathbf{n}}$ is parallel to the substrates but points in different directions. Such a structure exhibits a Schlieren texture when viewed between crossed polarisers on a polarising microscope. An example of the Schlieren texture is given in Fig 3.

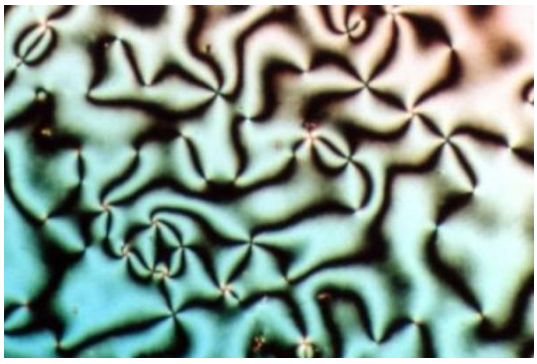

Figure 3 – The Schlieren texture of a nematic liquid crystal phase in a heterogenous planar orientation. Reproduced from Ref 9.

This texture is composed of dark brushes where the director, $\hat{\mathbf{n}}$, lies either parallel or perpendicular to the polariser/analyser axes (and so no light is transmitted). The points where brushes meet are called disclinations. When the LC sample is rotated between

crossed polarisers, the brushes move continuously indicating a continuous change of the director $\hat{\mathbf{n}}$.

When aligned in a homogeneous planar orientation between glass substrates the director $\hat{\mathbf{n}}$ is parallel to the substrates and points in the same direction. When rotated between crossed polarisers, the nematic texture is completely black when the LC director is aligned parallel or perpendicular to the polariser axis ($\varphi = 0$ or 90° in Equation 2.2). As the device is rotated, a uniform texture will be seen, as shown in Figure 4; the maximum transmission (the so-called 'bright state') will occur at $\varphi = 45°$.

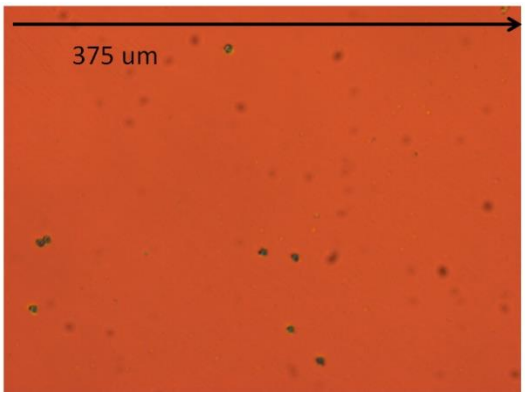

Figure 4 – The texture of the bright state of a planar, homogenously aligned nematic liquid crystal phase. The black dots are the spacer beads used to define the cell thickness (5µm). Results taken at 20°C.

2.3 – The chiral nematic liquid crystal phase

The chiral nematic LC phase is a chiral variant of the nematic phase that is also known as the cholesteric phase because it was first observed in cholesterol derivatives [10]. The chiral nematic phase occurs when the LC molecules are themselves chiral, or if chirality is added (for example using a chiral dopant, as in the work presented here). This chirality leads to a twisted configuration of the director profile which results in a macroscopic helix [11]. This helix is defined by the pitch, p, the distance it takes for the director to rotate through an angle of 2π (however, the periodicity is only half of the pitch due to the invariance between $\hat{\mathbf{n}}$ and $-\hat{\mathbf{n}}$).

When p is roughly equal to the wavelength of light shone upon a chiral nematic LC, selective reflection occurs – the LC acts as a 1D Bragg reflector for circularly polarised light that matches the rotation sense of the helix. The photonic band-gap has band-edges that occur at:

$$n_e p = \lambda_L \tag{2.3}$$

$$n_o p = \lambda_S \tag{2.4}$$

where n_e and n_o are the extraordinary (parallel to optic axis) and ordinary (perpendicular to optic axis) refractive indices respectively [12]. An example of a photonic band-gap for a chiral nematic LC illuminated with unpolarised white light is shown in Fig 5.

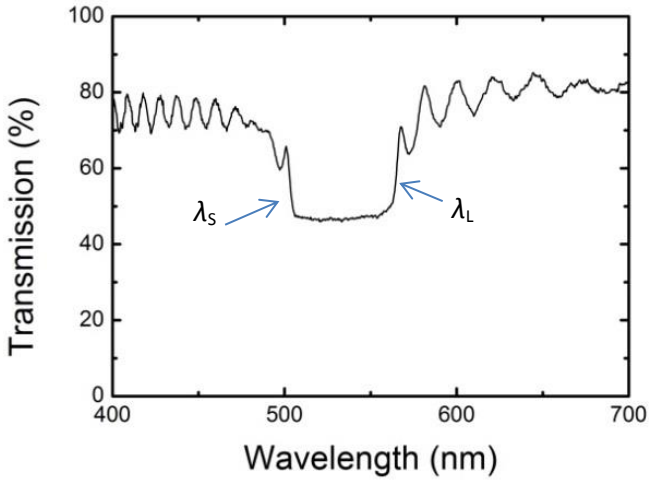

Figure 5 – an example transmission spectrum for a chiral nematic composed of the nematic E7 and a high twisting power chiral dopant. λ_L = 560 nm and λ_S = 500 nm.

From equations 2.3 and 2.4, the width of the photonic band-gap is $\Delta\lambda = \Delta np$. In Section 2.2.2, it was discussed that $n_e = n_{//}$ and $n_x = n_o = n_\perp$. However, chiral nematic LCs differ in that the optic axis is collinear with the helix axis; thus, $n_e = n_\perp$ and $n_o^2 = (n_{//}^2 + n_\perp^2)/2$. However, locally $n_e = n_{//}$ and $n_o = n_\perp$.

The photonic band-gap is one property which makes chiral nematic LCs such interesting optical materials – with applications such as lasers, displays and optical shutters [13-15]. A particularly useful property of the photonic band-gap is that its position may be tuned by a variety of external stimuli such as mechanical forces [16], light [17], magnetic fields [18], electric fields [19-21] and temperature [22]. Furthermore, the photonic band-gap is also of interest because it reflects only one handedness of circularly polarised light (that which matches the rotation sense of the helix). This means that it can be used to control the handedness of emission of species dispersed in it [23-24] by reflecting one circular polarisation of light and transmitting the other.

2.3.1 – Identifying chiral nematic textures

Chiral nematic LCs may be identified by studying their optical textures using optical polarising microscopy [7]. When planar-aligned between glass substrates, the helical structure aligns with its axis normal to the substrate (this is the so-called Grandjean or uniform standing helix alignment); if viewed along the helix (normal to the glass

substrates) using a polarising microscope a uniform colour (which does not disappear as the sample is rotated between crossed-polarisers) is seen because the optical axis is parallel to the direction of propagation of the light. This uniform colour will exhibit a 'Grandjean' alignment with defects known as 'oily streaks'. These can be minimised by carefully annealing the sample, as will be discussed in Section 2.10.4. An example of the chiral nematic texture is illustrated in Fig 6 where spacer beads and oily streaks disrupt an otherwise uniform texture.

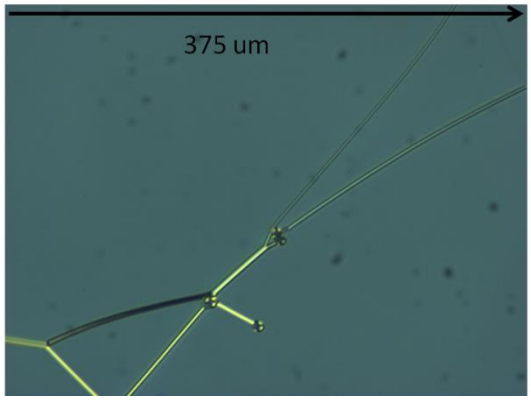

Figure 6 – The texture of a planar-aligned chiral nematic liquid crystal phase (p ~ 400 nm) in the uniform standing helix geometry. The black dots are the spacer beads (5 µm) used to define the cell thickness and the lines are 'oily streak' defects. Results taken at 20°C.

Optical polarising microscopy can also be used to determine the handedness of the chiral nematic LC (which handedness of circularly polarised light is transmitted and which is reflected) by rotating the analyser and observing the sequence of colour changes.

2.4 – The smectic A liquid crystal phase

Smectic LCs are phases of matter which exhibit positional as well as orientational order – the molecules all point in roughly the same direction and they are arranged into layers; within these layers, motion is restricted but the layers themselves can flow past each other because the inter-layer forces are weaker than the intra-layer forces [25]. This means that they are often more viscous than nematic LCs and tend to occur at lower temperatures. There are a variety of smectic phases with different degrees of order within the layers; these are characterised by their packing formation and their tilt angles. The smectic phases are defined by a letter of the alphabet, with the first discovered being the smectic A (SmA). In the SmA phase, the director is perpendicular to the smectic plane and there is no particular positional order within the layer.

2.4.1 – Identifying the smectic A liquid crystal phase

The smectic A phase can be identified by a fan-shaped focal conic texture when in a planar heterogeneous alignment. This texture does not flash under shearing forces (unlike the nematic and chiral nematic phases) [7]. In a planar alignment, as used here, the texture is superficially similar to that of a planar homogenous nematic LC alignment – it exhibits bright and dark states when rotated between crossed polarisers and the domains are mono-coloured. However, in contrast to the nematic LC phase, director fluctuations are suppressed by the layered structure in the SmA LC and so Brownian motion is not seen. Furthermore, the SmA phase has a long recovery length compared to nematic phases so it can be distinguished by a characteristic texture around defects (such as an 'eyelet' pattern seen around the spherical spacer beads in the cells used here), as shown in Fig 7.

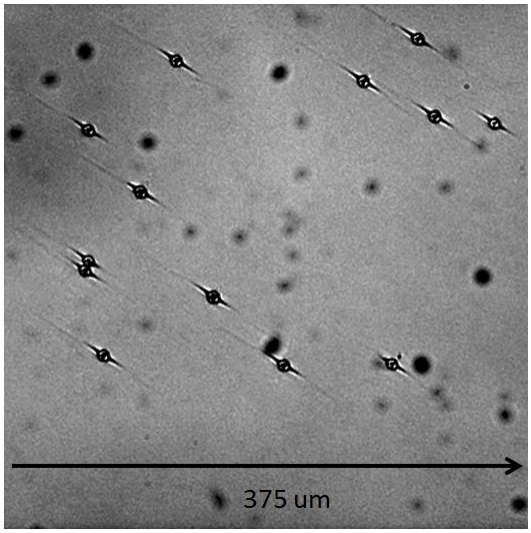

Figure 7 – A grey-scale mapped image of the texture of a smectic A liquid crystal phase (bright state) in a homogeneous planar alignment. The black dots are the spacer beads used to define the cell thickness (5µm).

2.5 – Other liquid crystal phases

There are a variety of other LC phases. These include the blue phase, a chiral phase that can form between the isotropic and chiral nematic LC phases if a chiral material with a high twisting power is used. The blue phases exhibit photonic band-gaps in three dimensions (as opposed to the 1D photonic band-gaps in chiral nematic LC phases). They are cubic arrangements of defects, and their texture generally appears as hexagons [26]. Although the first blue phases to be identified were blue, the phase may exhibit a variety of colours depending on the lattice constants. There are three types of blue phase – blue phase I, II and III (in order of increasing temperature).

Another example phase is the twist-grain boundary, a phase with a helical superstructure in which the helix axis is parallel to the layer planes; this disrupts the layers to give blocks separated by screw dislocations [27]. Such a phase forms due to competition between the chiral structure's tendency to form a helical director field (as seen in a chiral nematic LC) and the molecules' tendency to form a smectic layered structure, two things which are incompatible, leading to a distinct mesophase.

2.6 – Uniform alignment of liquid crystals

LC devices are usually made by capillary filling the LC into a glass cell made of two glass substrates separated by some distance defined by spacer beads. These beads are either spread through the cell or dispersed into the glue at the edges of the glass. The glass is often coated to yield a preferential alignment of the LC director. Two common alignments are planar and homeotropic alignments [28]. For a planar alignment (directtor parallel to the substrates), a thin film of polymer is placed on the surface of the glass and then mechanically 'rubbed' using an abrasive cloth to leave small grooves which help align the LC parallel to the glass surface as shown in Fig 8. This alignment may further be distinguished as parallel (the lines on the two substrates point in the same direction) or anti-parallel (the lines on the two substrates point perpendicular to each other). A homeotropic alignment (director perpendicular to the substrates) is created by coating a thin amphiphilic film (such as lecithin) onto the glass surface; this film has polar ends which cause the LC to align perpendicular to the substrate. In this work, glass cells with spacer beads spread throughout the cell coated with anti-parallel planar alignment layers are used.

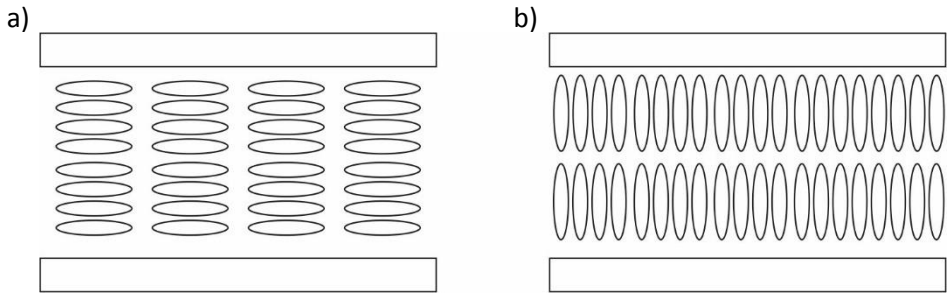

Figure 8 – Illustrations of two different liquid crystal alignments: a) a planar alignment; b) a homeotropic alignment.

2.7 – Lasers

A laser is a device that emits light through an optical amplification process based on the stimulated emission of photons [29]. Lasers consist of an emissive medium and some method of instigating optical feedback.

2.7.1 – Emission processes

There are three fundamental emission processes – absorption, spontaneous emission and stimulated emission. These are illustrated in Fig 9 where n_1 and n_2 represent the populations of the lower (E_1) and upper (E_2) states respectively. Absorption occurs when an atom is excited to some upper excited state by absorption of a photon (Fig 9a). Spontaneous emission occurs when an atom relaxes from an excited state to the ground state and emits an incoherent photon in a random direction (Fig 9b). The energy of the emitted photon will be $\Delta E = E_2 - E_1$ and its frequency will be $v = \Delta E/h$ where h is Planck's constant. Stimulated emission occurs when a photon interacts with an excited atom and causes emission of a second photon with the same energy and phase as the original photon (Fig 9c). This interaction can cause the atom to relax to the ground state radiatively and add E to the incident wave (with the same phase and direction).

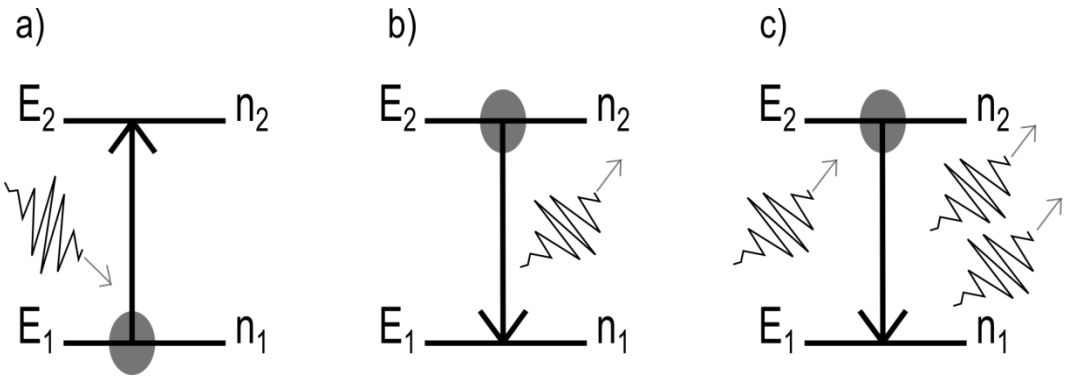

Figure 9 – The three fundamental emission processes: a) absorption of a photon; b) spontaneous emission; c) stimulated emission. $E_{1,2}$ are the energy levels involved and $n_{1,2}$ are the populations of those energy states.

The rate of absorption is then:

$$\frac{dn_1}{dt} \propto \rho(E_{21})n_1 \rightarrow \frac{dn_1}{dt} = -B_{12}\rho(E_{21})n_1 \tag{2.5}$$

Where B_{12} is the Einstein absorption coefficient and $\rho(E_{21})$ is the radiation energy density given by:

$$\rho(E) = \frac{8\pi h\nu^3}{c^3}\frac{1}{e^{E/kT} - 1} \tag{2.6}$$

Where h is Planck's constant, v is the frequency of incident light and k is Boltzmann's constant and c is the speed of light in a vacuum.

The rate of stimulated emission is:

$$\frac{dn_2}{dt} \propto \rho(E)n_2 \rightarrow \frac{dn_2}{dt} = -B_{21}\rho(E)n_2\,, \tag{2.7}$$

where B_{21} is the Einstein coefficient of stimulated emission.

The rate of spontaneous emission is:

$$\frac{dn_2}{dt} \propto n_2 \rightarrow \frac{dn_2}{dt} = -An_2\,, \tag{2.8}$$

where A is the Einstein A coefficient.

At equilibrium:

$$\frac{dn_1}{dt} = 0 \tag{2.9}$$

So, using Equations 2.5, 2.7 and 2.8:

$$B_{12}\rho(E_{21})n_1 = A_{21}n_2 + B_{21}\rho(E_{21})n_2 \tag{2.10}$$

Rearranging this yields:

$$\rho(E_{21}) = \frac{A_{21}n_2}{B_{12}n_1 - B_{21}n_2} = \frac{A_{21}}{B_{12}(\frac{g_1}{g_2}e^{\frac{E_{21}}{kT}}) - B_{21}} \tag{2.11}$$

by using the Boltzmann equation:

$$\frac{n_2}{n_1} = \frac{g_2}{g_1}e^{\frac{-E_{21}}{kT}} \tag{2.12}$$

where g_1 and g_2 are the degeneracies of the energy levels.

Using equations 2.6 and 2.11 it can be seen that:

$$g_1B_{12} = g_2B_{21} \tag{2.13}$$

And:

$$A_{21} = \frac{8\pi h\nu^3}{c^3}B_{21} \tag{2.14}$$

2.7.2 – Optical gain

To have optical gain, the rate of stimulated emission must be greater than the rate of absorption. i.e.,

$$B_{21}\rho(E_{21})n_2 > B_{12}\rho(E_{21})n_1 \quad (2.15)$$

Using Equation 2.13, this means that:

$$\frac{n_2}{g_2} > \frac{n_1}{g_1} \quad (2.16)$$

So, for optical amplification to occur, there must be a population inversion, i.e. it is necessary that $n_2 > n_1$ [29]. However, absorption processes usually dominate compared to emissive properties due to the much higher number of electrons in low energy states than in high energy states.

Thus, for a population inversion to be achieved there must be more than two energy levels involved otherwise absorption and emission will balance each other out (since they are identical but opposite transitions and so at best $n_2 = n_1$).

2.7.3 – Fluorescent dyes as gain materials

Fluorescent dyes are commonly used as gain materials in lasers. These dyes have 3 or 4 levels to enable a population inversion [29]. They are particularly important for the work presented here because they are the gain materials used in conventional LC lasers.

The structure of an example fluorescent laser dye, DCM (4-(Dicyanomethylene)-2-methyl-6-(4-dimethylaminostyryl)-4H-pyran) is shown in Fig 10. It is a brightly coloured, conjugated organic molecule which possesses two chromogenic groups linked by an unsaturated pi-conjugated bridge. The methyl-amine group is electron donating and the cyano groups are electron withdrawing. When the dye is optically excited, it fluoresces [30] – it emits light by a radiative process with the emission of a photon.

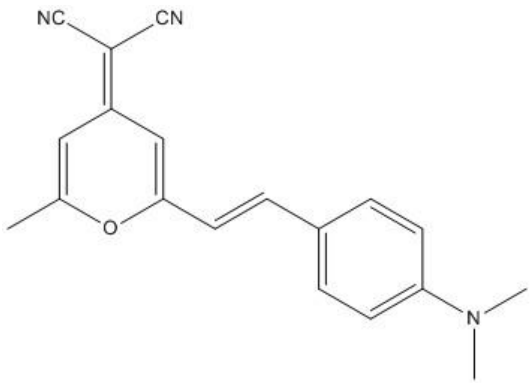

Figure 10 – the molecular structure of the fluorescent dye DCM (4-(Dicyanomethylene)-2-methyl-6-(4-dimethylaminostyryl)-4H-pyran)).

Fig 11 shows a simplified Jablonski diagram which illustrates the energy levels of the π electrons in the molecule. In the Jablonski diagram the bold lines are the ground or excited electronic states and the narrow lines are the vibronic sub-levels caused by simultaneous changes in the vibrational and electronic energy states of the molecule. The solid arrows are absorption processes, the dotted lines are non-radiative transitions and dashed lines are radiative transitions. The S states are singlet energy levels and the T states are triplet energy levels.

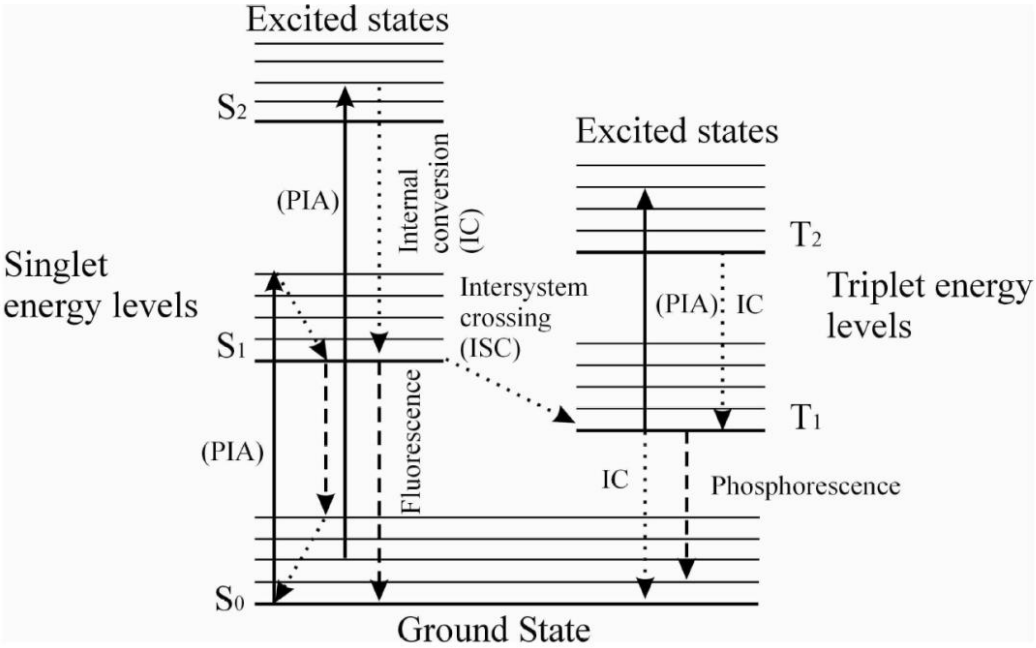

Figure 11 – A Jablonski energy level diagram for DCM. This shows the electronic and vibrational energy levels for a multi-level system. Reproduced from Reference 31.

This multi-level system may be simplified in several ways. In a LC laser, the dye is used in an aromatic solvent (the LC) and this hinders deactivation processes by making it impossible for molecules to closely approach; thus, non-radiative interactions (inter-system crossing, internal conversion) can be ignored. Aggregation of the dye molecules is minimised by using low dye concentration (~1 wt%) to ensure monomolecular dispersion. The triplet states can be ignored because the LC is a polar solvent and this will also reduce inter-system crossing; furthermore, the pulse-width of the pump beam (produced by a Nd:YAG laser) is less than the time required to build up the triplet state. This reduces the Jablonski diagram to a four-level system with four important processes: absorption $S_0 \rightarrow S_{1*}$, fast relaxation $S_{1*} \rightarrow S_1$, radiative spontaneous emission $S_1 \rightarrow S_{0*}$ and fast relaxation $S_{0*} \rightarrow S_0$. The two relaxation processes occur on the picosecond time scale and so a population inversion is maintained between the ground vibronic states of S_1 and S_0. This population inversion is needed so that the

initial spontaneous emission can start the laser oscillation process, and it must be sufficient that the gain must exceed the losses – the laser threshold must be exceeded. When it does, a standing wave forms and the oscillating field is sufficiently intense that interaction between it and excited molecules occur repeatedly and the molecule only decays by stimulated emission.

Despite these simplifications, the $T_1 \rightarrow T_2$ transition – an absorption process which depopulates the T_1 state – can become important (it is spin allowed) and contribute to photo-bleaching of the dye when the dye is continuously illuminated if its absorption band overlaps with the emission of the singlet states.

2.7.4 – Feedback

In addition to a gain material, a laser also needs a feedback mechanism. In a conventional Fabry-Perot laser, the feedback is provided by two mirrors and light experiences resonant feedback due to constructive interference as it is reflected between them. However, a LC laser does not rely on a mirror. Instead, the photonic band gap suppresses fluorescence inside the band gap but enhances it at the band edges; this can ultimately lead to lasing [12, 32] as will be described in more in Section 2.9.1. This simplifies device manufacture as it avoids the requirement of a precise separation of mirrors necessary in a conventional device can be avoided.

2.8 – Amplified spontaneous emission

Amplified spontaneous emission (ASE) is another route of emission of light from a gain medium. In this case, when the gain medium is excited, it will undergo spontaneous emission. This will then stimulate emission in the gain material next to it, and so the stimulated emission will propagate through the gain material [29].

In the case of a cylindrical rod of gain material (for example), a population inversion may be created by pumping the material. This results in upper excited levels which spontaneously emits in all directions. Much of this light will leave the rod after propagating a small distance and so will exhibit the spectrum expected of the bulk material. However, if the emission occurs along the material (particularly in the angle $\Omega/4\pi$ where Ω is the solid angle subtended by the other end of the cylinder), then the emission will propagate along the entire length of the gain material and will be amplified as it propagates.

If the gain is sufficient, an intense beam of radiation will be generated. This beam of radiation exhibits gain-narrowing and has a narrow divergence, which can make it

difficult to distinguish from true lasing. However, the output of ASE increases in intensity the longer the area of gain material involved; in contrast, a laser can allow stimulated emission to build up even if the single-pass gain length is small. Furthermore, the cavity in a true laser restricts oscillation to one or more longitudinal and transverse modes; the same is not true for ASE.

2.9 – Liquid crystal lasers

There are three main modes of operation for LC lasers – band edge, defect-mode and random lasers [13].

2.9.1 – Band-edge liquid crystal lasers

Band-edge lasing was first shown theoretically by Dowling et al. [33] before being demonstrated by Taheri [34] and Kopp [35] independently. The photonic band-gap of certain LCs (chiral nematics in the work in this Thesis) affects the emission of guest fluorescent molecules – in the band gap fluorescence is suppressed and at the band edges fluorescence is enhanced due to the high density of photon states, low group velocity and hence long dwell times of the photons at these frequencies. If the enhancement is sufficient, this leads to lasing.

The original method used for analysing the optical properties of LCs was postulated by de Vries [32] and involved treating the chiral structure as a series of rotating layers. This method was built upon by Schmidtke and Stille [12]. The most important result from this work is that:

$$\rho = \frac{d}{d\omega} Re(k) \tag{2.17}$$

where ρ is the photonic density of states, ω is the frequency and *Re(k)* is the real part of the wavenumber. It is the varying character of k which determines the characteristics of the band gap and results in ρ being equal to 0 in the band gap and large at the band-edges.

The analysis here will follow that of the two papers mentioned above [12,32]. The chiral structures are treated as a series of rotating layers. The mean refractive index of the nematic plane, $\bar{n}$, is defined as:

$$\bar{n} = \sqrt{\frac{n_o^2 + n_e^2}{2}} \tag{2.18}$$

where n_o and n_e are the ordinary and extraordinary refractive indices (perpendicular and parallel to the layers respectively). Additionally, α is defined as:

$$\alpha = \frac{(n_e^2 - n_o^2)}{2\bar{n}^2} \tag{2.19}$$

The director, $\hat{\mathbf{n}}$, is then converted from the laboratory frame $\hat{\mathbf{x}}, \hat{\mathbf{y}}, \hat{\mathbf{z}}$ to the to the rotating frame $\hat{\mathbf{a}}, \hat{\mathbf{b}}, \hat{\mathbf{c}}$ as illustrated in Fig 12.

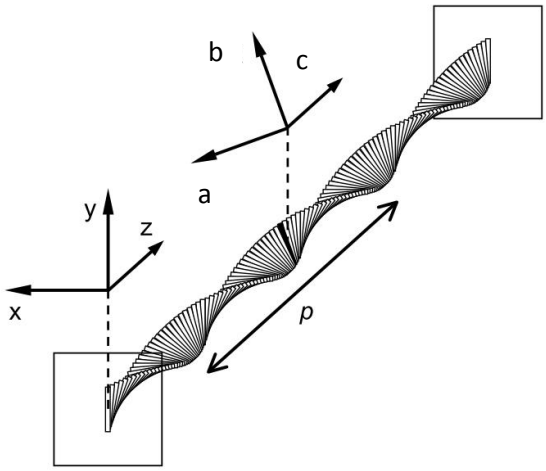

Figure 12 – Illustration of the laboratory frame laboratory frame $\hat{x}$, $\hat{y}$, $\hat{z}$ and the rotating frame $\hat{a}$, $\hat{b}$, $\hat{c}$. Reproduced from Reference 12.

In the laboratory frame:

$$\hat{\boldsymbol{n}}(z) = -\sin(k_p)\hat{\boldsymbol{x}} + \cos(k_p)\hat{\boldsymbol{y}} \tag{2.20}$$

where $k = \frac{2\pi}{0}$ and $\hat{\mathbf{z}}$ is parallel to the helix axis. This is converted to the rotating frame:

$$\hat{\boldsymbol{a}} = \cos(k_p z)\hat{\boldsymbol{x}} + \sin(k_p z)\hat{\boldsymbol{y}} \tag{2.21}$$

$$\hat{\boldsymbol{b}} = -\sin(k_p z)\hat{\boldsymbol{x}} + \cos(k_p z)\,\hat{\boldsymbol{y}} = \hat{\boldsymbol{n}} \tag{2.22}$$

$$\hat{\boldsymbol{c}} = \hat{\boldsymbol{z}} \tag{2.23}$$

By using Maxwell's equations, the two polarisation eigenstates for elliptically polarised waves with opposite handedness, E_1 and E_2, can be determined as:

$$E_{1,2} = \hat{\boldsymbol{e}}_{1,2} e^{ik_{1,2}c} \tag{2.24}$$

k_i is the wavenumber, $2\pi \frac{m_i'}{\lambda' p}$ and $\hat{\boldsymbol{e}}_{\boldsymbol{\iota}}$ is the polarisation of each eigenstate:

$$\hat{\boldsymbol{e}}_{\boldsymbol{\iota}} = \frac{1}{\sqrt{1 + |f_i|^2}}(\hat{\boldsymbol{c}} + i f_i \hat{\boldsymbol{b}}) \tag{2.25}$$

and m_i' are the reduced refractive indices and are the roots of:

$$m_i'^2 = 1 + \lambda'^2 \pm \sqrt{4\lambda'^2 + \alpha^2} \tag{2.26}$$

Where λ' is the reduced wavelength:

$$\lambda' = \frac{\lambda}{\bar{n}p} \tag{2.27}$$

where λ is the wavelength in a vacuum. At a given wavelength, $m_i'^2$ can take two values – one for each handedness of the elliptically polarised wave (i.e., $\widehat{\boldsymbol{e_1}}$ or $\widehat{\boldsymbol{e_2}}$). This is shown in Fig 13. For m_2' the values are always positive, regardless of the reduced wavelength, because the polarisation rotates opposite to that of the director and so it is unaffected by the photonic band gap. m_1', however, *is* affected by the band gap. Its real part is 0 in the bandgap; in that region, it is imaginary so there is only an evanescent wave in the band gap. At the band edges the ellipticity is 0 (short wavelength edge) or $\pm\infty$ (long wavelength edge) within the medium, leading to linearly polarised waves at both edges.

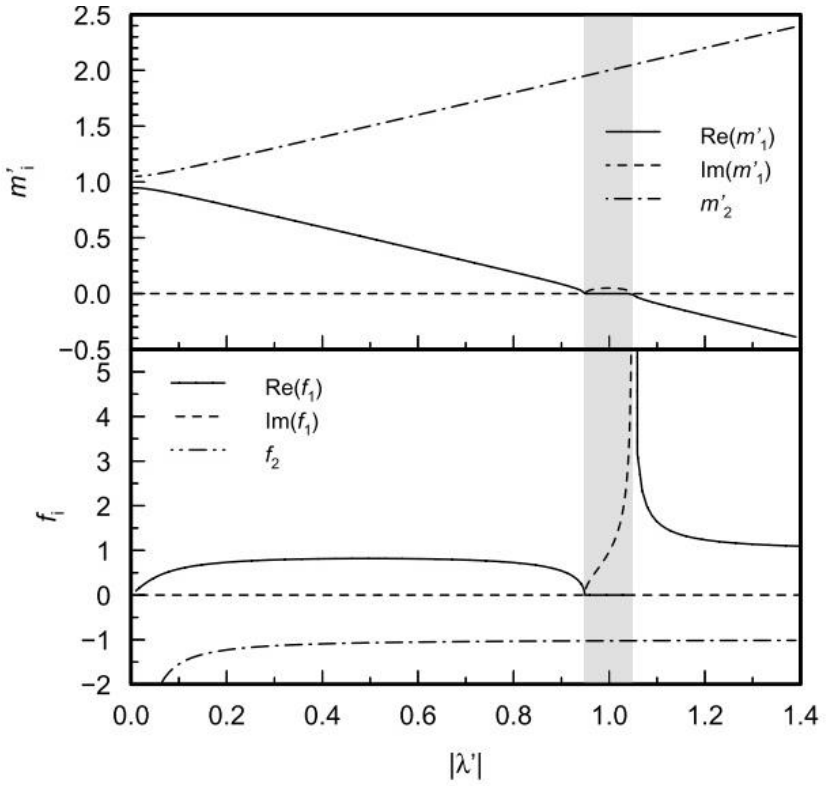

Figure 13 – Reduced refractive indices m_i' and ellipticities f_i' for E_1 and E_2 in a chiral nematic liquid crystal with α = 0.1. Reproduced from Reference 12.

(1 – α) and (1 + α) correspond to the band edges so it can be calculated that $\lambda_S = n_e p$ and $\lambda_L = n_o p$. λ_S is the short wavelength edge and λ_L is the long wavelength edge (as reported in Equations 1.3 and 1.4). Using these equations:

$$\Delta\lambda = \Delta np \tag{2.28}$$

where $\Delta\lambda$ is the difference in wavelength between the band edges (the width of the photonic band-gap) and Δn is the difference in refractive index parallel and perpendicular to the helical axis – the birefringence of the material.

In this treatment, due to the very fast non-radiative transitions, the four-level diagram of a laser dye may be (further) simplified to a 2-level system – an initial excited state and a final state after the emission of a photon – |i> and |f>. The spontaneous emission transition rate is then given by Fermi's golden rule:

$$W_{sp} = \frac{2\pi}{\bar{h}}\rho_\nu |< f|H|i >|^2 \tag{2.29}$$

where ρ_ν is the final density of photon states, H is the Hamiltonian for the interaction, μ.E, where μ is the dipole moment operator. The density of states is given by:

$$\rho = \frac{dk}{d\omega} = \frac{1}{V_g} \tag{2.30}$$

where V_g is the group velocity. In the band-gap there is an evanescent wave inside the photonic band-gap and so ρ is 0 and so too is the spontaneous emission rate; emission is suppressed and no lasing can occur. At the band edges, ρ becomes very large, V_g becomes small and so dwell times are long and stimulated emission is enhanced and lasing can occur when pumped appropriately – by a solid-state Nd:YAG laser in my work. Regardless of the angle of incidence of the pump beam, the angle of emission is always determined by the helical axis and is perpendicular to the glass substrates in the planar-aligned devices used here (where the chiral nematic LC is arranged in a uniform standing helix with the molecules aligned parallel to the substrates).

2.9.2 – Defect mode LC lasers

In a defect mode LC laser, a resonant channel exists within the photonic band-gap itself – this confines the energy to this mode by localising it in the defect [13]. This can be induced by adding a 90° phase slip in the periodicity [36-38], adding a thin isotropic or nematic layer between chiral nematic layers [39] or by introducing the defect in some other way, such as using TiO_2 [40]. The high density of states in the defect means that typically defect-mode lasers have lower excitation thresholds than their equivalent band-edge lasers although with lower maximum emission because the mode is pinned in the defect [13].

2.9.3 – Materials for liquid crystal lasers

A variety of LCs have been used in LC lasers – usually those that exhibit a periodic structure which gives rise to a photonic band-gap. These include: most commonly the chiral nematic phase [13] (including LC elastomers and glasses [41]), and also chiral smectic C phases [42] and blue phases (I and II) [43].

Although lasing has been seen without any additional gain material present (by pumping a chiral nematic LC using UV light at a wavelength which the LC absorbed [44]), a photoluminescent material is usually used to provide gain.

This gain material is most commonly a fluorescent dye, due to the existence of a wide variety of dyes with good quantum yields, high photoluminescence and good solubilities in LCs [14]. DCM, a commonly used fluorescent dye (as previously discussed), has an absorption coefficient of 0.02 μm^{-1}, a molar extinction coefficient of 1.3 $mol^{-1}\mu m^{-1}$, a quantum yield of 0.45 and a fluorescence lifetime of 2.1 ns (all measured at 1 wt% in ethanol with 532 nm pumping) [45]. Additionally, there are many dyes with a wide variety of emission wavelengths allowing easy tuneability. However, dye-based laser outputs may be degraded, and device lifetimes limited as they are bleached under continuous illumination [46].

Photo-bleaching is a broad term used to refer to a variety of processes which lead to degradation of the lifetime of a LC laser device, or a diminution of its output over time. It encompasses both irreversible damage done to the dye molecules and temporary effects such as triplet state generation (as discussed in Section 2.7.3) [48]. Temporary effects may be avoided by removing the pump source illumination for long enough that the dye can relax – meaning that lasers incorporating dyes can be pumped in a pulsed mode with relatively low repetition rates (10-20 Hz) [47]. This both precludes the use of continuous-wave operation and limits output powers of such a device.

There are various ways of circumventing bleaching in dyes – usually by finding some means to replenish the dye and avoid any given dye molecule being pumped for a prolonged period. Continuous wave or high repetition-rate pulsed operation of dye-based lasers has been achieved by several means, all of which require some complicating factor in an experiment: the fluid flow used in some dye lasers [48-49] is incompatible with thin-film LC lasers due to the importance of the LC alignment; the disks used to rotate the films in References 50 and 51 are inelegant and will not work with all types of LC laser (for example free-standing films). The adaptive pumping

technique [52] provides additional utility as well as avoiding the problem of bleaching fluorescent dyes but it adds complexity and size to a setup. The need for such technology could be entirely avoided in an LC laser simply by using a gain medium not susceptible to photo-bleaching.

A particularly promising set of materials that do not exhibit photo-bleaching are inorganic gain materials such as quantum dots, inorganic-organic perovskites and transition metal clustomesogens. However, incorporating inorganic materials into LCs in non-trivial given the general incompatibility of dispersal between inorganic and organic species. This will be explored further in Chapters 6 and 7.

2.9.4 – Characteristics of liquid crystal lasers

Two important characteristics of LC lasers are the excitation threshold (how much energy is required to trigger laser emission) and the slope efficiency (the gradient of the change in emission output with increasing pump input) [13]. These are affected by the birefringence, the orientational order parameter, the order parameter of the transition dipole moment of the dye, the quantum yield of the dye, and the dye absorption [13]. A dye such as PM597 greatly increases the slope efficiency, for example, and pyrene-derivatives can decrease the excitation energy by an order of magnitude [45]. Slope efficiencies can approach 70% [53] and excitation energies may be as low as 43 nJ/pulse [54].

2.10 – Experimental methods

2.10.1 – Sample preparation

In this work, a variety of mixtures are used; their compositions will be described in the respective chapters. All mixtures were prepared using a precision balance (Mettler Toledo AB104S) to weigh the materials with a precision of 0.1 mg. Here all mixture compositions are given as wt%. Thermal diffusion was used to mix the species by heating to a sufficiently high temperature that the liquid crystalline materials were in the isotropic phase. To do this, they were placed in an oven (Townson and Mercer 1445-2) for several hours to ensure thorough mixing (the exact times will be described in the relevant Chapters).

2.10.2 – Liquid crystal cell preparation

For much of this work, LC materials were studied in glass cells made of two glass substrates separated by some distance (5, 9 and 20 μm cells were used here). The LC

was filled into these by capillary action at a temperature above the isotropic temperature of the relevant LC.

Spacer beads are used to define the distance between the glass substrates – they are either spread throughout the cell (which gives consistent separation but can cause defects as they disrupt the LC alignment) or dispersed into glue placed around the edges of the glass to hold them together (which reduces defects but can result in an inconsistent thickness across the cell area). The exact cell thicknesses were determined using the interference fringes in the transmission spectra of empty cells. The cells used here have a transparent conducting layer (indium tin oxide) on the inside to allow electric fields to be applied. The glass was also coated with an alignment layer on the glass to aid in aligning the LC. For those used in the work presented here, an anti-parallel, planar (homogeneous) alignment was created by placing a thin film of polymer on the surface and then rubbing it to leave small grooves which help align the LC parallel to the glass surfaces. All cells used in this work were purchased pre-assembled from Instec.

2.10.3 – Temperature control of liquid crystals

A hot stage connected to a temperature controller was used to control the LC temperature and to aid in annealing. An optical polarising microscope (Olympus BX51, see Section 2.10.6) was used to inspect the LC textures and to identify the phase transitions. A hot stage is a temperature-controlled metal block with a small hole onto which a LC cell can be placed. The system used here can be placed on a microscope. The temperature controller could heat/cool at a steady rate and hold the temperature at a specified point. For this work, a Linkam TP93 controlled hot stage (0.1°C/min heating rate) was used.

2.10.4 – Annealing liquid crystals

For the chiral nematic samples (where a good alignment was particularly important), mechanical pressure was applied to the cells as they were cooled from the isotropic phase. This resulted in an improvement in the alignment compared to relying on the alignment layers alone. The alignment could be further improved by thermally annealing the devices. In this case, the devices were heated so that the LC was in the isotropic phase. The devices were cooled to just below the isotropic point while mechanical shearing was performed. The devices were then left at this temperature for several hours to allow the domains to grow and the oily streaks to diminish. Finally, the

cells were cooled to room temperature with a slow cooling rate (~1°C/min) using the hot-stage described above.

2.10.5 – Photo-polymerisation of reactive mesogens

For the work in Chapters 3-5, a mixture of photo-curable reactive mesogens, thermal inhibitor and photo-initiator was mixed into the LC. The mixtures were stored in brown bottles to avoid exposure to UV light and premature curing.

To photo-polymerise the reactive mesogens and to imprint the structure of the LC phase that they were in onto them, they were exposed to UV light using a hand-held UV light source (Thorlabs, CS2010, peak emission 365 nm, 185 mW/cm^2) was used. The spectrum of the light source is shown in Fig 14. This light source was held at a distance of 10 cm above the sample and turned on to fully illuminate the sample. A hot stage and temperature controller was used to control the curing temperature. Usually, this curing was performed from one side of the cell and then from the other to ensure uniform curing throughout the cell. The length of time of illumination varied depending on the sample/experiment and will be described in the relevant Chapters.

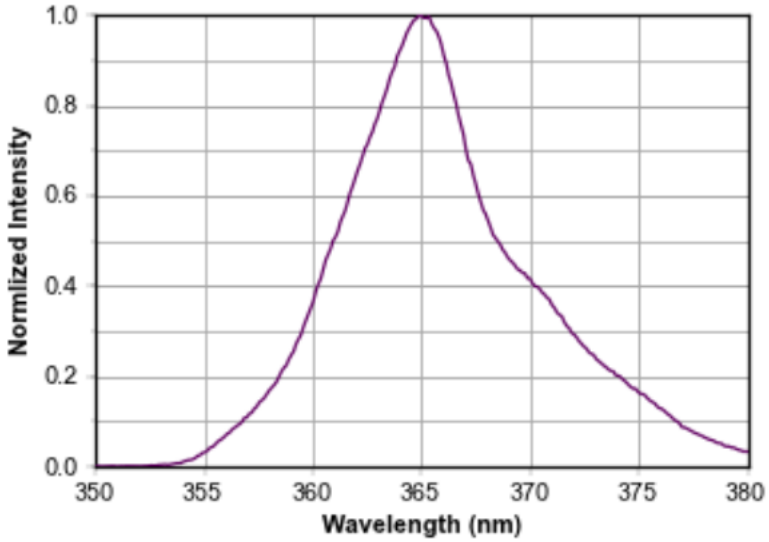

Figure 14 – The typical emission spectrum of the UV light source used in this work. Reproduced from Reference 55.

2.10.6 – Optical polarising microscopy

Optical polarising microscopy is used to characterise the LCs used in this work and to study their texture. In an optical polarising microscope, the sample stage is positioned between rotatable crossed-polarisers. Thus, with no sample present, nothing will be seen as the polarisers block all light. However, the LCs used in this thesis are birefringent and so allow light to be transmitted between crossed polarisers when appropriately aligned.

LCs generally rotate the plane of polarised light and different LC structures will produce different characteristic textures as described previously – a few example textures are shown in Fig.15.

In this work, I perform bright-field microscopy using an Olympus BX-51 optical polarising microscope. The microscope was fitted with a tungsten bulb which emitted between ~400-1200 nm. The light from the bulb passes through a condenser to concentrate it on the sample. A variety of infinity-corrected objectives (from 10 to 50X magnification, and numerical apertures as described in the relevant sections) were used to collect light that passed through the sample. A camera (QImaging QIcam Fast1394; 12-bit, colour, 1392 x 1040 pixels) was attached to the microscope to allow photographs to be taken.

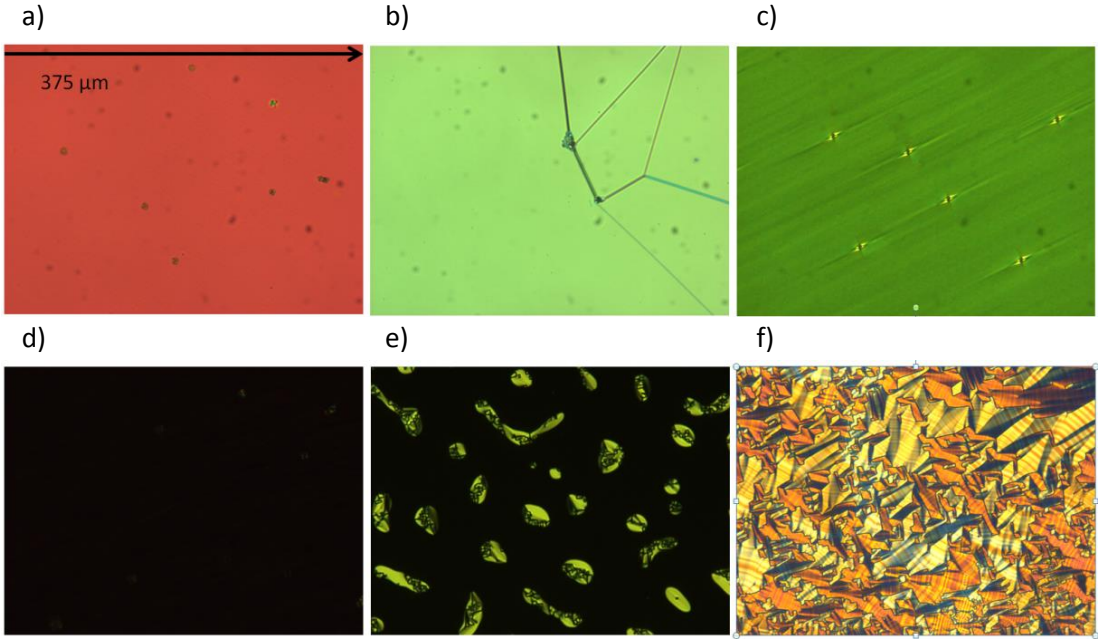

Figure 15– Various liquid crystal textures: a) nematic (planar homogeneous alignment), b) chiral nematic Grandjean texture (planar aligned), c) smectic A (planar aligned), d) isotropic, e) at the transition between the chiral nematic and isotropic, and f) focal conic.

2.10.7 – Transmission spectroscopy

Transmission spectroscopy measures the transmission of light by a sample as a function of wavelength. This can be used to probe the optical properties of a LC – in the work described here, to study the photonic band gap of chiral nematic LCs. Over the wavelength range defined by the photonic band gap, light of the same rotational sense as the helix and with a wavelength on the order of that of the helical pitch is reflected and the rest is transmitted.

The setup for such an experiment is shown in Fig 16. The samples were illuminated by a halogen white light source (Ocean Optics HL-2000-FHSA) focussed to a

spot size of ~500 µm diameter at the aperture using a 20X, 0.5 NA microscope objective. The transmission spectra were then collected by a 600 µm-diameter optical fibre (Ocean Optics QP600-1-UV-VIS) that was connected to a broadband spectrometer (Ocean Optics USB2000+ UV-VIS; resolution 1.7 nm, 200-850 nm range, 600 lines/mm).

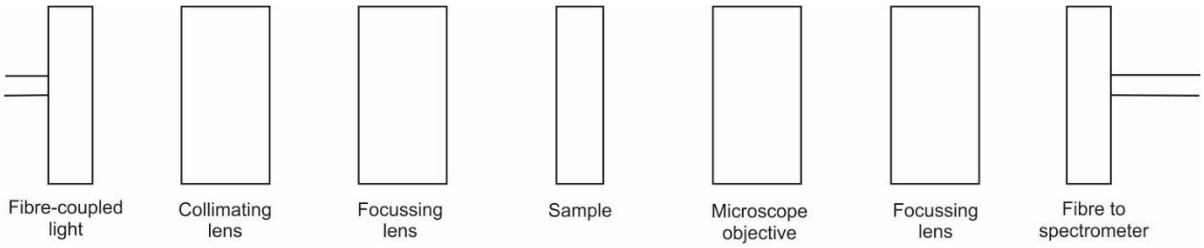

Figure 16 – The experimental setup for transmission spectrum measurements.

In addition to the setup described above, an ultraviolet–visible (UV-VIS) spectrometer (Agilent Cary 8454) was also used. The spectrometer could perform absorption and reflectance spectroscopy from ~300-1100 nm.

2.10.8 – Optical pumping setups

The lasers created in this work must all be optically pumped. For most of this work, I used a frequency-doubled Nd:YAG laser (CryLas 6FTSS355-Q4-S) emitting 1 ns pulses at 532 nm with a variable repetition rate (from 1 Hz to 1 kHz). The pump laser was focused onto the devices to a spot size of ~200 µm diameter and the output was measured either parallel or perpendicular to the devices, as shown in Figs 17a and b respectively. When measuring emission perpendicular to the plane of the device, a 550 nm long-pass filter was used to block the pump beam from being detected by the spectrometer. When measuring light emission parallel to the plane of the device, a dichroic mirror was used to avoid collection of the pump beam. Emission was collected using a microscope objective (5X, 0.25 NA) and coupled into a 600 µm-diameter fibre (Ocean Optics QP600-1-UV-VIS) attached to a spectrometer (Ocean Optics USB2000+ UV-VIS). The pump energy was measured using a pyroelectric sensor (OPHIR, PE9-ES-C, spectral range 0.12-12 µm, sensitivity 0.1 µJ). A combination of a quarter wave plate (zero-order, 530 nm) and Glan-Thompson polarizer was used to probe the handedness of the circular polarisation of the laser emission. The intensity of the emitted pump laser light was controlled using a combination of a half wave-plate and a Glan-Thompson polariser.

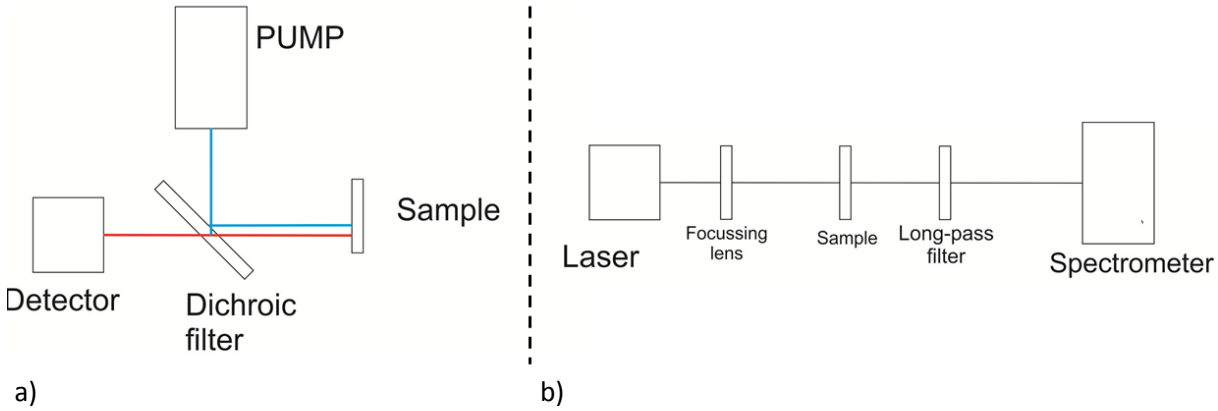

Figure 17 – Optical pumping experimental setups: a) for detecting emission perpendicular to the sample; b) for detecting emission parallel to the sample.

2.11 – Conclusion

This Chapter has described the background to the work in this Thesis. I have introduced the LCs that will be used in my work, their properties and methods for identifying them. Additionally, I have introduced lasers and how they operate – I have particularly focussed on the LC lasers that form a large part of the work presented here. This Chapter has also described the core experimental techniques used in my work. I introduced techniques required for creating LC devices – making mixtures, filling cells, annealing, photo-polymerisation and temperature control. Subsequently, I introduced the core techniques used for characterising devices – optical polarising microscopy, UV-VIS spectroscopy and transmission spectroscopy. I have also described the setup used to optically pump the devices created in later Chapters.

Chapter 3 will be the first experimental Chapter. In it, I describe my work to polymer-template the smectic A LC phase and to characterise its electro-optic properties. It shows that such devices exhibit 12 times better contrast ratios and 6 times faster response times than conventional nematic devices.

2.12 – References

1 Chap. I and II in 'The Handbook of Liquid Crystals' Vol. 1 ed. By D. Demus, J. Goodby, G. W. Gray, H. –W. Spiess, and V. Vill (Wiley-VCH, Weinheim) (1998).
2 'Structure of Liquid Crystal Phases' by P. S. Pershan (World Scientific, Singapore, 1998).
3 H. K. Bisoyi and S. Kumar, *Chem. Soc. Rev.* 2010, **39**, 264.
4 S. Jen, N. A. Clark, P. S. Pershan, and E. B. Priestly, 1997, *J. Chem. Phys.* **66**, 4635.
5 V. Tsvetkov, *Acta Physicochim.* 1942, **16**, 132.
6 Demus, et al. (Ed.), Physical Properties of Liquid Crystals, 1999, Chapter 3, WILEY.
7 I. Dierking, Textures of Liquid Crystals, 2003, WILEY.
8 S. M. Morris, Display Systems lecture notes, Cambridge University, 2013.
9 Liquid Crystals, https://en.wikipedia.org/wiki/Liquid_crystal, Wikipedia.com. Accessed online 13.07.2016.
10 S. Ermakov, A. Beletskii, O. Eismont, and V. Nikolaev, Brief Review of Liquid Crystals, Springer International Publishing, 2016, pp. 37–56.
11 I-C Khoo, Liquid Crystals, Second Edition (2007), Chapter 4.
12 J. Schmidtke and W. Stille, 2003, *Eur. Phys. J. B – Condens. Matter*, **31**, 179.
13 H. Coles and S. Morris, 2010, *Nat Photon.*, **4**, 10.

14 K.-H. Kim, J.-K. Song, 2009, *NPG Asia Mater*. 2009, **1**, 1.
15 Mohammadimasoudi, J. Beeckman, J. Shin, K. Lee, and K. Neyts, 2014**, Opt.** *Express*, **22,** 19098.
16 H. Finkelmann, S. T. Kim, A. Muñoz, P. Palffy-Muhoray, and B. Taheri, 2001, *Adv*. *Mater*., **13**, 1069.
17 S. Kurihara, Y. Hatae, T. Yoshioka, M. Moritsugu, T. Ogata, and T. Nonaka, 2006, *Appl*. *Phys*. *Lett*., **88**, 103121.
18 I. Lelidis, G. Barbero, and A. M. Scarfone, 2012, *Cent*. *Eur*. *J*. *Phys***10,** 587.
19 H. Nemati, S. Liu, R. S. Zola, V. P. Tondiglia, K. M. Lee, T. White, T. Bunning, and D.-K. Yang, *Soft Matter*, 2015, **11**, 1208.
20 J. Schmidtke, G. Jünnemann, S. Keuker-Baumann, and H.-S. Kitzerow, *Appl*. *Phys*. *Lett*., 2012, **101**, 5.
21 J. S. Patel and R. B. Meyer, *Phys*. *Rev*. *Lett*., 1987, **58**, 1538.
22 K. Funamoto, M. Ozaki, and K. Yoshino, *Jpn*. *J*. *Appl*. *Phys*., 2003, **42**, 1523.
23 A. L. Rodarte, R. J. Pandolfi, S. Ghosh, and L. S. Hirst, *J*. *Mater*. *Chem*. *C*, 2013, **1**, 5527.
24 S. M. Wood, M. Prévôt, M. Amela-Cortes, S. Cordier, S. J. Elston, Y. Molard, and S. M. Morris, *Adv*. *Opt*. *Mater*., 2015, **3**, 1368.
25 S. Singh, Liquid Crystals: Fundamentals, 2002, World Scientific Publishing, Chapter 6.
26 H. Stegemeyer, T. H. Blumel, K. Hiltrop, H. Onusseit, F. Porsch, *Liq*. *Cryst*., **1**, 3 (1986)
27 S. R. Renn and T. C. Lubensky, *Phys*. *Rev*. *A,* 1988l, **38**, 2132.
28 L. P. Jones, "Alignment Properties of Liquid Crystals," in Handbook of Visual Display Technology, Berlin, Heidelberg: Springer Berlin Heidelberg, 2012, pp. 1387–1402.
29 S. Hooker & C. Webb, Laser Physics, 1st ed. OUP, 2010, Chapters 1-2.
30 S. L. Bondarev, V. N. Knyukshto, V. I. Stepuro, A. P. Stupak, and A. A. Turban, *J*. *Appl*. *Spectrosc*., 2004, **71**, 194.
31 S. M. Morris, Steve Morris PhD thesis
32 H. de Vries, *Acta Crystallogr*., 1951, **4**, 219.
33 J. P. Dowling, M. Scalora, M. J. Bloemer, and C. M. Bowde, *J*. *Appl*. *Phys*., 1994, **75**, 1896.
34 V. I. Kopp, et al., *Opt*. *Lett*., 1998, **23**, 17071709.
35 B. Taheri, et al., *Mol*. *Cryst*. *Liq*. *Cryst*. 2001, **358**, 7382.
36 P. V. Shibaev, et al., *Macromolecules,* 2002, **35**, 3022.
37 K. Funamoto, et al., *Jpn*. *J*. *Appl*. *Phys*. 2003, **42**, L1523.
38 J. Schmidtke, et al., *Eur*. *Phys*. *J*. *B – Condens*. *Matter*, 2003, **31**, 179194.
39 Y. C. Yang, et al., *Phys*. *Rev*. *E*., 1999, 68524.
40 J. Yoon, *Appl*. *Phys*. *Lett*., 2006, **88**, 091102.
41 P. V. Shibaev,et al., *Liq*. *Cryst*., 2003, **30**, 1391.
42 M. Ozaki,et al., *Adv*. *Mater*., 2002, **14**, 306.
43 W. Cao, et al., *Nat*. *Mater*., 2002, **1**, 11.
44 A. Muñoz F., P. Palffy-Muhoray, and B. Taheri, *Opt*. *Lett*., 2001, **26**, 84.
45 C. Mowatt, et al., J. Appl. Phys., 2010, **107**, 043101.
46 M.Davidson,Photobleaching,micro.magnet.fsu.edu/primer/java/fluorescence/photobleaching [Accessed 13.07.2016].
47 O. G. Peterson, *Appl*. *Phys*. *Lett*. 1970, **17**, 245.
48 P. Runge & R. Rosenberg, 1972, **8**, 910.
49 R. Bornemann, et al., *Opt*.*Lett*., 2006, **31**, 1669.
50 A. Costela, et al., *Appl*. *Phys*. *Lett*., 2001, **79**, 452.
51 S. M. Wood, et al., *Opt*. *Lett*., 2013, **38**, 44836.
52 M. Fox, Optical properties of solids, 2nd ed., OUP, pp 67-75

Chapter 3 – Polymer templating Smectic A liquid crystal phase

Polymer-templating of liquid crystals (LCs) is a technique for imprinting the macroscopic alignment and structure of a LC phase onto other mesogenic materials. In this Chapter, I describe work to polymer-template the smectic A (SmA) LC phase for the first time. Firstly, I detail the background information relevant for this work – in particular, I discuss previous work to polymer-stabilise and polymer-template LCs. Then, I discuss the materials and techniques that I have used to create polymer-templated SmA LCs. Initially, I studied the materials using optical polarising microscopy before investigating their electro-optical properties. These properties are compared to those of conventional nematic devices and the templated SmA LC devices are shown to exhibit a faster response time (by 6 times) and an enhanced contrast ratio (by 12 times). Furthermore, unlike unpolymerised SmA LCs, this electric switching is reversible. Thus, the polymer-templating technique allows us to take advantage of the desirable optical properties of the SmA phase – such as the suppression of the (scattering) fluctuations of the director seen in nematic LCs while avoiding problems associated with the SmA LC phase, such as its irreversible switching when an electric field is applied.

3.1 – Background

3.1.1 – Polymer-stabilised liquid crystals

LC phases and alignments may be stabilised by adding low molecular weight monomeric materials that form a polymer-network when exposed to UV light. This results in a system with the structure and order of an LC phase but with enhanced mechanical stability [1].

In the work described in this thesis, such polymer stabilisation is performed by dispersing a photoinitiator and a reactive mesogen into the LC system. Reactive mesogens are LC species which possess reactive groups. An example of such a reactive mesogen is shown in Fig 1 – it is 'RM257'[1] a reactive mesogen with two reactive acrylate groups (one at each end of the molecule).

Polymerisation is performed by exposing the LC/reactive mesogen mixture to UV light. Exposure to UV light causes the photoinitiator to form free radicals (species with

[1] (4-((1-(4-(3-(acryloyloxy)propoxy)phenyl)vinyl)oxy)-3-methylphenyl 4-(3-(acryloyloxy)propoxy) benzoate)

unpaired electrons). These radicals may be formed by homolytic cleavage (a bond in the photoinitiator breaks to form two radical species) or by reduction of an aromatic carbonyl species by a co-initiator (such as an alcohol) [2]. Due to their unpaired electrons, these free radicals are very reactive. In the systems used in this thesis, the radicals then attack the reactive acrylate groups on the reactive mesogens [3]. This results in abstraction of electrons from the acrylate groups. Two acrylate groups on different reactive mesogens then react. Under continuous illumination, this process continues until the photoinitiator is exhausted or all the reactive mesogens have cross-linked.

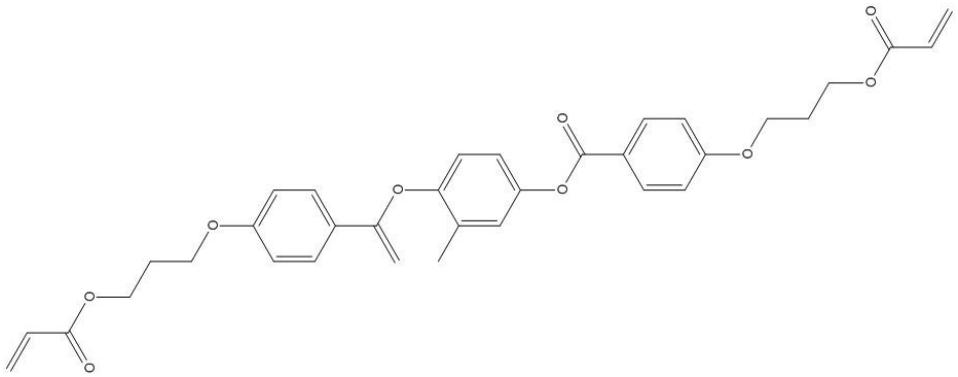

Figure 1 – The molecular structure of the reactive mesogen RM257.

Polymer-stabilisation of a LC can either involve low concentrations of polymer (<10 wt%) [4] or higher concentrations (>10s of wt%) where the polymer forms a dense matrix consisting of micron and nano-sized pores that contain the non-reactive LC components in interstitial sites [5-7], as has been shown by SEM studies [8]. Higher concentrations of reactive mesogen act to enhance the stability of the LC/polymer systems, but this can come at the expense of some of the electro-optic properties – for example it can supress the switching of the LC in an electric field [9]. A variety of LC phases have been polymer-stabilised, and the technique was first demonstrated using achiral nematic LCs [1], but chiral nematic [5-7], blue phase [8] and twist-bend nematic LC phases [9] have also been polymer stabilised to enhance theirmechanical stability.

With respect to smectic phases, much attention has been paid to the chiral smectic C (or ferroelectric) phase due to its rapid switching properties and bistability [1, 10-13]. This work has shown that the electro-optic properties may be improved by polymer-stabilisation but that switching is suppressed. The SmA phase itself has not been specifically studied in polymer-stabilised systems, although polymer-stabilised SmA LCs have been noted in some papers [14-15], where improved electro-optic properties

(such as contrast ratios and reduced scattering) were studied. The SmA* (a chiral variant of the SmA phase) has been specifically studied [15] and it was shown that polymer-stabilisation resulted in a high degree of orientational order in the material.

3.1.2 – Polymer templated liquid crystals

Polymer templating of liquid crystals is a technique in which the LC is removed from a polymer-stabilised LC structures using a solvent to leave a scaffold which can be used to imprint the alignment of the original phase onto other mesogenic materials [16-18]. It was first demonstrated using a chiral nematic LC and the process is illustrated in Fig 2. A mixture of reactive mesogen and LC are filled into a glass cell (step 1). This is then photo-polymerised (step 2). This leaves a polymer scaffold imprinted with the LC structure. The LC and any unreactive reactive mesogen may be washed out with a solvent to leave just the polymer scaffold (step 3). The scaffold may then be refilled with an achiral nematic LC (step 4). When refilled, the resulting structure exhibits many characteristics that are the same or similar to those of the original LC (a photonic band-gap for a chiral nematic, for example). This technique requires a large enough concentration by weight of reactive mesogen that the device is sufficiently robust to act as a template and to survive the washing out procedure [17].

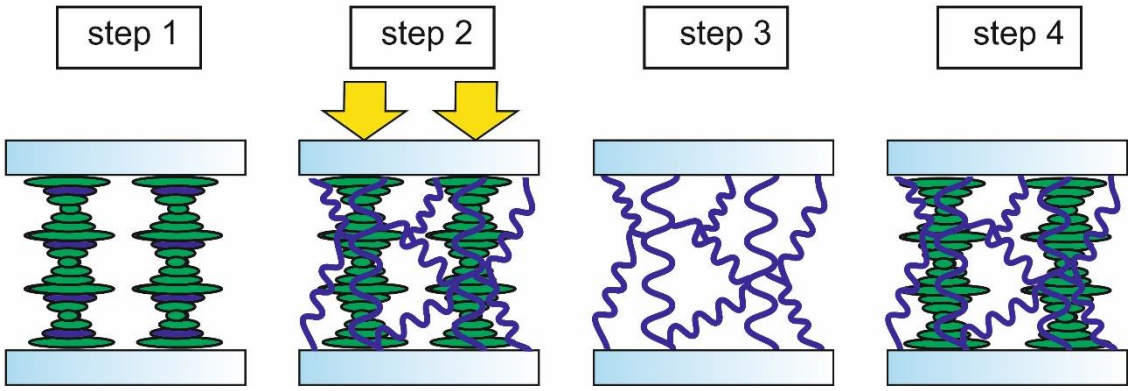

Figure 2 - An illustration of the templating procedure for a chiral nematic liquid crystal: a templated chiral polymer scaffold with an achiral nematic liquid crystal is formed by filling a chiral nematic liquid crystal/reactive mesogen mix into a glass cell (step 1) and then photo-polymerised using UV light (step 2); the liquid crystal and remaining unreacted reactive mesogens are then removed to leave a chiral polymer scaffold (step 3), which is then refilled with an achiral nematic liquid crystal (step 4).

Work has also been performed to polymer-template the blue phase [18]. This resulted in a templated 3D structure. The templated blue phases are stable to a broad range of temperatures (in contrast to the small temperature-range of most blue phase LCs) and may be used as lasers. In this Chapter, I will describe work to polymer-template the SmA phase for the first time.

3.1.3 – Applying electric fields to nematic and smectic A liquid crystals

When an electric field is applied to a nematic LC, the LC director aligns with the field [19]. This transition from a uniform director configuration to a deformed director configuration upon application of a sufficiently strong electric field is known as the Fréedericksz transition. The potential deformations are usually classified as splay, twist and bend [20]. This transition threshold voltage is given by:

$$V_{thr} = \pi\left(\frac{K_{xx}}{\varepsilon_o \Delta\varepsilon}\right)^{\frac{1}{2}} \tag{3.1}$$

Where V_{thr} is the threshold voltage for the splay (K_{11}), twist (K_{22}) and bend (K_{33}) deformations. Below the threshold, the director is undistorted. As the field is increased from this threshold, the director reorients towards alignment with the field.

The result of this realignment when a field is applied across a planar aligned cell (as used here, in which the nematic director profile is aligned parallel to the substrates and a positive dielectric anisotropy material is used) is for the director to align perpendicular to the substrates. This results in a change in the transmission through the glass cell as the director reorients and the birefringence changes. This is because, according to Equation 2.2 (repeated here for convenience):

$$T = T_0 \sin^2(2\varphi)\sin^2\left(\frac{2\pi d\Delta n}{\lambda}\right) \tag{3.2}$$

Where T is the transmission through the device, φ is the angle of the optical axis relative to the polariser axes and d is the cell thickness (d = 5 μm here) [21]. Thus, when an electric field is applied to a nematic LC, the transmission will change following the second $\sin^2(x)$ term if it is at a fixed angle with respect to the crossed-polarisers. When the electric field is removed, the nematic relaxes back to its original alignment due to elastic restoring forces. This reversible switching allows nematic LCs to be used as electrically-controlled intensity modulators. However, nematic LCs exhibit thermal fluctuation of the director which result in scattering and so reduce the contrast ratio of such devices (the contrast ratio is the ratio between the bright and dark state of the LC – the maximum and minimum transmission states).

When an electric field is applied to a SmA LC, the molecules cannot align with the electric field as they do in a nematic LC because the layer thickness must remain constant. This results in a transition from a layered structure to a scattering focal conic structure, as shown in Fig 3. This change is irreversible – when the electric field is

removed, the SmA alignment is not recovered. Thus, SmA LC devices cannot be used as intensity modulators in the same way as nematic LCs.

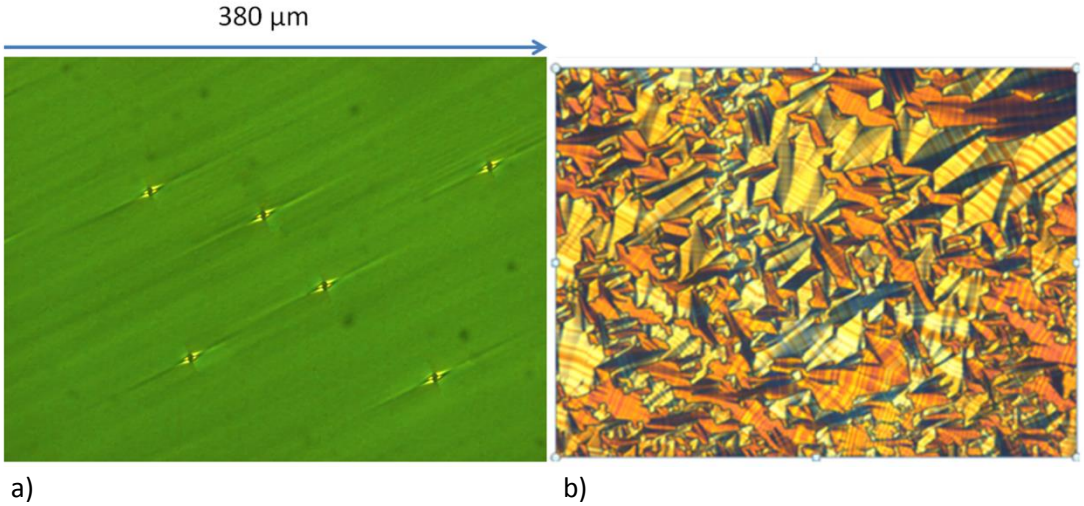

Figure 3 – a) a planar-aligned smectic A liquid crystal; b) A focal conic texture after an ac electric field (10 V/µm, 1 kHz) was applied to the texture shown in a). Measurements taken at 20°C in an antiparallel, planar aligned cell.

3.2 – Sample Preparation

3.2.1 – Polymer-stabilised smectic A phases

The SmA material used here was a mixture of a mono-mesogenic organosiloxane (40 wt%) dispersed into the nematic liquid crystal BL006 (Merck). The exact chemical structure of the organosiloxane material is shown in Fig 4. This organosiloxane was used as it has previously been studied and shown to exhibit a SmA phase over a wider temperature range than a corresponding chain-length alkloxy-cyanobiphenyl [19]. The molecule is mono-mesogenic and is composed of an aliphatic chain, an aromatic core and a siloxane (Si-O-Si) group. It is this bulky siloxane group that results in micro-segregation and consequently a SmA phase at room temperature [22]. On heating, the resulting mixture exhibited a SmA LC phase between room temperature (20°C) and 68°C, a multiphasic region from 68°C to 78°C and an isotropic phase above 78°C.

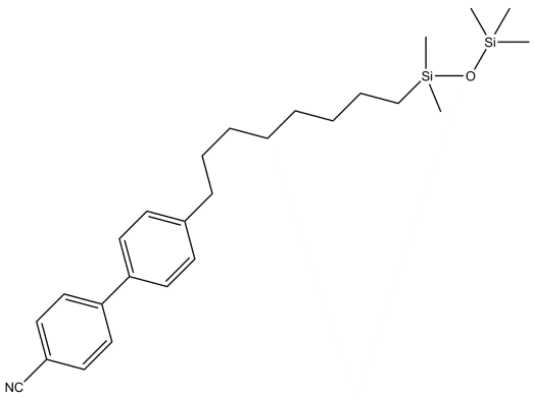

Figure 4 – The chemical structure of the organosiloxane mesogen used in this work.

This SmA was then dispersed into a mixture of reactive mesogens, photo-initiator and thermal inhibitor (UCL-011-K1, DIC, 30 wt%). This mixture was chosen because it contains all the necessary components for photo-polymerisation; furthermore, it has been previously used for related work on polymer-templating [17-18].

On heating, the resulting mixture exhibited a SmA phase from room temperature (20°C) to 53°C, and a nematic phase from 53°C to 74.2°C and an isotropic phase above 74.2°C. The SmA LC phase in a planar aligned geometry was identified by optical polarising microscopy as described in Chapter 2, Section 2.4.1. Due to the long recovery length of the SmA, there is a noticeable distortion of texture around any defects – where the ordering has been disrupted over a much longer distance than would be seen in a nematic or chiral nematic LC. In the case of the cells used here, there are spherical spacer beads that define the cell thickness and these act as defects. The SmA phase manifests as a characteristic 'eyelet' pattern around these spacers. The SmA phase may also be differentiated from the nematic phase because it does not exhibit Brownian motion. This is because in a smectic LC, the fluctuations of the director are overdamped by the layered structure.

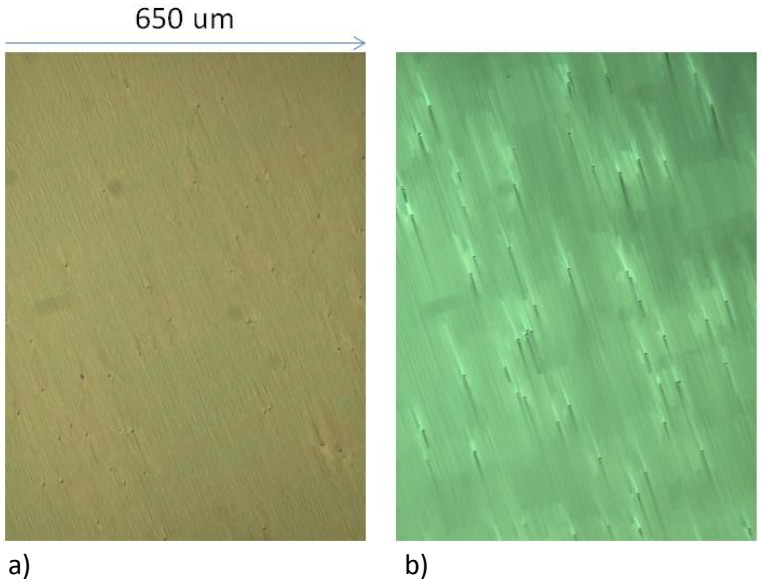

Figure 5 – The texture of the smectic A/reactive mesogen mixture filled into a planar-aligned cell. a) before and b) after photo-curing as seen on an optical polarising microscope. The black dots are spacer beads (5 µm). Results taken at 20°C.

To create polymer templated SmA devices, the SmA/reactive mesogen mixture was capillary-filled into 5 µm-thick glass cells made of indium tin oxide coated glass consisting of anti-parallel rubbed planar alignment layers (Instec). This was performed at temperatures above the nematic to isotropic transition temperature. These cells were then cooled to 20°C. The samples were confirmed to be in the SmA phase using optical

polarising microscopy; an example texture is shown in Fig 5a. To photo-polymerise the samples, they were illuminated with UV light (λ = 365 nm). To ensure a uniform curing throughout the cell, the samples were illuminated for 12 seconds from each side of the cell. A 185 mW/cm^2 high-powered LED UV light source system (Thorlabs CS2010) was held at a distance of 10 cm from the sample. This yielded a photo-polymerised SmA as shown in Fig 5b. In Figs 5a and b, the layered structure can be seen and the characteristic 'eyelet' texture is clearly visible around the spacer beads. On heating the SmA texture was retained to above 200°C.

3.2.2 – Polymer-templated smectic A phases

The polymer-stabilised devices contained a porous polymer network with LC and unreacted reactive mesogen in interstitial sites. To remove this LC, the cells containing the polymer-stabilised SmA materials were placed in acetone (99.9%) for 24 hours. This left only the polymer scaffold in the cell. Optical polarising microscopy was used to confirm that all remaining LC material had been removed, as shown in Fig 6a; the image is dark due to the absence of any birefringent (LC) material. The cells were left to dry at room temperature for 8 hours. Following this, the cells were refilled with just the achiral nematic LC BL006 (Merck). BL006 was chosen because it is commercially available and its properties are well-characterised. The LC was filled into the cells by capillary action at a temperature above the isotropic temperature of BL006 (120°C). This took around 24 hours (significantly longer than filling empty cells). Although the texture is less pronounced, the eyelet pattern is still seen. I believe that the washing out procedure does to some extent damage the polymer network and so this is not unexpected. The optical texture of the resulting devices is shown in Fig 6b.

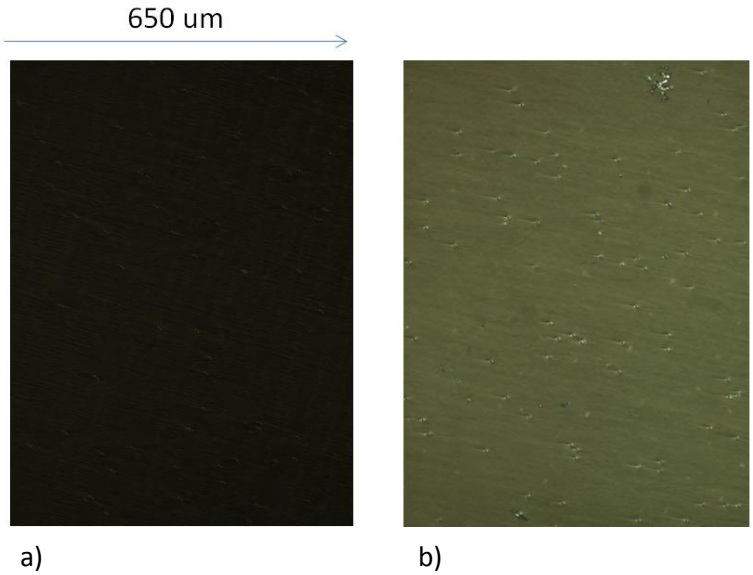

Figure 6 – Optical polarising microscopy images of the device a) after washing out the non-cross-linked mesogens and b) after refilling with the nematic LC BL006. The black dots are spacer beads (5 µm). Results taken at 20°C.

To further elucidate the texture of the devices at various stages in the templating procedure, Fig 7 shows grey-scale-mapped optical polarising microscopy images of the LC texture at room temperature at different stages of the templating process. Grey-scale mapping has been used to enhance the contrast of the images and to further elucidate the characteristic SmA texture. In the case of Fig 7a (the texture before forming the polymer network), layering can clearly be seen, and there are 'eyelet'-shaped defects around the spacer beads. This texture is maintained after photo-polymerisation and the layered structure and eyelet defects can still be seen as shown in Fig 7b. There is no visible texture in the washed-out sample as only the polymer scaffold remains. When the polymer scaffold was refilled with a nematic LC (BL006) the visible texture is regained, Fig 7c, although as previously discussed, the layering has been smoothed by the templating procedure.

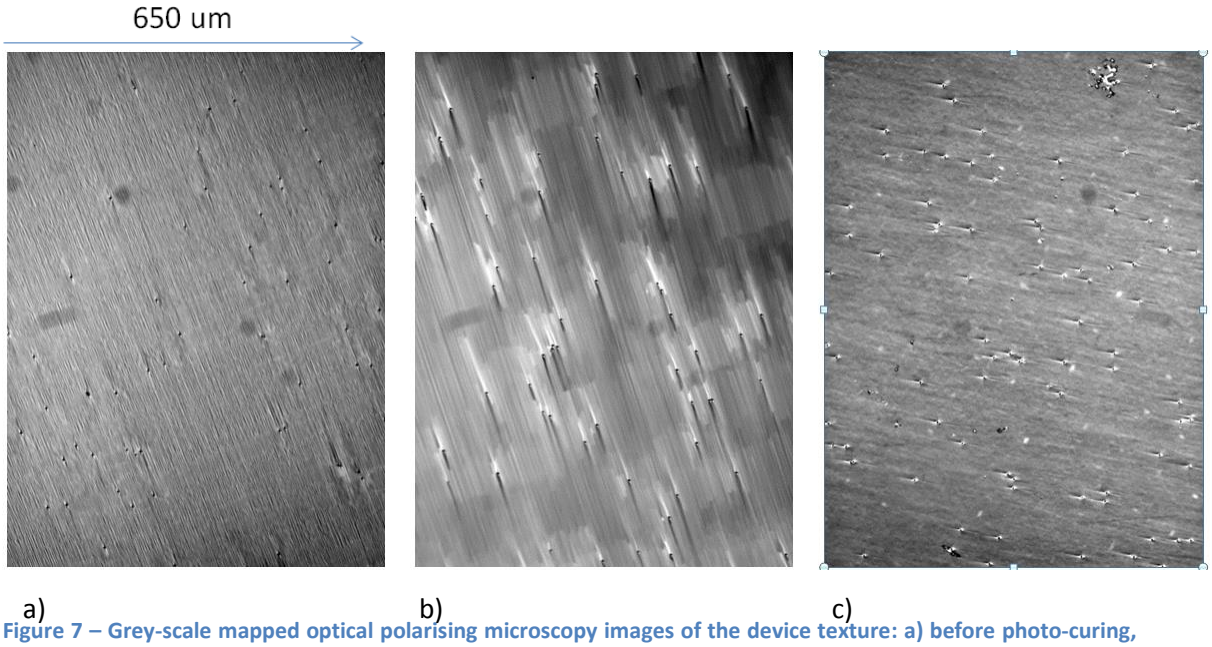

Figure 7 – Grey-scale mapped optical polarising microscopy images of the device texture: a) before photo-curing, b) after photo-curing and c) after washing the device our and refilling with the nematic liquid crystal BL006. The black dots are spacer beads (5 µm). Results taken at 20°C.

The retention of the SmA characteristic texture demonstrates that the polymer scaffold has imposed the texture of the SmA phase onto the infilled nematic LC. To further show that the polymer scaffold influences the texture, I created a cell that contains two regions: one that contains only a nematic LC and one which contains the nematic in a polymer-templated formed from the SmA phase; the optical texture of such a cell is shown in Fig 8.

To achieve this, the cell filled with the SmA LC/reactive mesogen mixture was masked before photo-curing. This meant that the polymer scaffold was only formed in one

region of the cell. The cell was then washed out and refilled. The masked areas contained only nematic LC while the unmasked area contained a polymer scaffold (and so resulted in a polymer-templated region). This can be seen in Fig 8 where there is an ordered polymer-templated SmA LC texture in the bottom half of the image (including 'eyelet' patterns around the spacer beads), and a uniform nematic LC texture in the top half. As well as the difference in texture visible in Fig 8, Brownian motion could clearly be observed by eye in the top (nematic) case, while it was absent in the SmA (bottom) case. These results suggest that this method does to some extent imprint the alignment of a SmA phase onto an achiral, nematic LC.

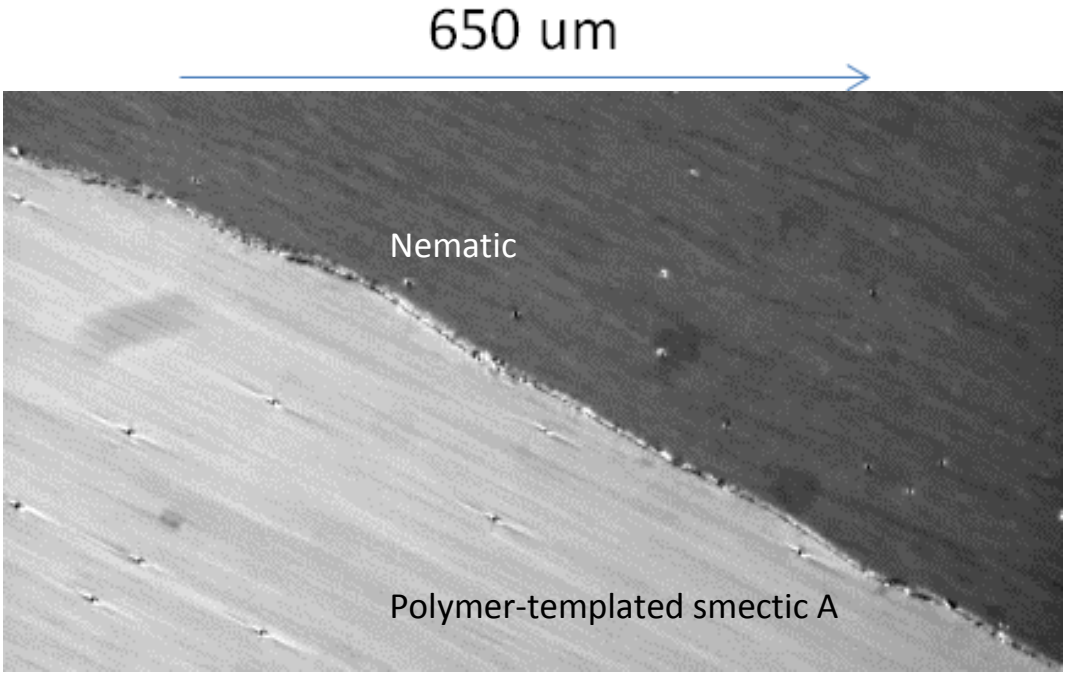

Figure 8 – A grey-scale mapped optical polarising microscopy image of a device containing areas of the nematic liquid crystal BL006 (top, darker) and SmA liquid crystal (bottom, lighter) The black dots are spacer beads (5 µm). Results taken at 20°C.

Our next step was to investigate how the electro-optic properties of the achiral nematic LC filled in to the polymer scaffold formed from the SmA phase compared to the behaviour of the neat nematic mixture in a glass cell under similar experimental conditions. For completeness, I also compared the response with that of a polymer-stabilised SmA liquid crystal.

3.3 – Electro-optic properties of polymer-templated smectic A phases

To create a nematic device, the nematic LC BL006 was filled into a 5 µm planar aligned cell at ~110°C. The comparison with a conventional nematic device is interesting because when an electric field is applied to a conventional nematic in a planar-aligned

cell (as used here), the LC director aligns with the electric field and the nematic switches from a planar alignment towards a homeotropic alignment (except near the surfaces). This results in an intensity modulation when the material is placed between crossed polarisers because there is an apparent refractive index change. However, in a nematic LC, there are director fluctuations that scatter light and decrease the contrast ratio (the difference in transmission between the bright and dark alignments). In SmA LCs, these fluctuations are suppressed due to the layered structure; however, SmA phases cannot be used as intensity modulators because when they are electrically switched the texture collapses irreversibly to the scattering focal conic texture. Thus, a material with the suppressed fluctuations of a SmA but the reversible switching of a nematic phase is an exciting prospect for improved intensity modulators. Here, I show that the SmA templated nematic materials exhibit reversible switching when an electric field is applied, and that their contrast ratios are improved compared to a conventional nematic device based upon the Freedericksz transition.

3.3.1 – Influence of an electric field on optical textures

The polymer-templated and polymer-stabilised SmA samples were observed on an optical polarising microscope as an electric field was applied. As discussed in Section 3.1.3, when an electric field is applied to an unpolymerised SmA LC, it irreversibly switches to a focal conic texture. However, as an electric field was applied to thje polymer-stabilised SmA LC sample, there was no change in the texture, only a slight darkening of the colour (as would be expected from a small change in the birefringence as the interstitial LC molecules align with the electric field). This is shown in Fig 9.

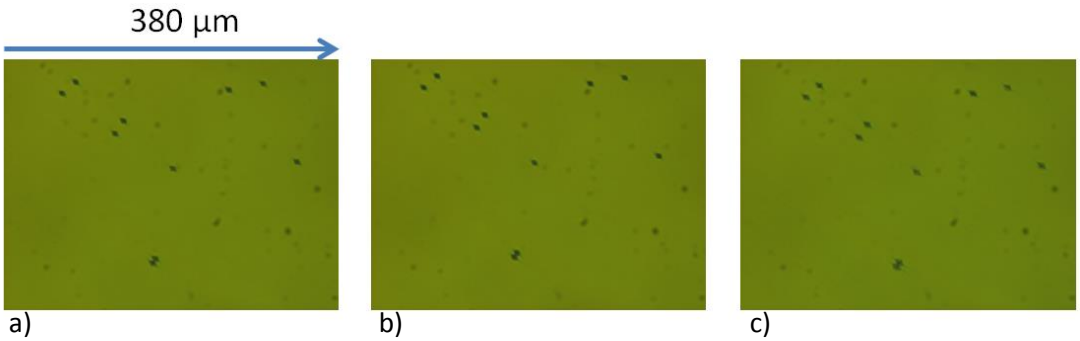

Figure 9 - optical polarising microscope images of a smectic A polymer-stabilised nematic liquid crystal: a) without a field applied; b) with a 10 V/µm electric field applied; c) with a 20 V/µm electric field applied. The black dots are spacer beads (5 µm). Results taken at 20°C.

In contrast, the polymer-templated sample exhibited significantly greater colour change without collapse of the optical texture as shown in Fig 10

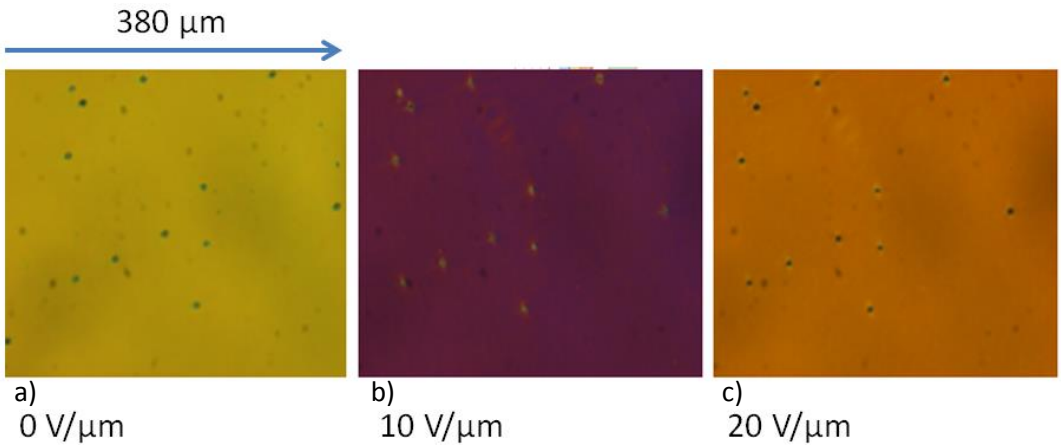

Figure 10 – optical polarising microscope images of a polymer-templated smectic A liquid crystal a) without a field applied; b) with a 10 V/µm electric field applied; c) with a 20 V/µm electric field applied. The black dots are spacer beads (5 µm). Results taken at 20°C.

3.3.2 – Transmission as a function of voltage

The transmission of the device when it is placed between crossed-polarisers was given by Equation 3.2 in Section 3.1.3. To characterise the electro-optic response of the devices, the samples were placed between crossed polarisers, as shown in Fig 11. They were aligned such that $\varphi = 45°$ to yield the maximum initial transmission and they were then illuminated by a continuous wave He-Ne laser (Melles-Griot) that emitted light with a wavelength of $\lambda = 633$ nm. A 1 kHz voltage was applied across the glass cells using a signal generator (Tektronix AFG-3022). To obtain voltages up to 200 Vp-p (20 V/µm for 5 µm cells) a voltage amplifier (FCC electronics F10AP) was used. The function generator output was internally amplitude modulated (100% depth) with a square-wave to provide a gated output of bursts of modulated E-field (up to 20 V/µm) interspersed with gaps of zero field. The transmitted light was recorded as a function of the applied electric field on a fast photo-diode (Thorlabs PDA55) that was connected to a 16-bit data acquisition card sampling at 50 kS/s (National Instruments PCI-6033E).

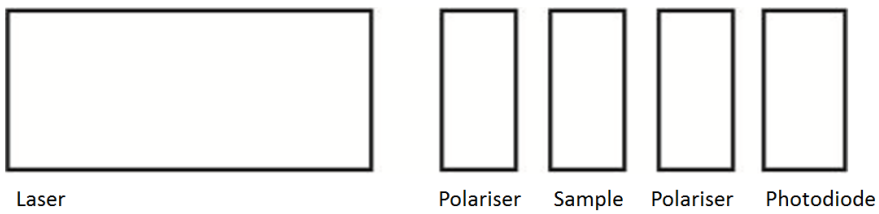

Figure 11 – Experimental setup for transmission measurements. The polarisers were crossed.

In the case of the polymer-stabilised SmA samples, there is only a very small change in the transmission even at the highest electric field amplitudes that were used in this study (20 V/µm) – as shown in Fig 12a. Fig 12b shows the change in the birefringence as a field is applied. There is only a small change (-0.01). This is because the polymerisation

procedure has 'locked in' the LC director orientation and prevents them from reorienting to align with the direction of the applied electric field; the switching has been suppressed. As a result, the alignment of the SmA texture (which would irreversibly collapse to a focal conic texture in the un-polymerised SmA) has been stabilised, but its switching has been curtailed.

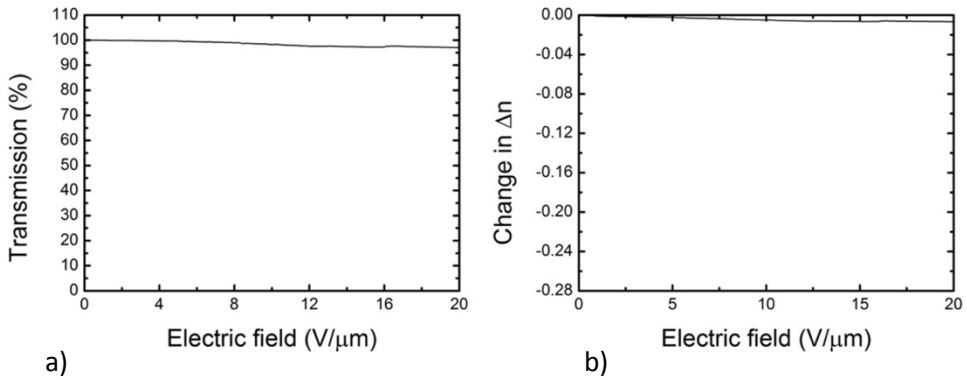

Figure 12 – a) Transmission as a function of voltage and b) change in birefringence as a function of voltage for a polymer-stabilised smectic A liquid crystal in the smectic A phase. Results taken at 20°C in 5 µm cells.

The same experiment was performed on the nematic LC BL006 (Δn = 0.278 at 633 nm and 20°C). The transmission as function of voltage is shown in Fig 13a. This follows the second $\sin^2(x)$ term in Equation 3.2 as I would expect given that I are using planar-aligned cells and that as the field is applied, the LC molecules align with the electric field so that the birefringence changes. That change in LC birefringence is plotted in Fig 13b; this was calculated using equation 3.2. There is a decrease in the birefringence of -0.25 as the field is increased up to 20 V_{pp} (2 V/µm). This is significantly greater than the change in birefringence seen in the polymer-stabilised SmA samples (-0.01). The birefringence of BL006 is 0.278 at 20°C and 633 nm so a -0.25 change in the birefringence corresponds to the director reorienting from predominantly lying in the plane of the device (planar alignment) to predominantly perpendicular to it (parallel to the electric-field).

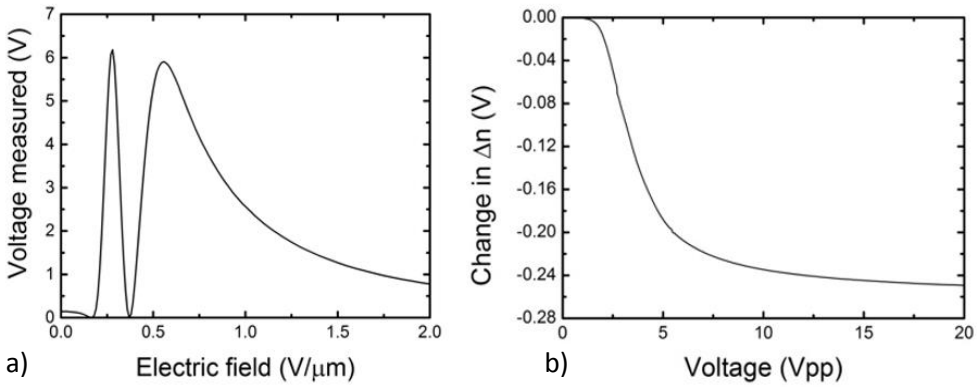

Figure 13 – a) Transmission as a function of voltage and b) change in birefringence as a function of voltage for the nematic liquid crystal BL006. Results taken at 20°C in 5µm cells.

Subsequently, the transmission as a function of voltage (Fig 14a) and the change in birefringence as a function of voltage were measured for the SmA polymer-templated nematic (Fig 14b). The SmA templated nematic exhibits a tuning of the birefringence (-0.09) that is intermediate between that of the achiral nematic and that of the polymerised SmA. Thus, it appears that the switching is still somewhat suppressed compared to a nematic LC. However, in contrast to the unpolymerised SmA sample, the switching is found to be reversible when the electric field is removed. Here the director relaxes back to the initial state that is governed by the anchoring conditions imposed by the polymer network. A further point to note is that the minimum in the transmission-voltage curve occurs at a higher voltage for the templated SmA than for the nematic LC (1.25 V/µm compared to 0.28 V/µm). For the polymer-stabilised case, the director is free to re-orientate within small domains that have a large surface area to volume ratio. The increased surface area leads to increased anchoring, which in turn leads to a greater resistance to reorientation of the director than that observed for the unpolymerized nematic sample. It should also be noted that if the templating procedure damages the polymer network then these domains will be larger in size and therefore the anchoring strength will be reduced resulting in a reorientation of the director at lower electric field strengths.

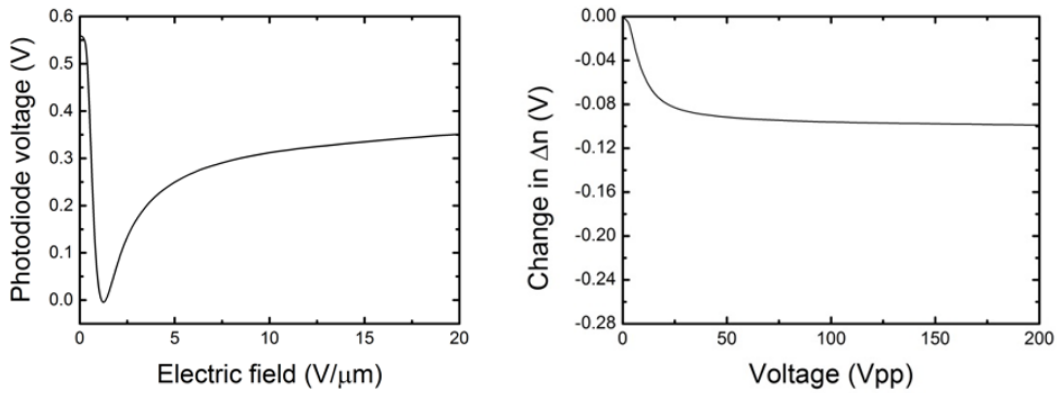

Figure 14 – a) Transmission as a function of voltage and b) change in birefringence as a function of voltage for a smectic A polymer-templated nematic liquid crystal. Results taken at 20°C in 5µm cells.

3.3.3 – Contrast ratios

I performed experiments to compare the contrast ratios for the templated SmA devices to those of the nematic LC BL006 to see if polymer-templating maintained the improved optical properties of the SmA phase compared to the nematic phase.

I defined the contrast ratio as the ratio of the light transmitted in the bright state to that transmitted in the dark state. Due to the variety of ways of measuring the contrast ratio

[25-26], I measured it using three different methods; these different methods resulted in different values of the contrast ratios, but in all cases the contrast was significantly greater for the SmA templated, and larger by a commensurate amount – around 12 times larger in all three cases. The results for the three methods are presented in Table 1 below.

	BL006	Polymer-templated smectic A	Improvement
Method 1 (rotating, 633 nm illumination)	550	6684	12x
Method 2 (rotating, white light illumination)	Red/green/blue = 24/31/27	Red/green/blue = 270/150/120	Red/green/blue = 11/5/5x
Method 3 (electric-field, 633 nm illumination)	320	4230	13x

Table 1 – comparison of the contrast ratios measured using three different methods.

In the first method, the sample was placed on a rotatable stage between crossed-polarisers and illuminated with a He-Ne laser emitting at 633 nm. No voltage was applied. The sample was rotated and the minimum and maximum transmissions were used to calculate the contrast ratio (i.e. the transmission when φ = 45° and 90° respectively). This gave a contrast ratio of 6700 for the polymer-templated SmA and 550 for BL006, an improvement of 12 times.

In practical display devices, the illumination is not as ideal as laser radiation, being both incoherent and emitting a broad range of wavelengths. Therefore, I performed a similar experiment using a white light source on a microscope in place of the laser. Again, no voltage was applied. The sample was placed on the rotation stage of an optical polarising microscope (Olympus BX51) and illuminated with the microscope white light source. A series of images were taken using a camera (PixelLink, PL-B686CU, 12-bit colour) with different integration times; from this, colour maps were obtained. From these, the contrast ratio for red, green and blue light was measured as red/green/blue = 270/180/130 for the polymer-templated SmA and as red/green/blue = 24/31/27 for the nematic. This gives an improvement of red/green/blue = 11/5/5 times. The red light gives roughly the same improvement (although with a lower value of the contrast ratio

compared to method 1). Green and blue light experience less of an improvement in the contrast ratio, although 5 times is still significant.

The third method that I used to measure the contrast ratio was to place the sample between crossed-polarisers at an angle of 45° and illuminate it with a He-Ne laser (emitting at 633 nm) as in method 1. However, rather than rotating the sample, I applied a 1 kHz square wave electric field (20 V/μm) and measured the transmission. The contrast ratio was calculated using the maximum and minimum in the plots of transmission as a function of voltage. In this case the contrast ratio was 4230 for the refilled SmA and 320 for BL006, an improvement of 13 times.

All three of these methods gave an improvement in the contrast ratio of 11-13 times for red light. The improvement was somewhat lower for green and blue light (5 times), although still a significant improvement.

3.3.4 – Response times

Finally, I studied the response time of the SmA polymer-templated nematic and compared it to that of the nematic BL006 to see how templating affected the switching speed. The change in birefringence as a function of time is shown in 15 for the nematic LC BL006 (Fig 15a) and for the polymer-templated SmA (Fig 15b). The shapes of the curve are very similar, although on different time-scales. The 90-10% ON-OFF response time (relaxation time) of BL006 was 90 ms, while that of the SmA polymer-templated nematic LC was 13 ms. This means that the templated SmA relaxation time is 6 times faster than that of the nematic it was refilled with.

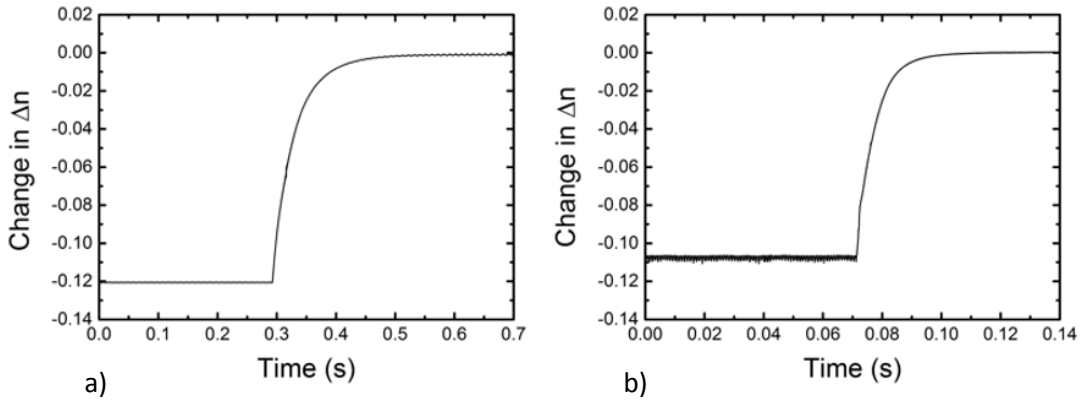

Figure 15 – Relaxation (ON-OFF) response times for a) the nematic liquid crystal BL006 and b) a Smectic A polymer-templated nematic liquid crystal. Results taken at 20°C in 5μm cells.

The response times were both significantly faster when driven (i.e. the OFF-ON response times), as would be expected. The OFF-ON response times are 8.6 ms for the

nematic LC and below the resolution limit of our setup (0.1 ms) for the SmA templated nematic; this is shown in Fig 16.

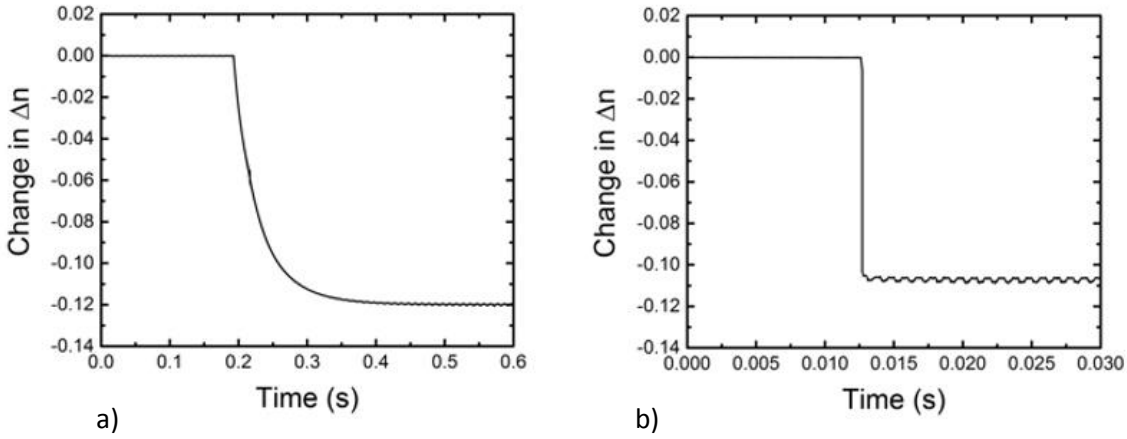

Figure 16 – Driven (OFF-ON) response times for a) the nematic liquid crystal BL006 and b) a Smectic A polymer-templated nematic liquid crystal. Results taken at 20°C in 5µm cells.

3.4 – Templating between the isotropic and chiral nematic phases of a liquid crystal

In the previous section, I described work showing that it was possible to apply the polymer templating technique to different LC phases. Subsequently, I worked to polymer-template at the boundary between different LC phases – specifically between the chiral nematic and isotropic phases. I found that when such a device was washed out and refilled, the isotropic regions exhibited nematic behaviour. This means that Ihave created a device that consists of chiral nematic droplets in a nematic texture – this is something that does not occur naturally. This preliminary work is described in more detail in Appendix 1.

3.5 – Conclusion

In this chapter, I have described work to polymer-template the SmA LC phase. This was performed by adding reactive mesogens to a SmA LC phase, photo-curing, washing out the LC with a solvent and then refilling the resulting polymer scaffolds with a nematic LC. This resulted in the alignment of a SmA LC phase being imprinted onto a nematic LC; the resulting devices exhibited the beneficial properties of both the nematic phase (reversible switching) and those of the SmA LC phase (improved contrast ratio) in addition to an increased response time.

In this Chapter, I described work to create the polymer-templated device and to study them using optical polarising microscopy. Subsequently, I investigated their electro-optical properties and compared them to those of conventional nematic devices. The

templated SmA devices exhibit switching with a faster relaxation response (by ~6 times) and a better contrast ratio (by ~12 times) than these nematic LCs.

The improved electro-optical properties of polymer-templated LCs ledmes to investigate polymer-stabilisation of other LC phases, such as the chiral nematic LC phase. This will be discussed in the next chapter where polymer-templating is used to extend the wavelength-tuning range of the chiral nematic photonic band-gap as an electric field is applied. This is particularly interesting given the wide range of applications of the chiral nematic photonic band-gap (such as LC lasers). Chapter 4 will also detail work to polymer-template LC lasers to extend their electric-tuning ranges by ~2.5 times.

3.6 – References

1. I. Dierking, *Polym. Chem.*, 2010, **1**, 1153.
2. J. Clayden, N. Grreves, S. Warren, Organic Chemistry, Second Edition (2012), OUP.
3. N. Kim and T. Kyu, *Liq. Crystals*, 2012, **6**, 255396.
4. I. Dierking, *Materials*, 2014, **7**, 3568.
5. M. Mohammadimasoudi, J. Beeckman, J. Shin, K. Lee, and K. Neyts, *Opt. Express*, 2014, 22, 190.
6. Y. Inoue, H. Yoshida, H. Kubo, and M. Ozaki, *Adv. Opt. Mater.*, 2013, **1**, 256.
7. H. Kim, Y. Inoue, J. Kobashi, Y. Maeda, H. Yoshida, and M. Ozaki, *Opt. Mater. Express*, 2016, **6**, 705.
8. H. Kikuchi, M. Yokota, Y. Hisakado, H. Yang, and T. Kajiyama, *Nat. Mater.*, 2002, **1,** 64.
9. S. H. Kim and L.-C. Chien, *Proc. SPIE*, 2003, **5003**, 44.
10. R. A. M. Hikmet and M. Michielsen, *Adv. Mater.*, 1995, **7**, 300.
11. C. A. Guymon, L. A. Dougan, P. J. Martens, N. A. Clark, D. M. Walba, and C. N. Bowman, Chem. Mater., 1998, **10**, 2378.
12. S. Kaur, I. Dierking, and H. F. Gleeson, *Eur. Phys. J. E. Soft Matter*, 2009, **30**, 265.
13. R. Kumar and K. K. Raina, *Liq. Cryst.*, **41**, 694
14. A. S. Sonin and N. A. Churochkina, *Polym. Sci. Ser. A*, 2010, **52**, 463.
15. P. Archer and I. Dierking, *J. Opt. A Pure Appl. Opt.*, 2009, **11**, 024022.
16. P. G. de Gennes, *Phys. Lett.* 1969, **28A**, 11.
17. S. S. Choi, S. M. Morris, W. T. S. Huck, and H. J. Coles, *Adv. Mater.*, 2010, **22**, 53.
18. F. Castles, F. V Day, S. M. Morris, D.-H. Ko, D. J. Gardiner, M. M. Qasim, S. Nosheen, P. J. W. Hands, S. S. Choi, R. H. Friend, and H. J. Coles, *Nat. Mater.*, 2012, **11**, 599.
19. Goodby, J. W., et al. Handbook of liquid Crystals volume 3, 2nd edition (2014), Wiley-VCH, Chapter 9
20. Dierking, I., Textures of Liquid Crystals, Wiley VCH (2004), Chapter 2
21. S. M. Morris, Display Systems lecture notes, Cambridge University, 2013.
22. A. A. Khan, S. M. Morris, D. J. Gardiner, M. M. Qasim, T. D. Wilkinson, and H. J. Coles, *Opt. Mater.*, 2015, **42**, 441.
23. D. J. Gardiner and H. J. Coles, *J. Phys. D. Appl. Phys.*, 2007, **40**, 977.
24. D. Yang, S.-T. Wu, Fundamentals of Liquid Crystal Devices, Wiley (2nd ed.), 2015, Chapter 8.
25. Y-C Choi, et al, *Nanotech.*, 2008, **19,** 38.
26. J. H. Lee, et al., *Opt. Lett.*, 2013, **21**, 26914.

Chapter 4 – Polymer templating the chiral nematic liquid crystal phase

In the preceding Chapter, I showed that it is possible to use polymer-templating to imprint the alignment of a smectic A liquid crystal (LC) onto a nematic LC. The resulting devices exhibited a reversible intensity modulation with a better contrast ratio and a faster response times than a conventional nematic LC. This Chapter continues the study on polymer-templating LC phases and focuses specifically on the chiral nematic LC phase. Chiral nematic LCs possess a 1-dimensional photonic band-gap which makes them interesting photonic material for applications such as lasers and tuneable optical filters.

This Chapter begins with an overview of methods that have previously been used to tune the wavelength position of the photonic band-gap of chiral nematic LCs by using electric fields. Subsequently, I describe a study to compare the electro-optical properties of a polymer-templated LC to those of a polymer-stabilised chiral nematic LC. From these studies, I discovered that while polymer-stabilised LCs exhibit a fast ($t \sim 1$ ms) blue-shift of only the long-wavelength band edge, the polymer-templated samples exhibit an additional, longer and slower shift ($t \sim 6.5$ s) of the entire band-gap (at the electric fields used in this work, 0-40 V/μm). From these observations, it appears that there are two different tuning mechanisms responsible for this differing behaviour, and in this Chapter I seek to provide a possible explanation for the relatively broad and slow tuning response that is observed in these polymer-templated LC devices.

I characterise the electro-optic properties of the polymer-templated chiral nematic LCs by studying the photonic band-gap as ac electric fields are applied. Subsequently, I show that these templates can be used to create wavelength tuneable laser devices by refilling the polymer scaffold with a dye-doped achiral LC. I compare the electro-optic properties of these lasers to LC lasers that have been created by polymer-stabilising LCs. The polymer-templated lasers exhibit longer wavelength tuning ranges when electric fields are applied.

4.1 – Background

4.1.1 – Electric-field tuning of the photonic band gap in a chiral nematic liquid crystal

Chiral nematic LC phases possess a photonic band-gap and this makes them interesting optical materials with applications from lasers to displays to optical shutters [1-3]. It is particularly important because the position of the band-gap may be tuned by a variety of external stimuli. From Equations 2.3 and 2.4 in Chapter 2:

$$n_e p = \lambda_L \tag{4.1}$$

$$n_o p = \lambda_S \tag{4.2}$$

These equations suggest numerous routes to wavelength-tune the band gap – by influencing the pitch of the helix (for example, using mechanical forces [4], light [5], magnetic [6] and electric fields [7-9]) or by influencing the relevant refractive indices (for example, using temperature [10] or electric fields [11-15]).

Of these various forms of external stimuli, electric fields are the most desirable option from a technological standpoint. However, the use of electric fields is complicated because the actual response of a chiral nematic LC to an externally applied electric field depends upon a number of factors. Specifically, this includes the orientation of the electric field direction relative to the helix axis (**h**) and the sign of the dielectric anisotropy (Δε), as discussed in Section 2.2.3.

The response of a chiral nematic LC to an electric field includes a term that corresponds to the free-energy density due to dielectric coupling: $-\frac{1}{2}\varepsilon_0\Delta\varepsilon(\boldsymbol{E}.\boldsymbol{n})^2$ which means that the magnitude and sign of the dielectic anisotropy are important [16]. With a positive dielectric anisotropy material, the LC director aligns with the electric field. If instead a negative dielectric anisotropy material is used, the director aligns perpendicular to the field.

If Δε>0 and the electric field is applied perpendicular to the helical axis the structure may be unwound and the chiral nematic pitch increased. Above a critical field, the chiral nematic will be entirely unwound and it will transition from the chiral nematic to the nematic LC phase.

The critical field, E_C is given by:

$$E_C = \frac{\pi^2}{p}\left(\frac{K_{22}}{\Delta\varepsilon}\right)^{\frac{1}{2}} \tag{4.3}$$

Where p is the pitch and K_{22} is the twist elastic constant [17].

However, realising a field perpendicular to the helix axis using conventional glass cells is non-trivial experimentally. This is because only the standing helix geometry (Grandjean alignment) can be aligned to a high degree of uniformity [8]. Consequently, to satisfy the requirement that the field direction is perpendicular to the helix axis, interdigitated electrodes are required. Unfortunately, this leads to an inhomogeneous electric field profile around the electrodes and results in a non-uniform change in the helicoidal structure – there are focal conic domains around the electrodes with a Grandjean alignment in the gap. This results in a degradation of the optical finesse of the band-gap [8]. Furthermore, an electric field applied perpendicular to the helix axis can also lead to flexo-electric coupling (whereby an external electric field couples to a LC and induces a macroscopic polarisation [18]). This can result in other modifications to the helical structure [9], however the flexo-electric effect is beyond the scope of this thesis.

If an electric field is applied parallel to the helix axis the behaviour again depends upon the sign of the dielectric anisotropy. When a high field is applied and $\Delta\varepsilon>0$, the helix axis is rotated by 90° (the helix 'lies down') which results in a focal conic optical texture and the removal of a photonic band-gap before any shift is seen [11]. At higher fields still, a homeotropic alignment is achieved with all of the LC molecules pointing in the direction of the field. If a low field and a low frequency is used a small blue-shift of the photonic band-gap can be seen because of the small inclination of the helix with respect to the electric field direction [19].

If the electric field is applied parallel to the helix axis and $\Delta\varepsilon<0$, a dynamic scattering state or a stabilised Grandjean texture are formed. This may be accompanied by a small shift in the photonic band-gap position as the helix is forced to align with the electric field [20] however this is only a small effect.

The critical field for collapse to the focal conic texture is:

$$E_C = \left(\frac{4\pi}{\Delta\varepsilon}\right)^{\frac{1}{2}} \left[K_{11}\left(\frac{\pi}{d}\right)^2 + K_{33}\left(\frac{2\pi}{p}\right)^2\right]^{\frac{1}{2}} \tag{4.4}$$

Where K_{11} and K_{33} are the splay and bend elastic constants and d is the device thickness. This is again proportional to $\sqrt{1/\Delta\varepsilon}$ and so the larger the dielectric anisotropy, the smaller the electric field required to collapse the chiral nematic phase [20].

Attempts have been made to maintain the geometry of a standing helix whilst using conventional planar electrodes at both substrates and still achieve wavelength tuning of the band-gap [12-15, 21-26]. For example, studies have been performed which use dc electric fields and chiral nematic LCs with a negative dielectric anisotropy ($\Delta\varepsilon<0$) to exploit an electromechanical effect [12-13]; ferroelectric LC compounds have been doped into chiral nematic LCs [14]; electrically commanded surfaces have been used [15]; and heliconical structure that can be observed in dimeric LCs have been studied [21].

One method for stabilising the standing helix geometry in the presence of an external electric field involves using reactive mesogens to polymer-stabilise the structure. This 'locks-in' the alignment and prevents it from collapsing in to a focal conic texture at high electric field amplitudes. It has been shown that these structures are robust to high electric fields, and that the reflection band can be tuned across a broad range of wavelengths (up to 141 nm has been reported [24]), and with a fast relaxation (field ON-OFF) response time (as low as 10 μs [25]), although in these studies very high (100s V/μm) electric fields were used.

In addition to polymer-stabilisation, polymer-templating has been performed to allow tuning of the chiral nematic photonic band-gap without collapse of the texture [25-7]. In the work described in Reference 26, broad tuning (>100 nm) was achieved by reorienting the LC molecules within the chiral polymer scaffold. This reorientation was ascribed to a change the effective refractive index of the material (and so a blue-shift of the long-wavelength band-edge to shorter wavelengths was seen); however, it was also observed that the quality of the band-gap was degraded by the washing out/refilling process.

In this Chapter, I describe work to determine the optimum concentration for polymer-templating the chiral nematic LC phase. I characterise the electro-optic properties of polymer-templated devices created using this optimum concentration; these results are used to compare the electro-optical properties of polymer-templated chiral nematics with equivalent polymer-stabilised chiral nematic LCs. I will study how the photonic band-gap changes as the applied electric field is increased, as well as the photonic band-gap temporal evolution; different behaviour is seen for the two types of device and here I seek to explain that difference. After the study of polymer-templated chiral nematic LCs, I describe work refill the polymer scaffolds with a dye doped nematic to yield LC

lasers that can be tuned when an electric field is applied to them. Polymer templated and polymer-stabilised LC lasers are compared and it is seen that the emission wavelength of polymer-templated LC lasers can be more widely wavelength tuned by applying an electric field than a corresponding polymer-stabilised sample.

4.2 – Polymer-templating the chiral nematic liquid crystal phase

4.2.1 – Determining the optimum polymer concentration for templating

In this section, I compare the electro-optic properties of polymer-templated and polymer-stabilised chiral nematic LCs. This begins with a study on polymer-stabilised samples containing different wt% of reactive mesogens to determine an optimum concentration that balances the need for a sufficiently dense polymer network that it can be used as a template, but also one that is not so dense that electric tuning of the band-gap is completely suppressed.

To form the base chiral nematic LC mixture consisting of non-reactive components, the high twisting power chiral dopant, R5011 (2.7 wt%, Merck KgaA), was dispersed into the achiral nematic LC, MDA-02-2149 (Merck KgaA). This was chosen because it exhibits a nematic phase at room temperature and has a high dielectric anisotropy of $\Delta\varepsilon = 38$ and so, the switching threshold will be lower (see equation 4.4 in Section 4.1.1). It has a birefringence of $\Delta n = 0.18$. This mixture exhibited a chiral nematic LC phase at room temperature with a right-handed helix, as confirmed by polarising optical microscopy – by observing the colour change as the chiral nematic LC in a Grandjean alignment was rotated between crossed-polarisers. To study the effect of the polymer concentration on the electro-optic and templating properties, eight samples consisting of different concentrations by weight of the reactive mesogen mixture (0-80 wt%) were prepared. This allowed a comparison of the effect of polymer concentration on the wavelength tuning ranges of the polymer-stabilised samples before carrying out the templating procedure. As in Chapter 3, I used the reactive mesogen mixture UCL-011-K1 (Dai Nippon Ink) which contained both mono- and di-acrylates, a photo-initiator and a thermal inhibitor. The mixtures were held above the clearing temperature of the LC (110 °C) for 16 hours to allow for thermal diffusion of the chemical constituents. These mixtures were then capillary filled into 5-µm thick planar-aligned glass cells (Instec) at 110°C and then annealed. The alignments were checked using optical polarising microscopy.

The transmission spectra of the different samples were then monitored as ac electric fields were applied to the polymer-stabilised samples containing different concentrations of the reactive mesogen mixture (0-80 wt%). This experiment was performed to understand the influence the polymer concentration has on the resulting wavelength tuning range of the band gap.

The electric field was applied across the glass cells using two bipolar square-wave signals in antiphase. These signals were created by splitting a 1 kHz (up to 20 Vp-p) signal from a function generator (Tektronix AFG-3022) into two and passing one through a unity gain inverting amplifier to provide two complementary outputs with a common ground. Each output was amplified to up to 200 Vp-p using a 2-channel voltage amplifier (FCC electronics F10AP). One output was connected to one electrode and the complementary output connected to the other electrode to provide a combined voltage across the cell of up to 400 Vp-p at 1 kHz (equivalent to an E-field of 40 V/μm for 5 μm cells). The signals from the amplifier were monitored using a digitising oscilloscope (Tektronix TDS224) to ensure that the waveform was not distorted at large voltage amplitudes.

When an electric field was applied to a sample containing 0 wt% reactive mesogen, no wavelength tuning of the band gap is observed, as demonstrated in Fig 1. This is because at relatively low electric fields (E ~ 1.4 V/μm) the Grandjean alignment of the chiral nematic LC collapses into a focal conic texture (as seen in the inset of Fig 1). As a result, the photonic band gap (seen at normal incidence to the cell) disappears. At polymer concentrations of 20 wt% and above, the Grandjean texture of the chiral nematic LC phase is stabilised by the polymer network and does not collapse into the focal conic state when a high-amplitude electric field is applied.

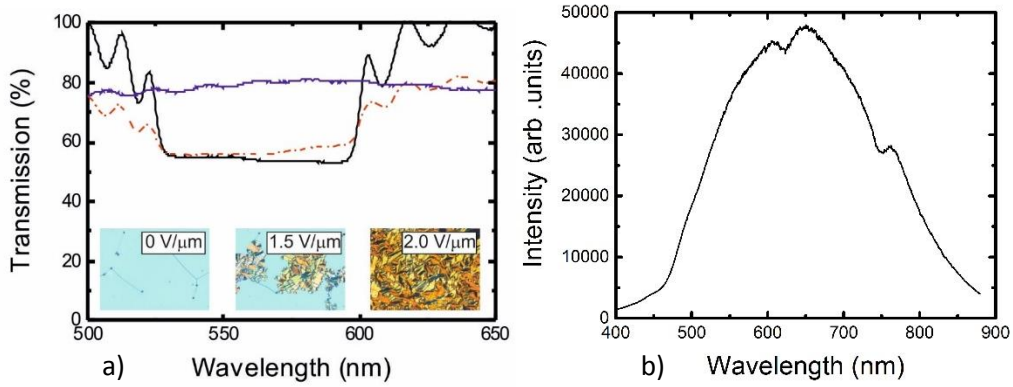

Figure 1 – a) The transmission spectra for white light showing the collapse of the band-gap as an electric-field is applied to a chiral nematic liquid crystal sample containing 0 wt% reactive mesogen. Black, 0 V/µm; Red, 1.5 V/µm Blue 2.0 V/µm. Inset: polarising microscope images showing the transformation of the Grandjean texture to a focal conic texture. Measurements taken at 20°C. b) The transmission spectrum of the white light source used for the measurements in this thesis.

As the electric field is increased, the long wavelength band-edge of a mixture containing 20 wt% polymer is blue-shifted continuously above the threshold electric-field ~ 20 V/µm, as shown in Fig 2a. The electric field needs to be so high because the polymer network suppresses switching compared to a conventional, unpolymerised chiral nematic LC. The extent of the blue-shift is found to decrease with increasing concentration of reactive mesogen until it is almost completely suppressed at concentrations above 50 wt%. Fig 2b shows the transmission spectra for a sample consisting of 50 wt% reactive mesogen; there is little change in the band gap for the same range of electric field amplitudes.

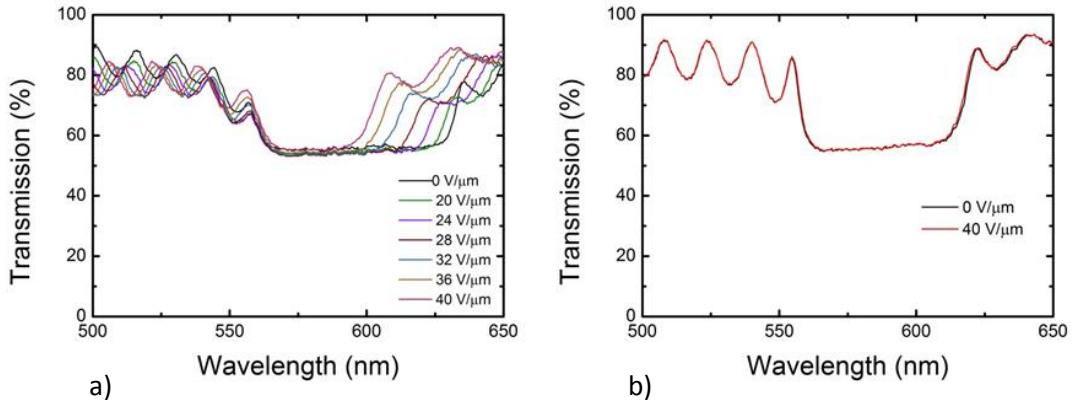

Figure 2 – a) A blue shift in the band-gap for a chiral nematic LC sample consisting of 20 wt% reactive mesogen as the magnitude of the applied E-field is increased; b) The transmission spectra for a chiral nematic LC sample consisting of 50 wt% reactive mesogen at different applied fields. Measurements taken at 20°C.

The decrease in tuning range with an increase in the concentration of reactive mesogen can be seen clearly when the tuning range is plotted as a function of reactive mesogen concentration, as shown in Fig 3. This shows that the extent over which the band gap blue shifts decreases considerably above 30 wt% of reactive mesogen. The largest shift

in the band gap that is observed is for a mixture consisting of 20 wt% reactive mesogen. However, at this concentration it was found that the polymer network was not robust enough to survive the washing out procedure and therefore it was not possible to use this as a template for other achiral nematic LCs. By increasing the concentration of the polymer to 30 wt%, I found that the polymer network was sufficiently rugged to survive the washing out procedure and thus could be used as a template. Therefore, this concentration represents the lowest concentration for which a large tuning range can be obtained whilst at the same time producing a robust polymer network that can be used as a template for other mesogenic compounds. Consequently, for the remainder of the work I used samples that consisted of 30 wt% of the reactive mesogen mixture.

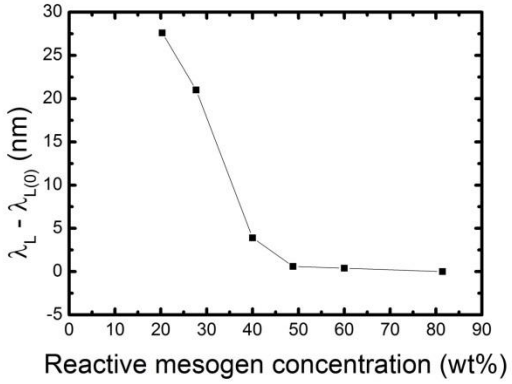

Figure 3 – The maximum blue-shift of the long wavelength band-edge (λ_L) from its initial position $\lambda_{L(0)}$ of the band-gap as a function of the reactive mesogen concentration (by weight). Measurements taken at 20°C.

4.2.2 – Wavelength tuning the band-gap of a polymer-stabilised chiral nematic liquid crystal

In this section, I characterise the electro-optic properties of a polymer-stabilised chiral nematic in terms of the wavelength tuning properties of the photonic band-gap while changing both electric field strength and over time. This will then be compared with a polymer-templated LC in the next section.

To begin with, I investigated the effect of applying an electric field on the position and integrity of the photonic band-gap. Fig 4a shows the change in the band-gap as an electric field is applied to a sample containing 30 wt% polymer. The band-gap maintains its integrity and sharp edges as the electric-field increases. Fig 4b shows position of the long wavelength band-edge as a function of electric field amplitude is shown, and an approximate threshold of $E \approx 20$ V/μm can be seen. On applying an electric field, it is found that the long-wavelength band-edge blue-shifts from 619 nm to 597 nm (corresponding to a total shift of $\Delta\lambda = 22$ nm) for amplitudes up to $E = 40$ V/μm.

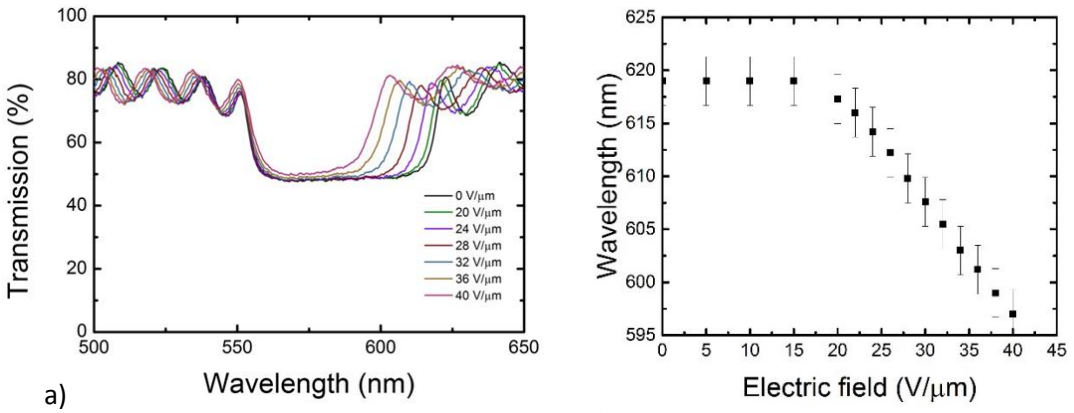

Figure 4 – Wavelength tuning of the band-gap for a polymer-stabilized chiral nematic liquid crystal containing 30 wt% reactive mesogen. a) The transmission spectra for different amplitudes of the applied electric field. B) A plot of the long-wavelength band-edge as a function of the applied electric field. Measurements taken at 20°C.

The optical polarising microscopy images show that although the colour darkens, the Grandjean texture is not noticeably distorted; this is shown in Fig 5.

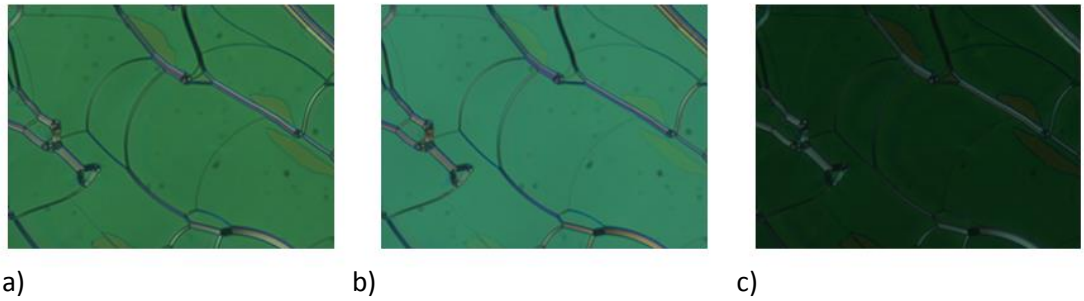

Figure 5 – polarising microscope images showing the Grandjean texture at different electric field strengths: a) 0 V/µm; b) 20 V/µm; c) 40 V/µm. Measurements taken at 20°C.

On the other hand, there was no resolvable blue shift in the short-band edge, as shown clearly in Fig 6a where the wavelength positions of both the long and short band-edges are shown. Consequently, upon increasing the magnitude of the electric field, the width of the band gap decreased from 65 nm to 43 nm (see Fig 6b).

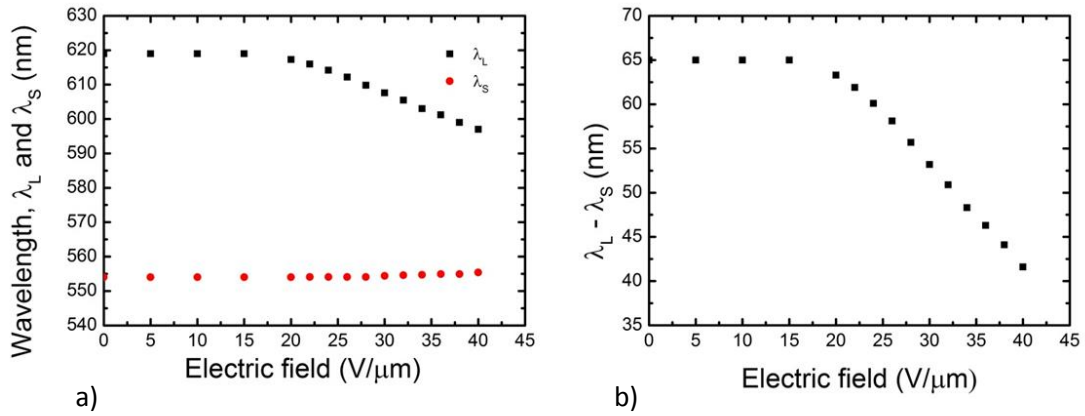

Figure 6 – a) Plots of both the long and short-wavelength band-edges of the photonic band-gap as a function of the applied electric field amplitude; b) the width of the photonic band-gap as a function of the applied electric field. Measurements taken at 20°C.

The next step was to look at the temporal evolution of the transmission spectrum. Fig 7a shows how the transmission spectrum changes with time after an electric-field of 40 V/µm was applied to the sample. Within the first 100 ms, the long wavelength band edge was found to shift by its maximum extent while the short wavelength band-edge remained fixed and did not subsequently change. This can be seen clearly in Fig 7b, where the wavelengths of the band-edges are plotted as a function of time; initially there is a relatively rapid shift of (only) the long wavelength band-edge within the first 100 ms; the long band-edge position then remains static with time. The response observed here is commensurate with a reorientation of the interstitial LC molecules within the polymer scaffold which results in a lowering of the effective n_e while n_o remains unchanged, in accordance with Equations 4.1 and 4.2 – and as discussed in previous studies [24-27].

Figs 7a and 7b indicate that the blue-shifts occurs within a timescale of 100 ms. To determine the time required to respond to the electric field being applied/removed more precisely, response time measurements were carried out. This change was reversible and only exhibited negligible hysteresis. The sample was illuminated by a 590 nm LED (Thorlabs M590L3). This was chosen so that there would be overlap of the LED emission and chiral nematic photonic band-gap in the absence of an electric field (as seen in Fig 4), but that this overlap would be diminished when an electric field was applied and the band-gap shifted. The output of a function generator was internally amplitude modulated (100% depth) with a square-wave to provide a gated output of bursts of modulated electric-field (up to 40 V/µm) interspersed with gaps of zero field. The optical response of the transmitted light was then measured using a fast-photodiode (Thorlabs PDA55), connected to a 16-bit data acquisition card sampling at 50 kS/s (National Instruments PCI-6033E).

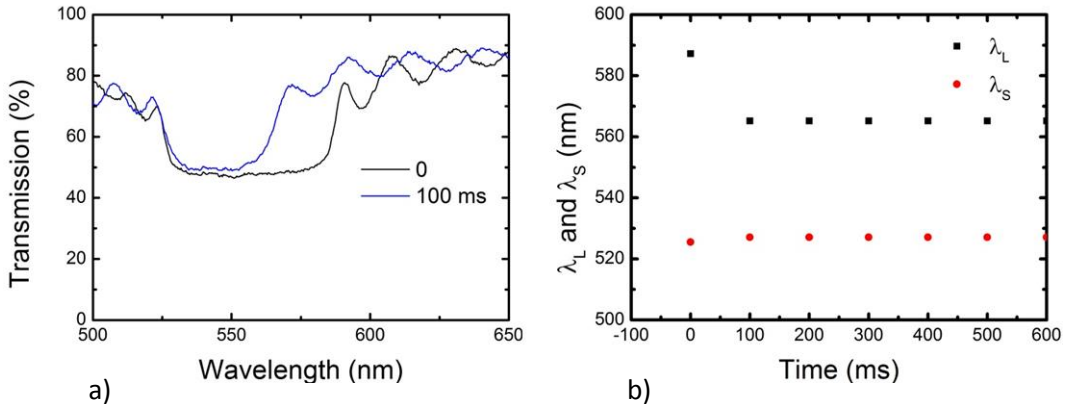

Figure 7 – The time required for wavelength tuning of the band-gap of a polymer-stabilised chiral nematic LC consisting of 30 wt% reactive mesogen. In this case, an electric field of 40 V/µm was applied to the sample and

was maintained during measurements: a) the blue-shift of the transmission spectrum after the electric field had been applied for 100 ms; b) The wavelengths of the long and short band-edges as a function of time following the application of the electric field.

When the electric field was applied to the sample, the blue shift of the long-wavelength band-edge resulted in an increase in the transmission intensity at the photodiode because the overlap between the emission spectrum of the LED and the band-gap of the chiral nematic LC was reduced. The voltage recorded on the photodiode was plotted as a function of time as the electric field was modulated between 40 V/μm and no electric field. This meant that I could measure both the ON to OFF response time (the relaxation time) as shown in Fig 8a and the OFF to ON response time (the driven response time) as shown in Fig 8b. Generally, the relaxation time (ON-OFF) is a more useful metric as it is independent of the applied E-field; however, real devices will often be driven so both are relevant measurements.

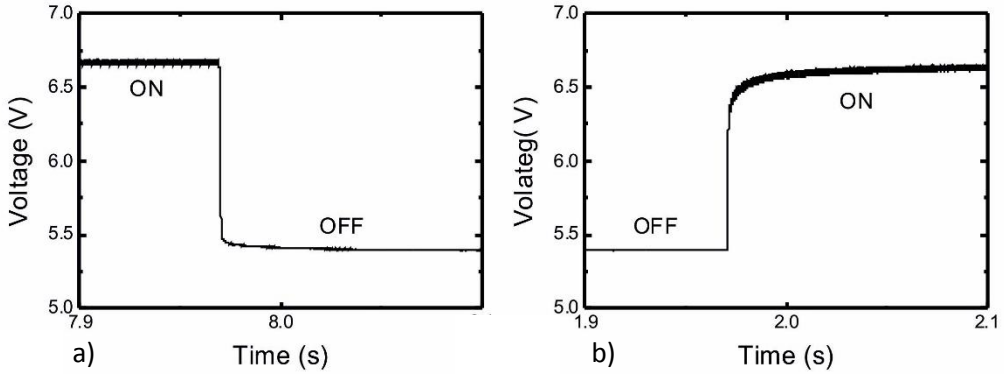

Figure 8 – The change in transmitted intensity recorded on the photodiode following the removal I and the application (b) of the applied electric field.

Here, the response times were calculated as the time taken for the voltage to change from 90% of the difference between the starting voltage and the end voltage to 10% of it (relaxation time), and vice versa for the driven response time. From Figure 8a, I find that the relaxation time was $\tau_{ON\text{-}OFF}$ ~1 ms whereas Figure 8b indicates that the driven response time, $\tau_{OFF\text{-}ON}$ ~ 8 ms. Although the OFF-ON response time is driven by the voltage, there will be some restoring force provided by the polymer network, potentially explaining why it is slower than the relaxation time.

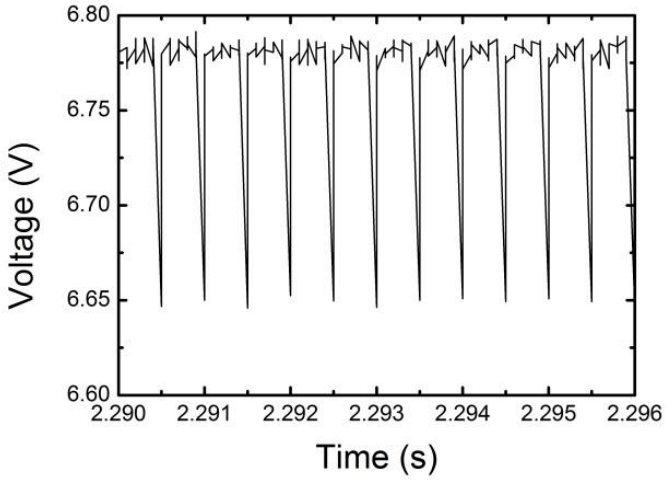

Figure 9 – The envelopes of extra features occurring at a frequency of 2 kHz. This is a zoomed in view of the top-right of Figure 8.

These graphs show envelopes of an extra feature occurring at a 2-kHz frequency when the field in 'ON'– a zoomed-in version of the top right of Figure 8b is shown in Fig 9. This occurs at twice the driving frequency of 1 kHz. This has been tentatively identified as the LC flexoelectrically coupling to the field – with the peaks occurring on both the rising and falling edges of the square wave used here. Flexoelectricity is the generation of a spontaneous polarisation in a liquid crystal due to a deformation of the director by an applied electric field [16]. I do not believe that this is an experimental artefact - several experiments were performed to ensure that this was a feature of the material – and that it is not related to charging and discharging of the parallel plate capacitance of the cell or our setup.

4.2.3 – Wavelength tuning of the band-gap of an achiral nematic LC in a chiral polymer scaffold

Having characterised the polymer-stabilised chiral nematic samples, the next step was to prepare templated samples and to thoroughly characterise them. To this end, polymer-stabilised samples were created using the same materials and preparation technique as described above. However, the LC was then washed out by immersing the 30 wt% reactive mesogen devices in a beaker of acetone for 48 hours. These were then left to dry at room temperature for four hours. Optical polarising microscopy was used to ensure that the washing out had thoroughly removed the LC. The resulting polymer scaffolds were then refilled with an achiral nematic LC using capillary action. This refilling took significantly longer than the initial filling process – the cells were left at 110°C for 24 hours (compared to < 1 minute before) to ensure thorough filling of the LC into the porous polymer network.

Once again, the response of the photonic band gap to an applied electric field was studied. It should be noted that, due to the refilling procedure, the photonic band-gaps do not occur at exactly the same wavelengths for the two different samples. This is likely due to the different birefringence of the infilled nematic and the original smectic A LC/reactive mesogen mixture. Fig 10 shows the change in the transmission spectrum of the templated samples as an external electric field was applied. A gap of 30 seconds was left between applying the field and taking the measurements to ensure that the band-gap had finished shifting. In a similar manner to that observed for the polymer-stabilised samples, the band gap was retained even at high electric field amplitudes and did not degrade or collapse – it only wavelength-shifted. However, for the polymer-templated samples, both the long and short wavelength band-edges (λ_L and λ_S) blue-shift as the electric field amplitude increases. For example, the long wavelength band-edge is seen to shift by $\Delta\lambda_L \approx 55$ nm and the short band-edge by $\Delta\lambda_S \approx 32$nm.

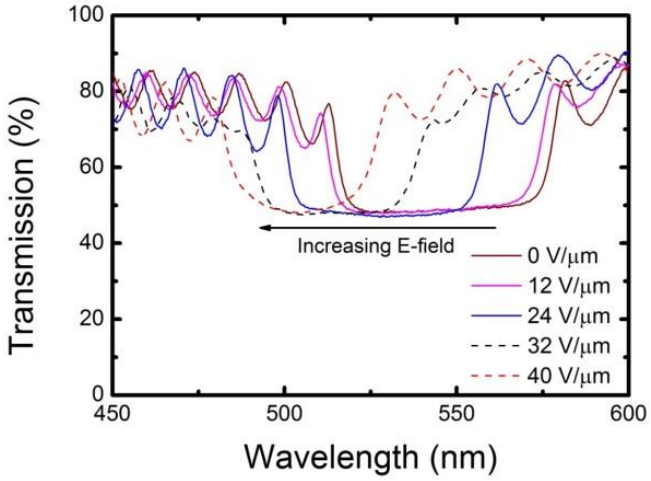

Figure 10 – The transmission spectrum of a polymer-templated chiral nematic liquid crystal as a function of the amplitude of the applied electric field. Measurements taken at 20°C.

Accompanying the shift in the band-gap, there is also a change in the optical texture that is observed when viewed on an optical polarising microscope; in this case the image darkens as the band-gap blue-shifts. In addition to the conventional Grandjean texture, a configuration of bright stripes appear as the electric field amplitude is increased; this is discussed in more detail in Section 4.2.4.

It was found that there was only a small degree of hysteresis between the band-gap positions measured on increasing and decreasing the magnitude of the E-field, which is shown in Fig 11. This demonstrates that the mechanism responsible for the longest shift in the wavelength is largely reversible. By applying a precise electric field strength, it is

therefore possible to obtain a defined wavelength for the band-edge. Furthermore, the band-gap is found to recover to almost the same initial spectral position when the electric-field is removed.

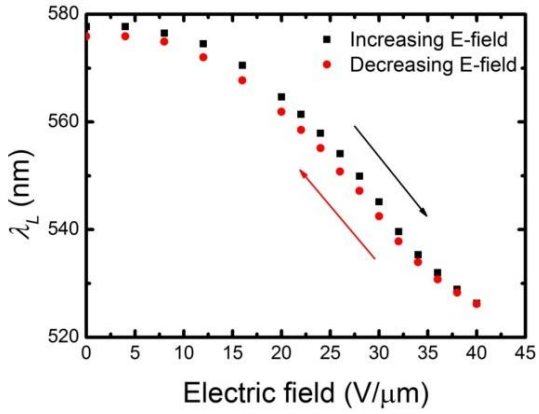

Figure 11 – A plot of the long-wavelength band-edge position upon increasing and decreasing the applied electric field.

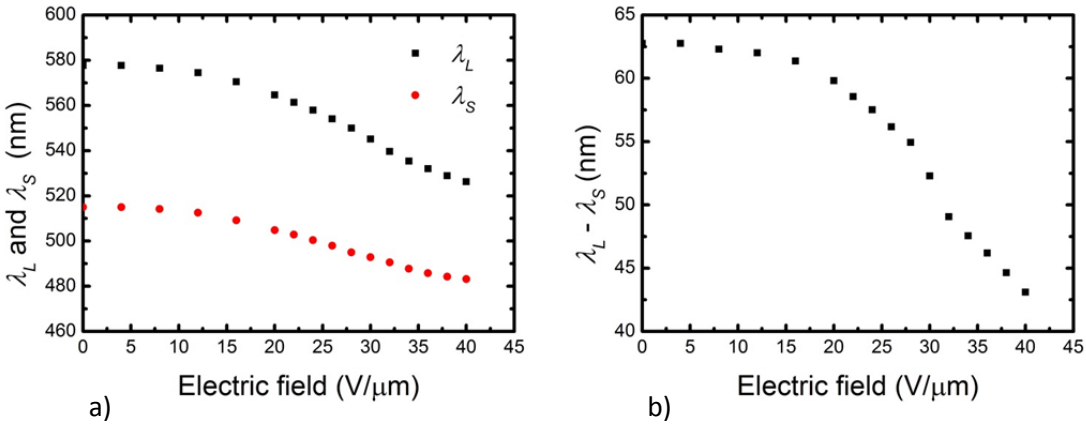

Figure 12 – a) Plots of both the long and short-wavelength band-edges as a function of an increasing applied electric field amplitude; b) The width of the band-gap as a function of the applied electric field. Measurements taken at 20°C.

Fig 12a shows the change in each band-edge with increasing electric field amplitude. In this case, the long band-edge evidently shifts by a greater amount than the short-band edge ($\Delta\lambda_L$ = 55 nm compared with $\Delta\lambda$s = 32 nm), as shown in Fig 12b.

As with the polymer-stabilised samples, I investigated the temporal evolution of the photonic band-gap after an electric field was applied. Fig 13a shows the temporal evolution of the transmission spectrum for a time period of 5 seconds after an E-field of 40 V/μm was applied to the sample. Within the first 100 ms, the templated sample exhibits a blue-shift of only the long wavelength band-edge as I saw for the polymer-stabilised case. However, this is followed by a subsequent blue shift of the entire band-gap that wasn't observed previously. The wavelengths corresponding to the two band-

edges are plotted as a function of the time after the external electric field has been applied in Fig 13b. Initially, the short wavelength band-edge is unchanged during the

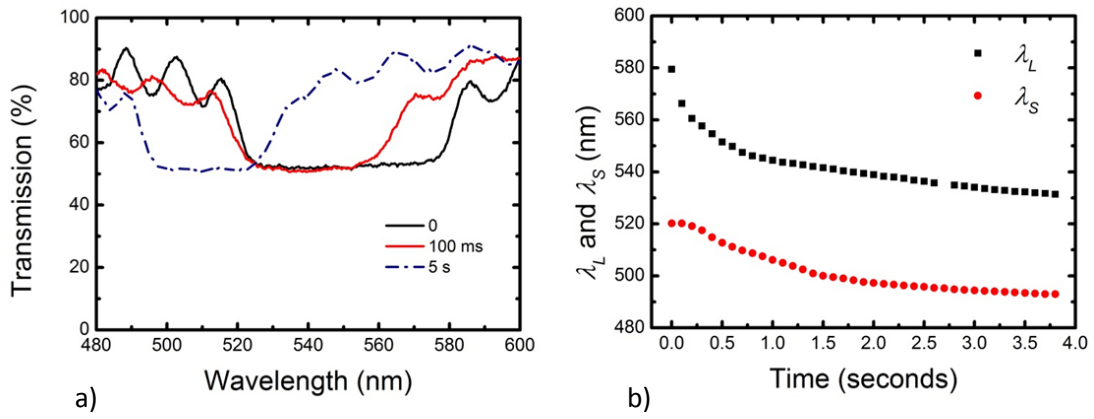

Figure 13 – The time required for wavelength tuning of the band-gap of an achiral nematic LC filled into a chiral polymer scaffold. In this case, an electric field of 40 V/µm was applied to the sample and was maintained during measurements. A) the blue-shift of the transmission spectrum after the electric field had been applied for 5 seconds; b) The wavelengths of the long and short band-edges as a function of time following the application of the electric field.

initial 200 ms. This is commensurate with the change seen for the polymerised case. However, the fast, long band-edge shift is then augmented by the slower shift of both band-edges that takes place over several seconds.

To measure the response time, a slightly different LED (565 nm peak emission) was used due to the different spectral location of the photonic band-gap; however, the measurement principle was identical to that used for the polymer-stabilised sample. Figs 14a and 14b show the relaxation (electric-field ON-OFF) and driven response time (electric-field) OFF-ON for the sample, measured as described above. In this case, when the external E-field is removed, the voltage on the photodiode dips below its final value before increasing. This is likely due to the interference fringes either side of the photonic band-gap (i.e., there are peaks and troughs in the transmission that can be seen in Fig 14a). The position of these fringes changes as a voltage is applied. The varying transmission of the fringes will change the overall transmission of the device, and could lead to an overall reduction in the device transition, leading to the voltage dropping below the final value.

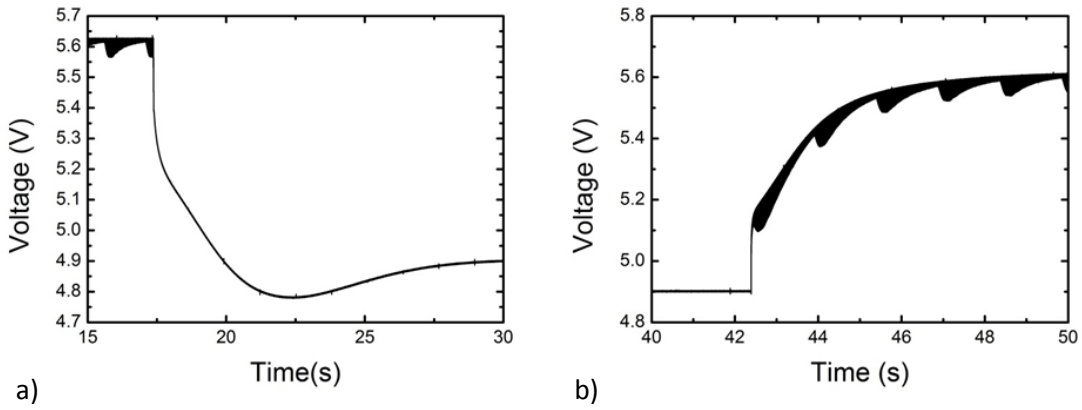

Figure 14 – The change in transmitted intensity recorded on the photodiode following a) the removal and b) the application of an applied electric field. Measurements taken at 20°C.

From Figs 13a and 13b the 10-90% response time (calculated as described above) is ~6.5 s for the ON-OFF and ~2.8 s for OFF-ON, in both cases much slower than in the polymer-stabilised case. It is likely that in the templated samples, the polymer network is weakened and so it will provide less restoring force. Again, there is extra structure with a 2-kHz frequency when the field is applied.

4.2.4 – Comparison of the electro-optic properties of a polymer-stabilised and a polymer-templated chiral nematic liquid crystal

From these results, it can be seen that the polymer-stabilised and templated samples exhibit different electro-optic band-gap characteristics. For the polymer-stabilised sample, the long wavelength band edge appears to blue shift by $\Delta\lambda_L \approx 22$ nm in a timescale on the order of ms, and this is the only change that is observed for the electric field amplitudes that are considered in this study. Interestingly, a similar blue-shift (on a comparable timescale) is also seen in the case of the templated samples, however there is then a subsequent, further blue-shift of the entire band-gap over a much longer timescale (on the order of seconds). It therefore appears as though both the polymer-stabilised and the templated samples behave in an identical manner initially, but that the templated sample exhibits a secondary, slower process involving an entire shift of the band-gap.

In the first (fast) process only the long-wavelength band-edge blue-shifts (by $\Delta\lambda_L \approx 22$ nm). This blue-shift occurs in a time of $\tau \approx 8$ ms and, for the polymer-stabilised sample, no further movement of the bandgap is observed. During this process, there is no apparent change in the Grandjean texture when viewed using an optical polarising microscopy apart from a slight change in the colour. I believe that, in this case, the blue-shift in the long-wavelength band-edge is due to a reduction in n_e while n_o and p remain fixed, in accordance with Equations 4.1 and 4.2. Such a change in the long wavelength

band-edge has been observed previously [19-20] where it was attributed to a change in the magnitude of n_e as the molecules within the network are aligned to the direction of the applied electric field. The wavelength tuning observed here corresponds to a small change in n_e of $\Delta n \sim 0.06$.

The second mechanism that is observed only in the templated sample results in an additional, slow ($\tau_{ON\text{-}OFF} \approx 6.5$ s) blue-shift of the long-wavelength band-edge (an extra $\Delta\lambda_L \approx 32$ nm); this is accompanied by a blue-shift of the short-wavelength band-edge as seen in the polymer-stabilised samples.

The timescale over which the second mechanism operates suggests that a flow-related phenomenon may be involved. This is perhaps somewhat surprising given that one might expect the pitch to be 'locked-in' by the polymer network. However, recent work [7, 26-30] has shown that it is possible for the polymer fibrils that make up the network to undergo a translational motion when subjected to dc electric fields, leading to a contraction of the pitch at one substrate and an extension at the other when the polymer network is tethered to both substrates.

Potential evidence for a translation of the polymer fibrils in our polymer-templated structures can be seen in the microscope images presented in Fig 15 in which I see an additional structure appearing as the amplitude of the electric-field increases. As the field is applied, bright streaks appear that are much lighter in colour. In accordance with previous studies, this could be the polymer fibrils coming into focus as they translate through the cell. Furthermore, the slow response time would be consistent with a translation of the network. Another possible explanation could be that it is the oily streaks coming into and out of focus. However, in that case, I would expect to see it in the polymer-stabilised case too and I don't here, as was shown in Fig 5.

In previous work, the change in the pitch (leading to a broadening of the band-gap) has been explained both experimentally [27-30] and theoretically [7] as an ion-facilitated translation of the polymer fibrils in the presence of an external electric field, which in turn results in a compression/extension of the helical structure. In my work, however, an ac electric field is used, indicating the possibility of a dielectrically driven process. This is possible if: (a) the polymer network is not strongly attached to at least one of the device surfaces, and; (b) diffusion and/or flow of the nematic liquid crystal material through the polymer network is possible. I know that the latter is possible because the LC material has been re-filled into the network template through a flow/diffusion

process. Additionally, if the process of washing out and re-filling with a nematic material has to some degree ‘damaged’ the polymer network then it is also reasonable that it may no longer be strongly attached to the surfaces. Evidence for a weakening of the network has already been seen from the slight degradation in the quality of the photonic band-gap upon refilling with a nematic LC, and in the samples using a low concentration (<30 wt%) of polymer which could not be used as templates (and in the optical polarising microscopy images of the polymer-templated smectic A materials described in Chapter 3). It is therefore entirely possible that some of the fibrils that make up the network have been broken in some places.

It can be seen from Fig 10 that the electric field induced tilt in the LC molecular axis within the polymer network does not reach the homeotropic state, but remains partially tilted within the network structure. (This is evident because the longer band edge blue-shifts, but does not reach the shorter band edge.) At higher electric fields, it appears that rather than inducing further tilt of the nematic LC within the polymer network, the LC material rather flows/diffuses through the network to form a homeotropic region near one or both surfaces, and the polymer network region is reduced in thickness, with a consequent reduction in the helix pitch. This is something that can occur for materials with a positive dielectric anisotropy if the dielectric energy change associated with the formation of the homeotropic region is greater than the elastic energy cost of reducing the thickness of the polymer network region. To reduce the thickness of this region, LC molecules must flow/diffuse into the homeotropic region(s) to conserve volume. As a diffusion/flow process this is slow and so fits with our measured response times.

In this section, I have described work to polymer-template the chiral nematic phase and compare its electro-optic properties compared to a polymer-stabilised LC phase and explained the differences. The next section will utilise the greater (by ~2.5 times) tuning range of a polymer-templated chiral nematic LC to create electrically wavelength-tuneable LC lasers.

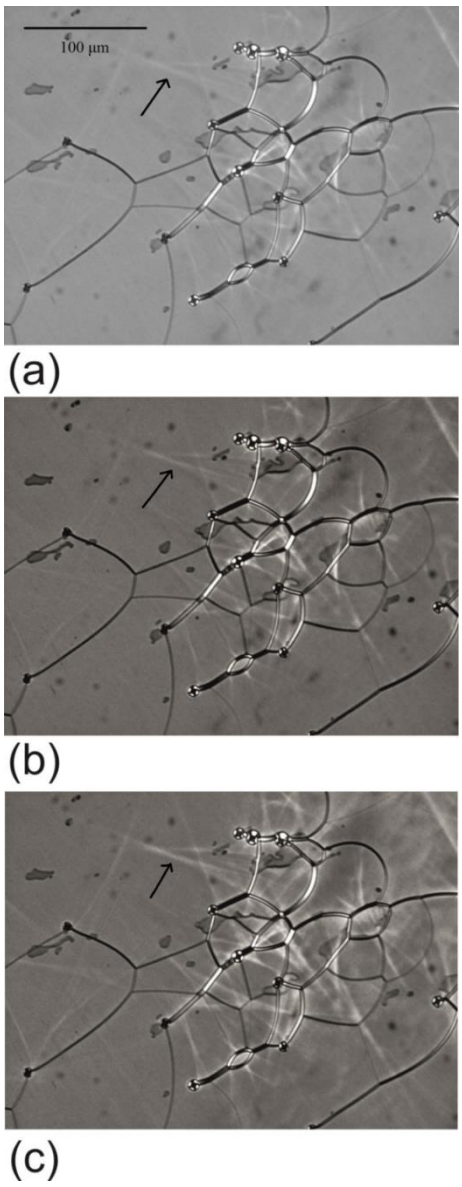

Figure 14 – Optical polarising microscopy images of an achiral nematic LC filled into a chiral polymer scaffold following the application of an ac electric field (E= 40 V/µm, f = 1 kHz). A) 100 ms and b)200 ms and c)300 ms after a 40 V/µm 1 kHz ac electric-field is applied to the cell. The images have been grey-scale mapped to improve the contrast. Measurements taken at 20°C.

4.3 – Polymer-templated liquid crystal lasers

The above work discussed methods for tuning the photonic band-gap of a chiral nematic LC using electric fields. This is particularly interesting due to the variety of applications of the photonic band-gap. Thus, the remainder of this Chapter will discuss applying the above work to one of these applications – specifically, the creation of LC lasers.

4.3.1 – Electric-field tuning of liquid crystal lasers

In general, electric field tuning of LC lasers is difficult as the photonic band-gap often collapses before significant tuning is achieved. For example, previously work has been performed to electrically tune a LC laser by using interdigitated electrodes, although in this case the inhomogeneous band-gap has led to the cessation of laser emission at large

electric field amplitudes with minimal tuning [31]. To circumvent this issue, polymer-stabilisation has been used. For example, Inoue, et al [25] demonstrated a small degree of wavelength tuning (~ 6 nm) of a band-edge laser at high electric fields (E~100s V/μm) by incorporating a dye into a polymer-stabilised network, and using the local reorientation of the LC molecules in the polymer network's nanopores to alter the refractive index. However, one difficulty of creating polymer-stabilised LC lasers is that there is a laser dye present during the photo-curing procedure. This dye can interfere with the photo-curing procedure by absorbing the UV radiation and/or being damaged by it.

In this section, I present results to demonstrate the advantage of the increased wavelength-shift of the long wavelength band-edge in a polymer-templated chiral nematic LC described above to create widely electrically tuneable LC lasers. The emission characteristics of a thin-film LC laser created using a polymer-stabilised, dye-doped chiral nematic LC is compared to that of a polymer-templated LC laser fabricated using an achiral, dye-doped nematic refilled into a chiral polymer scaffold. Both lasers exhibit wavelength tuning upon the application of an external electric field. However, as expected, for the templated sample, tuning of the laser wavelength is found to occur across a broader wavelength-range for the same electric field amplitude (by ~2.5 times, as would be expected from the increase in photonic band-gap tuning range seen in the preceding section). This allows the dye to be added after photo-curing has occurred; thus, the templating technique circumvents problems caused by the dye's presence during the photopolymerisation process.

4.3.2 – Electric field tuning of a polymer-stabilised liquid crystal laser

In this section, I describe work to dope a fluorescent dye into the chiral nematic materials used previously in this Chapter. I show that the addition of a dye does not affect the electro-optic properties of the photonic band-gap. Subsequently, I optically pump the devices and study the laser emission properties.

Polymer-stabilised LC lasers were created by using the MDA-02-2149 (nematic LC), R5011 (chiral dopant), UCL-011-K1 (reactive mesogen, photoinitiator, thermal inhibitor) mixture described above and mixing it with the laser dye pyromethene 597 (PM597, Exciton) at 110°C for 14 hours. The composition of the mixture was 67.9 wt% MDA-02-2149, 29.1 wt% UCL-011-K1, 2.4 wt% R5011 and 0.6 wt% PM597. PM597 was chosen as the dye because it has been shown to possess a high quantum efficiency (and therefore low excitation energy threshold) in chiral nematic LCs [32]. Furthermore,

the absorption band of the dye occurs at longer wavelengths than the UV wavelengths used (365 nm) during the photopolymerisation procedure.

This mixture was filled into a 9 µm-thick planar aligned cells (Instec), annealed and then photocured for 120 s from each side of the cell. The cell used here was thicker than that used to investigate chiral nematics without dyes earlier in this Chapter because the density of states (important for laser emission) is highly dependent upon the number of pitch twists [33]. Thus, the excitation threshold value depends on the cell thickness and the optimum is ~10 µm. This means that when I applied electric fields, the maximum voltage applied (400 Vp-p) becomes a 22.2 V/µm electric field (rather than the 40 V/µm for 5 µm-thick cells).

Fig 16 shows an optical polarising microscope image of the polymer-stabilised dye-doped chiral nematic LC sample after photo-polymerisation. Subsequent electro-optic studies revealed that when an electric field was applied to the cell parallel to the axis of the helix, the photonic band-gap was retained even at the highest electric field strength achievable with our experimental setup (22.2 V/µm), as I would expect from previous work on samples without any dye present.

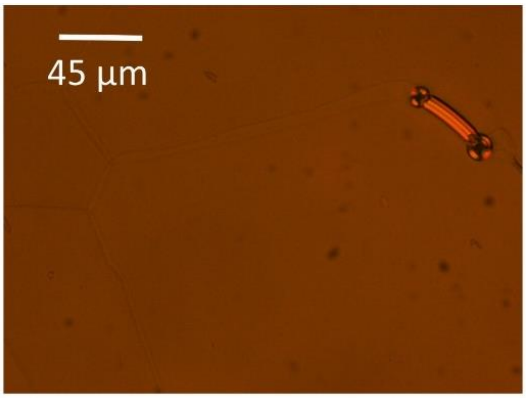

Figure 16 – An optical polarising microscope image of the Grandjean alignment of a dye-doped chiral nematic liquid crystal after photo-curing. Two spacer beads (9 µm diameter) can be seen in the top right of the image. Measurements taken at 20°C.

The transmission spectrum was then monitored as an electric field was applied. The photonic band-gap is less well defined (the edges are less sharp) than in the absence of the dye, likely due to the dye interfering with the photo-polymerisation procedure. Fig 17a shows the change in the photonic band-gap as the applied electric field is increased up to the maximum of E = 22.2 V/µm. There is a blue-shift of the long-wavelength band-edge on increasing the electric field amplitude. The change in the long band-edge as the electric field amplitude is increased is plotted in Fig 17b. Here, the results show

that there is almost no movement of the band-edge up until an electric-field of E = 12 V/µm when a blue shift in the wavelength is then observed. Above that field amplitude, the wavelength of the long band-edge appears to shift continuously with a further increase in the electric field resulting in a total blue-shift of ≈ 4.5 nm for the maximum electric field amplitude used in this study (22 V/µm). This result is commensurate with the work on polymer-stabilised chiral nematics described in Section 4.2, although in this case, the short band-edge is masked by the absorption of the laser dye (the peak absorption occurs at 530 nm), so it is impossible to confirm that the short band-edge doesn't wavelength shift. Thus, although the band-gap is slightly less well-defined, the addition of the dye does not significantly impact the electro-optic properties of the photonic band-gap.

The next step was to study this dye-doped polymer-stabilised device as it was optically pumped with the second harmonic of a frequency-doubled Nd:YAG laser (CryLas 6FTSS355-Q4-S) emitting 1 ns pulses at 532 nm with a variable repetition rate (from 1 Hz to 1 kHz). The pump laser was focused onto the devices to a spot size of ~200 µm diameter and the output was measured perpendicular to the devices; a 550 nm long pass filter was used to block the pump beam from being detected by the spectrometer.

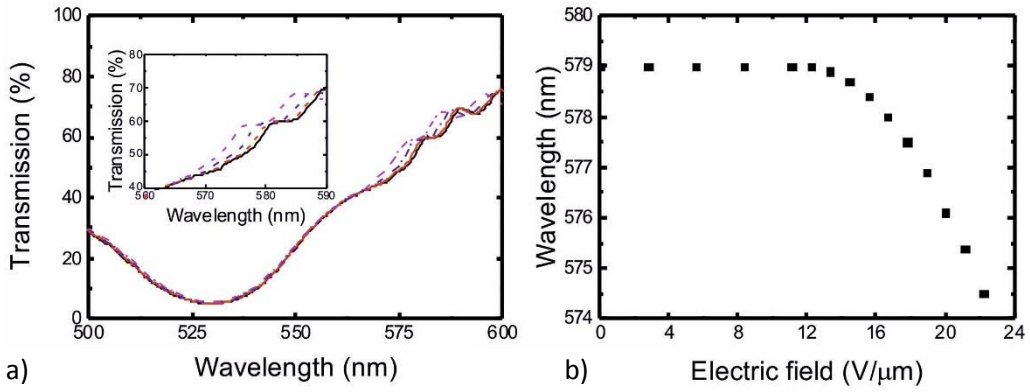

Figure 17 – a) The change in the transmission spectra as an ac electric field is applied to a polymer-stabilised, dye-doped chiral nematic liquid crystal (0, 15.6, 20, 22.2 V/µm from right to left); b) The wavelength of the centre of the long band-edge as a function of the applied electric field amplitude. Measurements taken at 20°C.

Emission was collected using a microscope objective (5X, 0.25 NA) and coupled into a 600 µm-diameter fibre (Ocean Optics QP600-1-UV-VIS) attached to a spectrometer (Ocean Optics USB2000+ UV-VIS). The pump energy was measured using a pyroelectric sensor (OPHIR, PE9-ES-C, spectral range 0.12-12 µm, sensitivity 0.1 µJ). A combination of a quarter wave plate (zero-order, 530 nm) and Glan-Thompson polariser was used to probe the handedness of the circular polarisation of the laser

emission. The intensity of the emitted pump laser light was controlled using a combination of a half wave-plate and a Glan-Thompson polariser.

Laser emission was observed along the normal of the cell substrates at a wavelength corresponding to the long wavelength band-edge of the chiral nematic photonic band-gap. The emission spectrum was found to be slightly broader than the resolution limit of the spectrometer (1.7 nm). This is likely due to inhomogeneities in the polymeric structure caused by the presence of the dye during photo-curing, resulting in a multimode laser output.

Fig 18a shows examples of the emission spectra for different electric field amplitudes. These indicate that the peak laser wavelength is blue-shifted as the magnitude of the electric field increases. This is in accordance with the blue-shift of the band-gap observed in the transmission spectrum (c.f. Fig 17a). The wavelength tuning-range of the peak laser wavelength was ≈4.5 nm, as shown clearly in Fig 18b.

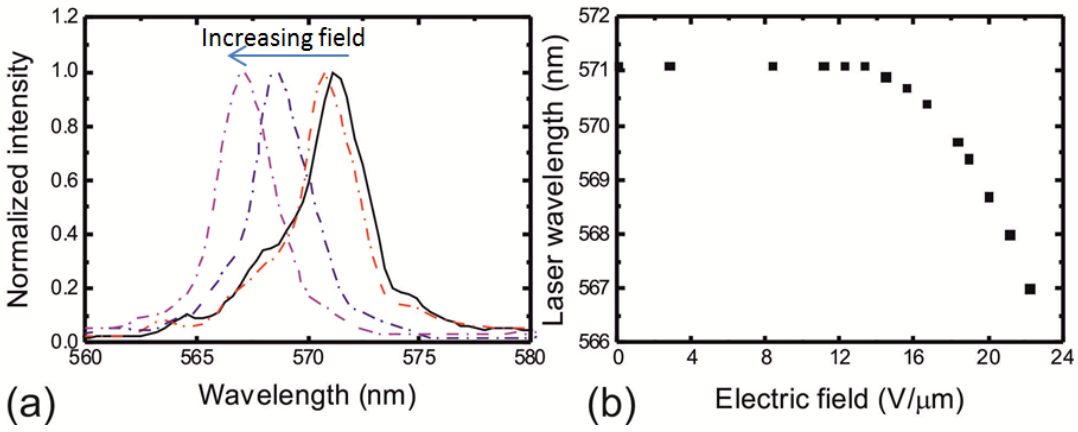

Figure 18 – Wavelength tuning of the emission from a dye-doped polymer-stabilised chiral nematic liquid crystal: a) emission spectra for four different electric field amplitudes (0, 15.6, 20, 22.2 V/μm from right to left); b) Peak wavelength as a function of the applied electric field amplitude. Measurements taken at 20°C

A plot of the input-output characteristics of the laser sample showing the peak output intensity as a function of the excitation energy per pulse is presented in Fig 19; from the discontinuity in the differential I estimate the threshold of the laser to be $E_{th} \approx 0.75 \pm 0.05$ $\mu J/cm^2$.

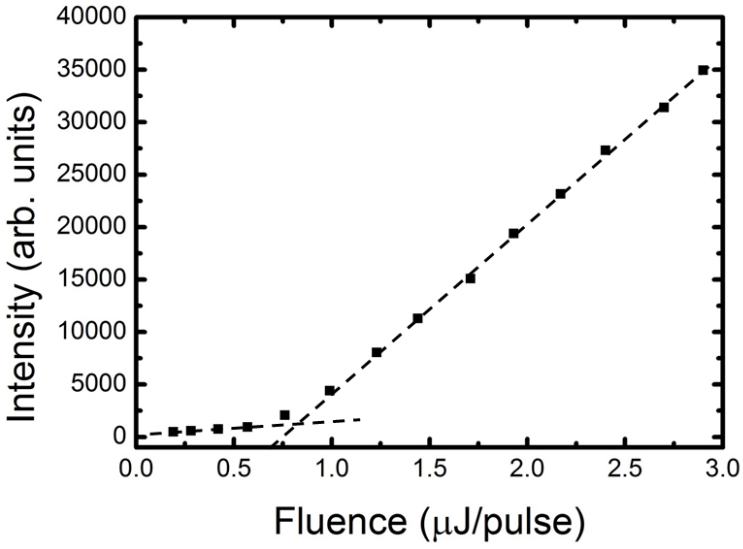

Figure 19 – Peak laser intensity as a function of the excitation energy per pulse.

4.3.3 – Electric field tuning of a polymer templated liquid crystal laser

To make the polymer-templated LC lasers, a mixture of 69.7 wt% MDA-02-2149, 27.5 wt% UCL-011-K1 and 2.8 wt% R5011 was created and was used to create polymer-stabilised chiral nematic LCs in 9 μm-thick Instec cells using the procedure described in Section 4.2.

To remove the unreacted reactive mesogens and the LC, the cells were placed in a beaker of acetone for 48 hours and then left to dry at room temperature for 4 hours. Optical polarising microscope images and spectral analysis were used to confirm that the LC had been fully washed out. Following this, a dye-doped achiral mixture (99.1 wt% MDA-02-2149 and 0.9 wt% PM597) was capillary-filled into the cells at 105ºC, a process that took around 24 hours (i.e. much slower than capillary filling into empty cells). This is the same weight of dye as a percentage of the LC material as that used to create the polymer-stabilised LC laser samples.

The same experiments that had been performed on the polymer-stabilised samples were then performed using the polymer template that had been refilled with a dye-doped nematic LC. Firstly, the alignment was checked. Fig 20 shows an optical polarising microscope image of the alignment of the chiral nematic LC. Although slightly more domains are apparent (separated by oily streaks) the domains are of the same colour, indicating that the pitch is the same. The texture does not change upon rotating the sample between crossed-polarisers indicating a Grandjean alignment. Therefore, even though there are more defects present than before the removal of the unreacted chiral nematic LC, it still exhibits good alignment after being refilled and the photonic band-

gap was found to reappear when the transmission spectrum was measured. The poorer alignment is likely due to the refilling procedure slightly damaging the polymer network, as previously discussed.

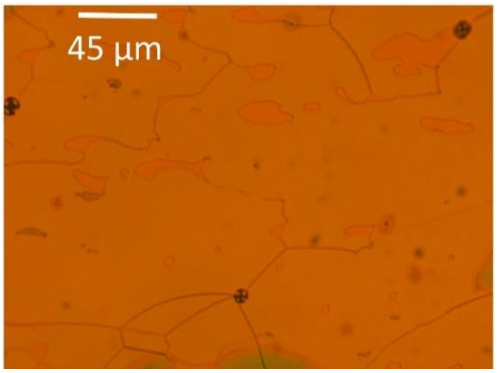

Figure 20 – An optical polarising microscope image of the optical texture after refilling the polymer template with a dye-doped nematic LC showing the reappearance of the Grandjean texture. The black dots are spacer beads (9 µm diameter). Measurements taken at 20°C.

The electro-optic properties were studied by monitoring the change in transmission as an electric field was applied was measured. The photonic band-gap was retained even up to a field of E = 22.2 V/µm – as shown in Fig 21a. However, for this sample, the long band-edge was found to shift by 11 nm (Fig 21b) for the same electric field amplitude, which is ~2.5 times greater than that observed for the polymer-stabilized sample. These values are commensurate with those described above for polymer-stabilised samples without any dye present (Section 4.2). The total shift is lower because the cells used in this work are thicker and so only lower total electric fields can be accessed.

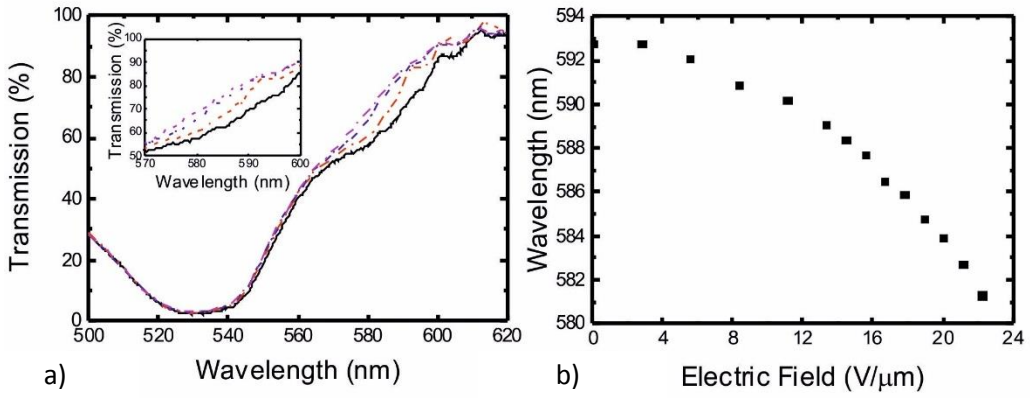

Figure 21 – a) The change in the long band-edge of the band-gap on increasing the applied electric field amplitude (0, 15.6, 20, 22.2 V/µm from right to left) and b) The wavelength of the long band-edges a function of the applied electric field amplitude. Measurements taken at 20°C.

The devices were then optically pumped and they exhibited laser emission. As an electric-field was applied, the laser emission wavelength-shifted. Again, a larger

wavelength-shift (~12 nm) was seen than in the polymer stabilised laser (by ~2.5 times). The laser emission spectrum for four different electric field strengths is shown in Fig 22a. The laser spectra have narrower linewidths than the polymer-stabilised lasers, indicating a more uniform periodic structure. This is believed to be a result of the dye not being present during the photo-

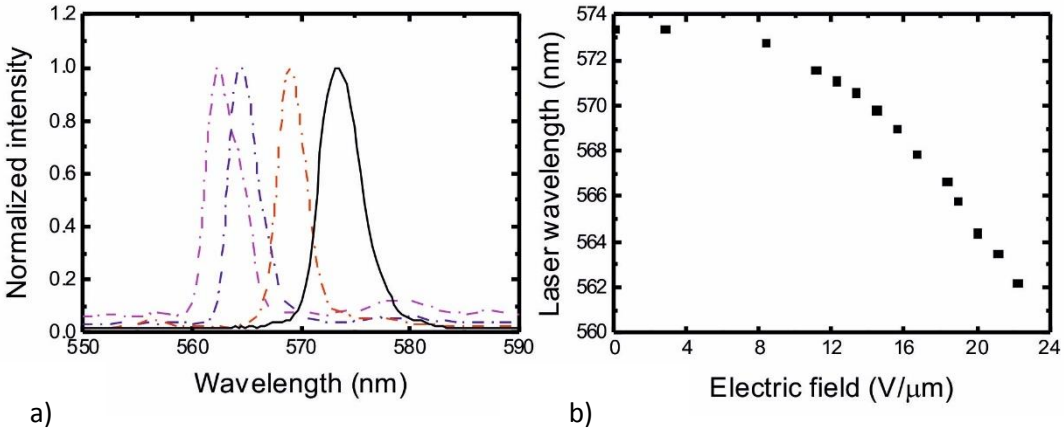

Figure 22 – Laser emission from a dye-doped nematic liquid crystal in a chiral polymer scaffold: a) the laser emission spectrum for four different applied electric field amplitudes (0, 15.6, 20, 22.2 V/μm from right to left); b) peak laser wavelength as a function of the applied electric field. Measurements taken at 20°C.

curing process (something which may adversely interfere with the morphology and formation of the polymer network). The change in peak laser wavelength as the amplitude of the electric field increases is further illustrated in Fig 22b. Again, a blue-shift of $\Delta\lambda_L \approx 11$ nm is observed, as would be expected from the shift of the long band-edge wavelength of the photonic band-gap.

The excitation threshold, extracted from the input-output plot shown in Fig 23, is found to be somewhat lower than for the polymer-stabilised laser sample presented in Fig 20 ($E_{th} \approx 0.5\pm0.05$ μJ/cm^2 for the polymer-templated laser compared to $E_{th} \approx 0.75\pm0.05$ μJ/cm^2 for the polymer-stabilised sample). This is likely because the dye is present during the photopolymerisation procedure. It could be due to either a reduction of the quantum efficiency of the dye in the presence of the unreacted free-radicals during photo-curing or due to increased losses caused by the inhomogeneous polymer morphology.

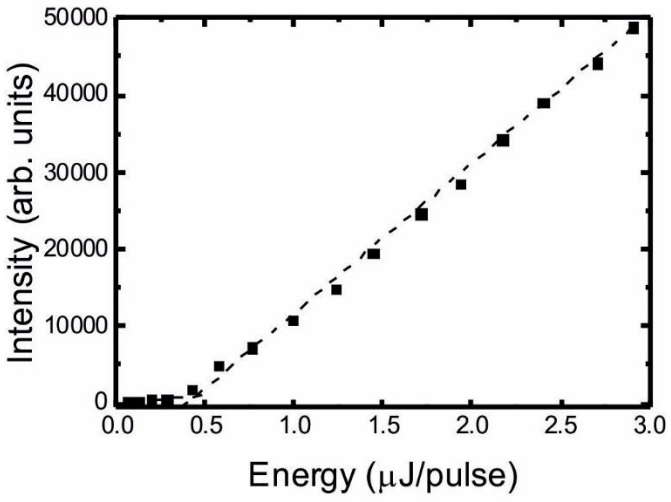

Figure 23 – Laser peak intensity as a function of the excitation energy per pulse.

4.4 – Conclusion

In this Chapter, I have studied the wavelength tuning characteristics of the photonic band-gap of an achiral nematic LC dispersed into a chiral polymer scaffold and compared it to that of a conventional, polymer-stabilised chiral nematic LC. By applying electric fields to a polymer-templated sample I have seen the photonic band-gap shift by 55 nm when a 40 V/μm field was applied. This tuning range is significantly greater (by 2.5 times) than that of conventional polymer-stabilised chiral nematic LCs. The shift appears to be comprised of an initial, fast (~1 ms) shift of 22 nm of only the long band-edge, followed by a slower shift of 32 nm of the entire band-gap. I have sought to explain the origins of these two effects – in terms of both changes in the refractive indices of the host LC as well as a translation of the polymer fibrils. Subsequently, I applied this larger wavelength-tuning range to create tuneable LC lasers by refilling the polymer scaffold with a dye-doped achiral nematic LC. When optically pumped, these devices were found to generate laser emission and, moreover, exhibited a broader electric tuning range than comparable polymer-stabilised LC lasers. They also have an additional advantage insofar as the dye is added after the photopolymerisation process and so any detrimental effects caused by the dye absorbing can be avoided.

In this Chapter, electric-field tuning of a LC laser has been demonstrated. In Chapter 5, mechanical tuning of a LC laser will be considered. Although using higher wt% of reactive mesogen supresses electric tuning, it allows freestanding laser films to be created. These films may then be elongated, and as they are stretched, the emission wavelength is blue-shifted – and not only that, but shifted reversibly, selectively, and without hysteresis.

4.5 – References

1. H. Coles and S. Morris, *Nat Photon*., 2010, **4**, 10.
2. K.-H. Kim, J.-K. Song, *NPG Asia Mater*., 2009, **1** , 1.
3. S. J. Woltman, G. D. Jay, and G. P. Crawford, *Nat*. *Mater*., 2007, **6**, 929.
4. H. Finkelmann, S. T. Kim, A. Muñoz, P. Palffy-Muhoray, and B. Taheri, *Adv*. *Mater*., 2001, **13**, 1069.
5. S. Kurihara, Y. Hatae, T. Yoshioka, M. Moritsugu, T. Ogata, and T. Nonaka, *Appl*. *Phys*. *Lett*., 2006, **88**, 103121.
6. I. Lelidis, G. Barbero, and A. M. Scarfone, *Cent*. *Eur*. *J*. *Phys*., 2012, **10**, 587.
7. H. Nemati, S. Liu, R. S. Zola, V. P. Tondiglia, K. M. Lee, T. White, T. Bunning, and D.-K. Yang, *Soft Matter*, 2015, **11**, 1208.
8. J. Schmidtke, G. Jünnemann, S. Keuker-Baumann, and H.-S. Kitzerow, *Appl*. *Phys*. *Lett*., 2012, **101**, 5.
9. J. S. Patel and R. B. Meyer, *Phys*. *Rev*. *Lett*., 1987, **58**, 1538.
10. K. Funamoto, M. Ozaki, and K. Yoshino, *Jpn*. *J*. *Appl*. *Phys*., 2003, **42**, 1523.
11. S. Furumi, S. Yokoyama, A. Otomo, and S. Mashiko, *Thin Solid Films*, 2006, **499**, 322.
12. V. T. Tondiglia, L. V. Natarajan, C. A. Bailey, M. M. Duning, R. L. Sutherland, D. Ke-Yang, A. Voevodin, T. J. White, and T. J. Bunning, *J*. *Appl*. *Phys*., 2011, **110**, 053109.
13. H. Lu, J. Hu, Y. Chu, W. Xu, L. Qiu, X. Wang, G. Zhang, J. Hu, and J. Yang, *J*. *Mater*. *Chem*. *C*, 2015, **3**, 5406.
14. S. S. Choi, S. M. Morris, W. T. S. Huck, and H. J. Coles, *Adv*. *Mater*., 2009, **21**, 3915.
15. S. S. Choi, S. M. Morris, H. J. Coles, and W. T. S. Huck, *Appl*. *Phys*. *Lett*. 2007**, 91**, 231110.
16. Goodby, J. W., et al. Handbook of liquid Crystals volume 3, 2nd edition (2014), Wiley-VCH, Chapter 16.
17. F. C. Frank, *Discuss*. *Farad*., 1958, **25**, 19.
18. J. L. Fergason, *Mol*. *Cry*., 1966, **1**, 293.
19. G. Chilya, et al, *Cryst*. *Res*., 1997, **32**, 401.
20. M. de Zwart and T. W. Lathouwers, *Phys*. *Lett*., 1975, **55A**, 41.
21. J. Xiang, Y. Li, Q. Li, D. A. Paterson, J. M. D. Storey, C. T. Imrie, and O. D. Lavrentovich, *Adv*. *Mater*., 2015, **27**, 3014.
22. R. A. M. Hikmet and H. Kemperman, *Nature*, 1998, 392, 476.
23. H. Kim, Y. Inoue, J. Kobashi, Y. Maeda, H. Yoshida, and M. Ozaki, *Opt*. *Mater*. *Express*, 2016, **6**, 705.
24. M. Mohammadimasoudi, J. Beeckman, J. Shin, K. Lee, and K. Neyts, *Opt*. *Express*, 2014, **22**, 19098.
25. Y. Inoue, H. Yoshida, H. Kubo, and M. Ozaki, *Adv*. *Opt*. *Mater*., 2013, **1**, 256.
26. S. S. Choi, S. M. Morris, W. T. S. Huck, and H. J. Coles, *Adv*. *Mater*., 2010, **22**, 53.
27. J.-D. Lin, C.-L. Chu, H.-Y. Lin, B. You, C.-T. Horng, S.-Y. Huang, T.-S. Mo, C.-Y. Huang, and C.-R. Lee, *Opt*. *Mater*. *Express*, 2015, **5**, 1419.
28. V. P. Tondiglia, L. V. Natarajan, C. A. Bailey, M. E. McConney, K. M. Lee, T. J. Bunning, R. Zola, H. Nemati, D.-K. Yang, and T. J. White, *Opt*. *Mater*. *Express*, 2014, **4**, 1465.
29. K. M. Lee, V. P. Tondiglia, M. E. McConney, L. V. Natarajan, T. J. Bunning, and T. J. White, *ACS Photonics*, 2014, **1**, 1033.
30. K. M. Lee, V. P. Tondiglia, T. Lee, I. I. Smalyukh, and T. J. White, *J*. *Mater*. *Chem*. *C*, 2015, **3**, 8788.
31. J. Schmidtke, G. Jünnemann, S. Keuker-Baumann, and H.-S. Kitzerow, *Appl*. *Phys*. *Lett*., 2012, **101**, 5.
32. T. K. Mavrogordatos, S. M. Morris, F. Castles, P. J. W. Hands, A. D. Ford, H. J. Coles, and T. D. Wilkinson, *Phys*. *Rev*. *E*, 2012, **86**, 011705.

Chapter 5 – Stretchable free-standing liquid crystal gels for thin-film lasers

The previous Chapters have described research to polymer-template various liquid crystal (LC) phases. I have shown that by polymer-templating the chiral nematic LC phase it is possible to create liquid crystalline lasers which exhibit broader electric wavelength-tuning ranges than are possible with conventional polymer-stabilised chiral nematic LCs. In this Chapter, I investigate another LC laser emission wavelength tuning mechanism – mechanical tuning. By combining LCs with high wt% of reactive mesogens, a fluorescent dye and photo-curing, I create free-standing laser gel films. As these lasers are stretched their emission wavelength blue-shifts (as the film contracts and the chiral nematic pitch is reduced). The tuning of the wavelength of emission is reversible, selective and repeatable – the gels can be repeatedly stretched and contracted without hysteresis, and a given film elongation consistently corresponds to a particular laser emission wavelength. Furthermore, the methodology used to create these lasers is much more versatile than previous techniques used to create elastomeric LC lasers, both in that it uses commercially available materials and because it relies on conventional alignment techniques and a quick, simple photo-polymerisation procedure.

This Chapter begins with a discussion of the relevant background information – including previous work on LC elastomers and elastomeric LC lasers. This is followed by an outline of the procedure for fabricating the stretchable gels. Subsequently, I present results to show how the mechanochromic range and sensitivity of films containing different concentrations of the reactive species are affected when the films are subjected to a mechanical strain. Next, I dope the gels with fluorescent dyes to create lasers. The wavelength of this emission can be continuously, repeatably and selectively tuned (by ~40 nm) without hysteresis by mechanically extending the films along a direction perpendicular to the helicoidal axis of the chiral nematic LC. Because the technique is so versatile, it is possible to photo-polymerise different areas of the thin-films at different temperatures to pattern the gels in such a way that different regions of the gel emit at different laser wavelengths.

5.1 – Background

In this section I describe the various methods previously used to create LC elastomers, particularly those based upon LC gels. This is followed by an overview of previous work in the literature on creating elastomeric LC lasers.

5.1.1 – Liquid crystal elastomers

LC elastomers are weak, highly extensible materials which require energy input to change their shape and which regain their original shape when external forces are removed [1]. LC elastomers may fall into a variety of categories depending on the materials used to fabricate them, and the preparation procedure that is required – broadly these are elastomers based upon side- or main-chain polymers, liquid single crystal elastomers and LC gels.

LC elastomers can be made of anisotropic networks formed via cross-linking of various LC monomers with reactive groups [1-3] (so called side- or main-chain polymers). In this case, the LC molecules themselves act as the monomers and the resulting elastomer retains many of the properties of the base LC but with enhanced mechanical stability. In the specific case of chiral nematic LCs, this technique often results in poorly aligned samples with poorly-defined photonic band-gaps because it is not compatible with conventional alignment techniques – the helix alignment occurs during a solvent deswelling step.

A second type of elastomer – the liquid single crystal elastomer – is formed by starting with a polydomain LC network which is then converted to a monodomain structure by using magnetic fields, electric fields or mechanical stresses [4]. This results in order on the macro-scale which will be locked in by a subsequent cross-linking reaction. Again, this technique precludes conventional alignment procedures and requires a long fabrication time (several days).

The third type of elastomer (and the one which is used in the work in this Chapter) is the so-called elastomeric LC gel. These are created by using a mixture of reactive and non-reactive low molecular weight mesogens and photo-polymerising it [5-6]. The technique for creating them is similar to that described in Chapters 3 and 4 for polymer-stabilised LCs, however, usually higher reactive mesogen concentrations are used. These gels offer advantages over the previous two methods due to their simplicity of manufacture. Whereas the previous two techniques require bespoke materials and complex preparation techniques, elastomeric gels can be made by combining commercially available materials and by using conventional alignment techniques. Thus, high-quality films (which have well-defined photonic band-gaps) may be created in a matter of minutes (compared to the days required for the techniques in Reference 4, for example). Furthermore, the technique allows additional versatility – for example

allowing the gels to be patterned by varying the curing conditions of different areas of the LC material [7].

When an elastomer is based upon chiral nematic LCs, an elongation of the elastomer perpendicular to the helical axis can result in a contraction of the LC helix, which in turn leads to an increase or decrease in the wavelength position of the photonic band-gap [8]. Such an elongation can be achieved by applying UV-light to induce a conformational change in the molecule which changes the structure (usually a UV-induced cis-trans conformational change yields an elongation or contraction of the structure) [9], by changing the temperature of the elastomer [10], by applying electric fields [11], or by applying mechanical stresses [8, 12-18], as described here. Thus, elastomers are versatile materials with properties that can be tuned by a variety of external stimuli – this means that they have a great deal of potential for use as tuneable LC lasers [8, 12-14] as will be discussed in detail in this Chapter.

Such tuneable photonic band-gaps could also be applied to create actuators or pressure sensors [14-17]. A variety of work has been performed to use LC elastomers as actuators. This is due to their potential to convert electrical signals into mechanical changes. The elastomer lasers discussed here possess a photonic band-gap that can be wavelength tuned by mechanically stretching them; if that mechanical stretching could be performed by electrical means, the laser emission/photonic band-gap wavelength could be electrically tuned.

The potential of using LC elastomers as strain sensors has also been explored. This is because their optical properties change when mechanical stresses are applied [14-17]; in the lasers discussed here, a given emission wavelength consistently corresponds to a particular elongation, it is possible to know the extension of the film by measuring the emission wavelength (and vice versa).

5.1.2 – Elastomeric liquid crystal lasers

Chiral nematic LC elastomers are ideal candidates for tuneable band-edge LC lasers due to the wide tunability of the photonic band-gap. Thus, chiral nematic LC elastomers have been combined with fluorescent dyes and optically pumped to yield tunable lasing. This has previously been performed using both liquid single crystal elastomers and side- and main-chain LC polymers.

Mechanically-induced wavelength tuning of a LC laser was first achieved in a liquid single-crystal elastomer [8], prepared via the anisotropic deswelling method [4]. However, as noted in Reference 4, the optical properties of such samples is far from perfect and, as a result, the laser performance is inferior to that of conventional well-aligned low molar mass chiral nematic LC sample. In particular, the lasing threshold in the elastomer was found to be three orders of magnitude larger than that seen in previous conventional systems due to the poor Grandjean alignment of the chiral nematic LC [8]. Tuning ranges of ~60 nm were achieved using this technique [13], however, the long processing time (days), complexity of the technique and poor alignment of the resulting chiral nematic mean that it is not ideal for practical applications.

An alternative approach to the anisotropic deswelling method was investigated by Schmidtke et al. They used uncrosslinked chiral nematic side-chain polymers which were prepared between two glass substrates and photo-crosslinked [12]. This yielded a more well-defined photonic band-gap with a tuning-range of ~90 nm. However, a uniformly aligned sample was again difficult to obtain via this method due to the large viscosity and disorder inherent in the initial polymer (for example, in Reference 12 the sample had to be annealed for two days to achieve the desired Grandjean texture).

In this Chapter, I describe work to investigate creating elastomeric LC lasers by using dye-doped elastomeric gels. The in-situ photo-polymerisation of reactive mesogens, as detailed in previous Chapters, facilitates the creation of very highly aligned samples, typically in a matter of seconds or minutes. While the efficacy of the method is limited to relatively thin samples (less than a few tens of μm thick), this is not a hindrance in the context of LC lasers, where the optimum LC layer thickness is ~10 μm [18]. This technique has already been successfully used to create elastomeric blue phase LC gels [19] and (non-elastomeric) liquid crystal lasers in Reference 20 (as well as Chapter 4 of this thesis). However, no lasers fabricated using this technique have previously been made free-standing or shown to be stretchable.

5.2 – Effect of reactive mesogen concentration on elastomer elongation and tuning range of the photonic band-gap

The first step of this work was to investigate the mechanochromic properties of films containing different concentrations by weight of the reactive mesogen mixture. This allowed me to probe the effect of the polymer density on the mechanical properties of

the film – the extent of elongation that could be achieved and the maximum possible spectral shift in the band gap.

To this end, polymer-stabilised films consisting of different concentrations by weight of the reactive mesogens were created. The base chiral nematic mixture was comprised of the previously-described high twisting power chiral dopant R5011 (2.4 wt%, Merck) and the achiral nematic LC E7 (Merck); E7 was chosen due to its ready availability and well-studied physical properties. The same reactive mesogen mixture (UCL-011-K1, Dai Nippon Ink) that was used in Chapters 3 and 4 was added to the base chiral nematic mixture. The reactive mesogen mixture was chosen because it is a complete mix containing all of the necessary components for photopolymerisation. Eight samples consisting of different concentrations by weight (~10-80 wt% in increments of 10 wt%) of the reactive mesogen mixture were prepared in order to study the effect of polymer concentration on the mechanochromic characteristics of the films.

These mixtures were filled into 20 μm-thick glass cells (Instec) that had anti-parallel rubbed polyimide alignment layers coated onto the inner substrates of the cell. To form a uniform standing helix (Grandjean) alignment, the samples were annealed to give a good monodomain alignment of the helical structure. The quality of the alignment was checked using a combination of polarising optical microscopy to study the texture and UV-VIS spectroscopy to check the optical finesse of the photonic band-gap. The mixtures were then photo-cured by exposure to UV light from a hand-held UV source (Thorlabs CS2010) emitting 185 mW/cm^2 of radiation with a wavelength of 365 nm at the head; they were held at a distance of 10 cm from the head illuminated for 12 s from each side to ensure uniform curing across the cell. According to the Beer-Lambert law: $\log_{10}(I/I_0) \propto \varepsilon l$ where I_0 is the initial intensity of light and I is the intensity of light after passing through a length, l, of a medium with a molar absorptivity of ε. This means that the intensity of radiation decreases as it passes through the cell and so this could lead to non-uniform curing and thus an uneven polymer density. Fig 1a shows a film photo-cured in a glass cell. The glass cells were then broken apart (as shown in Fig 1b) and delaminated using a scalpel; the average film size was ~5 x 10 mm with a thickness of ~ 20 μm – an example is shown in Fig 1c.

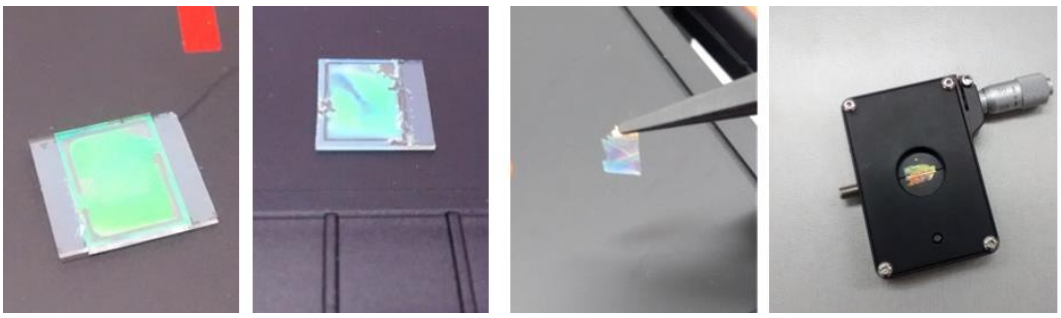

a) b) c) d)

Figure 1 – The process for creating the stretchable chiral nematic liquid crystal films. a) The mixture is aligned in a glass cell (20 µm spacing) and photo-cured; b) the cell is peeled apart with a scalpel; c) the film is delaminated using a scalpel; d) the film is placed across a variable aperture and elongated.

It was found that below a concentration of 30 wt% of the reactive mesogen mixture, the films did not possess adequate structural integrity to be delaminated from the glass cells without some polymer residue clearly remaining on either one or both of the glass substrates. Above this concentration, however, the films could be peeled intact without leaving any observable solid polymer residue.

The free-standing films were then placed across a variable-width aperture (Thorlabs VA100/M) comprised of two blades that had an opening that ranged from 25 µm to 6 mm, as shown in Fig 1d. At concentrations above ~60 wt%, the films were too rigid to enable substantial elongation before breaking. However, even at concentrations as high as 80 wt% of the reactive mesogen, the mixtures still exhibited a chiral nematic LC phase and possessed well-defined photonic band-gaps.

To take transmission spectra of the films in order to identify the wavelength and width of the photonic band-gaps, the samples were illuminated by a halogen white light source (Ocean Optics HL-2000-FHSA) that was focussed to a spot with a diameter of ~500 µm at the aperture using a 20X, 0.5 NA objective. The transmission spectra were then recorded on a fibre-coupled spectrometer (Ocean Optics USB2000+ UV-VIS; resolution 1.7 nm) with a 600 µm-diameter fibre.

The transmission spectra of the different gels were recorded as they were subjected to a uniaxial mechanical strain along a direction perpendicular to the helicoidal axis. This was achieved by increasing the separation of the variable aperture in 10 µm increments. In all cases the initial aperture width was the same (320 µm). Upon increasing the aperture width, the films were laterally stretched, leading to a mechanochromic effect whereby the selective reflection band blue-shifted; this is qualitatively consistent with a thinning of the film and a contraction of the pitch. Fig 2a-d show the change in band-

gap position for mixtures with different concentrations of reactive mesogen. This shows that the larger the reactive mesogen concentration, the greater the shift of the photonic band-gap (from 35 nm for 30 wt% to 63 nm for 58 wt%). Note that the transmission also increases on stretching because opening of the aperture allows more light to pass through to the spectrometer. The photonic band-gap is not perfectly sharp due to the presence of the polymer network; however, it does compare favourably to previous work on LC elastomers and, furthermore, the manufacturing process I use here is relatively straightforward compared to the complex techniques used elsewhere [8, 12-14].

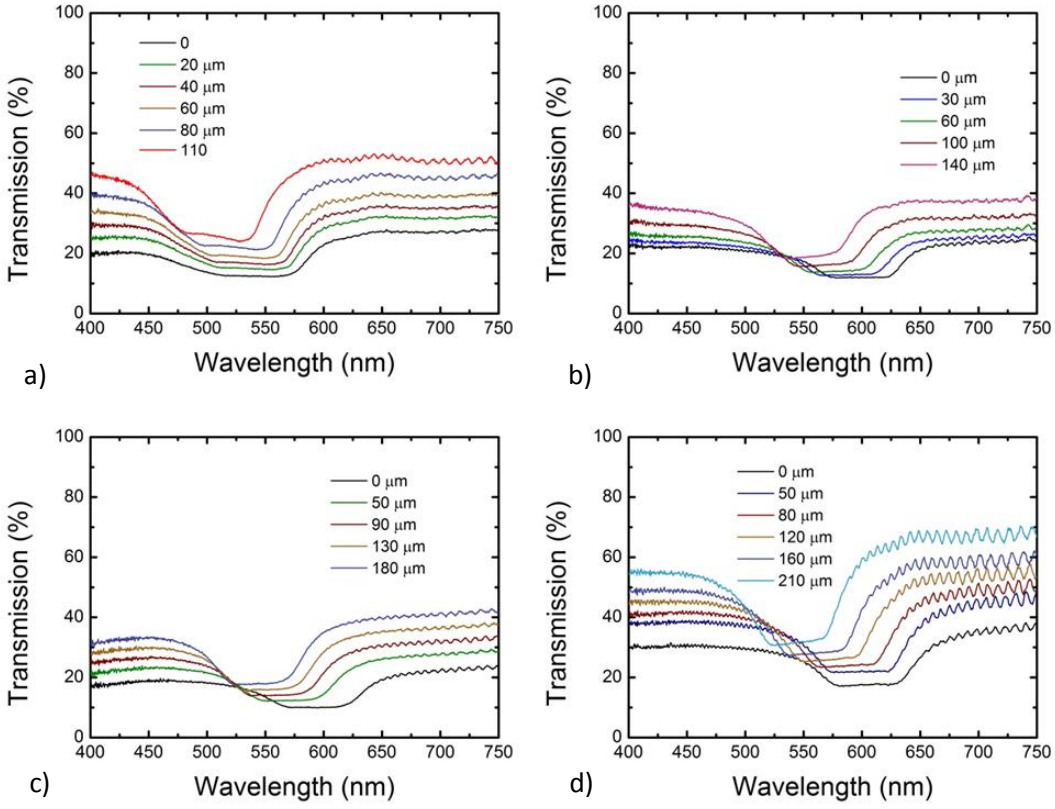

Figure 2 – The change in transmission spectrum as the film is stretched for reactive mesogen concentrations of: a) 30 wt%, b) 40 wt%, c) 50 wt%, d) 60 wt%. Measurement taken at 20°C.

As the films were elongated, the maximum wavelength shift increased. This is illustrated in Fig 3 for the different films. Fig 3 is a plot of the maximum shift of the long-wavelength band-edge, $\lambda_{L(max)}$, relative to the initial, unstrained wavelength, $\lambda_{L(0)}$. This demonstrates that larger concentrations of the reactive mesogen mixture allow a greater elongation to be achieved – and therefore a commensurately larger shift of the photonic band-gap. This data has been obtained from the transmission spectra shown in Fig 2. The long wavelength band-edges for the initial, unstrained films do not perfectly coincide with each other – this is due to the slight changes in the pitch of the chiral

nematic LC that arises because different reactive mesogen concentrations were used in the initial mixtures. Within experimental error, the wavelength varies linearly with elongation.

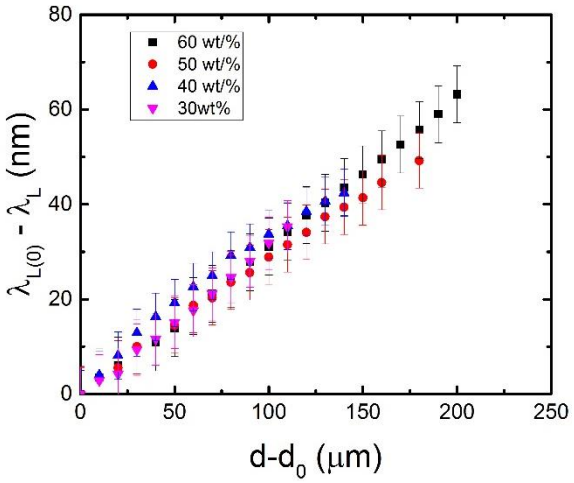

Figure 3 – The change in wavelength of the long band-edge for different concentrations of the reactive mesogen mixture. Measurement taken at 20°C.

The change in wavelength can be explained as a shortening of the pitch as the film is stretched. According to a first order approximation of Poisson's ratio (the ratio of the proportional decrease in a lateral measurement to the proportional increase in length in a sample of material that is elastically stretched), the film thins on elongation and this means that the helices are compressed. Previously, a linear variation of the pitch upon elongation has been reported [8, 12]. To further corroborate the theory that a shortening of the pitch is caused by a thinning film, I measured the film thickness during stretching and showed the thickness of the film decreases linearly with an increase in the

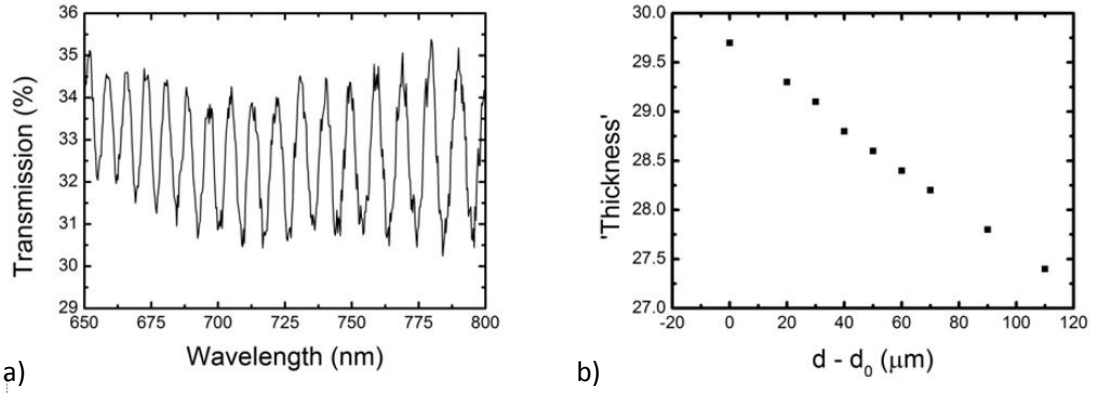

Figure 4 – Thickness measurements. a) An example of the interference fringes in the white light spectrum for an unstretched film when illuminated by left-polarised light; b) the change in film 'thickness' as it is stretched. Measurement taken at 20°C.

elongation of the film. These results are given in Fig 4. The sample (containing 58 wt% of polymer in this case) was illuminated with left-handed circularly polarised light (which is transmitted because the helix is right-handed) and the interference fringes (as shown in Fig 3a) were then studied on stretching the films. As the film stretched, the fringe spacing decreased; this corresponds to a thinning of the film.

Fig 5a is a plot of the maximum shift of the long-wavelength band-edge, $\lambda_{L(max)}$, relative to the initial, unstrained wavelength, $\lambda_{L(0)}$. Fig 5b, on the other hand, shows the relative change in the aperture width as a function of the concentration of polymer before the film breaks. Clearly, the results demonstrate that the larger the concentration by weight of the reactive mesogen, the greater the film elongation and therefore the greater the relative tuning range $\lambda_{L(max)}$- $\lambda_{L(0)}$. As the gradients in Fig 3 are the same (within experimental error), the greater polymer concentration allows elongation over a longer distance, but a given elongation provides the same degree of wavelength-tuning. Therefore, the mechanochromic sensitivity is unaltered by the increase in the concentration of the reactive mesogen.

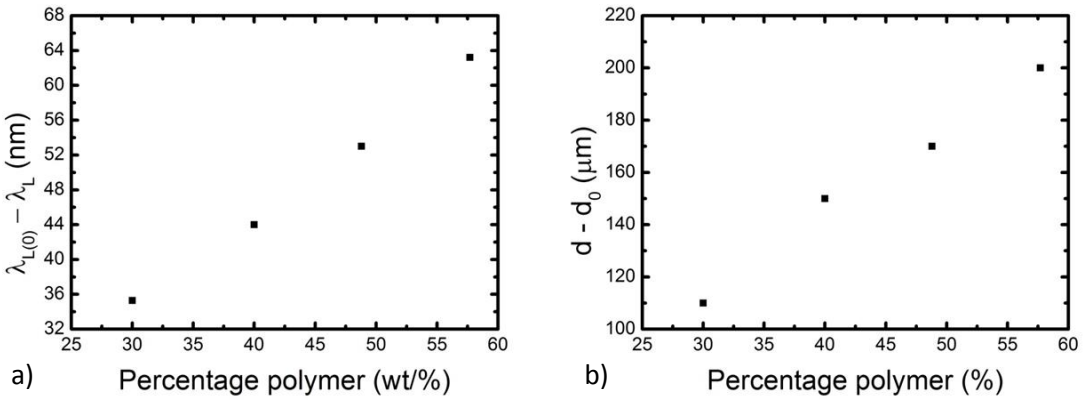

Figure 5 – a) the maximum tuning range for different percentages of reactive mesogen in the liquid crystal gel; b) the maximum elongation before breaking the film for different percentages of reactive mesogen mixture in the liquid crystal gel. Measurement taken at 20°C.

Fig 6 shows the change in the long wavelength band-edge as a function of the relative aperture width for the gel consisting of 58 wt/% of the reactive mesogen mixture. In this case, measurements were carried out upon both elongation and contraction of the film.

Firstly, the results show a linear dependence (within experimental error) on the aperture width and, importantly, there is negligible hysteresis even after more than ten cycles of stretching and relaxing the film. Since there is little hysteresis, it is then possible to select a desired wavelength by controlling the extent of elongation using the variable-

width aperture. The lack of hysteresis was not unique to this sample and was also observed in the other gels that contained lower polymer concentrations.

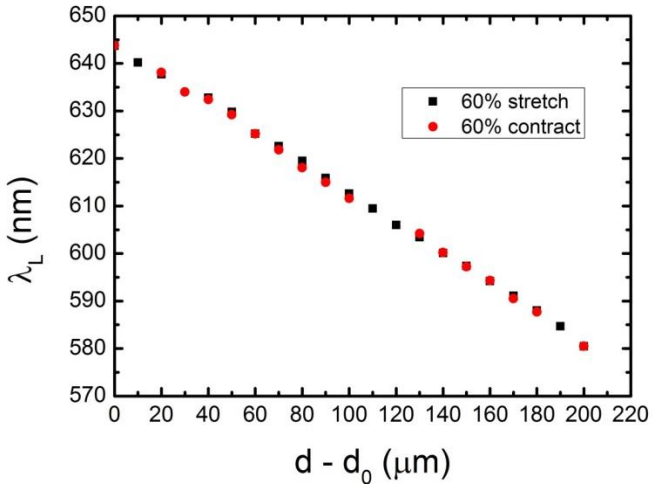

Figure 6 – The change in the long band edge wavelength position as a function of elongation on both stretching and contracting. Measurement taken at 20°C.

To observe the change in the appearance of the films as they are mechanically stretched, the variable-width aperture was mounted on an optical polarising microscope and images were captured for different aperture separations. Figs 7a-f provide example images of a film containing ~58 wt% polymer as it is elongated from 320 to 445 μm. In the images, the spacer beads (20 μm) can be seen (trapped in the gel after delamination), as can some defects in the alignment (e.g. oily streaks). On stretching, the film colour that is observed through crossed polarisers changes from green to orange (a red-shift) as the photonic band-gap itself blue-shifts and the light reflected by the film changes. Although a colour change can be observed in reflection, it is a subtle change; thus, I have used crossed polarisers to highlight clearly the change in the optical properties of the films.

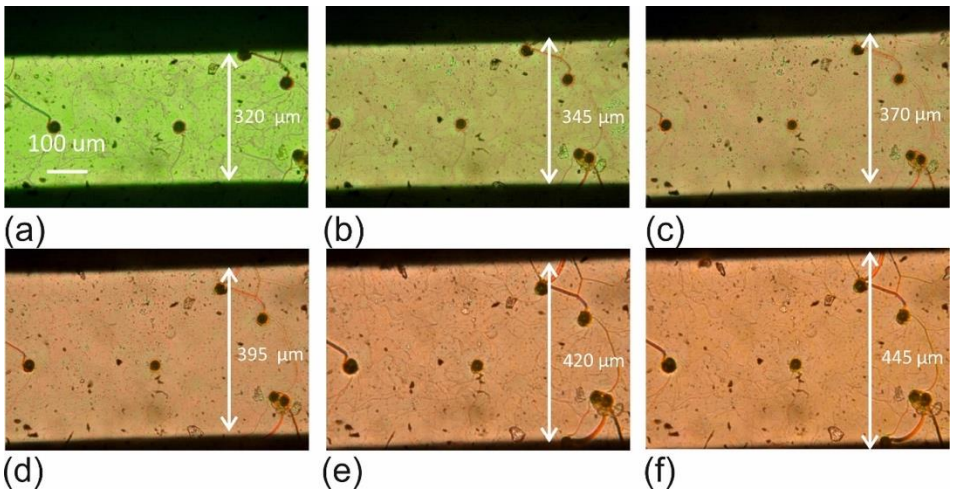

Figure 7 – Optical polarising microscope images of an elastomeric film made using 58 wt% reactive mesogen as it is stretched by: a) 0 µm; b) 25 µm; c) 50 µm; d) 75 µm; e) 100 µm; f) 125 µm from an initial spacing of 320 µm. Results taken at 20°C.

Together, the results shown in Figs 2-7 demonstrate that by using a combination of reactive and non-reactive mesogens, a stretchable chiral nematic gel may be created which has a selective reflection band that can be controlled reversibly and selectively – with a given elongation corresponding to a specific photonic band-gap wavelength position. The next step was to use these materials to create wavelength-tuneable lasers.

5.3 – Stretchable liquid crystal laser gels

To create wavelength tuneable lasers from our stretchable LC gels, a fluorescent laser dye, PM597 (1.0 wt%, Exciton), was added to the mixture containing 58 wt% reactive mesogen concentration, since it showed the greatest degree of tuning. PM597 was used as in Chapter 4 where it was shown that it did not significantly interfere with the photo-polymerisation procedure or degrade the photonic band-gap. However, the addition of the dye necessitated a longer UV exposure time (2 × 120 s) during the photo-curing procedure to ensure thorough photo-curing.

To observe laser emission from the gels, the samples were optically pumped with a frequency-doubled Nd:YAG laser (CryLas 6FTSS355-Q4-S) that emitted 1 ns pulses at a wavelength of 532 nm and a pulse repetition rate of 10 Hz. The pump laser was focused onto the devices to a spot size of ~200 µm diameter and the output was measured perpendicular to the films along the direction of the chiral nematic LC helicoidal axis. A 550 nm long-pass filter was used to block the pump beam from being detected by the spectrometer. Emission was collected using a microscope objective (5X,

0.25 NA) which was then coupled into a 600 µm-diameter fibre that was attached to a universal serial bus spectrometer (Ocean Optics USB2000+ UV-VIS). The emission energy of the pump beam was measured using a pyroelectric sensor (OPHIR, PE9-ES-C, spectral range 0.12-12 µm, sensitivity 0.1 µJ). A combination of a quarter wave plate and a Glan Thompson polariser was used to probe the handedness of the circular polarization of the laser emission. The pump laser energy was controlled using a combination of a Glan-Thompson polariser and a half wave-plate.

When the gels were optically pumped, I observed laser emission at a wavelength corresponding to the long band-edge of the chiral nematic LC. Upon extension of the films, the wavelength of the laser emission was found to blue-shift and the change was commensurate with the change in the photonic band gap and the decrease in the pitch shown previously in Fig 6.

Fig 8a presents the laser emission spectra for different extensions of the film – the lasing peak shifts to shorter wavelengths as the film is elongated. The full width at half maximum is found to be ≈ 1.7 nm, which is on the same order as the resolution limit of our spectrometer. Fig 8b shows the linear relationship between the laser wavelength and the elongation of the film in accordance with the results obtained for the selective reflection band as seen in Fig 6. Again, no hysteresis is observed and the films could be stretched and contracted over 10 times without degradation of laser emission. In this case, the finite bandwidth (cf Fig 11) of the dye's fluorescence spectrum limits the extent over which

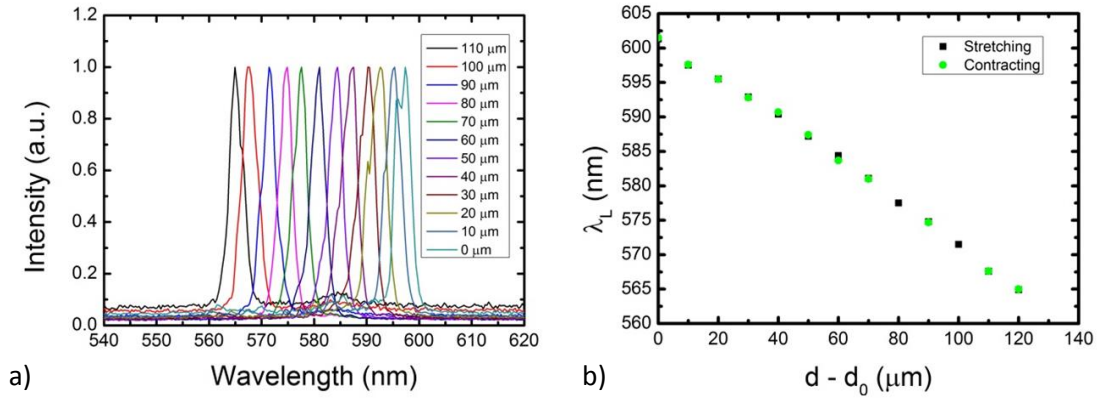

Figure 8 – a) The change in laser emission spectrum upon elongation of a stretchable laser gel; b) the wavelength of emission on stretching (black square) and contracting (green circle). Measurement taken at 20°C.

the laser wavelength can be tuned – and so the largest tuning ranges demonstrated for the chiral nematic gels without dye are not fully realised here (I see a ~36 nm tuning range of the lasing compared to ~63 nm for the photonic band-gap).

Input-output characteristics for the laser gel were obtained for different points during the film preparation procedure. Encouragingly, there appears to be no noticeable increase in the excitation threshold after the film preparation process, as shown in Fig 9. The results show that the threshold fluences per pulse are approximately the same for both the free-standing film and for the same sample before delamination (~1±0.2 μJ/cm^2/pulse).

Subsequently, the excitation laser threshold was obtained for four different film extensions. Example input-output charts for an un-stretched film (582 nm peak) and the same film after stretching (560 nm) peak are presented in Figs10a and 10b respectively.

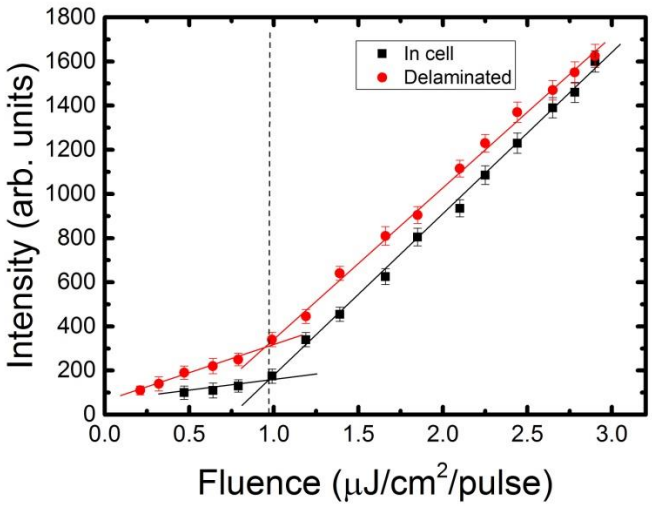

Figure 9 – Laser threshold for a film after photopolymerisation before (squares) and after (circles) the cell has been broken open and the film delaminated. In both cases, the threshold is ~1±0.2 μJ/cm^2/pulse, as indicated by the dashed line. Measurement taken at 20°C.

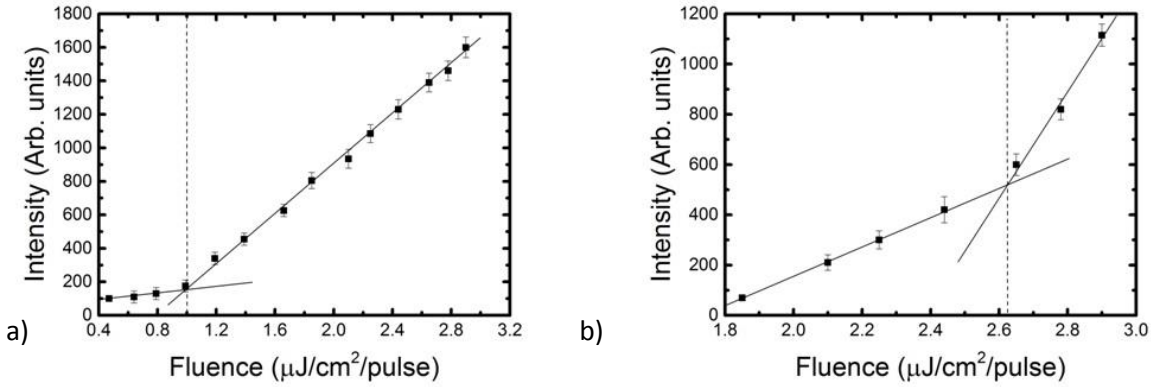

Figure 10 – Laser threshold for a) an unstretched film (582 nm emission), b) a stretched film; the dashed lines indicate the threshold position.

Fig 11 shows the threshold at different extensions of the films compared to the gain curve (fluorescence spectrum) of the dye dispersed in the nematic LC host, E7. It is found that the laser threshold exhibits a minimum near λ = 582 nm, which corresponds approximately to the gain maximum for PM597 dispersed in E7. This is in accordance with previous studies on LC lasers using PM597 as the laser dye [22]. The results in this work show that as the film is subjected to a uniaxial lateral extension, the laser threshold decreases to a minimum at 582 nm and then increases as the laser wavelength moves to shorter wavelengths. This is believed to be due to a change in the relative position of the band-edge with respect to the gain curve of the laser dye. At wavelengths away from λ = 582 nm, the gain curve decreases and there is a concomitant increase in the excitation threshold. Furthermore, the finite extent of the gain curve also explains why the laser tuning range is found to be smaller (≈36 nm) than the shift observed for the photonic band-gap seen in Figure 6 (≈63 nm). In terms of the tuning range, the limiting factor in this case is actually the gain curve of the laser dye (something further corroborated by the observation that the film could be stretched beyond the point at which laser emission ceased without the film breaking). Thus, a combination of multiple dyes (as shown in earlier studies [23]) may allow greater wavelength-tuning ranges to be achieved.

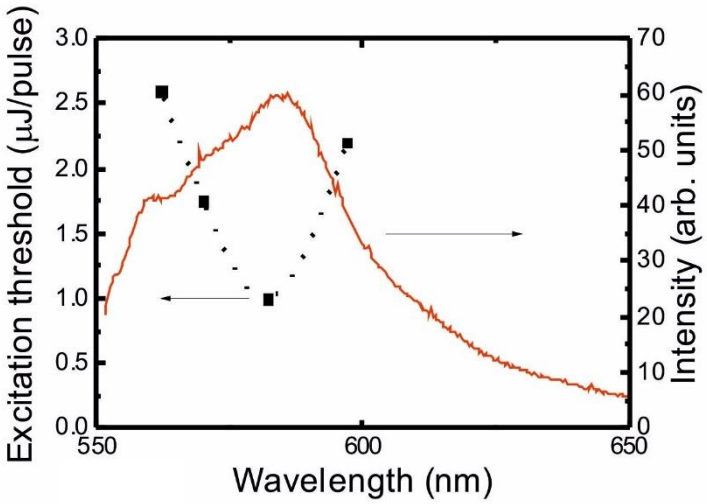

Figure 11 – Change in laser threshold on stretching (black squares, primary axis; the dashed line is to guide the eye) against the PM597 gain curve (red line, secondary axis). Results taken at 20°C.

To confirm that the handedness of the polarisation of the laser emission is unchanged during stretching, the emission spectrum for both left and right circularly polarised light emitted from the dye-doped chiral nematic LC were recorded. Since the helical structure is inherently right handed, I would expect the emission at the long band-edge to be right circularly polarised. Fig 12 shows the circular polarisation properties of the dye-doped gel before and after stretching; in both cases, laser emission is observed for right circularly polarised light, and the emission wavelength blue-shifts upon stretching; in contrast, no laser emission is observed for left circularly polarised light. It is clear that the right-handed helical structure is maintained upon stretching; this is in contrast to previous work on cross-linked elastomers where a change in the polarisation behaviour (and hence character of the helical structure) was observed on stretching [24]. This difference is not surprising given that the materials used here consist of polymer networks containing interstitial LC as opposed to LC molecules that are themselves integral to the polymer structure that are used in Reference 24.

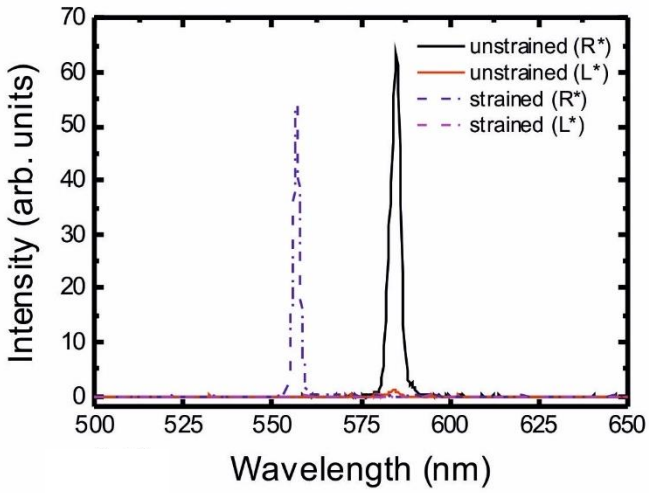

Figure 12 – The emission of a stretched and an unstretched film for right and left circularly polarised light

Our next step was to demonstrate the flexibility of using our technique to create multi-coloured lasers, something that is extremely difficult to achieve with the previous methods that have been used to fabricate elastomeric LC lasers.

5.4 – Multi-coloured, stretchable liquid crystal laser gels

To demonstrate the utility of the gels used in this work and the versatility of the fabrication process, a multi-coloured laser film was created by photo-polymerising half of the device at 25°C and the other half at 45 °C. Since the pitch is temperature-dependent, this process locked-in two separate domains with different pitches, as can be seen from the different colours evidenced in Fig 13.

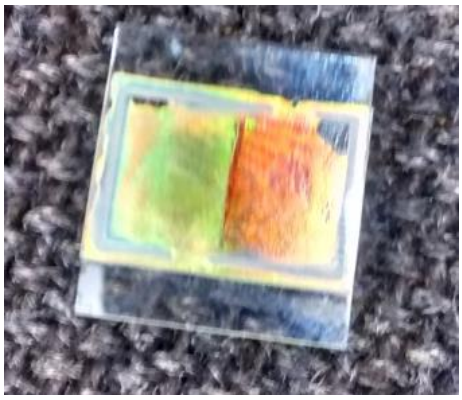

Figure 13 – A stretchable gel sample before delamination; it exhibits two regions with photonic band-gaps in different positions.

Transmission spectra measurements confirmed that the band gap for each domain occurred at different central wavelength positions. When subjected to a mechanical strain, the band-gaps were found to blue-shift simultaneously, reversibly and without hysteresis. The corresponding laser gel exhibited laser emission at a different laser

wavelength (603 and 566 nm) from each domain, which was consistent with the different pitch values (~347 and 325 nm). On stretching, the laser wavelengths in both regions were found to blue-shift simultaneously, as shown in Figs 14a and b.

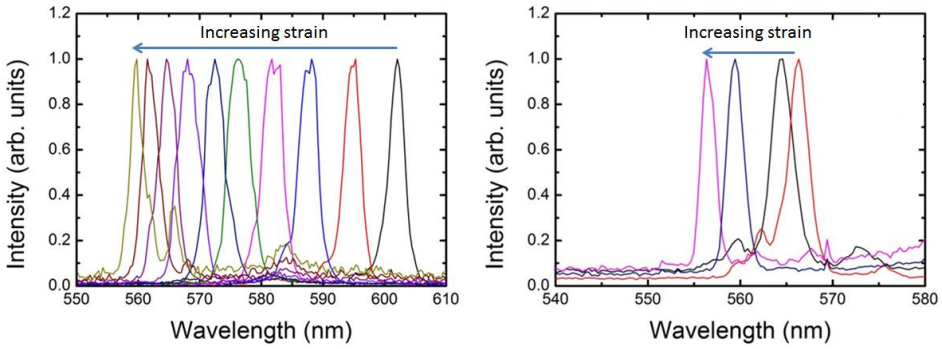

Figure 14 – A stretchable laser gel: a) change in laser emission spectrum for the region cured at room temperature; b) change in laser emission spectrum for the region cured at 40 °C. Measurement taken at 20°C.

As with the mono-domain sample in Fig 8, the tuning ranges were limited by the gain curve of the dye (lasing was curtailed at 555 nm for both regions), as shown by the dotted line in Fig 15; thus, the shorter pitch region exhibited a shorter tuning range (≈12 nm compared to a 45-nm tuning range for the long-pitch sample). Fig 15 shows that the two lines have different gradients (-0.38 µm/nm for the black squares vs -0.24 µm/nm for the red circles); a given elongation ($d-d_0$) corresponds to the same change in thickness in both cases, however, there will be different numbers of pitches present in the areas cured at different temperatures and this will lead to the subtle difference seen here.

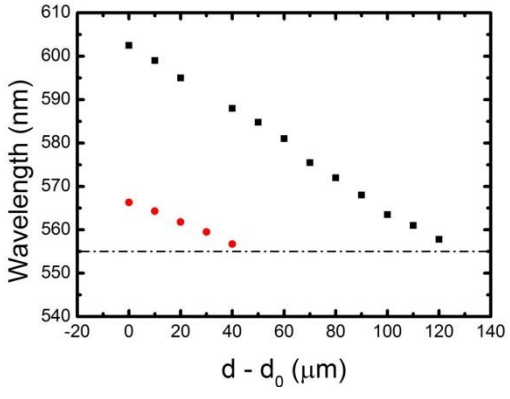

Figure 15 – The change in emission wavelength for two different regions of a patterned gel laser: shorter pitch region, red circles; longer pitch region, black squares. The dashed line at 550 nm shows the limit of the dye gain curve. Measurement taken at 20°C.

5.5 – Conclusion

In this Chapter, I have described a method for creating a stretchable, multi-coloured LC laser gel in which the emission wavelength can be precisely selected by controlling the

film elongation. To this end, I have presented results on the mechanochromic properties of LC gels containing different concentrations of reactive mesogen. I have shown how the tuning range increases with the concentration of reactive species within the mixture while the mechanochromic sensitivity remains unchanged. By doping these films with fluorescent dyes, I have observed reversible laser tuning across a 45 nm wavelength range upon stretching and contracting the films multiple times. Moreover, the tuning range did not appear to exhibit hysteresis, allowing a desired wavelength to be selected by controlling the elongation of the film. By varying the curing conditions, it was possible to pattern the films to exhibit regions of different pitch with different emission wavelengths. This simple, versatile manufacturing technique couples with the small dimensions of the lasers and their suitability for solution processing makes them an exciting prospect for a variety of applications such as pressure sensors and micro-actuators.

Although the work in both this Chapter and Chapter 4 present novel ways of widely wavelength-tuning LC lasers, such lasers still possess a major disadvantage insofar as they rely upon fluorescent dyes as the gain medium. These dyes are easily photo-bleached when continuously illuminated, limiting the utility of LC lasers. To this end, the next two Chapters will detail work to find alternative, photostable gain materials based upon inorganic materials. This will begin in Chapter 6 with a discussion of luminescent molybdenum clusters which possess long organic ligands which allow them to easily disperse into LCs, and will continue in Chapter 7 where inorganic-organic perovskites will be discussed.

5.6 – References

1. P. Xie and R. Zhang, *J. Mater. Chem.*, 2005, **15**, 2529.
2. H. Finkelmann, H.-J. Kock and G. Rehage, *Makromol. Chem., Rapid Commun.*, 1981, **2**, 317
3. R. Zentel and G. Reckert, *Makromol. Chem.*, 1986, **187**, 1915
4. S. T. Kim and H. Finkelmann, *Macrocol. Rapid. Commun.*, 2001, **22**, 429.
5. D. J. Broer, H. Finkelmann, and K. Kondo, *Die Makromol. Chemie*, 1988, **189**, 185.
6. D. H. Brown, V. Das, R. W. K. Allen, and P. Styring, *Mater. Chem. Phys.*, 2007, **104**, 488.
7. R. A. M. Hikmet and R. Polesso, *Adv. Mater.*,2002, **14**, 502.
8. H. Finkelmann, S. T. Kim, A. Muñoz, P. Palffy-Muhoray, and B. Taheri, *Adv. Mater.*, 2001, **13**, 1069.
9. P. M. Hogan, A. R. Tajbakhsh, and E. M. Terentjev, *Phys. Rev. E*, 2002, **65**, 041720
10. M. Warner, E. M. Terentjev, Liquid Crystal Elastomers, OUP, 2007, Chapter 1.
11. Y. Fuchigami, T. Takigawa, and K. Urayama, *ACS Macro Lett.*, 2014, **3,** 813.
12. J. Schmidtke, S. Kniesel, and H. Finkelmann, *Macromolecules*, 2005, **38**, 1357.
13. P. V Shibaev, P. Rivera, D. Teter, S. Marsico, M. Sanzari, V. Ramakrishnan, and E. Hanelt, 2008, *Opt. Express*, **16,** 2965.
14. A. Varanytsia, H. Nagai, K. Urayama, and P. Palffy-Muhoray, *Sci. Rep.*, 2015, **5**, 17739.
15. J. Naciri, A. Srinivasan, H. Jeon, N. Nikolov, P. Keller, and B. R. Ratna, 2003, *Macromolecules*, 2003, **36**, 8499.
16. C. Ohm, M. Brehmer, and R. Zentel, 2010, *Adv. Mater.*, 2010, **22**, 3366.

17. O. T. Picot, M. Dai, E. Billoti, D. J. Broer, T. Peijs, and C. W. M. Bastiaansen, 2013, *RSC Adv*., 2013, **3**, 18794.
18. Th. K. Mavrogordatos, S. M. Morris, F. Castles, P. J. W. Hands, A. D. Ford, H. J. Coles and T. D. Wilkinson, *Physical Review E* 2012, **86**, 011705.
19. F. Castles, S. M. Morris, J. M. C. Hung, M. M. Qasim, A. D. Wright, S. Nosheen, S. S. Choi, B. I. Outram, S. J. Elston, C. Burgess, L. Hill, T. D. Wilkinson, and H. J. Coles, *Nat*. *Mater*., 2014, **13**, 817.
20. Y. Inoue, H. Yoshida, K. Inoue, Y. Shiozaki, H. Kubo, A. Fujii, and M. Ozaki, *Adv*. *Mater*., 2011, **23**, 46.
21. C. Mowatt, S. M. Morris, M. H. Song, T. D. Wilkinson, R. H. Friend, and H. J. Coles, *J*. *Appl*. *Phys*., 2010, **107**, 043101.
22. S.S. Choi, S. M. Morris, W. T. S. Huck, H. J. Coles, *Adv*. *Mater*., 2010, **22**, 53.
23. S. M. Morris, P. J. Hands, S. Findeisen-Tandel, R. H. Cole, T. D. Wilkinson, and H. J. Coles, *Opt*. *Express*, 2008, **16,** 18827.
24. P. Cicuta, A. R. Tajbakhsh, and E. M. Terentjev, *Phys*. *Rev*. *E*, 2002, **65**, 051704.

Chapter 6 – Emission properties of transition metal clustomesogens in chiral liquid crystalline materials

Introduction

In the previous Chapters, I demonstrated two different methods for wavelength-tuning a liquid crystal (LC) laser. However, one of the major barriers to using these lasers in real-world applications is that they utilise fluorescent dyes as gain materials. These dyes are susceptible to photo-bleaching when optically pumped and so they can usually only be operated in low repetition rate pulsed mode. Consequently, this Chapter and Chapter 7 will detail work to find alternative gain materials for LC lasers that are not susceptible to photo-bleaching. This will begin here with an investigation into transition metal clustomesogens, and will be continued in Chapter 7 with an investigation into organic-inorganic perovskites.

In this Chapter, the photoluminescence properties of transition metal clustomesogens (CMs) – octahedral clusters of molybdenum with long organic ligands that exhibit liquid crystalline properties – are studied. Such CMs are potentially promising for use as alternative gain materials because they are not susceptible to photo-bleaching, have high quantum yields and good photo-stabilities [1-13]. Furthermore, they are liquid crystalline themselves, exhibit mesomorphic behaviour and are easily dispersed into other LC phases, such as the nematic and chiral nematic phases.

This Chapter will begin with an overview of the various inorganic materials that have been used as gain materials in lasers and a description of research into transition metal CMs. This will be followed by an overview of the experimental techniques specific to this Chapter.

The work described here begins with a study to find the highest possible concentration that can be dispersed into a nematic LC without aggregation. The photoluminescence properties of the resultant materials are investigated. Subsequently, the CMs are dispersed into chiral nematic LCs and the photonic band-gap of the chiral nematic is used to control the CM emission characteristics. Although my initial attempts to use them in lasers were unsuccessful, I have investigated the potential for their use as circularly-polarised light sources – particularly by dispersing the CMs into chiral nematic LCs I have shown that it is possible to create polarised light sources whose degree of polarisation can be controlled by applying ac electric fields. This is potentially important for a range of technologies, such as displays and quantum optics;

furthermore, it is a promising first step towards using CMs as gain materials in LC lasers.

6.1 - Background

6.1.1 - Inorganic gain materials for lasers

The use of inorganic gain materials in lasers has significant precedent. The first example of a laser – the ruby laser – was a solid state laser made from inorganic materials; in a ruby laser the gain is provided by trivalent chromium (Cr^{3+}), a transition metal ion [14] which acts as an impurity species in a solid host. Subsequently, a wide variety of solid state lasers have been created using various inorganic species for gain – including other transition metals (Ni^{2+}, Ti^{2+}), divalent rare earths (Sm^{2+}, Dy^{2+}) and trivalent rare earths (Nd^{3+}, Er^{3+}); Nd^{3+} for example is the gain material in the Nd:YAG lasers used to pump the LC lasers described in this thesis [15]. By doping materials into an optical fibre, fibre lasers may be created [16]. In these lasers, the gain material is usually a rare-earth element such as erbium or ytterbium.

Another type of laser based upon inorganic materials are semiconductor lasers – one of the most prevalent types of lasers due to their ease of manufacture and because they are inexpensive [17]. A semiconductor laser may also be electrically pumped which is important from a device perspective, and avoids the need for optical pumping – semiconductor lasers are often used to optically pump many types of solid state laser [18]. As well as photo-bleaching, another limitation of conventional LC lasers is the need for optical pumping (typically using a Nd:YAG laser). In the next Chapter this will be discussed in more detail in the context of the semiconducting inorganic-perovskites investigated there. Semiconductor lasers use various group III and V elements (e.g. GaAs) with the gain provided by the region between the p-type (containing free holes) and n-type regions (containing free electrons) [19] regions. One type of semiconductor laser is the quantum dot laser – in which the gain is provided by quantum dots– nanocrystals of semiconductor materials which are sufficiently small that they exhibit quantum mechanical properties. Their electronic properties are determined by their shapes and sizes – the band-gap is inversely related to size (which means that the emission wavelength can be tuned by varying the size, and they are tuneable across a broad range of wavelengths [20]). Quantum dots are often made of zinc or cadmium with chalcogenides, for example cadmium selenide.

6.1.2 – Inorganic gain materials for liquid crystal lasers

Quantum dots are an inorganic species that have been investigated as gain materials in LC lasers for the same reasons that I am investigating transition metal CMs and perovskites in this thesis – most notably, their photostability when continuously illuminated. Quantum dots have large absorption cross-sections, high quantum yields, broad excitation spectra, easy wavelength tunability by varying dot size, high stabilities and long lifetimes [21-25]. However, it is difficult to disperse them into LCs in large quantities without them aggregating.

In the literature, work has been carried out to combine the gain properties of quantum dots with tuneable LC resonators [21]. This has largely revolved around work on how LCs modify the fluorescence properties of quantum dots [22-23]. However, recently lasers composed of LC and quantum dots have been demonstrated [24]. These lasers have shown 1.66 times higher damage thresholds compared to dye-based lasers, showing promise in high repetition rate or continuous wave operation. However, these quantum dots-based LC lasers have higher energy thresholds and poorer slope efficiencies compared to dye-based lasers and require complex functionalisation to be dispersed into LCs. Thus, although LC lasers using inorganic gain materials have been demonstrated, but since they require complex manufacture procedures and even then can only be dispersed at very low ~0.1 wt% before they aggregate; thus, there is still a need to look for more compatible materials. Interestingly, one potential way of avoiding aggregation of quantum dots is by using the polymer templating technique described in Chapters 3 and 4 and refilling with quantum dots dispersed in toluene [25], something which is discussed further in the Future Work section of this Thesis.

6.1.3 – Transition metal clustomesogens

One particularly promising material for use as alternative, inorganic gain materials for LC lasers are transition metal clustomesogens – LC materials containing metallic cluster compounds that combine the self-organising ability and fluidity of LCs with the magnetic, electronic and photoluminescent properties of metallic clusters [1]. These are a subset of metallomesogens – compounds which contain metals and exhibit liquid crystalline behaviour; specifically, clustomesogens contain metallic clusters. Most clustomesogens so far investigated are based upon molybdenum clusters. These are highly emissive in the red-near-IR, have high PL quantum efficiencies (0.59) and long excited-state lifetimes (270 μs) as well as high photo-stabilities [2]. Alternative metals have been used, such as rhenium [3] and these have additional functionality, such as the

ability to reversibly switch between a green magnetic form to a red-NIR luminescent form.

The clusters are based upon a metallic octahedron surrounded by 8 face-capping and 6 terminal ligands $[M_6Q_8{}^iX_6{}^a]^{2-}$ where M is a metal, Q a chalcogen/halogen, X a halogen and *i* means inner and *a* means apical [4]. The structure of the CMs used in this work is shown in Fig 1. The apical ligands may be easily replaced with other ligands because the M-X bonds are much weaker and have much less covalent character than the M-Q bonds. This leaves the $M_6Q_8{}^i|^{4+}$ core intact. The ligands used to displace the X can be used to functionalise the core can be chosen to allow incorporation of the clustomesogens into a LC. Three types of ligand have been used to create clustomesogens – pro-mesogenic substituents (as used here) [1], specifically designed cations [2] and polymerisable substituents [4]. The materials themselves typically exhibit LC mesophases – usually smectic A [3-4], but nematic phases have also been observed [5]. These materials may be incorporated into other LC hosts by thermal or chemical diffusion, in a similar manner to fluorescent dyes but at much greater wt% (10-20 wt% compared to 1-2 wt% for fluorescent dyes – n.b. the molecular weight of the clustomesogens is greater than that of the fluorescent dye).

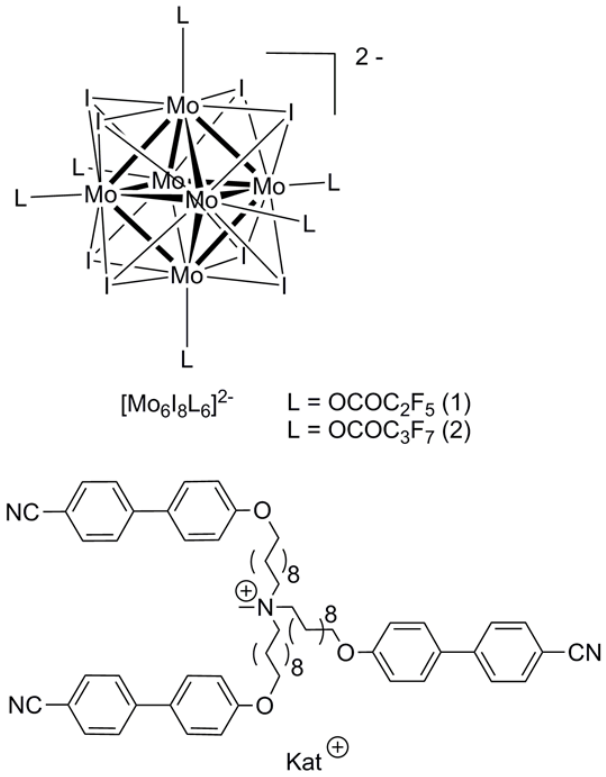

Figure 1 – The structure of the transition metal clustomesogens used in this study. a) general representation of octahedral molybdenum cluster units; b) the organic promesogenic cation Kat^+ used in this work.

In terms of emissive properties, CMs have slightly lower absorption coefficients than fluorescent dyes, such as DCM[2] (0.9 μm^{-1} compared to 1.3 μm^{-1}) [6, 26], much better quantum yields (in the literature, clustomesogen quantum yields of 1 have been reported [6], more than twice that of DCM) although they do have much longer photoluminescence lifetimes (270 µm compared to 2.1 ns – they are phosphorescent rather than fluorescent, something which is not ideal for laser emission) [6].

The clustomesogens used in this work were $Trisel_2[Mo_6I_8(OCOC_2F_5)_6]$ and $Trisel_2[Mo_6I_8(OCOC_3F_7)_6]$, synthesised by our collaborators from the University of Rennes 1 [7-10]. These LC were chosen because they exhibit a nematic LC phase across a wide temperature range (including room temperature), have high absolute quantum yields and good photostabilities under continuous illumination. The two materials have very similar emission properties and kinetic parameters [11], although slightly different miscibilities in other LCs. I

6.2 – Clustomesogens dispersed in nematic liquid crystals

Our first step was to disperse the CMs into LC hosts to investigate the potential for dispersing them as well as to investigate their emission and absorption properties.

Initially, the CM $Trisel_2[Mo_6I_8(OCOC_3F_7)_6]$ was dispersed into the nematic LC host, E7. This LC was chosen because it is well-characterised in terms of its macroscopic physical properties and it exhibits a nematic phase at room temperature. Various concentrations of CM in E7 were created (10, 15, 20, 30 wt% CM). To disperse the CM, it was added to the LC and heated to above the LC isotropic temperature (70^0C for E7 and 100^0C) for 24 hours. The nematic-isotropic transition temperatures of these mixtures were: 60.6, 59.9, 58.8, 57.5°C respectively.

The resulting mixtures were then studied using optical polarising microscopy. Fig 2 shows the bright and dark states (aligned at 45 and 90 degrees to the crossed-polarisers) of the various mixtures when filled capillary-filled into 5 µm thick planar-aligned glass cells. Although no aggregation can be seen in Fig 2a-c (10-20 wt%), at 30 wt% (Fig 1d), there is clear change in the optical texture, as has been previously reported [7].

Fig 3 shows a photograph of the photoluminescence (PL) that is observed when the glass cell containing the 20 wt% mixture is illuminated with UV (λ = 365 nm) light.

[2] 4-(Dicyanomethylene)-2-methyl-6-(4-dimethylaminostyryl)-4H-pyran

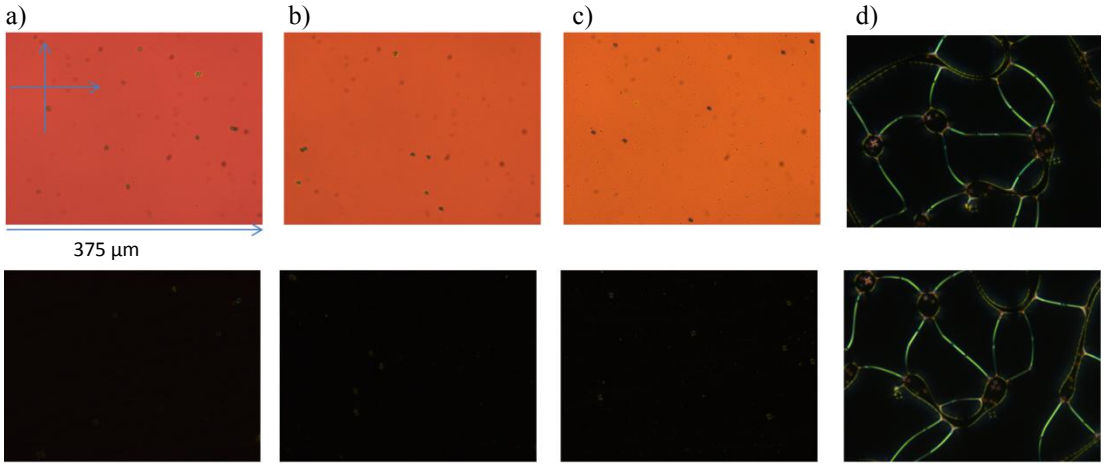

Figure 2 – Optical polarising microscopy images of different wt% clustomesogen in the nematic liquid crystal E7 in 5µm cells. a) 10 wt%, b) 15 wt%, c) 20 wt%, d) 30 wt%. The circles in a-c are spacer beads (5 µm) Results taken at 20°C.

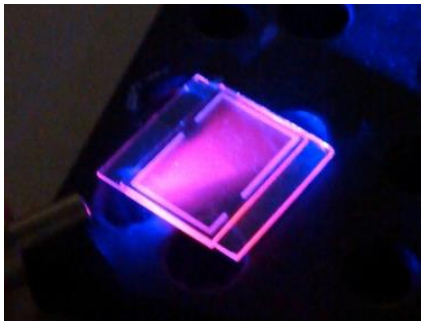

Figure 3 – Device photoluminescence when optically excited using 365 nm irradiation from an LED. Results taken at 20°C in a 9 µm cell.

The PL properties were further probed by recording the absorption and emission spectra as shown in Fig 4. The absorption (black line) has a peak at 323 nm and the emission (blue and red lines) occurs in the deep red at 660 nm. This is a large Stoke's shift (337 nm) caused by non-radiative transitions within the clusters, as has previously been reported [1]. The dashed blue line represents illumination with a 405 nm LED while the red line shows the PL when illuminated with a 365 nm LED. 365 nm is closer to the absorption maximum for the CM and so results in a larger emission intensity.

The photoluminescence of the clustomesogens was measured by illuminating the samples with a high-power LED (365 nm, 4.1 mW output or 405 nm, 37 mW output, Thorlabs). A 495-nm long-pass filter was used to prevent the detection of the LED emission. The emission was then collected by a 600 µm-diameter optical fibre that was connected to a broadband spectrometer (Ocean Optics USB2000+ UV-VIS; resolution 1.7 nm).

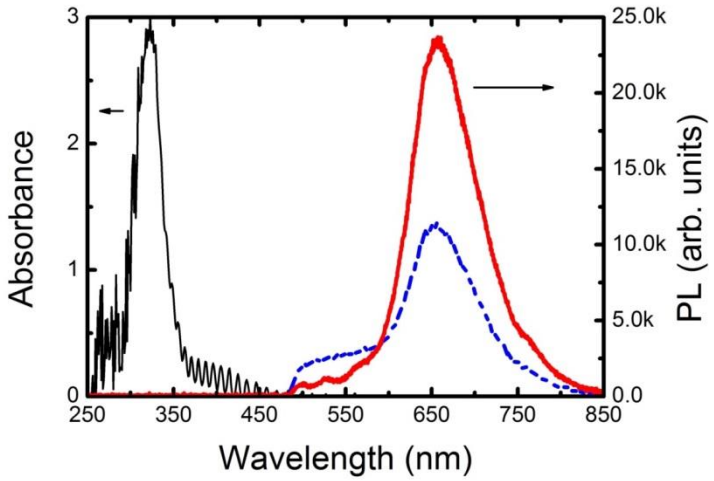

Figure 4 – Absorption (primary axis, black line) and phosphorescence (secondary axis: red line – 365 nm illumination, dashed line – 405 nm illumination). Results taken at 20°C in 9µm cells.

To further investigate the magnitude of the PL and its uniformity across the cell area, PL-mapping experiments were performed. PL-mapping is a spectroscopic technique which provides information on the optical properties of a material. Measurements were performed across the area of the entire cell and the emission intensity and wavelength at different positions is collated to give a 'map' of the PL properties.

In this work, the PL-mapping experiments were performed by our collaborators from the University of California, Merced on samples that I fabricated. Their experimental setup consists of a custom-built, high resolution scanning confocal microscopy system. The excitation sources are several ultrafast, tuneable, mode-locked lasers that cover the spectral region 350-1200 nm, a high power Ti:Sapphire laser (MIRA 900) and two optical parametric oscillators. The excitation is focused onto the sample using a high numerical aperture objective (100X). The samples are mounted on a computer-controlled 3D scanning stage. The emitted PL is collected by the same objective used for excitation. The images are produced using a spectrometer connected to a thermo-electrically cooled CCD camera; this produces images across an area of 1 mm^2 [27].

Fig 5 shows the PL-maps of the glass cells containing different wt% of the CM as described above. As the concentration of the photoluminescent CM material increases, the intensity of the PL increases from 2500 a.u. for 5 wt% to 4000 for 20 wt% CM. However, the PL decreases to ~650 a.u. for the 30 wt% mix, consistent with the distinct change seen in the optical polarising microscopy images shown in Fig 2. This results in a decrease in the PL intensity caused by quenching; this quenching is a similar effect to that seen in the case of fluorescent dyes. As the dye molecules come close to each other,

their quantum yields drop as their energy levels overlap and non-radiative processes dominate. For all four samples, the peak PL occurs at ~662 nm (within experimental error) as I saw in the spectrum shown in Fig 4 and has been seen for the CMs before dispersal [7]. The PL-maps provide further information – although the maps in Fig 5a-c are uniform, consistent with good dispersal of the CM, Fig 5d is much less uniform, corroborating the textures observed using optical polarising microscopy.

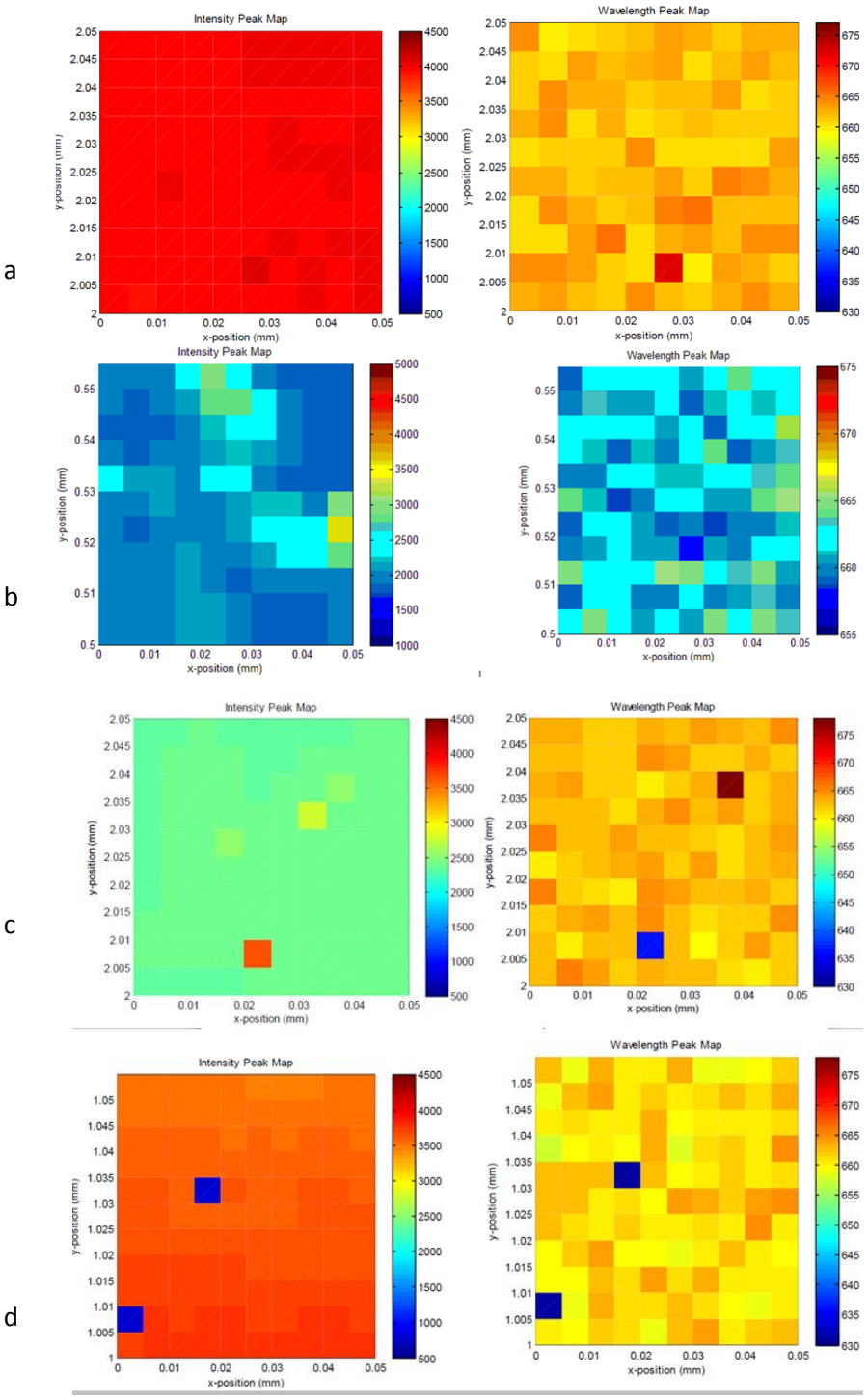

Figure 5 – Photoluminescence maps of different wt% clustomesogens in nematic liquid crystal. Left: intensity peak maps; right: peak wavelength maps. a) 10 wt%, b) 15 wt%, c) 20 wt%, d) 30 wt%. Images recorded by Prof. Sai Ghosh, et al from the University of California, Merced.

To check that there is no difference in emission in the mode parallel and the mode perpendicular to the nematic director, the linear-polarisation dependence was checked. The 20 wt% CM in the nematic LC E7 mix was filled into a 5 µm planar aligned cell (EHC; the nematic director in perpendicular to the glass substrates) and into a 5 µm homogenous-aligned cell (EHC; the nematic director is parallel to the glass substrates). The emission from these two devices when they were pumped with 365 nm radiation was then measured and compared. There was no evidence of linear polarisation dependence and the dichroic ratio $I_{\parallel}/I_{\perp}$ was found to be ~1 for all wavelengths, as shown in Fig 6a. This contrasts with a fluorescent dye, such as DCM, in which the molecular orientation of the dye is influenced by the orientation of the host LC due to both steric effects and its transition diploe moment. The DCM dichroic ratio at different wavelengths is shown in Fig 6b (measured from devices that contained ~1 wt% DCM in E7 filled into glass cells as described above). Outside the fluorescence range of the dye it is ~1 but it is significantly greater across the fluorescence range.

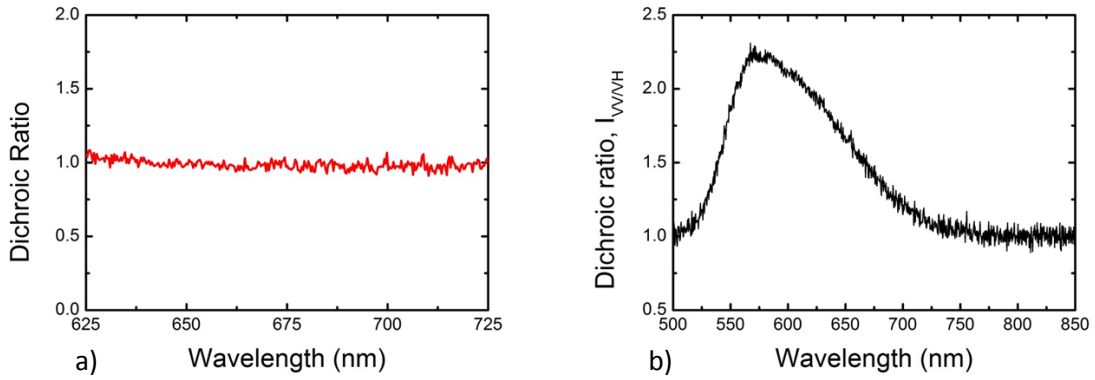

Figure 6 – The dichroic ratio of a) the 20 wt% clustomesogen/nematic liquid crystal mixture and b) the laser dye DCM (1 wt%) in E7 across their photoluminescence spectral ranges. Results taken at 20°C in 5µm cells.

The photo-stability of the clustomesogens under continuous-wave illumination is shown in Fig 7. The PL intensity of a sample illuminated with a 365 nm high-powered LED was recorded over time and compared to an equivalent mixture consisting of E7 doped with 1.5 wt% DCM. The output for the dye diminishes over time as the molecules are photo-bleached. Conversely, the output from the CM-doped nematic shows an initial increase in the PL and then reaches a steady-state output without any degradation of the emission intensity. Clearly, the output from the CM mixture is considerably more stable than the organic dye-doped mixture. The initial increase in output has been noted before [10] and may be attributed to a decrease in the local molecular oxygen concentration around the emissive clusters during the first few minutes of irradiation in the LC host matrix.

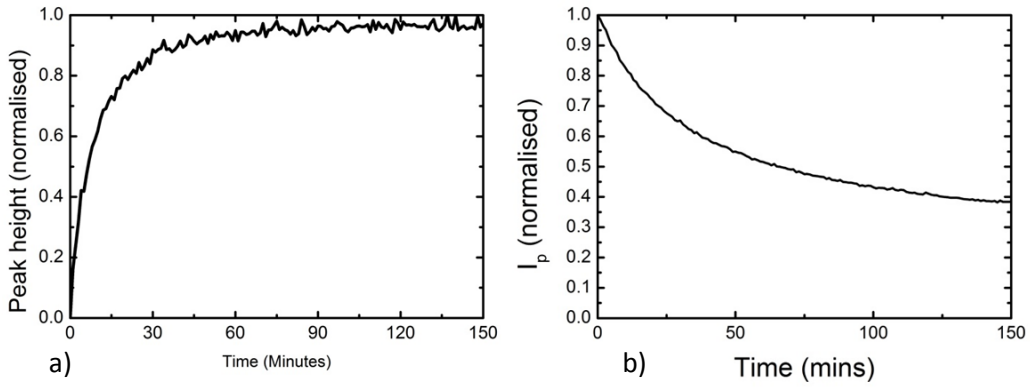

Figure 7 – Time dependence of the photoluminescence intensity when optically excited at 365 nm at room temperature for a period of 150 minutes for a) the clustomesogen (20 wt%) in a nematic liquid crystal and b) fluorescent dye (DCM, 1wt%) doped into the same nematic LC. Results taken at 20°C in 9 µm-thick cells.

6.3 – Clustomesogens dispersed into chiral nematic liquid crystals

After studying the CMs in nematic LCs, the CMs were dispersed into chiral nematic LCs to study the effect of the chiral nematic LC photonic band-gap on the CM emission.

A chiral nematic mixture was made using the nematic ZLI-1840 ($\Delta\varepsilon$ = 0.15, nematic-isotropic transition = 95.6 °C). This nematic was used because it does not absorb at the same (UV) wavelengths as the CMs (where they should be optically pumped). The high twisting power chiral dopant BDH1281 was added at a concentration such that the photonic band-gap was centred at the PL peak of the CM (~660 nm). The chiral nematic LC used contained 2.2 wt% BDH1281 and 20 wt% $Trisel_2[Mo_6I_8(OCOC_2F_5)_6]$ in ZLI-1840 (long band-edge ~710 nm, T_{iso}=95.6^{0}C). This was mixed by heating the mixture to above 100°C for 24 hours. The CM dispersed well into this mixture with no visible aggregation, as can be seen in the optical polarising microscopy image of the mixture filled into a 9 µm-thick glass cell; this is shown in Fig 8.

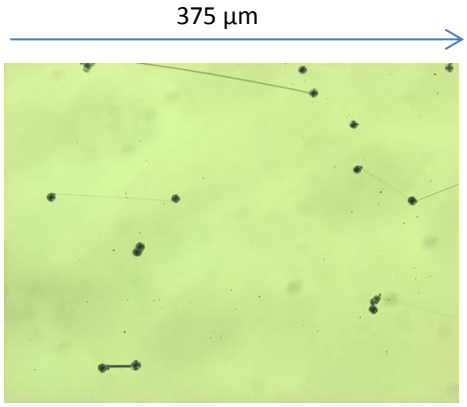

Figure 8 – Optical polarising microscope image of a chiral nematic liquid crystal/clustomesogen (20 wt%) mixture in a 9 µm-thick glass cell. The black dots are spacer beads used to define the cell thickness. The lines are oily streak defects. Results taken at 20°C.

To use these materials as lasers, I optically pumped the cells in an attempt to excite them and induce laser emission. Some enhanced emission was seen at the edges of the band-gap of the LC, however, no clear evidence of lasing was seen. This could be because it is phosphorescence (whereby the electron loses energy accompanied by a change in spin) rather than fluorescence (where there is no change in spin and angular momentum is conserved). However, given that molybdenum has not been used for other types of lasers at these wavelengths (only x-ray lasers have been shown using molybdenum for gain) this may indicate that they are not fundamentally suitable. Further work to decipher the PL and photophysical properties may help to identify the reason they are not currently suitable for lasing. Additional difficulties were caused by the CM absorbing in the UV, and the high intensity UV pump source damaged the LCs.

Thus, to use these materials as the gain materials in lasers, it is likely that more complex devices will be necessary – such as Q-switched lasers or defect mode lasers; this will be discussed in more detail in the Future Work section.

Although our devices did not exhibit lasing, they were still highly emissive. Furthermore, because the chiral nematic photonic band-gap selectively reflects one handedness of circularly polarised light, the CM emission was polarised. Thus, I investigated the potential for using our devices as polarised light sources.

6.4 – Polarised light sources based on liquid crystal materials

Polarised light sources are of interest because active optical devices that combine a light source, colour generation and polarisation control into a single element have potential applications ranging from displays [28] to quantum optics [29] and optical information processing [30]. For example, a polarised light source would be of significant benefit to the LC display industry where polarised light is typically generated using a combination of an unpolarised white light source and linear absorptive polarisers, which results in losses and increases energy consumption. Quantum cryptography can use different polarisation states of light to give different quantum representations of zero and one [30]. Consequently, a means of generating polarised light that could be tuned to give different polarisation states offer great advantages towards a number of photonic technologies.

Previous work has considered generating linearly polarised light using electroluminescent LC polymers that are aligned in one particular orientation [31] in addition to species dispersed into nematic LCs (such as organic fluorescent dyes

exploiting the dye-guest host effect [30, 32] and inorganic emitters like lanthanide-complexes [33]). However, there are many applications for which circularly polarised light would be advantageous, including quantum cryptography [29] and 3-dimensional autostereoscopic displays [30]. Furthermore, the transmission-voltage curves for LC display devices have been found to be steeper when circularly polarised light is used instead of linearly polarised light [34].

Circularly polarised emission has been demonstrated using luminescent conjugated LC polymers [35-36] and metallomesogens [37-38]. Also, much work has focussed upon doping fluorophores into the chiral nematic LC because when the photonic band gap of the chiral nematic overlaps the emission spectrum of a fluorophore, the emission is dominated by a specific circular polarisation determined by the rotation sense of the helix. The ease with which the chiral nematic photonic band-gap can be controlled externally using electric fields, offers large potential for altering the polarisation properties of the emitted light in-situ. A variety of fluorophores have been combined with such LCs, including organic materials like fluorescent dyes [39] and inorganic species such as lanthanides [38] and quantum dots [20-24].

However, the fluorophores that have previously been combined with LCs to create polarised light sources all have drawbacks – organic dyes are highly susceptible to photo-bleaching [39], curtailing their usefulness when illuminated continuously; inorganic compounds such as quantum dots are typically restricted to very low concentrations by weight in the LC host [21] or require complex preparation procedures [22] and they typically exhibit low quantum efficiencies; alternative inorganic structures such as metallomesogens generally exhibit mesophase transition temperatures that are significantly greater than room temperature and they have poor thermal stabilities which makes them less applicable to devices [37].

Transition metal CMs avoid these limitations. As previously discussed, they are photostable to continuous illumination, may be dispersed at high wt% into other LC materials without any complex functionalisation procedure, their mesophases exist at room temperature and they have high quantum efficiencies.

6.5 – Polarised light sources using clustomesogen materials

For our work, I illuminated our samples with a 365 nm LED and detected the circular polarisation of the output using a combination of a zero-order quarter wave-plate and a Glan-Thompson polariser at the output of the LC/CM device. The transmission spectra

for both left and right circularly polarised output when illuminated with white light are shown in Fig 9, demonstrating that the band-gap only occurs for right circularly polarised light (as would be expected as it has a right-handed helicoidal structure).

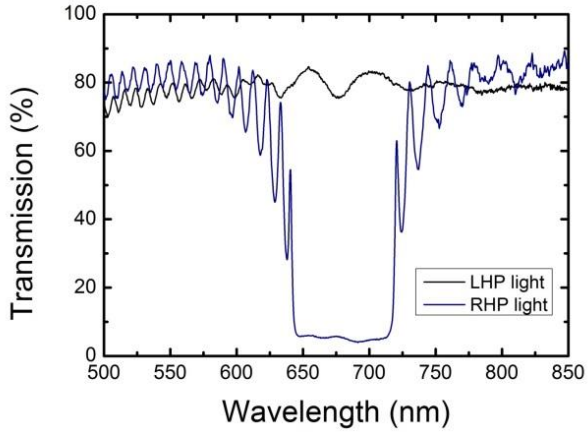

Figure 9 – Left (LHP) and right handed-polarised (RHP) light measured at the output of a chiral nematic liquid crystal/clustomesogen device illuminated with a white light source. Results taken at 20°C in 9 µm-thick anti-parallel, planar-aligned glass cells.

Fig 10a shows the transmission spectrum when illuminated with a white light source overlaid onto the right-handed PL when illuminated with a 365 nm LED; this clearly shows that the modification of the PL is caused by the chiral nematic LC photonic band-gap. The left and right circularly polarised emission when pumped with a 365 nm LED are shown in Fig 10b; the left-handed emission resembles that of the CM in a nematic, however, the right-handed polarised emission exhibits a clear modification of the PL spectrum – the band-gap can be seen and there is PL enhancement at the band-edges.

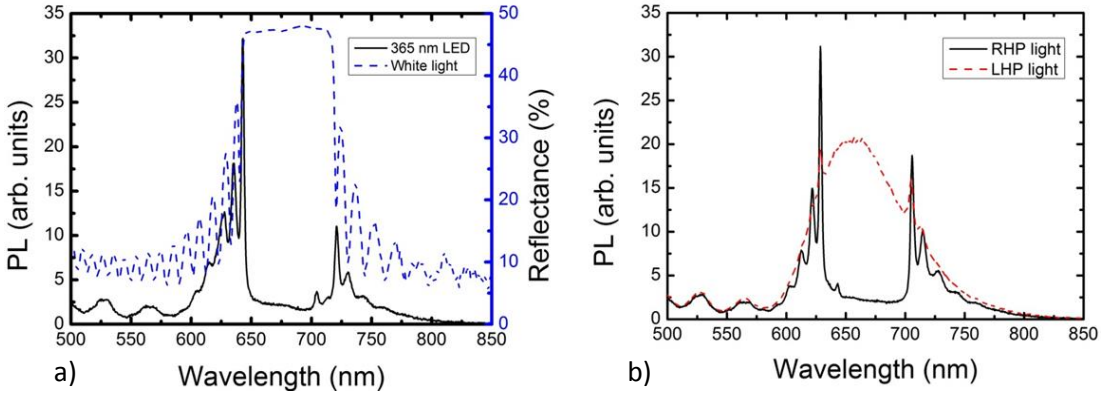

Figure 10 – a) the clustomesogen-chiral nematic mixture photoluminescence of left circularly polarised light when illuminated by an LED (black line) and a white light source (blue dashed); b) the effect of the chiral nematic photonic band gap (black line) on the clustomesogen photoluminescence (red dashed line) under illumination by a 365 nm LED. Results taken at 20°C in 9 µm-thick anti-parallel, planar-aligned glass cells.

To quantify the degree of circular polarisation of the emitted light, I use the dissymmetry factor. The dissymmetry factor, g_e, is a measure of the degree of circular polarisation of the emitted light [11]. It is defined as:

$$g_e = 2\frac{\left(I_L(\lambda) - I_R(\lambda)\right)}{\left(I_L(\lambda) + I_R(\lambda)\right)}, \tag{6.1}$$

where I_L and I_R are the intensity of the left- and right-handed circularly polarised emission. g_e is wavelength dependent and varies from 0 (no circular polarisation of emission) to ±2 (complete left- or right-handed circularly polarised emission).

I have plotted the dissymmetry factor, g_e, calculated using the data from Figure 10 and Equation 1. This dissymmetry factor is shown in Fig 11 for a mixture filled into a 9 µm cell. g_e rises sharply to large positive values inside the band gap where the emission consists of a large proportion of left circularly polarised light (i.e., $I_L >> I_R$). Conversely, at the band-edges, the emission is mainly right circularly polarised light – there is fluorescent enhancement of right polarised light due to the large density of photon states. Outside of the band-gap, g_e oscillates between positive and negative values due to the variation in the density of photon states outside the photonic band-gap. At some point the enhancement of photoluminescence at the band-edges means that there the right-handed photoluminescence is actually higher than the base photoluminescence of the material. This oscillation of the handedness of the light means that the dissymmetry factor also oscillates. In the band-gap right-handed light is reflected resulting in much lower photoluminescence within the band-gap. Consequently, the dissymmetry factor is positive in this region.

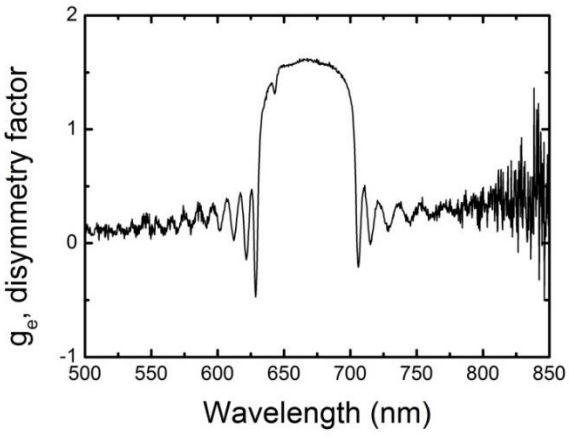

Figure 11 – The dissymmetry factor of the chiral nematic-clustomesogen mixture. Results taken at 20°C in 9 µm-thick anti-parallel, planar-aligned glass cells.

As shown in Fig 6, there is no dye-guest host effect between the nematic LC and the CM, g_e can be entirely ascribed to the photonic band structure of the chiral LC and not from any preferential alignment of the CM in the LC. The maximum value of g_e ~1.6 for CM-chiral nematic mixture is comparable or better than many literature values for other materials which vary from 0.3 for metallogen-based compounds [38] to ~1.8 for fluorescent LC polymers [36], and as previously discussed does not suffer from the disadvantages of these materials.

The value for g_e varies slightly with cell thickness, as shown in Fig 12 – the thicker the cell, the greater the dissymmetry factor. The 100% reflection of one handedness of circularly polarised light assumes an infinitely thick chiral nematic LC, so I would expect that the thicker the cell, the closer to 100% reflection for one handedness of light, and so the better the dissymmetry factor. The thickness dependence of the dissymmetry factor has been noted by Chen, et al. [30] where a similar effect was seen.

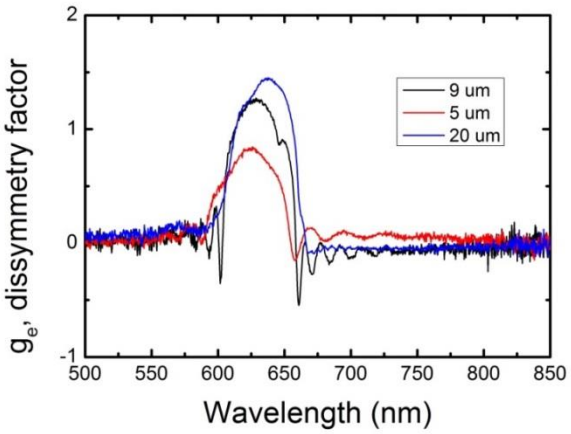

Figure 12 – The dissymmetry factor, g_e, for the same chiral nematic/clustomesogen mixture filled into anti-parallel, planar-aligned cells with different thicknesses. Results taken at 20°C.

6.6 – Effect of changing the photonic band-gap position on clustomesogen emission properties

After studying the polarisation properties when the photonic band-gap was centred at the photoluminescence maximum (~660 nm), I subsequently made chiral nematic/CM mixtures with photonic band-gaps at different wavelength positions. For this work, the nematic LC E7 was used with the high twisting-power chiral dopant BDH1281 dispersed into it. The different chiral dopant concentrations result in different chiral nematic pitches, and so different photonic band-gap position. The resulting photonic band-gaps of the four mixtures are shown in Fig 13. There is a mixture with the long

band-edge near the PL peak (660 nm), one with the band centre ~660 nm, one with the short-band-edge at 660 nm and one with the photonic band-gap entirely to the right of the CM PL. The mixtures contained 20 wt% CM ($Trisel_2[Mo_6I_8(OCOC_3F_7)_6]$), and 2.3, 2.8, 3.5 and 3.9 wt% BDH1281 (more BDH1281 yields a more blue-shifted photonic band-gap). These were mixed by heating the mixture to above 70°C for 24 hours.

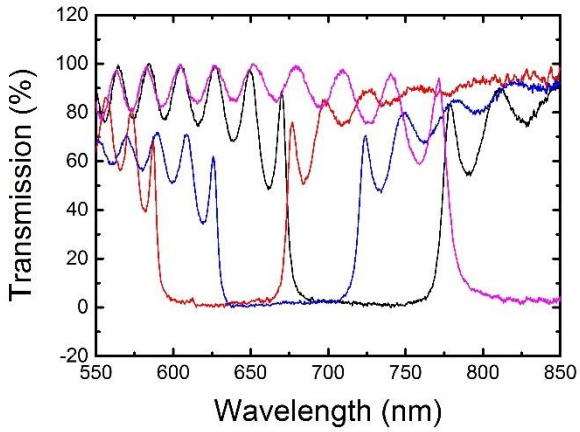

Figure 13 – The transmission spectra of four different chiral nematic mixtures with different pitch values. Red – long band-edge at ~660 nm; blue – band centre at ~660 nm; black – short band-edge at ~660 nm; pink – photonic band-gap outside of the photoluminescence range (short band-edge~720 nm). Results taken at 20°C in 9 µm-thick anti-parallel, planar-aligned glass cells.

Fig 14 shows optical polarising microscopy images of the mixtures filled into 5 µm planar-aligned glass cells. As would be expected, there are differences in colour depending on the pitch of the helix (and consequently the spectral location of the photonic band.

Fig 15 shows the PL of the devices when they were illuminated with 365 nm illumination overlaid with the transmission spectra for the different mixtures. Clearly the spectral location of the photonic band-gap directly influences the resulting photoluminescence spectrum – it occurs at 660 nm when the photonic band-gap falls outside the PL range (Fig 15a) or at the position of the band-edges when these overlap the PL-range (670 nm in 15b and c, and 625 nm for 15d).This shows that the PL emission can be controlled by changing the chiral nematic pitch values (and hence the photonic band-gap position).

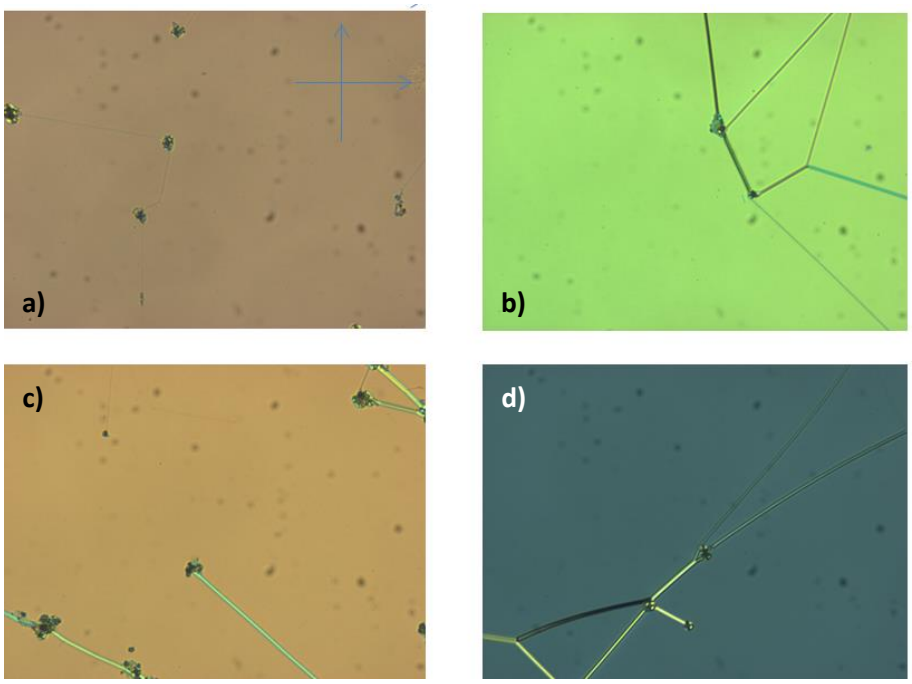

Figure 14 – Optical polarising microscopy images of different chiral nematic/clustomesogen (20 wt%) mixtures with different pitch values. Red – long band-edge at ~660 nm; blue – band centre at ~660 nm; black – short band-edge at ~660 nm; pink – photonic band-gap outside of the photoluminescence range (short band-edge~720 nm). Results taken at 20°C in 9 µm-thick glass cells.

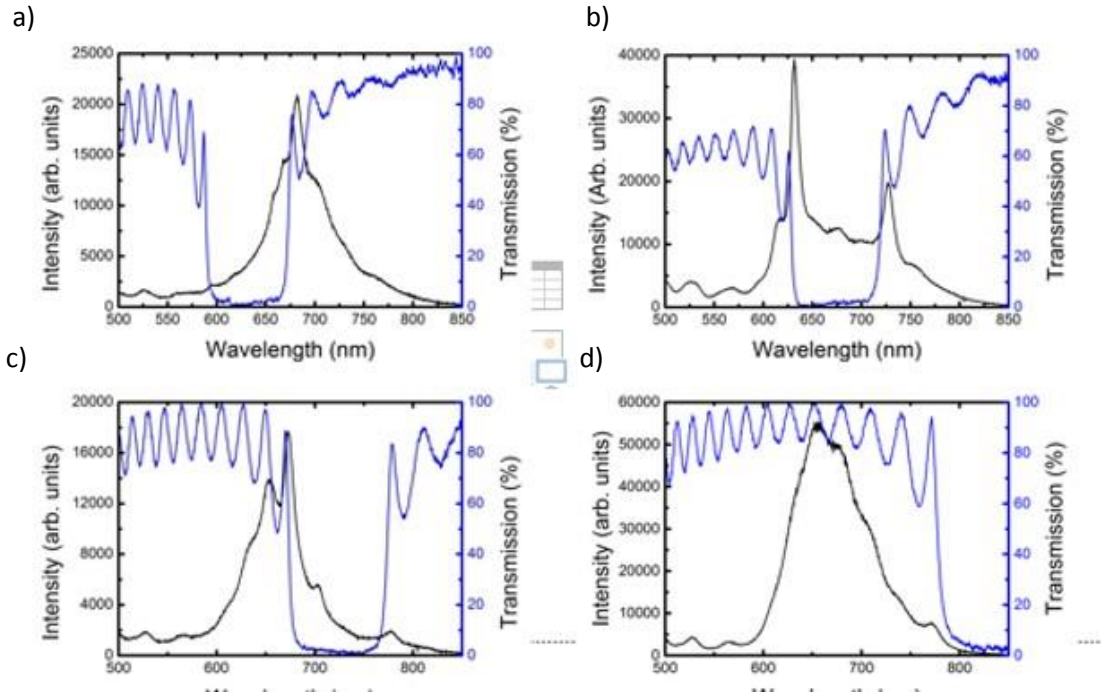

Figure 15 – Emission spectra of different chiral nematic/clustomesogen mixtures of four different chiral nematic mixtures with different pitch values overlaid onto their transmission spectra. a) – long band-edge at ~660 nm; b) – band centre at ~660 nm; c) – short band-edge at ~660 nm; d) – photonic band-gap outside of the photoluminescence range (short band-edge~720 nm). Results taken at 20°C in 9 µm-thick glass cells.

6.7 – Electrical control of emission polarisation

In the previous section, I demonstrated that a circularly polarised light source could be created by matching the spectral location of the photonic band-gap to the PL maximum

of the CM. In this section, I will demonstrate that this strong degree of polarisation can be controlled and even switched off by applying an electric field. This has potential applications in quantum optics, which requires polarised light sources, and displays where light is polarised using a polariser which wastes 50% of the light passing through it and so reduces device efficiency.

By applying an external electric field to the device described above, the planar Grandjean alignment is lost as the LC undergoes a chiral nematic-nematic transition as the helix is disrupted. The helicoidal structure is removed and so too is the photonic band-gap for visible light. This is shown in Fig 16a where g_e diminishes as the electric field is increased. Between E = 0.6 and 1 Vμm^{-1} the oscillating features at the band-edge are lost but the band-gap is maintained and g_e remains positive across the wavelength region probed. At an electric field of E = 1.3 Vμm^{-1} the band-gap is completely lost and $g_e \sim 0$ – the emission no longer shows any circular polarisation. Fig 17b shows the change in g_e at a fixed wavelength (λ = 670 nm), demonstrating that the dissymmetry decreases continuously as the electric field increases. This corresponds to a change from left circularly polarised light to unpolarised light.

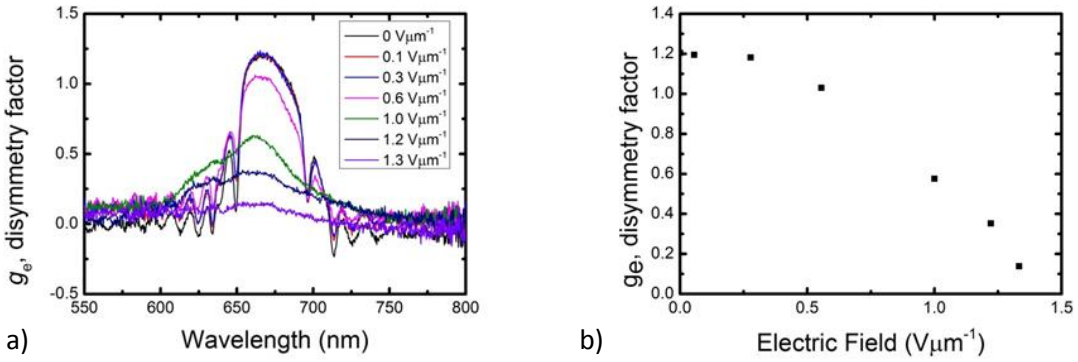

Figure 16 – a) The change in dissymmetry factor on application of an electric-field; b) the change in dissymmetry factor at a fixed photoluminescence wavelength (670 nm).

6.8 - Conclusions

In this chapter, I have presented results on transition metal CM materials that can be combined with chiral nematic LCs to act as active and photo-stable circularly polarised luminescent devices with polarisation properties that may be manipulated in-situ by influencing the LC host, such as with electric-fields. This combination of materials offers potential for next generation light sources – including single photon sources and low-threshold lasers.

I have performed work to disperse CM materials into nematic LCs to determine the maximum concentration that will disperse. The absorption/emission properties of these mixes were then studied. Subsequently, the materials were dispersed into chiral nematic LCs and this resulted in circularly polarised light sources. The effect of changing the photonic band-gap position on the emission was also studied. Finally, electric fields were investigated as a means for controlling the degree of polarisation of the CM polarisation.

Although the work to use them as gain materials in LC lasers was unsuccessful, they exhibit a great deal of potential, as will be discussed in the Future Work section. Inorganic-organic perovskites are other potential gain materials – they have suitable photoluminescence properties (such as tuneable emission and high quantum yields) as well as potential for electrical pumping. However, unlike CMs, perovskites cannot simply be dispersed into LCs. Chapter 7 will detail work to design and make layered LC/perovskite structures and to create distributed feedback lasers using perovskites as the gain materials.

6.9 – References

1. Y. Molard, F. Dorson, V. Cîrcu, T. Roisnel, F. Artzner, S. Cordier, *Angew. Chem. Int. Ed. Engl.*, 2010, **49**, 19.
2. M. Amela-Cortes, A. Garreau, S. Cordier, E. Faulques, J.-L. Duvail, Y. Molard, *J. Mater. Chem. C*, 2014, **2**, 8.
3. Y. Molard, A. Ledneva, M. Amela-Cortes, V. Cîrcu, N. G. Naumov, C. Mériadec, F. Artzner, S. Cordier, *Chem. Mater.*, 2011, **23**, 5122.
4. Y. Molard, F. Dorson, V. Cîrcu, T. Roisnel, F. Artzner, and S. Cordier, *Angew. Chem. Int. Ed. Engl.*, 2010, **49**, 3351.
5. M. A. Cortes, F. Dorson, M. Prévôt, A. Ghoufi, B. Fontaine, F. Goujon, R. Gautier, V. Cîrcu, C. Mériadec, F. Artzner, H. Folliot, S. Cordier, Y. Molard, *Chemistry*, 2014, **20**, 28.
6. K. Kirakci, P. Kubát, J. Langmaier, T. Polívka, M. Fuciman, K. Fejfarová, K. Lang, *Dalton Trans.*, 2013, **42**, 19.
7. M. Prevot, M. Amela-Cortes, S. K. Manna, R. Lefort, S. Cordier, H. Folliot, L. Dupont, Y. Molard., *Adv. Funct. Mater.*, 2015, **25**, 4966.
8. M. N. Sokolov, M. A. Mihailov, E. V. Peresypkina, K. A. Brylev, N. Kitamura, V. P. Fedin, *Dalton Transactions*, 2011, **40**, 6375.
9. K. Kirakci, P. Kubát, J. Langmaier, T. Polívka, M. Fuciman, K. Fejfarová, and K. Lang, *Dalton Trans.*, 2013, **42**, 7224.
10. M. Amela-Cortes, S. Cordier, N. G. Naumov, C. Meriadec, F. Artzner, Y. Molard. *J. Mat. Chem. C.*, 2014, **2**, 46.
11. H. Shi, B. M. Conger, D. Katsis, S. H. Chen, *Liq. Cryst.*, 1998, **24**, 2.
12. M. Prévôt, M. Amela-Cortes, S. K. Manna, S. Cordier, T. Roisnel, H. Folliot, L. Dupont, Y. Molard, *J. Mater. Chem. C*, 2015, **3**, 5152.
13. S. K. Nayak, M. Amela-Cortes, C. Roiland, S. Cordier, Y. Molard, *Chem. Commun.*, 2015, **51**, 3774.
14. T. H. Maiman, R. H. Hoskins, I. J. D'Haenens, C. K. Asawa, V. Evtuhov, *Phys. Rev.*, 1961, **123**, 1151.
15. S. J. Hooker and S. Webb, Laser Physics, First edition (2012), OUP, page 132.
16. S. J. Hooker and S. Webb, Laser Physics, First edition (2012), OUP, page 267.
17. S. J. Hooker and S. Webb, Laser Physics, First edition (2012), OUP, page 226.
18. S. J. Hooker and S. Webb, Laser Physics, First edition (2012), OUP, Chapter 9.
19. N. N. Ledentsov, *Semicond. Sci. Technol.*, 2011, **26**, 014001.

20. M. Fox, Optical properties of solids, 2nd ed. (2012), OUP, pp 67-75
21. A. Y. Bobrovsky, N. I. Boiko, V. P. Shibaev, J. H. Wendorff, *Adv. Mater.*, 2003, 15, 4.
22. A. Bobrovsky, K. Mochalov, V. Oleinikov, V. Shibaev, *Liq. Cryst.*, 2011, 38**,** 6.
23. A. L. Rodarte, C. Gray, L. S. Hirst, S. Ghosh, *Phys. Rev. B*, 2012, **85**, 3.
24. A. Bobrovsky, K. Mochalov, V. Oleinikov, A. Sukhanova, A. Prudnikau, M. Artemyev, V. Shibaev, I. Nabiev, *Adv. Mater.*, 2012, **24**, 46.
25. A. L. Rodarte, R. J. Pandolfi, S. Ghosh, and L. S. Hirst, *J. Mater. Chem. C*, 2013, **1**, 5527.
26. S. L. Bondarev, V. N. Knyukshto, V. I. Stepuro, A. P. Stupak, and A. A. Turban, J. Appl. Spectrosc., 2004, 71, 194.
27. A. L. Rodarte, F. Cisneros, J.E. Hein, S. Ghosh and L.S. Hirst, *Photonics*, 2015, **2**, 855.
28. K.-H. Kim and J.-K. Song, *NPG Asia Mater.*, 2009, **1**, 1
29. S. G. Lukishova, L. J. Bissell, C. R. Stroud, R. W. Boyd, *Opt. Spectrosc.*, 2010, **108**, 3.
30. S. H. Chen, D. Katsis, A. W. Schmid, J. C. Mastrangelo, T. Tsutsui, T. N. Blanton, *Nature*, 1999, **397**, 6719
31. M. Grell, W. Knoll, D. Lupo, A. Meisel, T. Miteva, D. Neher, H.-G. Nothofer, U. Scherf, A. Yasuda, *Adv. Mater.*, 1999, **11**, 671.
32. R. Porras Aguilar, J. C. Ramirez-San-Juan, O. Baldovino-Pantaleon, D. May-Arrioja, M. L. Arroyo Carrasco, M. D. Iturbe-Castillo, D. Sánchez-de-la-Llave, R. Ramos-Garcia, *Opt. Express*, 2009, **17**, 5.
33. K. Driesen, C. Vaes, T. Cardinaels, K. Goossens, C. Görller-Walrand, K. Binnemans, *J. Phys. Chem. B*, 2009, **110**, 10575.
34. M. Schadt, *Annu. Rev. Mater. Sci.* 1997, **27**, 305.
35. B. A. San Jose, S. Matsushita, K. Akagi, *J. Am. Chem. Soc.*, 2012, **134**, 48.
36. B. A. San Jose, J. Yan, K. Akagi, *Angew. Chem. Int. Ed. Engl.*, 2014, **53**, 40.
37. K. Binnemans, *J. Mater. Chem.*, 2009, 19, 448.
38. S. Petoud, G. Muller, E. G. Moore, J. Xu, J. Sokolnicki, J. P. Riehl, U. N. Le, S. M. Cohen, K. N. Raymond, *J. Am. Chem. Soc.*, 2007, 129, 1.
39. F. J. Duarte, L. W. Hillman, Dye lasers and their applications, 1990, Academic Press, Inc., p10-11.

Chapter 7 – Amplified emission sources based on inorganic-organic perovskite films

The previous Chapter described transition metal clustomesogens and their potential as gain materials in liquid crystal (LC) lasers. There, I detailed work to disperse the clustomesogens into LCs and to probe their photoluminescence properties. By dispersing them into chiral nematic LCs it was possible to control their emission properties. Although the fluorescence enhancement at the band-edges was not sufficient to result in lasing, the photonic band-gap still supressed the emission of one handedness of light. This meant that it was possible to use clustomesogens as polarised light sources.

In this Chapter, I consider a different potential gain material for lasers – inorganic-organic perovskites. These are exciting materials due to their promising emissive properties (high efficiencies, broad range of potential emission wavelengths) and because they offer a potential route towards electrically pumped hybrid organic-inorganic lasers.

Unlike the clustomesogens described in Chapter 6, or the fluorescent dyes used in conventional LC lasers, perovskites materials cannot be easily dispersed into organic solvents such as LCs. Thus, I investigated a variety of layered device structures. These include structures that use a layer of perovskite sandwiched between a 50% chiral nematic reflector and a gold reflector. This device exhibited enhanced amplified spontaneous emission, a precursor to lasing. The amplified spontaneous emission threshold was further improved by using a flexible 80% LC reflector. In order to move further towards laser devices, I created devices consisting of a thin layer of perovskite between chiral nematic reflectors.

In the second part of this Chapter, I will describe work to use the photoluminescence properties of these perovskite materials in laser structures that do not involve LCs. Specifically, I create perovskite distributed feedback lasers by imprinting the perovskite with a grating pattern. These structures lase and the lasing wavelength may be tuned by changing the grating spacing. Here, I describe work to both create these lasers and to characterise them.

This work was performed in collaboration with Prof Henry Snaith's team from the Department of Physics at the University of Oxford and the research group of Prof. Albert Schenning from the University of Eindhoven.

7.1 – Introduction

7.1.1 – Inorganic-organic perovskites

The perovskite structure is that of a molecule with the same structure as $CaTiO_3$ (calcium titanium oxide) [1], as shown in Fig 1. The general formula is ABX_3 where A and B are cations and X is an anion. In this work, I use methylammonium lead halide perovskites. These have the structure $CH_3NH_3PbX_3$ where the cations are methylammonium ($A = CH_3NH_3^+$) and lead ($B = Pb^{2+}$) and the anion ($C = X^-$) is a halide, or mix of halide anions (iodide, bromide or chloride). These materials have recently been shown to offer a great deal of promise for next-generation photovoltaics [2-5]. This is because they are high performance absorbers with high efficiencies (up to 22.1% has been reported [5-6]) and they possess band-gaps that can be tuned across visible and near-infrared wavelengths (from 390-790 nm) by varying the chemical composition. For pure iodide perovskites ($CH_3NH_3PbI_3$), the emission peak occurs at 790 nm. This peak is blue-shifted when the iodide is replaced by bromide (pure $CH_3NH_3PbBr_3$ peak = 550 nm) and further still when it is replaced by chloride (pure $CH_3NH_3PbCl_3$ peak = 390 nm) due to the differing sizes of the anions; intermediate wavelengths may be achieved with 'mixed-halide' perovskites containing a mix of different anions.

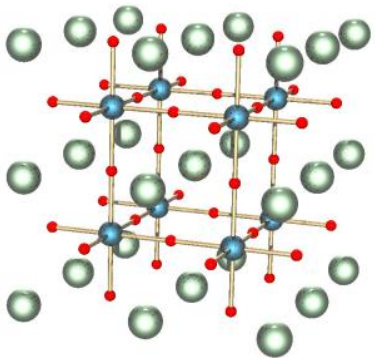

Figure 1 – The perovskite structure. Red spheres are cations ($CH_3NH_3^+$); blue spheres are lead (II) cations (Pb^{2+}); green spheres are halide anions (Cl^-, Br^- or I^-) in the materials used in this work. Image reproduced from Reference 7.

7.1.2 – Deposition of perovskites

These inorganic-organic perovskites may be deposited by a variety of different methods, including solution-based growth of large single-crystal perovskites [6-7], spin-coating [8], vapour deposition [9] and evaporation [10], all of which will be described in more detail below. The flexibility of manufacture is another major reason that perovskite materials are considered here. These techniques will be described further in Section 7.2.

7.1.3 – Perovskite emission properties

These perovskite materials have attracted particular interest for photovoltaic applications due to the rapid improvements that have been seen in their efficiencies (which have increased from 6.5% in 2012 to 22.1% reported in 2016 [12]). However, many of the properties of these perovskites that make them exciting materials for photovoltaic applications are also important for emissive devices. The perovskites have high absorption cross-sections (10^4 cm^{-1} [13]) which is higher than materials such as gallium arsenide (a semiconductor material that is used in current high-performance commercial photonic devices). Perovskites have high carrier mobilities (greater than 10 $cm^2V^{-1}s^{-1}$ [14]) and so they offer potential for high brightness emission even at low driving voltages. Additionally, they have sharp electronic band-gaps. Perovskite materials can be created with minimal charge-trapping defects which improves the efficiency of radiative recombination. This, when coupled with the fact that non-radiative pathways are unfavourable, results in high photoluminescent quantum yields (up to 70% have been reported [15]). In addition, because they are semiconductors, they offer potential for electrical pumping, something which has been demonstrated in a variety of light emitting diode devices [16-17], and which would be of great utility in a laser device if it could be shown. This would be particularly exciting for LC lasers, where one of the major limitations is the requirement for optical pumping – a LC laser requires another light source – often a laser – as the pump source.

7.1.4 – Using perovskites in emissive devices

The first work to create emissive devices from perovskites involved 2D perovskites (which had larger organic cations than the methylammonium cations used in this work). These were reported to exhibit electroluminescence [19-20] at cryogenic temperatures and they were used to create light emitting diodes (LEDs) [20-21]. More recently, the materials used in this Thesis have been used to create LEDs and these have been shown to have improved photoluminescence properties [22] compared to the early work.

When I began this work, there were no reports of lasers which used these perovskites for gain. However, subsequently there has been a great deal of research that has been reported during and after the work I describe here. Much work has also been performed towards using these perovskites as the gain materials in laser devices. There have been many reports [22, 25, 28-30] of optically pumped amplified spontaneous emission (ASE) with values of the ASE threshold ranging from 12 $\mu J/cm^2$ with 150-ns excitation [22] to 60 $\mu J/cm^2$ with 2-ns excitation [25]. These initial values compare favourably to

the leading values achieved using more established and well-studied materials such as semiconductor polymers, colloidal nano-platelets and colloidal quantum dots [28-30].

Lasing has also been reported in a variety of devices [11, 24-25, 31-36]. The first report of lasing in perovskites was in work where a thin film of perovskite was sandwiched between a Bragg reflector and a highly reflective gold mirror; the resulting device lased when optically pumped with 400-ps green light [11]. Lasing from the inorganic-organic perovskite materials described here were subsequently demonstrated in a whispering gallery mode resonator both in spherical resonators where optical modes were guided around a circumference of a circular resonator [25], and in planar device that used perovskite nano-platelets that were grown by chemical vapour deposition [13]; similar devices were also created using solution processed micro-disks of perovskites [31]. Nanowires of perovskite have been grown and used to create lasers [32-35]. Finally, by using disordered perovskite thin films, random lasing has been demonstrated from a perovskite [24, 36]. However, no single mode laser which used the perovskites described here had been reported prior to our work on distributed feedback lasers (described in section 7.3 in this Chapter).

7.2 – Enhanced amplified spontaneous emission of liquid crystal/perovskite structures

In this section, I will describe work to create a layered structure containing a chiral nematic LC reflector, a perovskite layer and a gold reflector. Unlike the transition metal clustomesogens or fluorescent dyes described previously, perovskites cannot be simply dispersed directly into LCs. This has led to us investigating the layered structures described here. I use chiral nematics as the reflector because it offers several advantages: a LC reflector can be fabricated to reflect a range of wavelengths by varying its material properties, there is great scope for wavelength-tuning the band-gap position in-situ, and by creating a pitch gradient across the LC there is potential to access a range of wavelengths simultaneously. The LC reflector can be made flexible (see Section 7.2.3) and by using two LC reflectors, an entirely solution processable device could be created.

This work was performed in collaboration with the Department of Physics, University of Oxford and the University of Eindhoven.

7.2.1 – Building a perovskite amplified spontaneous emission source with a chiral nematic liquid crystal reflector

The architecture of the first device I built is illustrated in Fig 2. This stack was composed of a chiral nematic LC reflector coated onto glass. This layer reflects one handedness of circularly polarised light – so it reflects 50% of unpolarised light. A buffer layer of Al_2O_3 was then deposited by atomic layer deposition to protect the LC from subsequent deposition steps. Vapour assisted solution processing was then used to deposit a perovskite layer as described below. The perovskite was then protected from both air and subsequent deposition steps by a spin-coated layer of the polymer PMMA (Poly-methyl methacrylate). Finally, a gold reflector was evaporated onto the top of the stack. The manufacture procedure is described in more detail later in this Section.

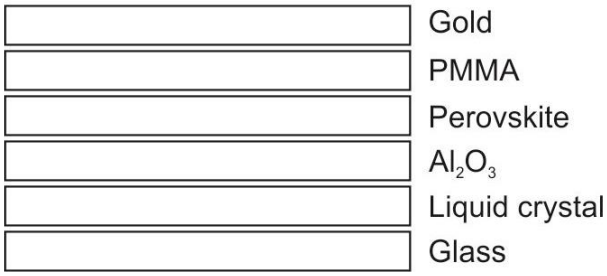

Figure 2 – A layered structure. A 50 nm-thick perovskite layer is sandwiched between a polymerised chiral nematic liquid crystal layer and a gold reflector. The polymer PMMA and Al_2O_3 are used as buffer layers.

To create the stacks illustrated in Fig 2, a ~7 μm layer of chiral nematic LC (with a band-gap centred at 780 nm and a pitch of ~500 nm) was deposited onto a glass substrate. This step was performed by our collaborators from the University of Eindhoven. To create an alignment layer, a polyimide solution was spin coated onto clean glass plates (5000 rpm, 30 s). This was photo-cured at 180°C for 45 minutes and the resulting polyimide was then rubbed with a velvet cloth to obtain the alignment layer. A mixture of the reactive mesogen RM257 (94.8 wt%, Merck), the chiral dopant LC-765 (3.2 wt%, BASF), the photo-initiator Irgacure 651 (1 wt%, Acrose) and a surfactant (1 wt%) was created. 1.1 wt% of this mixture was dissolved xylene and stirred for 1 hour at 40°C. This mixture was spin-coated onto the polyimide-coated glass (1000 rpm, 30 s). It was then photo-polymerised using UV light (7.5 $mWcm^{-2}$) for 5 minutes to yield a solid polymer film. The thickness was then checked using interferometry measurements and confirmed to be 7 ± 1 μm.

The chiral nematic LC band-gap was chosen to match the peak emission of the pure-iodide perovskite (780 nm) since I need the reflection band of the LC reflector to be

centred at the peak photoluminescence of the gain material. The tri-iodide perovskite was used because it has the highest photoluminescence quantum efficiency of the various perovskite halogen concentrations [37]. Fig 3 shows the transmission spectrum for the LC reflector overlaid onto the perovskite emission spectrum.

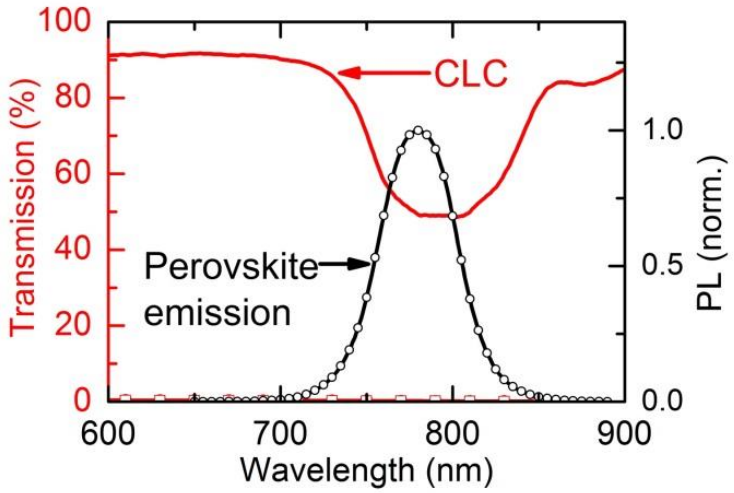

Figure 3 – The chiral nematic liquid crystal transmission spectrum (red line) overlaid onto the tri-iodide perovskite photoluminescence emission spectrum (black line).

Alumina (Al_2O_3) was deposited as a buffer layer by using atomic layer deposition. Atomic layer deposition is a technique in which gas phase precursors are applied to a substrate to build up thin films [38]. In this work, I used an in-house atomic layer deposition machine in the Department of Physics. Trimethylaluminium and water vapour were placed in separate gas chambers. Each chamber was pulsed in turn and evacuated in between. The trimethylaluminium chemisorbed to the substrate and the excess was removed by the vacuum pump. When water vapour was added, the trimethylaluminium methyl groups were replaced with oxygen. The system was purged and a monolayer of Al_2O_3 was formed. This was repeated to build up a layer of 170-nm thickness.

Depositing perovskite directly onto the LC layer yielded non-uniform films with reduced photoluminescence quantum efficiencies; furthermore, the alumina helped to protect the perovskite and prevent it degrading in air.

Transmission measurements and optical polarising microscopy were used to check that this deposition process did not damage the LC layer or alter its properties by checking both the optical texture on an optical polarising microscope and the photonic band-gap properties.

Vapour assisted solution processing was used to deposit a 50-nm thick layer of the tri-iodide perovskite [18] onto the alumina layer. Initially, lead iodide (PbI_2) was evaporated onto the substrate (50 nm). The substrate was then placed in a sealed container with methylammonium iodide powder and heated to 155°C for three hours to convert the PbI_2 into the perovskite. The substrates were then rinsed with isopropyl alcohol and annealed at 100°C for 30 minutes. Vapour assisted solution processing was used because the resulting perovskites generally exhibit a uniform grain structures (grain sizes up to micrometres) and 100% precursor transformation [17].

A 170 nm-thick layer of the polymer (PMMA) was then spin-coated on top to insulate the perovskite from air and moisture and so that it was not damaged by the evaporation of gold in the next step. The PMMA (10 mg/ml in chlorobenzene) was spin coated at 700 rpm for 30 s.

A gold back reflector was then evaporated onto the stack to reflect both the perovskite emission and the (laser) pump beam. This reflective layer allows a second pass of the pump beam through the stack and so increases the absorption of light in the perovskite layer.

Gold was chosen due to its reflectivity at the wavelength used her (780 nm) and because (unlike silver for example) it does not leach through the other layers. The gold was placed on a metal filament inside a vacuum chamber (at a pressure of 10^{-6} Torr). A current was passed through the filament to heat up the gold to evaporate it. The evaporated gold then hit the substrate and condensed to form a film. In this case, a 75-nm thick film was built up at a rate of 0.1 nm/s using a Kurt J. Lesker Company NANO36 evaporator.

A scanning electron microscope image confirming the cross-section structure of the full device stack is shown in Fig 4 where the different layers can clearly be seen. An SEM produces an image of a sample by scanning it with a focussed beam of electrons [50]. The electrons in the beam interact with the sample in various ways – they can be reflected by elastic scattering, they can cause emission of secondary electrons by inelastic scattering, or they can cause emission of electromagnetic radiation. These interactions can then be detected and used to create an image. In this work, our devices were coated with palladium and then imaged using a Hitachi S-4300 SEM.

In performing this work, I discovered that the alumina buffer layer also helped extend the photoluminescence lifetime and increased the photoluminescence quantum efficiency (PLQE) of the perovskite deposited upon it.

The PLQE is a measure of the number of photons emitted per absorbed photon. For a given material, the higher the PLQE, the greater its emission for a given excitation [29]. However, it is difficult to determine for thin films due to the complexity of measuring the angular distribution of emission, reflectivity and absorbance.

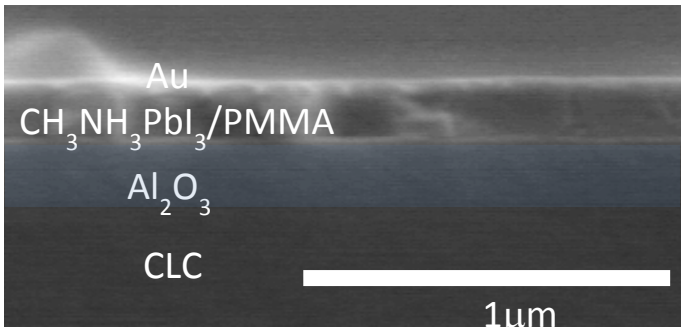

Figure 4 –A scanning electron microscope cross-section image of the device structure. The alumina layer has been shaded for contrast.

Here, PLQE experiments were performed using a 532 nm continuous wave laser (Suwtech LDC-800, ~200 mW/cm^2 excitation power density) illuminating the sample in an integration sphere (Oriel Instruments 70682NS). The laser scatter and photoluminescence were then collected using a fiber-coupled spectrometer (Ocean Optics MayaPro) which had been calibrated using a spectral irradiance standard.

The laser light striking the sample is considered as two components – the incident laser beam striking the sample, and the diffuse laser light which strikes the sample after scattering from the integrating sphere walls. Initially, a laser is shone into an empty integrating sphere. Then the sample is placed inside but out of the direct beam path. Finally, it is placed in the direct beam path. The resulting spectra will have a laser peak (unabsorbed light) and a photoluminescence peak (light absorbed by the sample). From the areas under these two components, the PLQE can be calculated [39].

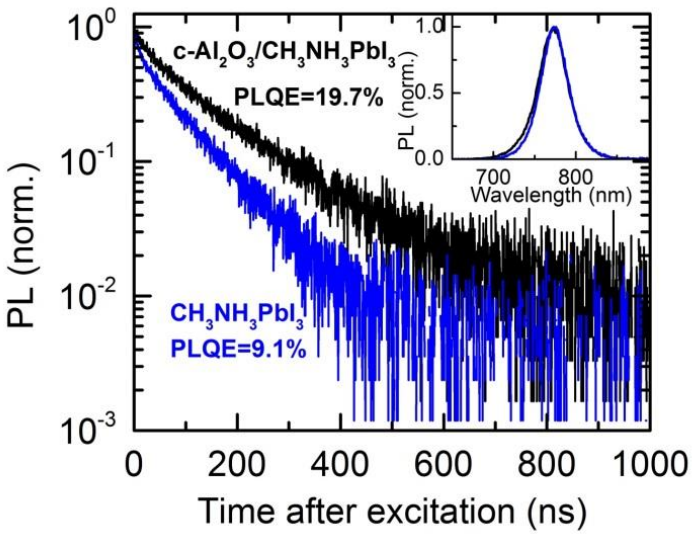

Figure 5 – Time resolved photoluminescence decays from perovskite coated onto neat glass (blue) and onto an alumina layer (black). Inset: the steady-state photoluminescence spectra of the samples.

The improvement in PLQE when an alumina buffer layer is used is shown in Fig 5. This improvement may be due to supressed luminescence quenching at the surface of the perovskite and because the alumina layer structures the perovskite surface and reduces surface defects. The alumina layer increased the photoluminescence quantum efficiency from 9.1 to 19.7%.

7.2.2 – Studying the cavity emission properties

To test the emission properties of the cavity, the device was pumped using a Q-switched laser and a nanosecond optical parametric oscillator (EKSPLA, NT340) operating at 530 nm with 4 ns pulses at a repetition rate of 10 Hz with a fluence of up to ~60 $\mu J/cm^2$/pulse. The spectrometer used was an Ocean Optics MayaPro spectrometer (1.8 nm full-width half-maximum resolution), fibre coupled with a 50 µm fibre and a 0.16 numerical aperture collection lens.

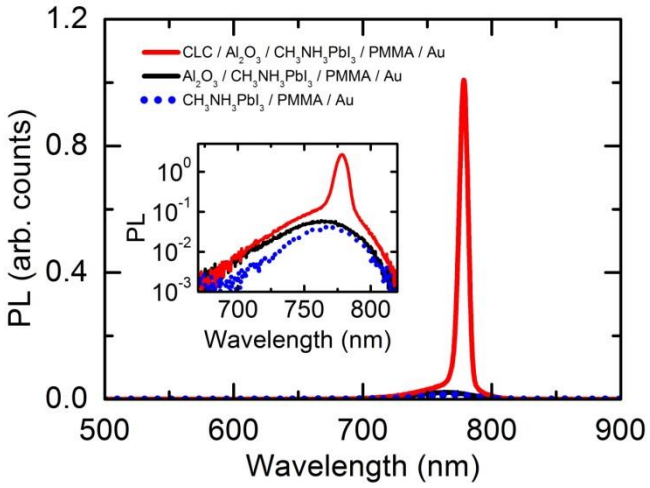

Figure 6 – Emission from the layered structure when optically pumped (red), compared to a stack without the liquid crystal reflector (black) and one without the liquid crystal reflector or the alumina layer (blue-dashed). The inset shows a zoomed-in version of the same data plotted on a log scale.

This resulted in enhanced emission, as shown in Fig 6 where the red line shows emission from our cavity. As a control, I also tested a stack with the same PLQE but without the LC layer (inset: black – with alumina, blue – without alumina) and these clearly showed only the perovskite photoluminescence, allowing us to attribute the narrowing to the presence of the chiral nematic LC reflector.

Next, the pump fluence dependence of the emission was studied at room temperature (20°C), as shown in Fig 7. Fig 7a shows the photoluminescence of the device at different pump fluences. At low fluences the emission is broad photoluminescence (full width half maximum ~40 nm) which collapses to ASE with a full-width at half-maximum of ~7 nm. Fig 7b shows the peak of the emission as a function of fluence. In this case, the threshold is measured as 15.3 μJ/cm^2/pulse. At high fluences, the emission intensity saturates and higher fluences do not yield any improvement in the emission. Again, the control stacks without the chiral nematic LC layer only exhibited photoluminescence even at the highest fluences (600 μJ/cm^2/pulse).

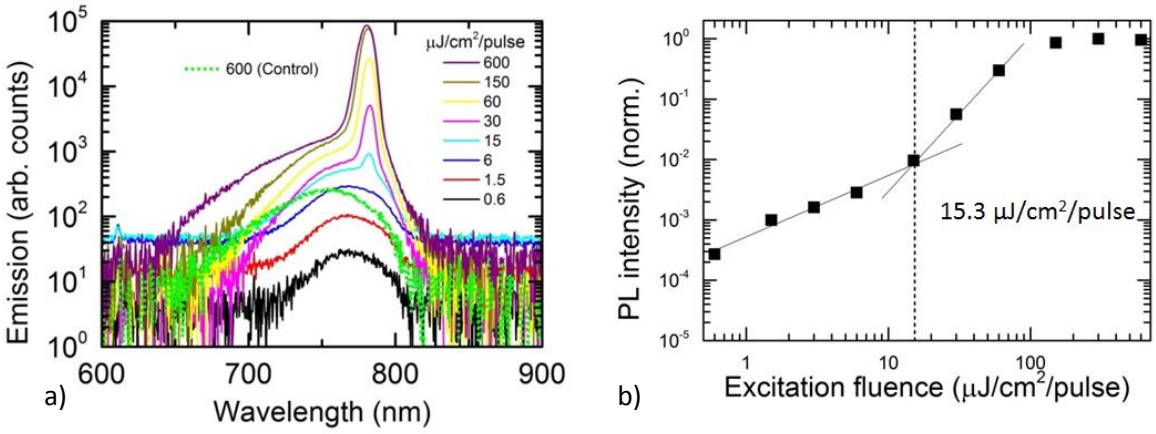

Figure 7 – a) Emission spectra of the layered structure when optical pumping at various excitations fluences at a temperature of 300 K. Emission from the control at the highest excitation fluence is also shown (green line); b) The photoluminescence intensity as a function of excitation fluence.

To investigate the temperature-dependence of the emission, I optically pumped the devices at a lower temperature (200 K) and measured the emission spectrum. I observed a narrowing of the photoluminescence line-widths with a slight red-shift and an increase in absolute emission intensity compared to the room temperature measurements; these results are shown in Fig 8. Furthermore, there is a lowering of the excitation threshold – the threshold for ASE occurs at 6.2 μJ/cm^2/pulse for the sample at 200 K (compared to a threshold of 15.3 μJ/cm^2/pulse for the sample at 300 K). This is consistent with previous work on perovskites where it was shown that the photoluminescence quantum efficiency increases at lower temperatures [40]; this is because the fluence of incident light is reduced by thermally activated atomic vacancies (caused by point defects in the perovskite) which 'trap' photons. At lower temperatures, fewer of these vacancies are activated and so the excitation fluence required is lower.

Our collaborators from the University of Cambridge (from the group of Prof. Richard Friend) performed measurements to study the temporal variation of the emission; these confirmed that our devices showed ASE and not laser emission. They studied this using a gated intensified CCD camera system (Andor iStar DH740 CCI-010) that was connected to a grating spectrometer (Andor SR303i). Femtosecond laser pulses from a homebuilt setup by second harmonic generation in a BBO crystal from the fundamental output (pulse energy 1.55 eV, pulse length 50 fs) of a Ti:Sapphire laser system (Spectra Physics Solstice) were used to excite the devices. The laser pulses generated had a photon energy of 2.3 eV and apulse length of 1 ns.

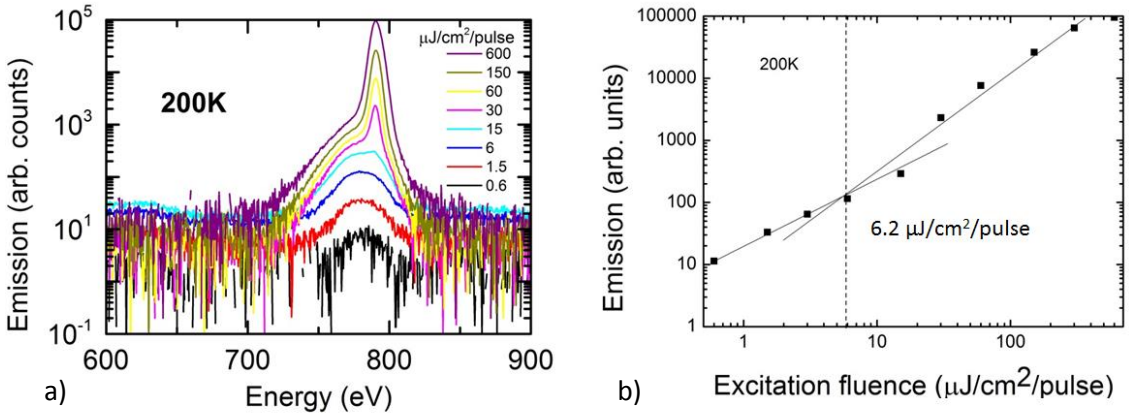

Figure 8 – a) Emission spectra of the layered structure when optical pumping at various excitations fluences at a temperature of 200K; b) The photoluminescence intensity as a function of excitation fluence.

Results from these experiments are shown in Fig 9. Fig 9a-c are snapshots (gate-length = 30 ns, scanning rate = 6 Hz) of the emission profile after pulsed excitation at 530 nm (100 fs pulses at a 1 kHz repetition rate) at various excitation fluences. Fig 9a shows results for a device pumped with an excitation fluence that is below the ASE threshold (12 μJ/cm^2/pulse) and the emission is broad and featureless. Fig 9b shows results for a device pumped with an excitation fluence close to the ASE threshold (19 μJ/cm^2/pulse); the peak at the red end of the spectrum evolves. Fig 9c shows the results for a device pumped with an excitation fluence above the ASE threshold (32 μJ/cm^2/pulse); here, the peak increases in intensity and red-shifts further. There are clear fluctuations in the distribution of modes over time – i.e., there is no sustainable laser emission.

Although I see ASE with a much lower threshold energy using a LC reflector, it is not sufficient for laser emission. There are a variety of potential reasons for this: our reflectors only reflect one handedness of circularly polarised light (so only 50% of unpolarised light), the perovskite field is still rapidly developing and both the materials and their deposition techniques are not fully optimised, our control over the layer thickness is not perfect – particularly when it comes to the perovskite thickness. Thus, to achieve true laser emission, the device stacks need to be refined. Our first refinement was to create stacks that combine the chiral nematic LC with a half wave-plate to yield a higher reflectivity substrate (~80% reflective for unpolarised light), as described in the next section.

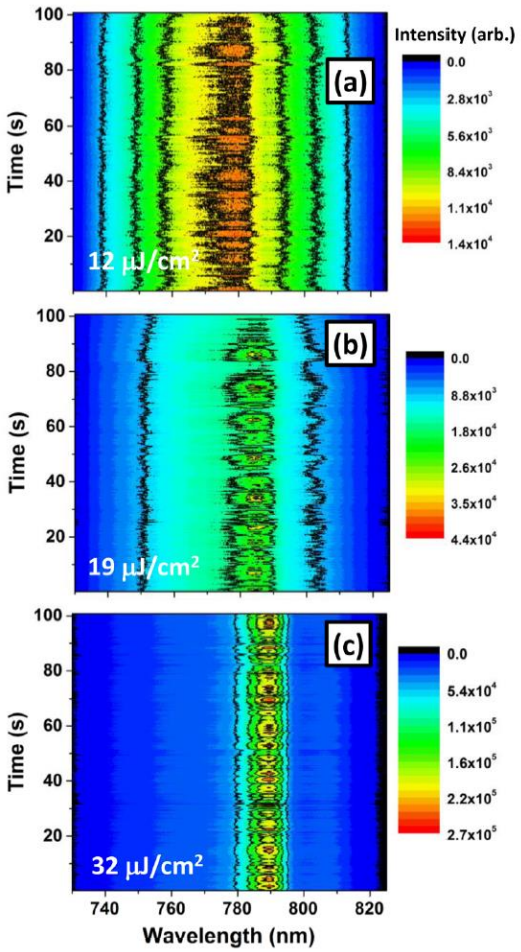

Figure 9 – Temporal evolution of the device stack measured at a 6 Hz acquisition rate and various excitation fluences: a) below threshold (12 μJ/cm^2/pulse); b) near threshold (19 μJ/cm^2/pulse); c) above the threshold (32 μJ/cm^2/pulse) for amplified spontaneous emission. Results taken by Felix Deschler at the University of Cambridge.

7.2.3 – Creating devices using more highly reflective liquid crystal substrates

To optimise the device, I used a chiral nematic LC layer with a higher reflectivity. This meant that more light was being reflected by the LC layer and so more was passing through the perovskite gain layer. 80% reflectors (compared to the 50% reflectors used previously) were fabricated by our collaborators from the University of Eindhoven by spin coating the LC onto each side of a half-wave-plate film. The half-wave film changes the handedness of the light as it passes through so that some of the 50% of light transmitted by the first chiral nematic LC will be reflected by the second layer and so on, leading to a net reflectivity of ~80%.

These were created by rubbing a half-wave film with a velvet cloth to give an alignment layer. A mixture of reactive mesogen LC-242 (94.8 wt%, BASF), chiral dopant LC-756 (3.2 wt%, BASF), photoinitiator Irgacure 651 (1 wt%, Ciba) and a surfactant (1 wt%) were dissolved in 0.75 wt% xylene at 40 °C for 1 hour. This was then spin coated onto

the half wave film (1000 rpm 25 s). Subsequently, it was polymerised using Uv light (7.5 mW/cm^2) for 5 minutes at 60 °C. The LC was then spin coated onto the other side of the half-wave film using the same procedure. The resulting films were free-standing and flexible which allowed us to create free-standing, flexible emissive devices. The transmission spectrum of the 80% LC reflector chiral is shown in Fig 10.

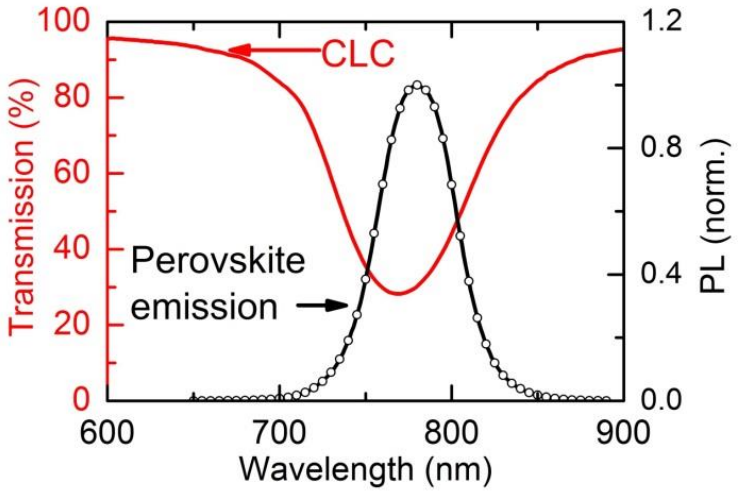

Figure 10 – The transmission spectrum of the 80% chiral nematic liquid crystal reflector (red line) overlaid onto the perovskite emission (black line).

Using this improved LC reflector, I built a similar device as before; the device structure is illustrated in Fig 11. In this case, instead of an alumina buffer layer between the perovskite and the LC, a PMMA layer (50 nm) was spin coated onto the LC (PMMA was used because the wave-plate is temperature-sensitive and the deposition of alumina requires elevated temperatures) as described in Section 7.2.1. The perovskite layer (200 nm) was evaporated on top of this. Evaporation was used because it allows lower processing temperatures than the vapour assisted solution processing used in the previous section.

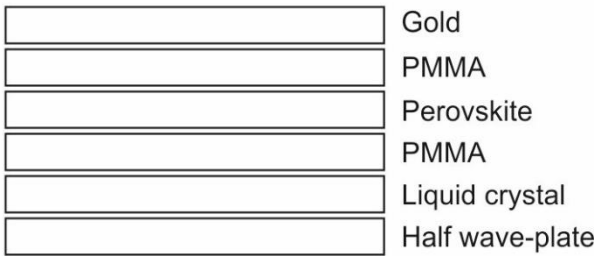

Figure 11 – A layered structure with perovskite sandwiched between a high reflectivity polymerised chiral nematic liquid crystal/wave-plate layer and a gold reflector.

A dual-source evaporation technique was used [41]. This allows uniform coatings on the order of 100s of nm. There are two sources: one organic, which contains

methylammonium iodide (from methylamine, ethanol and hydrogen iodide) and the other inorganic, containing $PbCl_2$ in a 4:1 ratio. The $PbCl_2$ and methylammonium iodide were placed in separate crucibles in a ratio of 1:4, heated above the desired deposition temperature for 5 minutes to remove impurities and then deposited by heating the CH_3NH_3I to 110°C and the $PbCl_2$ to 330°C. The deposition rate and duration were set to yield the desired perovskite thickness (50 nm in this case). Subsequently, the perovskite was annealed at 100°C in a nitrogen-filled glove-box for 30-45 minutes. All evaporation was performed by our collaborators in the department of Physics.

To compete the device, PMMA was spin coated on top (50 nm) as a protective layer; this was followed by a layer of gold (75 nm), evaporated as described above. A photograph of the device stack is shown in Fig 12 to demonstrate the device flexibility.

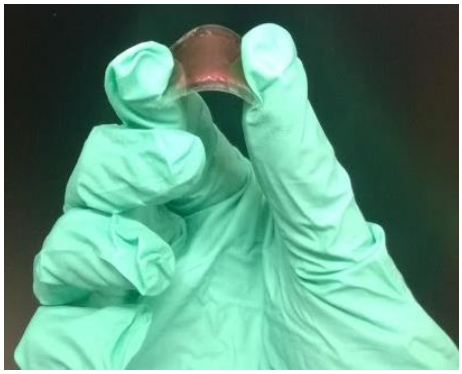

Figure 12 – Photograph of a flexible device based upon an 80% liquid crystal reflector.

The device was then pumped with a laser emitting 4-ns pulse at 530 nm with a 10 Hz-repetition rate and fluences of up to ~60 μJ/cm^2/pulse. Fig 13a shows the emission spectra from the flexible device at different excitation fluences; higher fluences yield higher emission intensities. Fig 13b shows the emission intensity from the stack as a function of the excitation fluence. The threshold has been reduced by a factor of two to 7.6 μJ/cm^2/pulse (compared to 15.3 μJ/cm^2/pulse for the rigid stacks with 50% reflectors). This lower threshold emission can be attributed to the improved reflector because our control samples (without the LC reflector) did not exhibit ASE even at the highest achievable excitation fluences. The threshold is lower than that seen in previous work (12 and 60 μJ/cm^2/pulse in Refs 22 and 25].

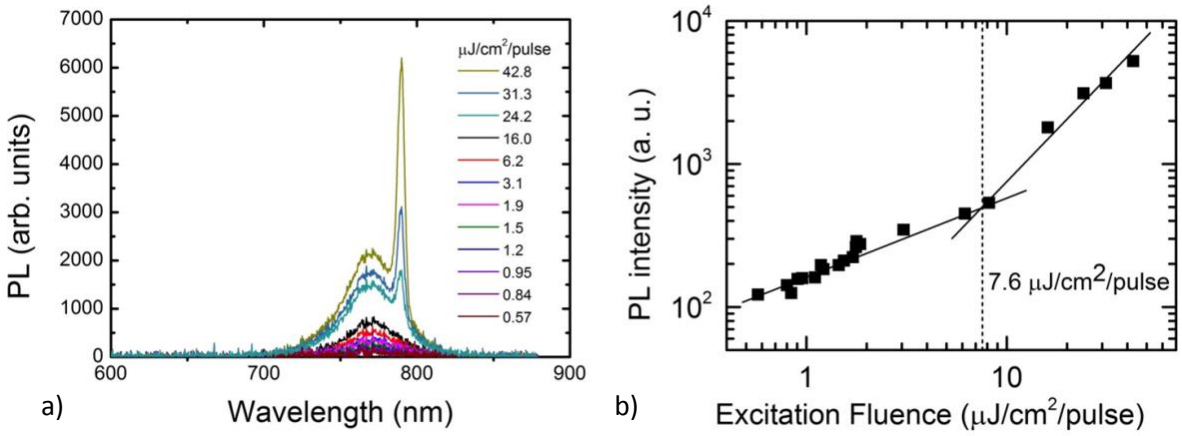

Figure 13 – a) Emission spectra from the layered structure when optically pumped at various excitation fluences at 300K; b) The photoluminescence intensity as function of excitation fluence.

A comparison of the full width half maximum of the emission from our device and a control film as a function of excitation fluence is shown in Fig 14. Above the threshold, there is a clear narrowing of the emission peak from our device; in contrast, the control stack does not exhibit this sharp change. This narrowing is indicative of an amplified emission process.

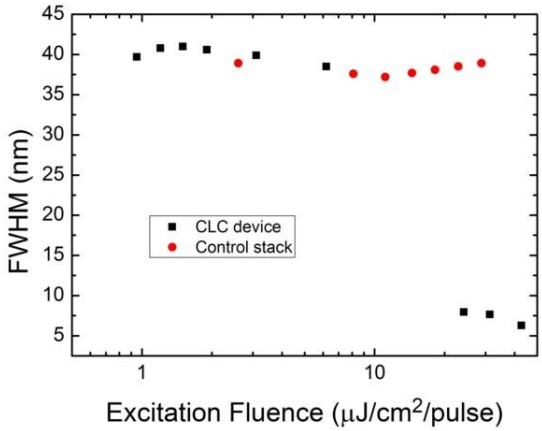

Figure 14 – The extracted full-width at half-maxima of the emission spectrum of the device stack using the 80% liquid crystal reflectors (black squares) compared to devices made on glass without the liquid crystal layer (red circles).

7.2.4 – Studying the cavity built with two liquid crystal reflectors

To improve the emission properties further I then made a layered device that utilised two chiral nematic reflector cavities, as shown in Fig 15. This had an additional advantage insofar as it may be entirely solution processed. A layer of glass was coated with a polyimide alignment layer. A mixture of chiral nematic LC, reactive mesogens, photo-initiator and surfactant were then spin-coated onto it and photo-polymerised by our collaborators from the University of Eindhoven – the same technique was used as described to create the 50% reflectors in Section 7.2.1.

Atomic layer deposition was used to deposit a compact layer (170 nm) of alumina (Al_2O_3) to act as a transparent insulating layer between the LC and the perovskite.

Figure 15 – A layered structure with perovskite sandwiched between two polymerised chiral nematic liquid crystal reflector layers.

I spin-coated a thin layer (~100 nm) of pure iodide perovskite ($CH_3NH_3PbI_3$) onto a glass/LC/Al_2O_3 substrate and then sandwiched this with a glass/LC substrate using a transparent resin (two-component epoxy resin, UHU) to yield a device consisting of a perovskite layer between two chiral nematic reflectors.

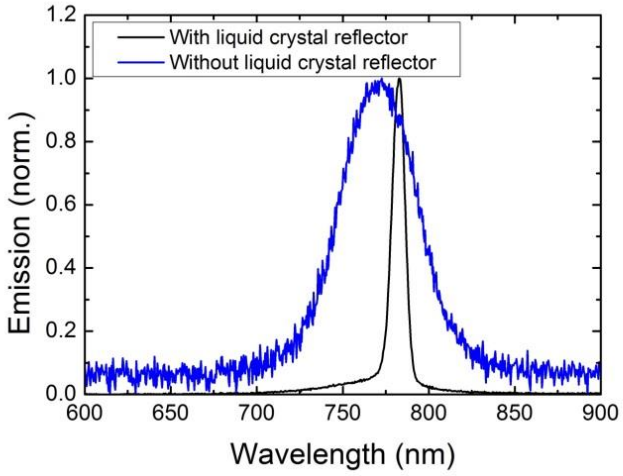

Figure 16- Emission spectrum of a 'sandwiched' device consisting of perovskite between two chiral nematic liquid crystal reflectors when optically pumped (black line) compared with the emission spectrum of a control device without any liquid crystal reflectors (blue line).

When these devices were optically pumped with a laser emitting 4-ns pulse at 530 nm with a 10 Hz-repetition rate and a fluence of ~60 μJ/cm^2/pulse, they exhibited amplified ASE with a full-width at half-maximum of ~9 nm as can be seen in Fig 16. Despite the presence of the resin between the two substrates, it is likely that there was still some air gap, and the lack of precision with which the resin layer thickness could be controlled means that the exact cavity dimensions are unknown. To overcome this, the second

reflector could be spin-coated directly onto the perovskite layer. This will be described in more detail in the Future Work section at the end of this thesis.

In this section, I have described three different cavity configurations using chiral nematic LC reflectors that combine the reflective properties of chiral nematic LCs with the emissive properties of inorganic-organic perovskites to yield ASE. The first involved a perovskite layer (deposited by vapour-assisted solution processing) sandwiched between a chiral nematic LC reflector and a gold layer. To improve on this, one of the LC layers was replaced with a higher reflectivity (80% compared to 50%) LC layer on a flexible substrate. These devices exhibited ASE with a threshold of only ~7.6 $\mu J/cm^2$/pulse, significantly lower (by 2 times) than the thresholds achieved elsewhere for ASE in these perovskite materials [22, 25]. Subsequently, I worked to create devices with two LC reflector layers. These also exhibited enhanced ASE. This work offers a promising route towards single-mode, mirrorless lasing from perovskite materials; furthermore, the use of LC materials allows additional functionality to be realised – such as the device flexibility demonstrated here, and potentially, another route towards in-situ wavelength tuning (by altering the LC photonic band-gap). Particular experiments to take this work forwards to achieve true lasing will be discussed in the Future Work section.

7.3 – Perovskite-based distributed feedback lasers

In this section I describe work to create the first distributed feedback (DFB) laser using perovskite as the gain material. In contrast to the previous section, I did not create a layered structure with reflectors at each end; instead, I used nanoimprinting to pattern a layer of inorganic-organic perovskite with a diffraction grating. This serves two purposes – firstly, it demonstrates that lasing is possible using the perovskite materials and secondly it allows us to combine the beneficial emission properties of the perovskites (high quantum efficiencies, broad range of emission wavelengths, versatile manufacturing methods) with the advantageous properties of the DFB structure (e.g. they are inexpensive to manufacture and exhibit low threshold, single-mode lasing). This work was performed in collaboration with the Department of Physics, University of Oxford.

7.3.1 – Distributed feedback lasers

DFB lasers have been used extensively because they are cheap to manufacture, have low excitation thresholds, do not require mirrors, have tuneable single-frequency output across the visible, can be modulated rapidly and have long operating lifetimes [42-43].

In a DFB laser, the refractive index is varied periodically within the gain medium. This is typically achieved by patterning a grating onto the substrate. An incident plane wave is reflected by a series of reflectors spaced *d* apart (i.e. the corrugation periodicity). For constructive interference, the Bragg condition must be satisfied, i.e.:

$$m\lambda = 2dsin\theta \qquad (7.1)$$

where *m* is the mode order, λ is the wavelength of the incident light, *d* is the grating spacing, and θ is the scattering angle. For 180° reflection, the equation becomes:

$$m\lambda = 2n_{eff}\mathrm{d} \qquad (7.2)$$

Where n_{eff} is the effective refractive index of the material.

When the Bragg condition is met, there is optical feedback along the waveguide. Usually only one mode lies within the gain bandwidth of the material. In this case, the second mode (*m*=2) is the mode that falls within the gain bandwidth. Because Bragg scattering is highly frequency selective, it results in narrow linewidths for DFB lasers; furthermore, the emission wavelength of a DFB is tuneable simply by changing the grating period.

DFB systems have been created using a variety of active gain media. Such gain materials include dyes [44], organics [45], inorganics [46] and semiconducting polymers [47].

7.3.2 – Building the distributed feedback laser

To build the DFB laser, I used direct nano-imprinting to pattern a perovskite with a grating structure. Perovskites are not soft materials and so I nanoimprinted a corrugated structure onto a polymer template and then evaporated the perovskite ($CH_3NH_3PbI_3$) onto it. This is in contrast to much work on DFB lasers where the active material is usually an organic which is itself nano-imprinted,

Nanoimprinting is a technique used to fabricate nanometre scale patterns with a low cost, a high throughput and a high resolution [48]. A stamp is created and then pressed into the substrate to imprint its pattern. In this case, the stamp was imprinted onto a polymer and then the perovskite was patterned on top of this.

Two different stamps were used here – a Thorlabs diffraction grating with a period of 416 nm and a multi-stamp created by electron beam lithography on a Si/Cr substrate. This multi-stamp was composed of 9 ‘pixels’ patterned with grating periods of 370 to 440 nm in 10 nm increments; the gratings were 100 nm deep. These hard stamps were

used to create soft stamps using Obducat's Eitre nanoimprint lithography system – the hard stamps were pressed into a flexible intermediate polymer stamp (IPS, Obducat) at 115°C and a pressure of 40 bar. This soft stamp was then used to transfer the pattern to a microscope slide that had been cleaned and spin-coated with 100 nm of photo-resist (STU, Obducat). This was done with a simultaneous thermal and UV imprint process (70°C, 30 bar for 210 s). The polymer resist was then exposed to UV light for 60 s. Finally, the soft stamp was lifted off the microscope slide and successful pattern transfer was confirmed by taking scanning electron microscopy images and by checking the visible interference pattern. The perovskite was then deposited onto this (by evaporation, as described in Section 7.2.1).

An image of the multistamp is shown in Fig 17a; Fig 17b shows the corresponding 'pixels' and their grating spacing. (The 9th pixel is smaller than the others to leave an area without a grating that can be used as a control region). These periodicities were chosen because I was looking at the surface emitting mode (m = 2) and so to a first approximation, from the Bragg equation (Equation 7.1) and using 780 nm as the wavelength (the peak emission of the tri-iodide perovskite) I would want d, the grating spacing, to be ~390 nm. Figure 17c shows an example of a DFB device that I built – the different grating spacings of each pixel result in different visible colours for each pixel.

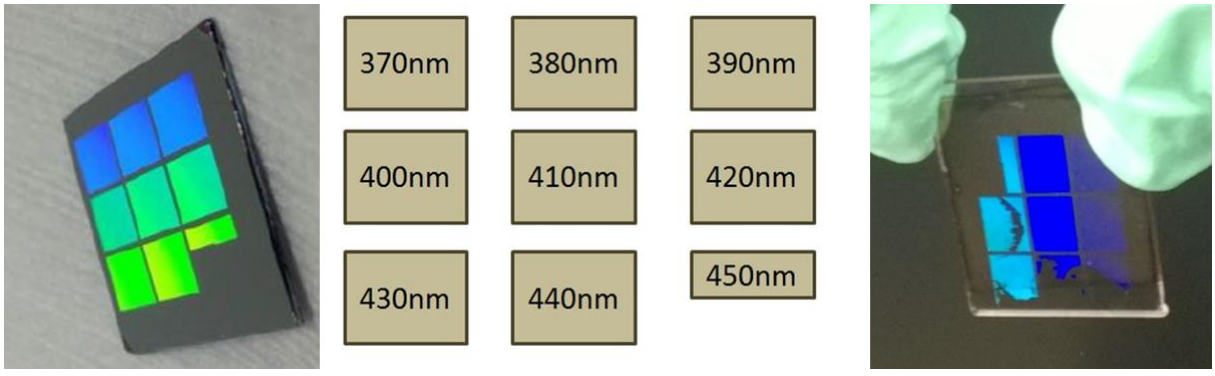

Figure 17 – Multistamp containing 9 different grating spacings from 370-450 nm in 10 nm intervals; b) shows the grating spacing of each pixel; c) shows an example device where the multistamp has been used to imprint the grating patterns onto a perovskite layer.

To check that the nanoimprinting technique was working I investigated the materials using an atomic force microscope (AFM). An AFM is a type of scanning probe microscope in which a mechanical probe investigates a surface [49]. The probe is sensitive to very small changes in the surface and so can give a precise surface map. In this work, the non-contact mode is used. In non-contact mode AFM, the probe is attached to a cantilever which oscillates at its resonant frequency. This is then passed

just above the surface (~10 nm away) and its resonance frequency is altered by Van-der-Waals forces. This allows a topographic map of the surface to be built up.

In this work, AFM images were taken using a ThermoMicroscopesAutoProbeM5 housed in an acoustic isolation enclosure in noncontact mode, with a scan rate of 0.2 Hz and a 256×256-pixel image area. Aluminium-coated antimony-doped Si tips (Bruker) were used, with typical tip radii of 8 nm, resonant frequencies of 75 kHz, and stiffnesses of 3 N m^{-1}.

Fig 18 shows AFM image of the stamp and the device stack. Fig 18 a is the 3D profile of the stamp, corresponding to an 80-nm grating depth and a 410 nm periodicity. This is further corroborated using the 2D AFM image shown in Fig 18b and the depth profile in Fig 18c. AFM images were then taken of the patterned perovskite. Fig 18d shows the 2D AFM profile for the patterned perovskite. Fig 18e shows the corresponding height

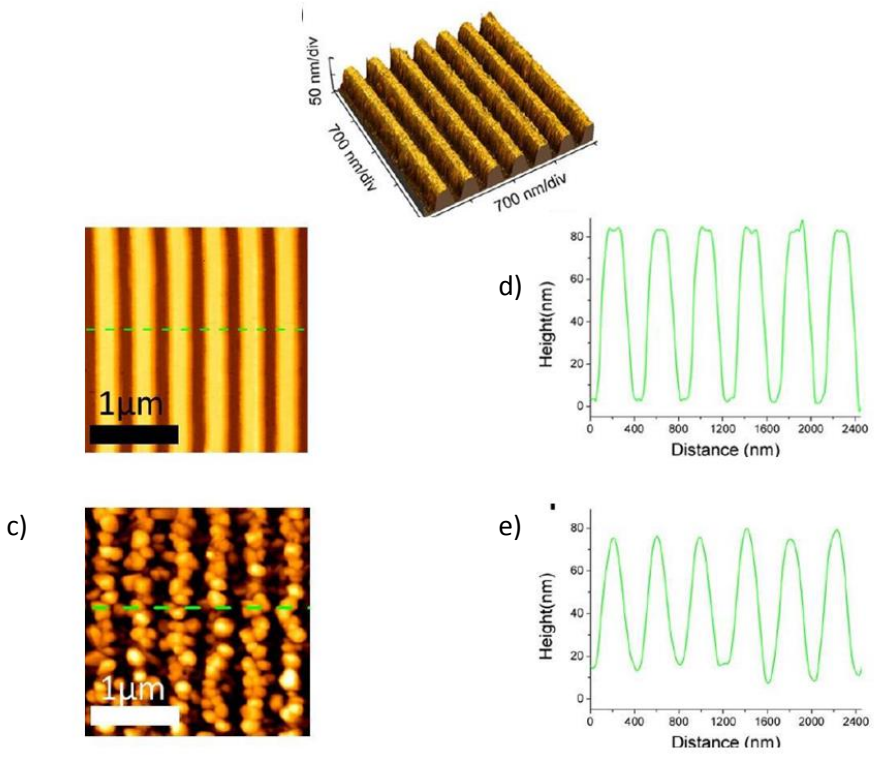

profile. These show that perovskite coating is conformal and periodic.

a)

Figure 18 – a) 3D and b) 2D AFM images of the patterned polymer resist; c) height profile of the polymer resist; d) 2D AFM image and e) height profile of the patterned perovskite evaporated onto the polymer resist.

b)

To further check our samples, Fig 19 shows SEM images that clearly show the corrugation of the tri-iodide perovskite layer. SEM images were taken as described in

b)

c)

Section 7.2.1. The corrugation can be seen both from the side of the device (Fig 19a) and from above (Fig 19b). These further demonstrate the conformal coating of the evaporated perovskite onto the underlying polymer that had been nanoimprinted using the multi-stamp.

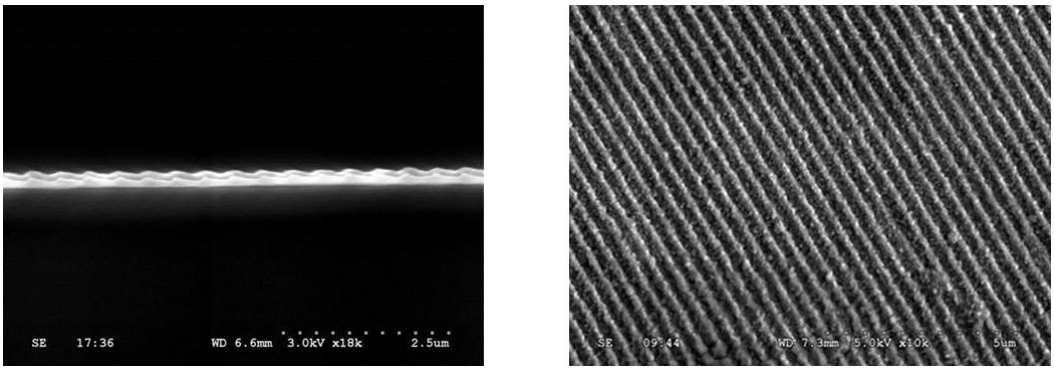

Figure 19 – Scanning electron microscope images of perovskite evaporated onto the patterned polymer resist. a) side-view and b) top-view.

7.3.3 – Characterising the DFB laser

I measured the emission from the surface emitting DFB cavity (second order Bragg scattering) using the device created using the multistamp. The pump laser (a 532 nm laser emitting 5-ns pulses with a 1 kHz repetition rate) was scanned across the different pixels (which had 370-450 nm grating spacings in steps of 10 nm) and the unpatterned reference area. Three of the pixels yielded sharp emission peaks – 400, 410 and 420 nm, as shown in Figure 20, while the others simply exhibited unmodified perovskite photoluminescence (with an emission peak at ~760 nm, a slightly longer wavelength than the steady-state photoluminescence peak). 'Lasing' occurred at different wavelength for different pixels; this would be expected as they have different grating spacings.

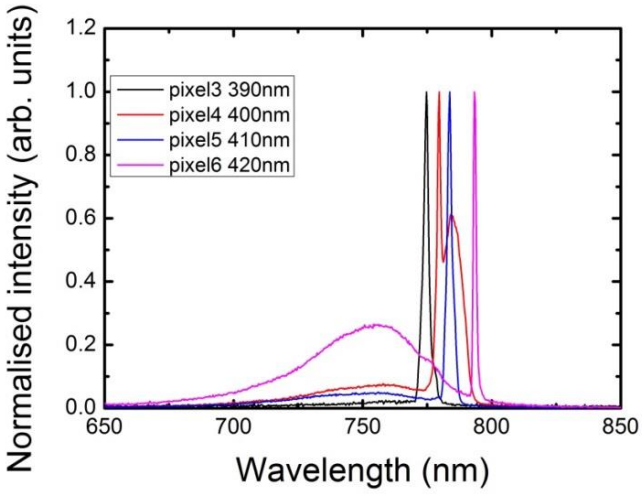

Figure 20 – Emission from different pixels when optically pumped.

It should be noted that I have not unequivocally proved that the emission from our device is lasing (as opposed to significantly narrowed ASE). However, there is a great deal of evidence that points to it as being lasing. Although I have not performed photon statistic measurements, I have seen a narrow line-width (to the resolution limit of our spectrometer). Additionally, the wavelength of emission changes with the grating spacing (I would expect ASE to occur at the photoluminescence maximum of the perovskite, regardless of the patterning of the material). With this corollary, the output of these devices will be described as lasing for the remainder of this Thesis.

The pump fluence was varied and the output measured to yield excitation thresholds for the lasers, as shown in Fig 21a. In the case of a 400-nm grating spacing, the peak intensity increases rapidly with increasing excitation fluences, narrowing to a full width at half maximum of 2.2 nm for the highest excitation fluences. As an example, for Λ = 400 nm, the emission peak increases rapidly with increasing excitation fluences accompanied by a narrow full width at half maximum of 2.2 nm for the highest excitation fluence at 4.35 $\mu J/cm^2$/pulse. For grating periodicities of 410 and 420 nm the lasing peaks also increase rapidly in intensity with full width at half maxima of 2.1 and 1.4 nm respectively. As shown in Fig 21b there is at first a linear increase in the

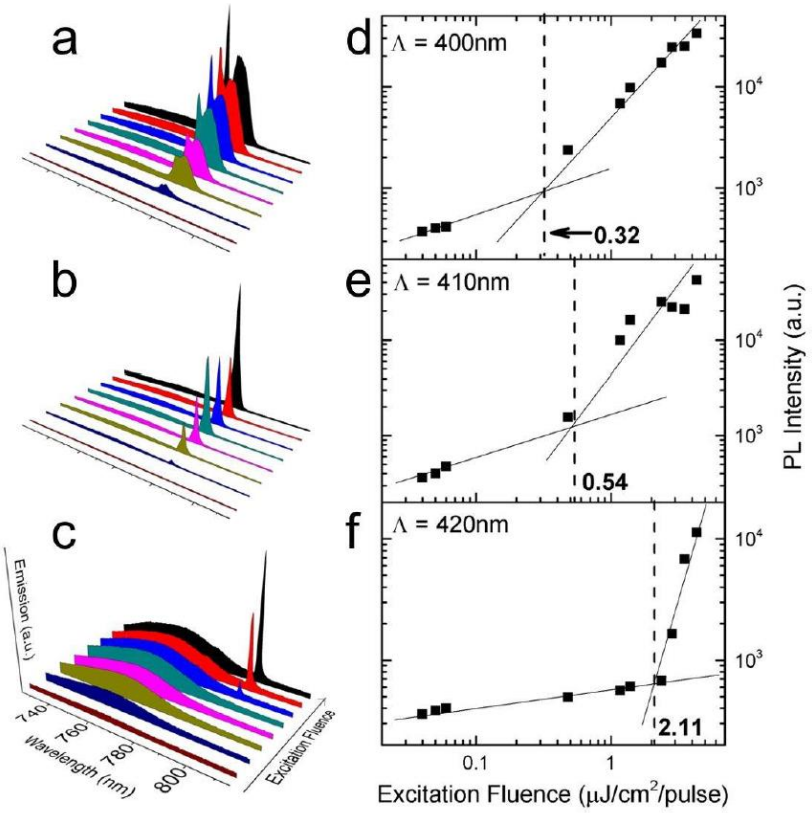

Figure 21 – Left: emission from the distributed feedback structure with a grating spacing of a) 400 nm, b) 410 nm and c) 420 nm when they are optically pumped. Right: the peak emission intensity as a function of the excitation fluence for d) 400, e) 410 and f) 420 nm grating spacing. The dashed lines correspond to the thresholds for amplified emission, determined from the discontinuities in the graphs.

intensity (due to spontaneous emission) followed by a rapid increase at the respective fluence thresholds of ~0.32 (400 nm grating), ~0.54 (410 nm grating), and ~2.11 (420 nm grating) μJ/cm^2/pulse, significantly lower than most values of ~10-20 μJ/cm^2/pulse reported in literature for lasing structures using similar perovskites [11, 19-22]. The 400-nm grating yield lasing at a wavelength of ~780 nm – the photoluminescence maximum of the tri-iodide perovskite used here.

As would be expected, the emission blue-shifts as the grating spacing decreases. Lasing occurred at 770 nm for a 380-nm grating, 774 for a 390-nm grating, 779 nm for a 400-nm grating, 784 nm for 410-nm grating, and 793 nm for a 420-nm grating spacing Fig 22 shows the change in peak wavelength with grating spacing.

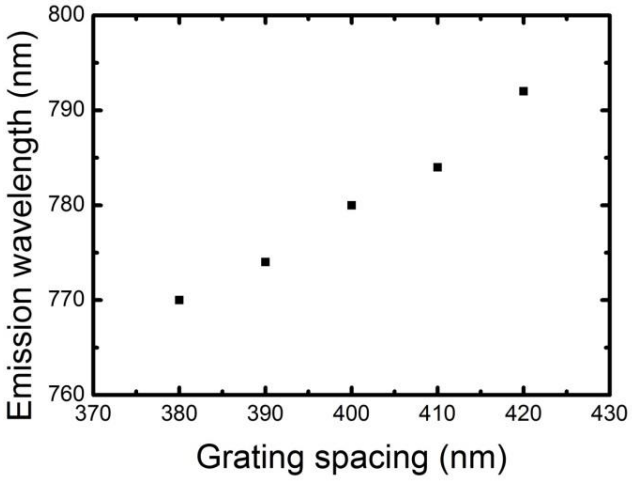

Figure 22 – Change in emission wavelength as the grating spacing is varied.

This change does not quite fit with the Bragg scattering law with a constant refractive index (I would expect a ~20 nm separation of modes whereas I see a ~ 5 nm separation of modes). However, our collaborators simulated the modes using a more complex reckoning than our simple first order approximation and found that our experimental results are in accordance with their predictions [51]. They simulated the fundamental modes for different grating spacings. They estimated the effective indices of the waveguide modes by numerically solving the phase-matching conditions for a waveguide consisting of a polymer substrate, a 100-nm thick perovskite layer and air. From this, they showed that the dispersion of the refractive indices accounted for the 20-nm mode separation.

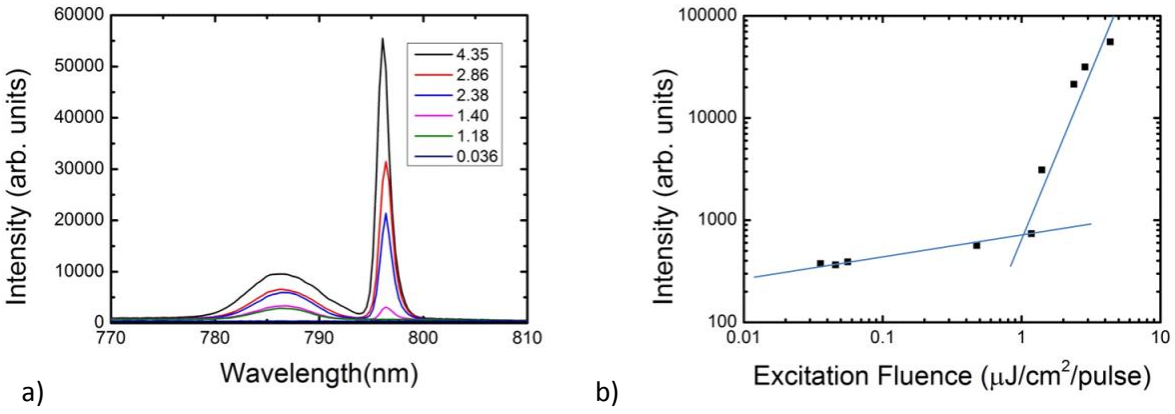

Figure 23 – a) Emission from the DFB structure with a grating spacing of 416 nm when optically pumped at different fluences. b) The peak emission as a function of the excitation fluence.

I also created device imprinted with a single stamp with a periodicity of $\Lambda \sim 416$ nm and these also exhibited lasing. These results can be seen in Fig 23. They exhibit lasing

with a peak at 796 nm (full width at half maximum = 1.4 nm) and an excitation threshold of ~1 μJ/cm^2/pulse.

7.4 – Conclusion

In this Chapter, I have described work investigate the viability of using inorganic-organic perovskites as the gain materials in lasers. The potential for combining them with chiral nematic LCs has been demonstrated, and it has been shown that layered structures of LC and perovskite exhibit enhanced amplified spontaneous emission and that has been characterised here. This work demonstrates the potential for LC-perovskite lasers which utilise both the qualities of LCs (flexibility, in-situ tunability by a variety of stimuli) and those of perovskites (stability to illumination, high efficiencies). Future work is required to improve the devices so that they can act as lasers.

Subsequently in this Chapter, I described a method for creating distributed feedback lasers from patterned perovskites This work resulted in the creation of the first single mode laser which used perovskites as the gain material. Perovskite materials were conformally evaporated onto a nanoimprinted polymer resist to create patterns of various different grating spacings that allow tuneable emission from 770 to 793 nm simply by varying the region that is being pumped. These DFB perovskite lasers have potential for use as inexpensive, mirror free, widely-tuneable, single mode lasers that are easy to manufacture on a large scale.

The next section of this Thesis provides a conclusion of the work presented here. This is followed by a Future Work section which details work that could be performed to take the various projects described here further, as well as to discuss other, related avenues or research.

7.5 – References

1. M. Johnsson and P. Lemmens, Crystallography and Chemistry of Perovskites, in Handbook of Magnetism and Advanced Magnetic Media, Edited by H. Kronmüller. John Wiley & Sons, New York, 2006, 2098–106.
2. S. D. Stranks, H. J. Snaith, *Nanotechnol*. 2015, **10**, 391.
3. M. A. Green, A. Ho-Baillie, H. J. Snaith, *Nat*. *Photonics*, 2014, **8**, 506.
4. M. Gratzel, *Nat*. *Mater*. 2014, **13**, 838.
5. W. S. Yang, J. H. Noh, N. J. Jeon, Y. C. Kim, S. Ryu, J. Seo, S. I. Seok, *Science, 2015,* **348,** 1234.
6. Research Cell Efficiency Records http://www.nrel.gov/ncpv (National Renewable Energy Laboratory, accessed 13 July 2016).
7. Perovskite Structure http://en.wikipedia.org/perovskite_strucure (Wikipedia, accessed 13 July 2016)
8. Shi, D. et al. *Science*, 2015, **347,** 519.
9. Dong, Q. et al. *Science*, 2015, **347**, 967.
10. G. E. Eperon, *Adv*. *Funct*. *Mater*., 2014, **24**, 151.

11. M. M. Lee, J. Teuscher, T. Miyasaka, T. N. Murakami, H. J. Snaith, 2012, **338**, 643.
12. M. Z. Liu, M. B. Johnston, H. J. Snaith, *Nature*, 2013, **501**, 395.
13. B. R. Sutherland and E. H. Sargent, *Nat*. *Photonics*, 2016, **10**, 295.
14. De Wolf, S., *J*. *Phys*. *Chem*. *Lett*., 2014, **5**, 1035.
15. Leijtens, T. et al. *ACS Nano*, 2014, **8**, 7147.
16. F. Deschler, M. Price, S. Pathak, L. E. Klintberg, D. D. Jarausch, R. Higler, S. Huttner, T. Leijtens, S. D. Stranks, H. J. Snaith, M. Atature, R. T. Phillips, R. H. Friend, J. Phys. *Chem*. *Lett*. 2014, **5**, 1421.
17. Song, J. et al. *Adv*. *Mater*. 2015, **27**, 7162.
18. Zhang, X. et al. *Nano Lett*. 2016, **16**, 1415.
19. M. Era, S. Morimoto, T. Tsutsui, S. Saito, *Appl*. *Phys*. *Lett*. 1994, **65**, 676
20. T. Gebauer, G. Schmid, Z. Anorg. Allgem. *Chem*. 1999, **625**, 1124.
21. Z. K. Tan, R. S. Moghaddam, M. L. Lai, P. Docampo, R. Higler, F. Deschler, M. Price, A. Sadhanala, L. M. Pazos, D. Credgington, F. Hanusch, T. Bein, H. J. Snaith, R. H. Friend, *Nat*. *Nanotechnol*. 2014, **9**, 687.
22. G. Xing, N. Mathews, S. S. Lim, N. Yantara, X. Liu, D. Sabba, M. Gratzel, S. Mhaisalkar, T. C. Sum, *Nat*. *Mater*. 2014, **13**, 476.
23. X. Hong, T. Ishihara, A. V. Nurmikko, *Solid State Commun*.1992, **84**, 657.
24. R. Dhanker, A. N. Brigeman, A. V. Larsen, R. J. Stewart, J. B. Asbury, N. C. Giebink, *Appl*. *Phys*. *Lett*. 2014, **105**, 151112.
25. B. R. Sutherland, S. Hoogland, M. M. Adachi, C. T. Wong, E. H. Sargent, *ACS Nano* 2014, **8,** 10947.
26. F. Panzer, S. Baderschneider, T. P. Gujar, T. Unger, S. Bagnich, M. Jakoby, H. Bässler, S. Hüttner, J. Köhler, R. Moos, M. Thelakkat, R. Hildner, and A. Köhler, *Adv*. *Mater*., 2016, **9**, 277
27. Y. Fu, H. Zhu, A. W. Schrader, D. Liang, Q. Ding, P. Joshi, L. Hwang, X.-Y. Zhu, and S. Jin, *Nano Lett*., 2016, **16**, 1000.
28. Xia, R., Heliotis, G. & Bradley, D. D. C. *Appl*. *Phys*. *Lett*., 2003, **82,** 3599.
29. Dang, C. et al., *Nature Nanotech*., 2012, **7**, 335.
30. She, C. et al. *Nano Lett*. 2014, **14**, 2772.
31. Liao, Q. et al., *Adv*. *Mater*. 2015, **27**, 3405.
32. Zhu, H. et al., *Nature Mater*., 2015, **14**, 636.
33. Gu, Z. et al. Two-photon pumped lead halide perovskite nanowire lasers. Preprint at http://arXiv.org/abs/1510.03987v1 (2015).
34. Xing, J. et al., *Nano Lett*. 2015, **15**, 4571.
35. Fu, Y. et al., *Nano Lett*., 2016, **16,** 1000.
36. Liu, S. et al. Random lasing actions in self-assembled perovskite nanoparticles. Preprint at http://arXiv.org/abs/1512.07377 (2015).
37. M. Liu, M. B. Johnston, and H. J. Snaith, *Nature*, 2013, **501**, 395.
38. R. W. Johnson, A. Hultqvist, and S. F. Bent, *Mater*. *Today*, 2014, **17**, 236.
39. J. C. de Mello, H. F. Wittmann, and R. H. Friend, *Adv*. *Mater*., 1997, **9**, 230.
40. S. D. Stranks, V. M. Burlakov, T. Leijtens, J. M. Ball, A. Goriely, H. J. Snaith, *Phys*.*Rev*. *Appl*. 2014, **2**, 034007.
41. X. Hong, T. Ishihara, A. V. Nurmikko, *Solid State Commun*.1992, **84**, 657.
42. H. Kogelnik, C. V. Shank, *Appl*. *Phys*. *Lett*. 1971, **18**, 152.
43. J. E. Carroll, J. Whiteaway, D. Plumb, Distributed Feedback Semiconductor Lasers, Vol. 10, IET, 1998.
44. M. Berggren, A. Dodabalapur, R. E. Slusher, A. Timko, O. Nalamasu, *Appl*. *Phys*. *Lett*. 1998, **72**, 410.
45. T. N. Smirnova, O. V. Sakhno, P. V. Yezhov, L. M. Kokhtych, L. M. Goldenberg, J. Stumpe, *Nanotechnology*, 2009**, 20**, 245707.
46. N. Tessler, G. J. Denton, R. H. Friend, *Nature*, 1996, **382**, 695.
47. R. W. Johnson, A. Hultqvist, and S. F. Bent, *Mater*. *Today*, 2014, **17**, 236.
48. N. Kooy, K. Mohamed, L. Pin, and O. Guan, *Nanoscale Res*. *Lett*., 2014, **9**, 320.
49. H. G. Hansma, L. Pietrasanta, 1998. *Curr*. *Opin*. *Chem*. *Biol*. 1998, **2,** 123.
50. A. Bogner, P. H. Jouneau, G. Thollet, D. Basset, C. Gauthier, *Micron*, 2007, **38**, 390.
51. M. Saliba, S. M. Wood, J. B. Patel, P. K. Nayak, J. Huang, J. A. Alexander-Webber, B. Wenger, S. D. Stranks, M. T. Hörantner, J. T.-W. Wang, R. J. Nicholas, L. M. Herz, M. B. Johnston, S. M. Morris, H. J. Snaith, and M. K. Riede, *Adv*. *Mater*., 2015, **28**, 923.

Conclusion to thesis

This thesis has described work to create a variety of thin-film photonic devices, including polymer-templated liquid crystals (LCs) and emissive devices such as lasers and polarised light sources. Much of this work has focussed on LCs in combination with other materials such as reactive mesogens and photoluminescent materials.

Chapter 1 presented an introduction to the Thesis. It provided an overview of the work I described in the subsequent Chapters. Chapter 2 described the background to the work and the core experimental used in this Thesis.

In Chapter 3, I described my work to polymer-template the smectic A LC phase to create devices with improved electro-optic properties. A smectic A LC was combined with reactive mesogens and photo-cured to yield a polymer-stabilised LC. The LC was then washed out of this device using a solvent to leave a polymer scaffold which was templated with the original phase. When the scaffold was then refilled with a nematic LC, the smectic A alignment was imprinted onto a nematic LC. I described my technique for fabricating these devices and methods for identifying their textures. Subsequently, I studied their electro-optic properties and I showed that polymer templated smectic A LCs exhibit improved electro-optical properties such as larger contrast ratios (by ~12 times) and a faster response times (by ~ 6 times, 13 ms vs. 90 ms) when compared with a conventional nematic LC. Furthermore, unlike in an unpolymerised smectic A LC, the electric switching was reversible, allowing the device to be repeatably switched.

In Chapter 4, I described work to utilise this polymer-templating technique to improve the electro-optical properties of another interesting LC phase – the chiral nematic LC phase (which exhibits a 1D photonic band-gap). To this end, I studied the electro-optic properties of polymer-templated chiral nematic LCs and compared them to those of more conventional polymer-stabilised LCs. I reported that the polymer-templated samples exhibited a much broader (by 2.5 times; 55 vs. 22 nm) wavelength tuning range when electric fields were applied. Furthermore, this shift is composed of an initial blue-shift of the long-wavelength edge of the band-gap that occurs on a relatively rapid timescale (τ ~1 ms) followed by a considerably slower blue-shift (τ ~6.5 s) of the entire band-gap. (In a conventional polymer-stabilised chiral nematic LC a fast blue-shift (τ ~1 ms) of only the long-wavelength band-edge is observed). In Chapter 4, I sought to elucidate the nature of the different tuning mechanisms and to provide an explanation

for them. Specifically, I provided evidence that suggests that the fast shift of only one band-edge is caused by a reorientation of LC molecules which leads to a decrease in the refractive index and that the slower, broader shift of the entire photonic band-gap is caused by a flow of the polymer network which reduces the pitch.

Subsequently in Chapter 4, the broader tuning range of the polymer-templated chiral nematic LCs was applied to create tuneable LC lasers by refilling the polymer scaffold with a dye-doped achiral nematic LC. This resulted in the first polymer-templated chiral nematic LC laser. I then compared this polymer-templated LC laser to a polymer-stabilised LC laser. I reported that polymer-templating allows a greater tuning range (by 2.5 times) than in the polymer-stabilised case. Furthermore, the templating technique offers additional advantages for the creation of electrically-tuneable LC lasers – because the dye is added after the photo-curing process, it cannot interfere with the curing process; this results in an improved device morphology, lower laser thresholds and allows a wider range of dyes to be used.

In Chapter 5, I investigated polymer-stabilised lasers which contained sufficiently high concentrations of reactive mesogens that they could be delaminated from their substrates to yield free-standing laser films. These free-standing lasers could have their output wavelength tuned (by 45 nm) by elongating them – as the films are stretched, they thin, the LC pitch decreases and so the photonic band gap blue-shifts. In Chapter 5, I described my work to study different elastomeric chiral nematic films made using various concentrations of reactive mesogens and probed their mechanochromic properties. From this, I determined an optimum concentration of reactive mesogen (60 wt%). By doping the resulting mixture with a dye, I created an elastomeric laser. In Chapter 5, I described the technique for manufacturing these lasers and showed that they could be mechanically wavelength-tuned and that this tuning was reversible, repeatable and did not exhibit hysteresis; thus, a desired emission wavelength may be selected simply by controlling the extent of the film elongation. Our technique presents additional advantages because it is significantly simpler than the methods previously used to create elastomeric LC lasers and allows further functionality to be achieved – specifically, here, I created multi-region laser films in which different areas emit light at different wavelengths simply by curing different regions of the LC at different temperatures.

After two Chapters that dealt with methods for wavelength-tuning a LC laser, the subsequent Chapters described work towards mitigating the major disadvantages of LC lasers – the use of easily photo-bleached fluorescent dyes and the need for optical pumping. Thus, in Chapter 6 and 7, I investigated transition metal clustomesogens and inorganic-organic perovskites as gain materials for LC lasers due to their photo-stability, and, in the case of perovskites, potential for electric pumping.

In Chapter 6 I detailed work to investigate the potential of transition metal clustomesogens (CMs) as alternative gain materials in LC lasers. Inorganic materials are usually incompatible with organic solvents (such as LCs). However, due to the long organic ligands around the metal clusters, the CMs are themselves liquid crystalline and are easily dispersed into a variety of other LC phases – making them ideal candidates for alternative gain materials. In Chapter 6, I dispersed these materials into both nematic and chiral nematic LCs and investigated their photoluminescence properties. Although the devices created didn't lase, I showed that it was possible to use CMs dispersed in chiral nematic LCs as polarised emitters – with a polarisation that can be controlled simply by applying electric fields. This was done by overlapping the chiral nematic photonic band-gap with the CM emission. The photonic band-gap selectively reflects one handedness of circularly polarised light and transmits the other, resulting in polarised emission. This gave left polarised emission with a dissymmetry factor of 1.6. The photonic band-gap could then be collapsed by applying an electric field, allowing electrical control of the emission polarisation; when an electric field was applied, the circular polarisation was 'switched off' and unpolarised light was emitted.

Chapter 7 detailed work to use inorganic-organic perovskites as the gain materials in lasers. As with the CMs, these materials are not susceptible to photo-bleaching, but they offer further potential – as semiconductors they could possibly be used in electrically pumped lasers. Furthermore, they may be solution processed, have high efficiencies, high quantum yields and can exhibit photoluminescence at different wavelengths (from 390 to 790 nm) depending on their composition.

Firstly, the perovskite was sandwiched between a chiral nematic LC reflector and a gold layer; such devices exhibited amplified spontaneous emission, a precursor to lasing with a threshold of 15.3 $\mu J/cm^2$/pulse. Subsequently the device was optimised with a higher reflectivity LC reflector. This further improved the amplified spontaneous emission properties (the threshold was reduced to 7.6 $\mu J/cm^2$/pulse for example). These devices

also had the additional functionality of being flexible. To create fully solution processable devices, a sandwiched structure with perovskite sandwiched between two LC reflectors was created and exhibited a threshold of 6.2 $\mu J/cm^2$/pulse; further improvements in material properties and device manufacture are necessary to achieve true lasing.

In Chapter 7 I also described our work to use the perovskites as the gain materials in a laser without any LC element. To this end, I created a single-mode, wavelength tuneable distributed feedback laser – the first single mode laser using inorganic-organic perovskites as the gain materials – by patterning the perovskite with a grating. Our lasers could be wavelength tuned (770-793 nm) by changing the grating spacing.

The next section of this Thesis describes future work that could be performed to continue the research described here, as well as to discuss avenues of research suggested by my results.

Future work

This section discusses the potential future work that could be performed to continue the research discussed in this Thesis. Additionally, I discuss some new areas of research that my work suggests.

Polymer-templating different liquid crystal phases

The polymer-templating technique described in Chapters 3 and 4 can be applied to a variety of other liquid crystal (LC) phases. One that has not been investigated but that would be particularly interesting is the chiral smectic C phase. This would be interesting as the phase exhibits fast ferroelectric tuning. Furthermore, like the smectic A phase, the chiral smectic C layered structure damps thermal fluctuations and so offers potential for improved electro-optic properties. Additionally, the chiral smectic C phase possesses a photonic band-gap and so could potentially be refilled with a dye-doped material to yield a laser in a similar manner to the chiral nematic materials described in Chapter 4. However, it is often the case with chiral smectic C materials that it is difficult to add enough chirality to the system to move the photonic band-gap wavelength position into the visible regime without creating a material which no longer exhibits the chiral smectic C phase. Thus, either new materials would need to be found, or a laser that emits at longer wavelengths than the visible could be created – this would require an investigation into appropriate dyes (or potentially alternative gain materials) which emit at that wavelength.

Stretchable liquid crystal lasers

The next step in the work on stretchable LC lasers would be to use a combination of two or more fluorescent dyes to extend the gain bandwidth – this would allow broader wavelength-tuning to be achieved (in my work in Chapter 5, the laser films could be stretched well beyond the point at which lasing ceased due to the finite bandwidth of the dye used there).

It would also be possible to make lasers using different polymer-stabilised LC phases. Of particular interest would be the blue phase – a LC phase which possesses a photonic band gap in three dimensions. Previous work has shown the possibility of creating lasers using blue phases [1-3], and that blue phase LC lasers tend to have lower thresholds than equivalent chiral nematic LC lasers. Furthermore, due to their 3D band-gaps, they could emit simultaneously in multiple dimensions, and by stretching these may be tuned simultaneously in those dimensions. A uniaxial stretch, as used here,

would result in a blue-shift in one dimension, and a red shift in another as the film is elongated (with an increase in the pitch) in one dimension and simultaneously thinned in another dimension (with a consequent decrease in the pitch). Elastomeric blue phases have been demonstrated [4-5], so the logical first step would be to create such elastomers and then dope them with a fluorescent dye. This is non-trivial due to the small temperature range over which the blue phases generally exist [6] (which may be circumvented using bespoke materials such as bimesogens [7]), and their sensitivity to curing conditions (which the presence of a dye can also interfere with).

Additionally, the elastomeric films could be patterned more elaborately than the two-region devices used here – several different areas of the lasers could be cured using different conditions. This could be used to yield arbitrary patterns of different regions that can simultaneously lase. If the alternative gain materials discussed in Chapters 6 and 7 could be used successfully, they could be integrated into these stretchable lasers to circumvent bleaching issues.

Clustomesogen-based liquid crystal lasers

In my work on making polarised emitters using clustomesogens (CMs) in LCs, it is the photonic band gap of the LC that is controlling the polarisation sense. I showed that it could be switched off by applying an electric field. However, to make this switching reversible, the CMs could be combined with the polymer-stabilised and polymer-templated LC systems described in Chapters 3 and 4. However, this is non-trivial due to the CM absorption interfering with photocuring, and, in the case of polymer templating, the magnitudes of the electric fields required and the highly ionic nature of the CMs leads to destruction of the devices before any tuning is seen.

Due to their high photoluminescences, photo-stabilities and easy dispersal into chiral nematic LCs, transition metal CMs offer large potential for use as photo-stable gain materials in LC lasers. If such devices were created and were stable to continuous illumination, one of the major limitations of LC lasers would have been overcome and their potential for real-world applications would be greatly enhanced. One of the barriers to this is that CMs are phosphorescent – their excited states have longer lifetimes than the fluorescent dyes usually used to create LC lasers. To overcome that various laser architectures could be investigated. Example of this are Q-switched lasers (by using a saturable absorber to modulate the losses and hence Q-factor of the cavity to generate short pulses of emission), defect mode architectures where CMs dispersed into

a nematic LC could be filled between substrates coated with polymerised chiral nematic LC reflectors (and so would act as a defect layer), or polymer dispersed LCs – in this case the LC laser would be acting as a random laser in which the long lifetime of the excited states would be less of an issue.

Additionally, there are numerous similar materials that our collaborators have been working to synthesise that I could try to incorporate into LC systems. These materials include magnetically switchable rhenium clusters with a colour that drastically changes when a magnetic field is applied [8], ytterbium-sensitised systems – in these, both a CM compound and an ytterbium-based compound are used to give enhanced photoluminescence with a shorter lifetime [9].

Our collaborators have also recently developed zinc oxide functionalised with mesogenic ligands. These materials are liquid crystalline themselves and can be dispersed into other LCs. There has been a great deal of work performed on zinc oxide as emitters because they have wide direct band-gaps yielding bright room temperature emission; if these new materials offer a route towards dispersing zinc oxide into LCs then a great deal of additional functionality may be unlocked, and an alternative gain material for LC lasers may have been found.

It was seen in Chapter 6 that the photoluminescence of the CMs initially increased when pumped. This was ascribed to the oxygen content around the cluster. This means that there is potential for the materials to be used as oxygen sensors due to the change in photoluminescence properties in the presence/absence of oxygen.

Perovskite based liquid crystal lasers

Enhanced amplified spontaneous emission of liquid crystal/perovskite structures

Although I have shown enhanced amplified spontaneous emission from our LC/perovskite structures, I have not seen true lasing. The next step with this work would be to further optimise the devices to create lasers.

The reduction is amplified spontaneous emission threshold when moving from 50 to 80% reflectors is encouraging and thus it is likely that a further improvement in reflector quality will allow sufficient amplification of the emission to allow us to see lasing. One way of improving the reflectivity would be to create stacks of multiple chiral nematic LC films, including left- and right-handed chiral nematics to approach 100% reflectivity. Additionally, I could optimise the layer thicknesses in the stack – by

considering their refractive indices I should be able to improve the optical path through the stacks (here our devices were 390 nm thick, half the wavelength of the photoluminescence of the perovskite I was using).

Another step would be to process a second chiral nematic LC directly onto the top of the stack to create a sandwiched cavity without the need for an adhesive resin layer. This would both remove the need for the gold layer and allow lasing from both ends of the cavity. This step is complicated by the current requirement for depositing the LC as both the curing conditions and the need for a mechanically rubbed alignment layer may damage the perovskite.

The perovskite layer itself could also be improved. The perovskite field is constantly evolving with higher efficiency materials being regularly reported. Furthermore, some of the deposition techniques used here (such as spin coating the protective polymer layer) do not allow precise thickness control. By using methods that allow ultra-smooth layers of perovskite, I could create improved devices (and this would aid in optimising the layer thicknesses as discussed above).

The perovskite emission wavelength can easily be tuned across the visible by changing the halogen content (increasing the bromide content blue-shifts emission for example) and the chiral nematic LC reflectors can be engineered to match the emission peak; this means that our technique offers potential for creating a wide range of devices emitting at different wavelengths.

Furthermore, because the chiral nematic LC photonic band-gap may be influenced by a variety of external stimuli it may be possible to create devices which may have their output wavelengths tuned in-situ – for example by applying electric fields, as described in Chapter 4.

Perovskite-based distributed feedback lasers

There are a variety of avenues for further work using our perovskite-based distributed feedback lasers. Particularly, due to the semiconductor nature of the perovskite materials used, the distributed feedback lasers presented here provide a potential route to the exciting prospect of an all-electrically pumped perovskite laser– a device that will have a multitude of commercial applications from sensors to lab-on-chip technology.

Furthermore, because the emission wavelength of the perovskite is determined by the halogen composition, exposing a perovskite to a halogen gas can result in a change in

the emission wavelength. This means that they offer potential for use as halogen gas sensors.

Other work using perovskite materials

It is possible to create nanocrystals of perovskites [10]. These are brightly emissive and there are a range of material compositions that may be created and so the peak emission wavelength can be varied continuously across the visible spectrum. Currently, these cannot be dispersed into LCs without significant aggregation. However, if they could be made to disperse at high concentrations (such as by functionalising them in some way) that would open up vast avenues of potential research and would greatly simplify the manufacture of LC lasers (and would dispense with the need for the layered structures discussed above). Unlike the phosphorescence clustomesogens, these nanocrystals fluoresce (and I have already shown that the perovskite material can lase in Chapter 7); additionally, the perovskites used in my work absorb at 550 nm so would not interfere with the photo-curing process the way the clustomesogens and some dyes do.

Additionally, the nano-imprinting technique used in this work offers huge potential in and of itself. It is the first example of 2D in-plane structuring of perovskites and there are many more potential patterns that could be utilised than simple gratings. This means that the technique could be used to create and improve devices such as LEDs and solar cells, and also in applications such as wave-guiding or plasmonics.

References

1. W. Cao, A. Muñoz, P. Palffy-Muhoray, and B. Taheri, *Nat. Mater.*, 2002, **1**, 111.
2. C.-W. Chen, H.-C. Jau, C.-T. Wang, C.-H. Lee, I. C. Khoo, and T.-H. Lin, *Opt. Express*, 2012, **20**, 23978.
3. H. Coles and S. Morris, *Nat. Photonics*, 2010, **4**, 676.
4. F. Castles, S. M. Morris, J. M. C. Hung, M. M. Qasim, and H. J. Coles, *Nat. Mater.*, 2012, **1,** 2.
5. F. Castles, S. M. Morris, J. M. C. Hung, M. M. Qasim, A. D. Wright, S. Nosheen, S. S. Choi, B. I. Outram, S. J. Elston, C. Burgess, L. Hill, T. D. Wilkinson, and H. J. Coles, *Nat. Mater.*, 2014, **13**, 817.
6. A. Yoshizawa, *RSC Adv.*,2013, **3**, 25475
7. H. J. Coles and M. N. Pivnenko, *Nature*, 2005, **436**, 997.
8. Y. Molard, A. Ledneva, M. Amela-Cortes, V. Cîrcu, N. G. Naumov, C. Mériadec, F. Artzner, and S. Cordier, *Chem. Mater.* 2011, **23**, 5122.
9. Unpublished work
10. S. Pathak, N. Sakai, F. Wisnivesky Rocca Rivarola, S. D. Stranks, J. Liu, G. E. Eperon, C. Ducati, K. Wojciechowski, J. T. Griffiths, A. A. Haghighirad, A. Pellaroque, R. H. Friend, and H. J. Snaith, *Chem. Mater.*, 2015, **27**, 8066.

Appendix 1 – Templating at the interface between the chiral nematic and isotropic phases

A1.1 – Introduction

In Chapters 3 and 4 of this thesis, I presented work to polymer-template the smectic A and chiral nematic liquid crystal (LC) phases. Additionally, work has been performed to polymer-template blue phase LCs [1]. However, no work has yet been performed on photo-curing at the interface of different LC phases. In this Appendix, I describe my work to polymer-template LC materials at the interface between the chiral nematic and isotropic phases.

I describe work to polymer-stabilise chiral nematic droplets in an isotropic matrix. When this was washed out and refilled with an achiral, nematic LC, the isotropic regions exhibited nematic behaviour. This means that I have created a device that consists of chiral nematic droplets in a nematic texture –something that does not occur naturally.

A1.2 – Experimental

Initially, I created mixtures containing 29.4 wt% UCL-011-K1 (a mixture of reactive mesogens, photoinitiator and thermal inhibitor, DIC), 2.4 wt% R5011 (chiral dopant, Merck) and the nematic LC E7 (Sigma Aldrich). This mixture was a chiral nematic LC which contained reactive mesogens and so could be photo-cured.

This mixture was filled into 5 μm-thick planar aligned cells (Instec). The texture of the resulting LC was checked using optical polarising microscopy and it was seen that it exhibited the Grandjean texture of a chiral nematic LC, as shown in Fig 1a. This material was then heated to just below the isotropic texture (57.5°C) where it exhibited a Maltese cross pattern (Figure 1b) and to (58°C) where it exhibited a texture of chiral nematic droplets on an isotropic background, as shown in Fig 1c. Above 58°C the LC existed wholly in the isotropic state (and so appeared black on an optical poalrising microscope).

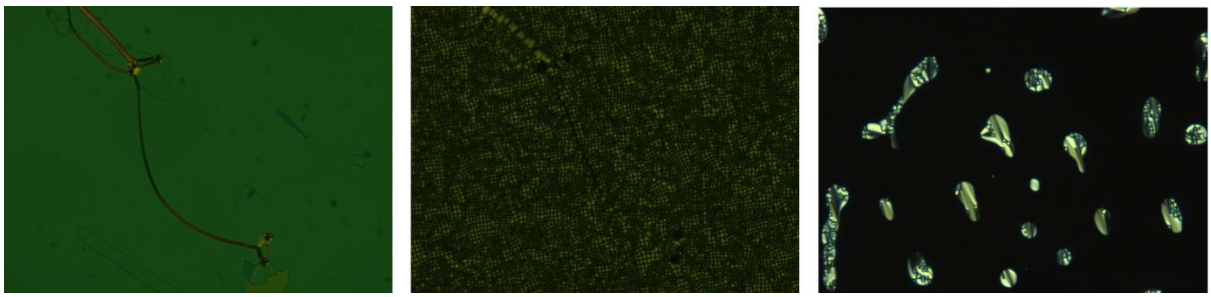

a) b) c)

Figure 1 - Optical polarising microscopy images of the texture of a chiral nematic liquid crystal in a planar aligned cell at a) 20°C, b) 57.5°C and c) 58°C.

My first step was to photo-stabilise the texture illustrated in Fig 1c – a pattern of chiral nematic droplets on an isotropic texture. The mixture was held at 58°C and photo-cured. Due to the temperature dependence of the texture, a 360 ±5 nm notch filter was used on the UV light source to avoid any unnecessary heating during the photo-curing process. The device was photo-cured for 6 seconds from each side and then allowed to cool to room temperature. The texture before curing is shown in Fig 2a – coloured shapes exist on a darker background. After photo-curing, the pattern is maintained, although the background appears blue, rather than black – as shown in Fig 2b. There is no change seen when rotating between crossed polarisers. The photo-curing extended the temperature range of the texture from ~0.2°C (57.9-58.1°C) to a much wider range extending from 20°C to over 200°C.

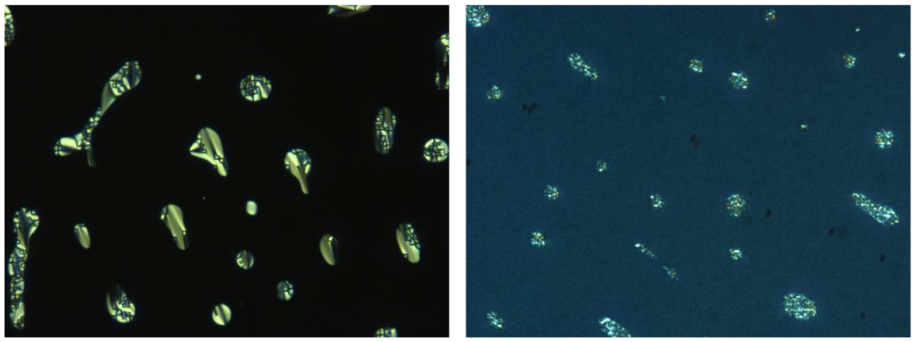

a) b)

Figure 2 – Liquid crystal held at the interface between the isotropic and chiral nematic phase a) before and b) after photo-curing.

Upon applying fields to this device, there was no change in the droplets although the background changed colour, as shown in Fig 3. Fig 3 shows the device when no field has been applied (Fig 3a) and when a 200 V/µm had been applied (Fig 3b).

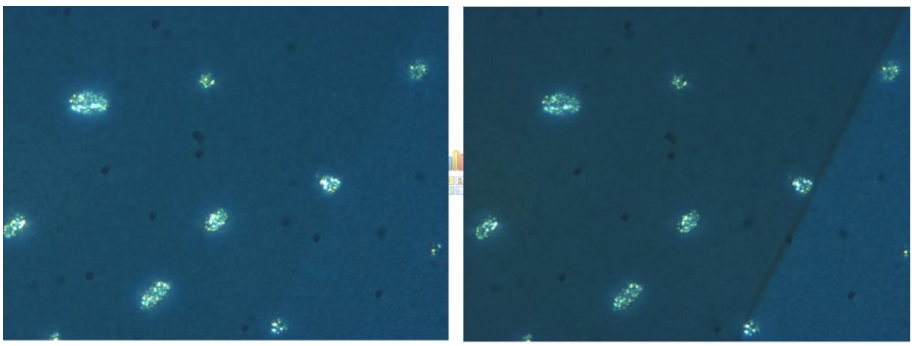

a) b)

Figure 3 - Polymer-stabilised liquid crystal a) before and b) after application of a 200 V/µm electric field (the electrode region is on the left). Results taken at 20°C.

These devices were then washed out by placing the cells in acetone for 48 hours and leaving them to dry for 6 hours. The resulting devices appeared black when inspected using optical polarising microscopy. When these devices were refilled with a nematic LC (E7), the texture returned, as shown in Fig 4. However, for these templated samples, the background now changes between crossed-polarisers. The bright state is shown in Fig 4a and the dark state in Fig 4b. Thus, the background texture is more indicative of a nematic phase than the isotropic phase previously seen.

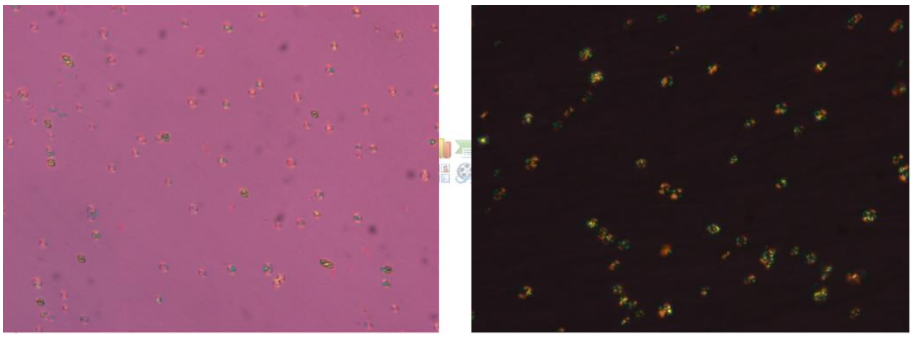

a) b)

Figure 4 - Polymer-templated liquid crystals in the a) bright and b) dark state. Results taken at 20°C.

In the case of these polymer-templated LCs, when an electric field is applied, the background colour now changes as illustrated in Fig 5; again this is behaviour more akin to a nematic LC than the isotropic phase.

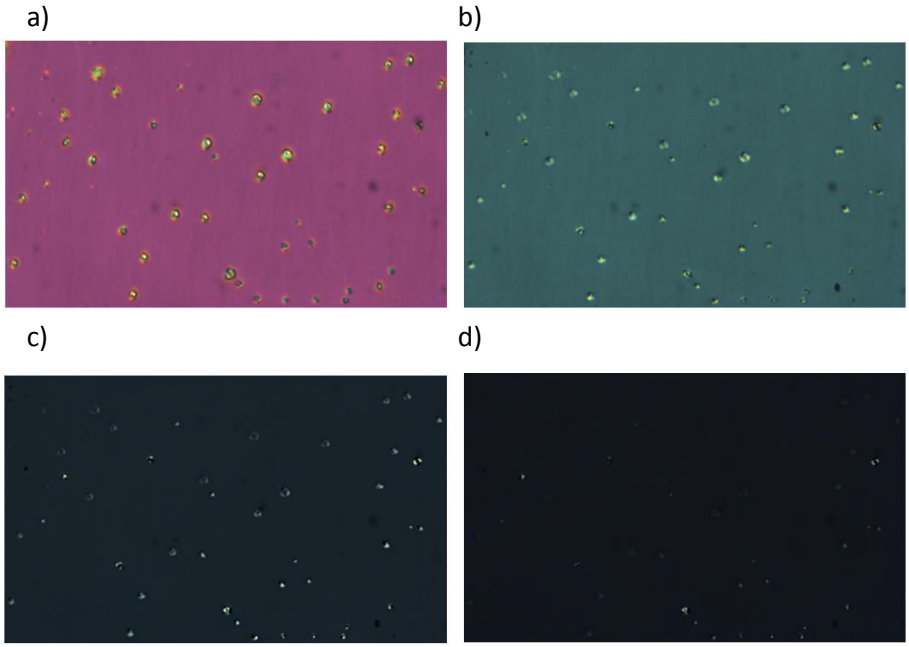

Figure 5 - Polymer-templated liquid crystal with an electric field applied: a) 0 V/µm; b) 10 V/µm; c) 20 V/µm; d) 30 V/µm. Results taken at 20°C.

By curing at a slightly lower temperature (57.5°C) the Maltese cross phase boundary texture (Fig 6a) may be locked into the 'Maltese cross' pattern (Fig 6b). Whereas the Maltese cross pattern exists over a range of ~0.2°C (57.4-57.6°C) in the unpolymerised mixture, it exists from 20°C to over 200°C in the polymer-stabilised sample. Furthermore, the device could be washed out and refilled as shown in Fig 6c. Upon refilling, it regained the pattern of the original LC and the polymer-stabilised device

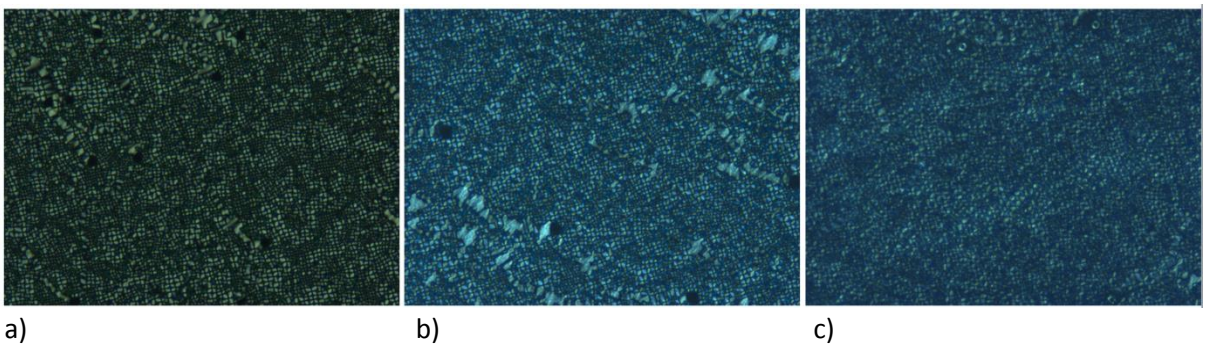

Figure 3 - Maltese cross pattern a) before photo-curing (57.5°C), b) after photo-curing (20 °C) and c) After washing out and refilling with a nematic liquid crystal (20°C).

A1.3 – Conclusion

In this Appendix, I have demonstrated the potential for applying polymer-templating to the interface between different LC phases to achieve systems that do not occur naturally (such as chiral nematic droplets in a nematic phase). This study requires more work to be completed, however it highlights the versatility of polymer-templating LCs as a means of imparting order onto achiral materials, as well as to create systems that do no naturally occur.

A1.4 – References

1. F. Castles, F. V Day, S. M. Morris, D.-H. Ko, D. J. Gardiner, M. M. Qasim, S. Nosheen, P. J. W. Hands, S. S. Choi, R. H. Friend, and H. J. Coles, *Nat. Mater.*, 2012, **11**, 599.